







Ingeniaritza Goi Eskola Teknikoa  
Escuela Técnica Superior de Ingeniería  
Bilbao

eman ta zabal zazu



UPV EHU

**UNIVERSIDAD DEL PAÍS VASCO / EUSKAL HERRIKO UNIBERTSITATEA  
ESCUELA TÉCNICA SUPERIOR DE INGENIERÍA DE BILBAO  
BILBOKO INGENIERITZA GOI ESKOLA TEKNIKOA**

Ph.D. THESIS

**DEVELOPMENT OF CATALYTIC METHANE REFORMING  
SYSTEMS INTEGRATING HYDROGEN SELECTIVE PdCu  
MEMBRANE MODULES**

A dissertation submitted to the University of the Basque Country  
for the degree of Ph.D. in Chemical Engineering by:

**Esther Acha Peña**

**Bilbao, 2012**

Thesis Advisors: **Prof. José Francisco Cambra Ibáñez**  
**Prof. Pedro Luis Arias Ergueta**

ISBN: 978-84-9860-986-8

*A mis padres*  
*Porque soy quien soy gracias a ellos*

*Giving up is the ultimate tragedy.*  
Robert J. Donovan



*Tras un largo camino de aprendizaje, que espero sea un punto y seguido, me gustaría agradecer a mis directores de tesis por su apoyo, disponibilidad, sugerencias y las horas y horas de discusiones científicas. También querría agradecer al grupo Supren y al departamento de Ingeniería Química y del Medio Ambiente por el apoyo mostrado. En especial a Ana, Astrid e Iratxe. Si mi experiencia durante el PFC no hubiera sido tan buena, estoy segura de que ahora no estaría aquí!*

*Durante estos años, que han sido como una carrera de obstáculos donde a veces cuesta levantarse, han sido imprescindibles también todas esas charlas del día a día con el resto de la becaria. Y es que, lo más difícil de este trabajo es esa parte de la que ni siquiera se puede escribir, porque no hay nada. A vosotros espero haberos agradecido en su momento el apoyo y, por supuesto, las risas y buenos ratos, que espero que sigan por muchos años. En esta parte me gustaría recordar a la gente de ECN. It was a pleasure to be at ECN for some months, not only for the scientific point of view but also in a personal side. I would like to specially mention the spam people and my flat mates.*

*Y por último, pero no menos importante, a mi familia que siempre ha estado ahí, tanto a mis padres como al precioso regalo que me hicieron que son mis hermanas. A Mar y Susana. Y por supuesto, a mis amigas, por todos esos momentos buenos, como el de “los martes cierran y se van a esquiar”, y malos compartidos juntas. Estoy orgullosa de ser parte de vosotras! Y como no, a ti que has vivido las subidas y bajadas en primera persona, y que siempre has conseguido que me volviera a levantar. Esta tesis es casi tan tuya como mía, ¡gracias por estar ahí!*

*Por último me gustaría agradecer la ayuda económica recibida para llevar a cabo esta tesis doctoral al Ministerio de Educación y Ciencia y al Gobierno Vasco.*





# **TABLE OF CONTENTS**



# Contents

TABLE OF CONTENTS	VIII
<u>List of tables</u>	XVI
<u>List of figures</u>	XVIII
<u>Abstract</u>	1
<u>Laburpena</u>	3
<u>Resumen</u>	5
<b>1. STATE OF THE ART</b>	<b>11</b>
1.1 Hydrogen uses	13
1.2 Hydrogen production from natural gas	14
1.2.1 Natural gas	14
1.2.2 Chemical processes	15
1.3 Catalysts	17
1.3.1 Supported Ni-based catalysts for CPO	18
1.3.2 Supported Ni-based catalysts for SR	20
1.4 Hydrogen purification membranes	22
1.4.1 Pd and PdCu membranes	23
1.4.2 PdCu phase diagram	24
1.4.3 Electroless plating	29
1.4.4 Electroless deposition of Cu on Pd membrane	31
1.4.5 Mechanism of Cu electroless plating	35
1.4.6 Alloying of PdCu membranes	37
1.4.7 Hydrogen transport in dense Pd alloy membranes	40
1.4.8 Effect of reforming mixtures on PdCu membrane performance	43
1.5 Membrane reactor	49
<b>2. SCOPE AND OBJECTIVES</b>	<b>59</b>
<b>3. EXPERIMENTAL PROCEDURES</b>	<b>65</b>
3.1 Bench-scale pilot plants description	67
3.2 Catalyst preparation	69

3.3	Catalyst characterization	70
3.3.1	Elemental chemical analysis	70
3.3.2	X-Ray diffraction	71
3.3.3	Electron microscopy	72
3.3.4	Nitrogen adsorption isotherms (BET)	73
3.3.5	Temperature programmed reduction (TPR)	74
3.3.6	X-ray photoelectron spectroscopy (XPS)	74
3.4	Catalyst activity tests	75
3.5	Membrane preparation	76
3.6	Membrane characterization	78
3.7	Membrane permeance measurements in pure H <sub>2</sub>	78
3.8	Membrane permeation measurements in complex mixtures	79
3.9	Membrane permeation measurements with H <sub>2</sub> S addition	80
<b>4.</b>	<b>EXPERIMENTAL RESULTS. CATALYSTS</b>	<b>83</b>
4.1	Thermodynamic and diffusion studies of hydrogen production processes	85
4.2	Catalysts performance in methane CPO, wet-CPO and SR	95
4.3	Catalysts characterization	102
4.3.1	Chemical analysis (ICP)	102
4.3.2	Scanning electron microscopy (SEM) and transmission electron microscopy (TEM)	102
4.3.3	X ray diffraction	104
4.3.4	Nitrogen adsorption isotherms (BET)	108
4.3.5	Temperature programmed reduction (TPR)	111
4.3.6	X-ray photoelectron spectroscopy (XPS)	113
4.4	Discussion	119
<b>5.</b>	<b>EXPERIMENTAL RESULTS. MEMBRANES</b>	<b>123</b>
5.1	Membrane preparation	125
5.1.1	Plating recipe	125
5.1.2	Kinetic study of Cu plating	127
5.1.3	Membrane alloying	128
5.2	Visual analysis	131
5.3	Gas permeation measurements	132

5.4	Membrane morphology	141
5.5	Discussion	147
<b>6.</b>	<b>EXPERIMENTAL RESULTS. PROCESS INTEGRATION</b>	<b>151</b>
6.1	Coke formation in the membrane plant (MP)	153
6.2	Process integration parameters selection	158
6.2.1	Feed pressure	158
6.2.2	Sweep gas flow	161
6.3	Membrane performance under complex mixtures	164
6.4	Membrane lifetime during pure H <sub>2</sub> and complex mixture tests	170
6.5	Membrane performance with H <sub>2</sub> S addition	180
6.5.1	H <sub>2</sub> S and H <sub>2</sub> mixture (I)	180
6.5.2	CPO process with H <sub>2</sub> S addition	182
6.5.3	Permeance recovery test (I)	184
6.5.4	H <sub>2</sub> S and H <sub>2</sub> mixture (II)	185
6.5.5	Wet-CPO process with H <sub>2</sub> S addition	187
6.5.6	Permeance recovery test (II)	188
6.5.7	Complete lifetime of the M8 membrane	189
6.5.8	M8 membrane characterization	191
6.6	Discussion	197
<b>7.</b>	<b>CONCLUSIONS AND FUTURE RESEARCH</b>	<b>203</b>
	<b>APPENDIX</b>	<b>211</b>

## **List of tables**

Table 1.1. Review of some recipes for electroless plating of Cu used in the literature.....	34
Table 1.2. Alloying methods for some PdCu membranes used in the literature.....	38
Table 1.3. Comparison of the H <sub>2</sub> S effect on PdCu membranes. ....	48
Table 3.1. Recipe of the metal solution for Cu plating. ....	76
Table 3.2. Recipe of the reducing solution for Cu plating. ....	77
Table 4.1. S/C and O/C ratios of the CPO and wet-CPO conditions. ....	85
Table 4.2. Results of the external and internal mass transport criteria for the PP with the equilibrium (Eq conv) and the experimentally observed (Obs conv) conversions for 30Ni/MgO at CPO and 1 bar. ....	93
Table 4.3. Results of the external and internal mass transport criteria for the PP with the equilibrium (Eq conv) and the experimentally observed (Obs conv) conversions for 30Ni/MgO at wet-CPO and SR at 1 bar. ....	94
Table 4.4. Results of the external and internal mass transport criteria for the PM with the equilibrium (Eq conv) and the experimentally observed (Obs conv) conversions for 30Ni/MgO tested with M8 membrane in CPO and wet-CPO at 3.5 bar(g).....	94
Table 4.5. Deviations, (inlet-outlet)/inlet in %, of C, O and H material balances during the CPO tests with 30Ni/MgO, 40Ni/MgO and 40Ni/Al <sub>2</sub> O <sub>3</sub> at 1 bar. ....	95
Table 4.6. Real Ni content of the catalysts prepared for hydrogen production measured with ICP. ....	102
Table 4.7. Average crystallite size of the fresh and calcined catalysts. ....	107
Table 4.8. Al <sub>2</sub> O <sub>3</sub> , NiO and Ni crystallite sizes in the fresh, reduced and used 40Ni/Al <sub>2</sub> O <sub>3</sub> catalyst. ....	108
Table 4.9. Surface area and pore data of the prepared catalysts and supports. ....	110
Table 4.10. XPS spectra peaks and their relative atomic percentage area of the freshly-reduced and used catalysts in wet-CPO at 1200 h <sup>-1</sup> and S/C 0.5-3.0. ....	115
Table 4.11. Atomic element ratios determined by XPS for fresh and used catalysts in wet-CPO at 1200 h <sup>-1</sup> with S/C=0.5-3. ....	118

Table 4.12. Catalysts Ni/Mg or Ni/Al ratio calculated from the ICP composition and compared to the XPS results. ....	118
Table 5.1. Recipe for PdCu membrane electroless plating, [1]. ....	125
Table 5.2. Hydrogen permeation performance of PdCu and Pd membranes reported in literature and in this work. ....	133
Table 5.3. Standard deviation of the Pd wt% calculated for membranes composition by metal layer thicknesses measured by SEM and the number of points analysed in each membrane ring. ....	134
Table 5.4. Correlation index values obtained in the hydrogen permeance results at 673 K. ....	134
Table 5.5. Correlation index values obtained in the hydrogen permeance results at 673 K and 773 K. ....	136
Table 5.6. Activation energies calculated for M6, M7 and M8 membranes and for some PdCu, Pd, PdAg and PdAu reported in the literature. ....	137
Table 5.7. EDX composition of two membranes on the outside (Out) and inside (In) of the metal layer after alloying and after the hydrogen permeance test. ..	143
Table 5.8. Images of blackish and whitish area and spots observed in some membranes after Cu plating. ....	143
Table 5.9. Comparison of the average surface morphology with the black, dull and white areas of membranes after Cu plating. ....	144
Table 5.10. Comparison of the average surface morphology of the membranes after the Cu plating, the alloying and the H <sub>2</sub> permeance tests. ....	145
Table 5.11. Surface composition study of the M7 membrane from the third batch. ....	146
Table 5.12. SEM images of the membranes that were not dense after alloying. ....	147
Table 6.1. Reaction conditions in R1 and their effect in coke formation in MM. ....	155
Table 6.2. Average composition of the 316 Stainless steel (wt%). ....	156
Table 6.3. Test conditions in the catalytic reactor and in the membrane module for the analysis of the optimal feed pressure. ....	159
Table 6.4. Average composition produced in the catalytic reactor and fed to the membrane module. ....	160
Table 6.5. The employed process operating conditions and mixtures dry composition in the complex mixtures tested with M6. ....	166
Table 6.6. Average percentages of the outflow of the catalytic reactor and fed to the membrane module at different operating conditions. ....	168

Table 6.7. Lifetime summary of the M7 membrane. ....	175
Table 6.8. Lifetime summary of the M8 membrane. ....	179
Table 6.9. Elemental composition measurements performed at three different positions of the M8 samples with SEM-EDX. ....	194

## **List of figures**

Figure 1.1. World natural gas production Source: Energy Information Agency (2007), International Energy Outlook 2007. ....	14
Figure 1.2. Diagram of hydrogen production from natural gas reforming integrating hydrogen selective membranes [65]. ....	23
Figure 1.3. Phase diagram for Pd-H system at standard pressure [67]. ....	24
Figure 1.4. Crystal structure of the PdCu alloy. Body centred cubic (bcc) on the left, and face centred cubic (fcc) on the right [83]. ....	25
Figure 1.5. Phase diagram of the PdCu alloy [86]. ....	26
Figure 1.6. Hydrogen permeability data of PdCu membranes over ceramic supports with between 1-27 $\mu\text{m}$ thickness from the literature [81, 87-92]. ....	27
Figure 1.7. Hydrogen permeability values (proportional to circle diameter) of PdCu membranes over ceramic supports with metal thickness of 1-13 $\mu\text{m}$ from the literature at different temperatures and with different compositions. In blue colour [88-91, 94] and in purple colour McKinley and Nitro [87]. ....	28
Figure 1.8. Effect of the temperature change on the hydrogen permeability of PdCu membranes with different composition. Estimated data from [93]. ....	29
Figure 1.9. An electrode with lower electrode potential ( $E^0$ ) will reduce ions of an electrode with higher electrode potential [99]. ....	30
Figure 1.10. Electroless copper deposition rate as a function of pH [112, 113]. ....	33
Figure 1.11. Two types of coalescence of the three dimensional crystallites (TDC): (a) coalescence with proper filling and (b) coalescence without proper filling [99]. ....	36
Figure 1.12. Effect of the surface roughness in the light refraction [99]. ....	37



Figure 1.13. Energetically favoured surface structure of PdCu. White: Cu (100) surface. Grey: Cu atoms. Black: Pd atoms. [131].....	40
Figure 1.14. H <sub>2</sub> transport in dense Pd alloy membranes.....	40
Figure 1.15. Schematic representation of hydrogen concentration variation when diffusing through a supported dense metallic membrane. ....	43
Figure 1.16. Atomic Force Microscopy (AFM) image published in [141] showing the result of annealing a 80 nm Pd film in oxygen at 1173 K for 1 h.....	45
Figure 1.17. Air purge representation and implications for nitrogen leakage and surface area increase [98].....	46
Figure 1.18. Hydrogen permeance results for 60 wt% Pd – 40 wt% Cu alloy membranes as a function of temperature. Reported in Morreale et al. [147].....	48
Figure 2.1. Main research areas of this Ph.D. thesis.....	62
Figure 3.1. Diagram and image of the bench-scale pilot plant PP for catalysts activity tests. ....	67
Figure 3.2. Nomenclature of the flows involved in the membrane reactor. ....	68
Figure 3.3. Diagram of the membrane plant.....	69
Figure 4.1. Thermodynamic effect of temperature on methane conversion with CPO and wet-CPO processes with S/C ratio from 0.5 to 3 at 1 bar. ....	86
Figure 4.2. Thermodynamic effect of temperature on methane conversion with CPO and SR processes with S/C ratio from 0.5 to 3 at 1 bar. ....	86
Figure 4.3. Thermodynamic effect of temperature on hydrogen yield with CPO and wet-CPO processes with S/C ratio from 0.5 to 3 at 1 bar.....	87
Figure 4.4. Thermodynamic effect of temperature on hydrogen yield with CPO and SR processes with S/C ratio from 0.5 to 3 at 1 bar.....	87
Figure 4.5. Thermodynamic effect of pressure on methane conversion in CPO, wet-CPO and SR processes at 1073 K. ....	88
Figure 4.6. Thermodynamic effect of pressure on hydrogen yield in CPO, wet-CPO and SR processes at 1073 K.....	88
Figure 4.7. Thermodynamic effect of S/C ratio on methane conversion in wet-CPO and SR processes at 1 bar and 1073 K.....	89
Figure 4.8. Thermodynamic effect of S/C ratio on hydrogen yield in wet-CPO and SR processes at 1 bar and 1073 K.....	89

Figure 4.9. Activity results of 40Ni/MgO catalyst in CPO conditions at 1 bar in the PP.....	97
Figure 4.10. Activity results of 30Ni/MgO catalyst in CPO conditions at 1 bar in the PP.....	97
Figure 4.11. Activity results of 40Ni/Al <sub>2</sub> O <sub>3</sub> in CPO conditions at 1 bar in the PP.....	98
Figure 4.12. Activity results of 30Ni/MgO, 40Ni/MgO and 40Ni/Al <sub>2</sub> O <sub>3</sub> at 1 bar, 600 h <sup>-1</sup> and 1073 K in CPO and wet-CPO conditions in the PP. ....	99
Figure 4.13. Activity results of 30Ni/MgO, 40Ni/MgO and 40Ni/Al <sub>2</sub> O <sub>3</sub> in the PP at 1 bar, 600 h <sup>-1</sup> and 1073 K in SR conditions. A: methane conversion results, B: H <sub>2</sub> yield results. ....	100
Figure 4.14. Activity results of 30Ni/MgO, 40Ni/MgO and 40Ni/Al <sub>2</sub> O <sub>3</sub> at 1 bar, 1200 h <sup>-1</sup> and 1073 K in CPO and wet-CPO conditions in the PP. ....	101
Figure 4.15. Activity results of 30Ni/MgO, 40Ni/MgO and 40Ni/Al <sub>2</sub> O <sub>3</sub> at 1 bar, 1200 h <sup>-1</sup> and 1073 K in SR conditions. A: methane conversion results, B: H <sub>2</sub> yield results in the PP. ....	101
Figure 4.16. SEM images of the Ni/MgO catalysts. A: 30Ni/MgO. B: 40Ni/MgO. ....	103
Figure 4.17. SEM image of the 40Ni/Al <sub>2</sub> O <sub>3</sub> catalyst. ....	103
Figure 4.18. TEM images of the Ni/MgO catalysts: A: 30Ni/MgO. B: 40Ni/MgO. ....	104
Figure 4.19. TEM image of the 40Ni/Al <sub>2</sub> O <sub>3</sub> catalyst. ....	104
Figure 4.20. XRD diffraction spectra of the freshly-calcined 30Ni/MgO and 40Ni/MgO catalysts with the NiO and MgO diffraction patterns. ....	105
Figure 4.21. XRD diffraction patterns of the freshly-calcined 40Ni/Al <sub>2</sub> O <sub>3</sub> catalyst with the NiO and Al <sub>2</sub> O <sub>3</sub> diffraction patterns. ....	106
Figure 4.22. Nitrogen adsorption-desorption isotherms of the MgO support and Ni/MgO catalysts.....	109
Figure 4.23. Nitrogen adsorption-desorption isotherms of the $\alpha$ -Al <sub>2</sub> O <sub>3</sub> support and the Ni-Al <sub>2</sub> O <sub>3</sub> catalyst. ....	109
Figure 4.24. TPR profiles of the 30Ni/MgO, 40Ni/MgO and 40Ni/Al <sub>2</sub> O <sub>3</sub> catalysts with 0.1 g of sample and heated at 10 K/min. ....	112
Figure 4.25. TPR profiles of 30Ni/MgO. A: heated with 3 K/min and maintained at 1073 K 4 h, and the temperature variation in time. B: heated at 3 K/min and 10 K/min. ....	112
Figure 4.26. XPS spectra of the fresh-reduced Ni-based catalysts. ....	114

Figure 4.27. XPS for 30Ni/MgO catalyst fresh-reduced and used in wet-CPO at 1200 h <sup>-1</sup> with S/C=0.5-3.....	115
Figure 4.28. XPS for 40Ni/MgO catalyst fresh-reduced and used in wet-CPO at 1200 h <sup>-1</sup> with S/C=0.5-3.....	116
Figure 4.29. XPS for 40Ni/Al <sub>2</sub> O <sub>3</sub> catalyst fresh-reduced and used in wet-CPO at 1200 h <sup>-1</sup> with S/C=0.5-3.....	117
Figure 5.1. SEM surface image of membranes plated with the original recipe at 323 K (A), and with the simplified recipe at 318 K (B). .....	126
Figure 5.2. Cu(OH) <sub>2</sub> precipitate formation probability in electroless copper baths [4]. .....	126
Figure 5.3. Comparison of the Cu thickness obtained at different plating times. ....	127
Figure 5.4. Membrane colour before the Cu plating (left), after Cu plating (middle) and after alloying (right). .....	128
Figure 5.5. Comparison of membranes alloyed in the three different batches: in the first one (A), in the second one (B) and in the third one (C). .....	129
Figure 5.6. Membrane ring piece for the EDX composition measurement after the alloying. ....	130
Figure 5.7. EDX composition of two membranes with different plating times (0.5 and 1.0 h) on the outside and inside of the metal layer after alloying at 673 K for 150 h in the first batch. ....	130
Figure 5.8. Hydrogen permeance in the membranes while alloying in nitrogen gas at 673 K. ....	131
Figure 5.9. Delamination problems could be visually predicted in the membranes before and after Cu plating. ....	132
Figure 5.10. Hydrogen permeance results for PdCu membranes at 673 K using the experimental n value at 2 bar of pressure difference. ....	134
Figure 5.11. Hydrogen flux results for PdCu membranes with the experimental n value tested at 673 K and 773 K. ....	135
Figure 5.12. Comparison of the prepared PdCu membranes permeance values with some reported in the literature [8, 32-35]. Circle diameter is proportional to permeance. Small points represent phase limits. ....	139
Figure 5.13. Hydrogen permeability, n=0.5, with temperature cycles in inert and hydrogen atmospheres at 673 K. ....	140

Figure 5.14. Hydrogen permeability test, $n=0.5$ , with temperature cycles in inert and hydrogen atmospheres at 773 K at 2 bar of pressure difference. ....	141
Figure 5.15. SEM image of the M2 after Cu plating (A), after alloying (B), and after the hydrogen permeance test at 673K (C).....	142
Figure 5.16. SEM images of the M7 membrane from the third alloying batch. (A) SEI image, (B) COMPO image.....	146
Figure 6.1. Membrane plant (MP) scheme for hydrogen production in R1 followed by hydrogen purification in MM. ....	153
Figure 6.2. Coke formation in the membrane module during the initial tests with complex mixtures. ....	154
Figure 6.3. Stainless steel tube located in the MM. ....	154
Figure 6.4. The steel tube of the membrane module after tests at 1073 K.....	156
Figure 6.5. Membrane module with the hard chrome plating inside. ....	157
Figure 6.6. Coke formed in the “stainless steel membrane” inside the hard chrome plated tube. ....	157
Figure 6.7. Hard chrome plated tube and the “stainless steel membrane” covered with a high temperature tape after performing CPO. ....	158
Figure 6.8. Feed pressure effect on the amount of hydrogen produced by CPO in the catalytic reactor (reactor temperature 1073 K and methane feed flow 700 NmL/min) and on the purified H <sub>2</sub> flow in the MM at 673 K. ....	159
Figure 6.9. Feed pressure effect on hydrogen recovery at different sweep gas flows (M6 membrane at 673 K). ....	161
Figure 6.10. Hydrogen recovery of M7 (membrane area of 53.7 cm <sup>2</sup> ) in the membrane module with 0.54 NL/min of H <sub>2</sub> diluted with Ar to obtain different feed gas compositions and using different sweep gas flows at 3.5 bar pressure difference across the membrane and 773 K.....	162
Figure 6.11. Hydrogen recovery of M7 (membrane area of 53.7 cm <sup>2</sup> ) in the membrane module with 0.54 NL/min of H <sub>2</sub> diluted with Ar to obtain different feed gas compositions and using different sweep gas flows at 2.0 bar pressure difference across the membrane and 773 K.....	163
Figure 6.12. Hydrogen production via CPO in R1 at 1073 K with 0.35 g of catalyst and 600 h <sup>-1</sup> of WHSV and purification in MM with M7(membrane area 53.7 cm <sup>2</sup> ) at 773 K with a 20 % of sweep gas and 3.5 bar of pressure difference.....	165

Figure 6.13. Performance of the CPO-membrane system. R1 at 1073 K with 0.35 g of catalyst and 600 h <sup>-1</sup> of WHSV, membrane module with M6 (membrane area of 58.9 cm <sup>2</sup> ) at 673 K with a 20 % of sweep gas, feed pressure=3.5 bar(g) and sweep gas at atmospheric pressure. ....	167
Figure 6.14. Hydrogen production in the catalytic reactor R1 at 1073 K with 0.35 g of catalyst and 600 h <sup>-1</sup> of WHSV and purification with M8 (membrane area of 33.0 cm <sup>2</sup> ) at 773 K in the MM with a 20 % of sweep gas at 3.5 bar of pressure difference.....	169
Figure 6.15. Pure hydrogen and nitrogen permeance throughout the M6 lifetime (feed pressure=2 bar(g) and sweep gas at atmospheric pressure).....	171
Figure 6.16. M6 membrane peeling off detected at 3600 h.....	172
Figure 6.17. SEM image of the detached M6 metal layer, x18000 magnification.....	173
Figure 6.18. XRD diffractogram of the used M6 membrane.....	175
Figure 6.19. Pure hydrogen and nitrogen permeance throughout M7 membrane lifetime measured with 2 bar of pressure difference.....	176
Figure 6.20. Picture of the detached metal layer in the close cap area of the used M7 membrane.....	177
Figure 6.21. SEM images of both end caps of the M7 membrane at x2.000 and x10.000 enlargements. ....	177
Figure 6.22. Pure hydrogen and nitrogen permeance throughout M8 membrane lifetime (feed pressure=2 bar(g) and sweep at atmospheric pressure).....	179
Figure 6.23. Hydrogen and nitrogen permeance through the M8 membrane in 100 and 40 ppmv H <sub>2</sub> S/H <sub>2</sub> mixtures and in pure H <sub>2</sub> at 773 K (feed pressure=2 bar(g) and sweep at atmospheric pressure).....	181
Figure 6.24. H <sub>2</sub> S addition effect on hydrogen production in R1 via CPO with 40Ni/MgO at 600 h <sup>-1</sup> (1073 K) and purification in MM with M8 (773 K) at 3.5 bar of pressure difference. ....	183
Figure 6.25. First thermal cycle in hydrogen atmosphere attempt with M8 for hydrogen permeability and leakage recovery (feed pressure=2 bar(g) and sweep at atmospheric pressure).....	184
Figure 6.26. Hydrogen and nitrogen flow through the M8 membrane in 100 and 60 ppmv H <sub>2</sub> S/H <sub>2</sub> mixtures and in pure H <sub>2</sub> at 773 K (feed pressure=2 bar(g) and sweep at atmospheric pressure).....	186

Figure 6.27. H <sub>2</sub> S addition effect on hydrogen production in R1 via wet-CPO with 40Ni/MgO at 600 h <sup>-1</sup> and 1073 K, and on purification in MM with M8 at 773 K and with 3.5 bar of pressure difference. ....	188
Figure 6.28. Second thermal cycle in hydrogen atmosphere attempt with M8 for hydrogen permeability and leakage recovery (feed pressure=2 bar(g) and sweep at atmospheric pressure). ....	189
Figure 6.29. Complete lifetime summary of the M8 membrane. Pure hydrogen and nitrogen flows were measured at 2 bar(g) of feed pressure and atmospheric in the sweep. ....	190
Figure 6.30. M8 membrane general image at the end of its lifetime (A) and in the area exposed to the highest H <sub>2</sub> S concentrations (B).....	192
Figure 6.31. M8 membrane image at the end of its lifetime near the area exposed to the lowest H <sub>2</sub> S concentrations. ....	192
Figure 6.32. SEM images of both endings of the used M8 membrane at x2.000 and x10.000 enlargements.....	193
Figure 6.33. XRD diffractogram of the M8 membrane at the end of its lifetime in the area exposed to the high H <sub>2</sub> S concentrations (High) and the low concentrations (Low) in both internal (A) and external (B) surface of the metal layer. ....	195
Figure 6.34. Position of the most intense diffractogram peaks observed in the M8 membrane and the characteristic maximums of pure Pd.....	196
Figure 7.1. Structure and approach of the research presented in this thesis. ....	205

---

**ABSTRACT**

This thesis is concerned with the preparation of Ni-based catalysts and hydrogen selective PdCu membranes that allow the integration of hydrogen production and purification processes. With this purpose, Ni-based catalysts supported over MgO and Al<sub>2</sub>O<sub>3</sub> were prepared by wet-impregnation method. These catalysts' activity was tested in CPO, wet-CPO and SR processes from methane, varying operating parameters according to the kinetics and thermodynamics of the reactions involved. Their characterization was performed using diverse chemical and structural techniques. Ni/MgO showed better activity and stability than Ni/Al<sub>2</sub>O<sub>3</sub> operating at CPO or wet-CPO with S/C=0.5 at 1073 K and atmospheric pressure.

PdCu membranes for hydrogen purification were prepared at ECN facilities, in The Netherlands, by electroless plating of Cu over Pd ceramic membranes. The preparation method was optimized in order to prepare thin and dense membranes with a Pd concentration between 44-82 wt% and 0.7-1.7 μm thickness. Membranes were firstly tested under pure hydrogen to study their performance and stability with thermal cycles. Uncontrolled cooling was found to be critical for membranes behaviour.

Once the catalysts and the membranes were prepared and tested, both processes were integrated. Critical process parameters were optimized, such as feed pressure and sweep gas flow, and the problem of coke formation in the membrane module due to CO containing gases was solved. Afterwards, hydrogen purification from complex mixtures produced in the catalytic reactor was analysed. It was concluded that CO did not negatively affect hydrogen permeability and water seemed to have a positive effect on it. Around 60-65 % of the hydrogen fed to the membrane module was recovered in diluted mixtures (20-30 %).

Finally, a more realistic process integration was performed testing the membranes, the catalysts and the integrated process with H<sub>2</sub>S addition, with concentrations lower than 100 ppmv. The used Ni/MgO catalyst was not deactivated. It was observed that sulphur was not irreversibly adsorbed on the membranes surface but led to a decrease of selectivity.





## **LABURPENA**

Tesi honetarako katalizatzaile berriak eta hidrogenoari selektiboak diren PdCu mintzak prestatu dira hidrogenoa ekoizteko eta arazteko prozesuak integratzeko helburuarekin. Helburu hau lortzeko MgO eta Al<sub>2</sub>O<sub>3</sub> euskarriztat dituzten nikelezko katalizatzaileak prestatu ziren inpregnazio hezea metodoa erabiliz. Katalizatzaileen aktibitatea metanotik hidrogenoa ekoizteko hiru prozesuetan (oxidazio partziala, oxidazio hezea eta lurrin bidezko erreformatua) eta lan-baldintza desberdinetan neurtu zen. Katalizatzaileak prestatu eta erabili ondoren teknika kimiko eta estrukturalak erabiliz karakterizatu ziren. Ni/MgO katalizatzaileek jokaera hoberena aurkeztu zuten oxidazio partzialean 1073 K-etan eta presio atmosferikoan edo oxidazio ezean lurrin/karbono erlazio txikiarekin, 0.5ekoa hain zuzen ere.

Hidrogenoa arazteko mintzak Herbehereetan dagoen ECN instalazioetan prestatu ziren, zeramikazko Pd mintzak eta jalkitze ez elektrolitikoak erabiliz. Mintzak prestatzeko metodoa optimizatu zen %44-82 Pd pisutan eta 0.7-1.7 µm-ko PdCu mintz meheak eta selektiboak lortzeko. Mintzen iragazkortasuna eta egonkortasuna aztertzeko lehenengo saiakuntzak hidrogeno puruarekin eta ziklo termikoak erabiliz egin ziren. Kontrolik gabeko hozteak oso kaltegarriak izan ziren mintzen bizi iraupenerako.

Katalizatzaileak eta mintzak prestatu eta banaka probatu ondoren, prozesu biak integratu egin ziren. Hidrogenoa ekoizteko eta arazteko prozesuan garrantzizko parametroak optimizatu ziren, hala nola elikadura presioa eta arraste-gasaren emaria. Aldi berean, CO-z osatutako nahasteek mintz moduluan sortutako koke arazoa ere konpondu zen. Ondoren, hidrogeno arazketa saiakuntzak egin ziren, baina erreaktore katalitiko batetik sortutako gas nahastea zuzenean mintzera elikatuz. Lortutako emaitzetatik ondorioztatu zen CO-ak ez zuela hidrogenoaren iragazkortasunean eragin negatiborik eta bazirudien urak eragin positiboa zuela. Mintzetara heltzen zen hidrogeno diluitutik (%20-30 hidrogeno) %60-65a berreskuratzen zen.

Gas naturalean metanoarekin batera sufre trazak aurkitzen direnez, prozesu osoa (katalitiko eta mintza) sufre konposatu bat gehituta probatu zen. Saiakuntza desberdinak egin ziren 100 ppmb H<sub>2</sub>S baino gutxiagoko gas nahasteekin. Erabilitako Ni/MgO katalizatzailea ez zen desaktibatu sufrearen eraginez. Mintzean sufre adsortzioa itzulgarria izan zen, baina bere H<sub>2</sub>:N<sub>2</sub> selektibitatea jaitsi zen.



## **RESUMEN**

El hidrógeno se presenta en la actualidad como uno de los vectores energéticos del futuro, debido a las ventajas que presenta con respecto a los combustibles empleados hoy en día. Una de ellas es que se puede producir de forma descentralizada, permitiendo, por ejemplo, el aprovechamiento del exceso de energía producido en parques eólicos mediante electrólisis de agua. Otra ventaja se encuentra en su uso en vehículos, disminuyendo la polución, principalmente en las ciudades. Empleando hidrógeno como combustible en vehículos con motor eléctrico y pila de combustible se produce como único producto vapor de agua.

Hasta la completa implantación de la llamada economía del hidrógeno es necesaria una etapa de transición durante la cual se prepare la infraestructura necesaria. En ese periodo se hace necesaria la posibilidad de obtener hidrógeno en grandes cantidades y a un precio competitivo. Con este propósito, y mientras la obtención de hidrógeno mediante energías renovables continúa desarrollándose, la fuente más adecuada de hidrógeno es el gas natural. El principal componente del gas natural es el metano, cuyo porcentaje puede oscilar entre el 85-97% en función del origen del gas. Y esta molécula es la que mayor ratio H:C presenta, por lo que para una misma cantidad de hidrógeno producido se emite menor cantidad de CO (tóxico) o CO<sub>2</sub> (gas de efecto invernadero). Además, apenas produce productos secundarios que puedan ocasionar mayores problemas ambientales.

La tecnología más extendida actualmente en la industria para la producción de hidrógeno a partir de gas natural es el reformado con vapor (RV). Si bien, existen procesos prometedores como la oxidación parcial catalítica (OPC), que es un proceso exotérmico, y la oxidación parcial catalítica húmeda, que presenta ventajas tanto del RV como de la OPC. El empleo de gas natural, de gran accesibilidad debido a la extensa red de gasoductos de la que se dispone en la actualidad, permitiría un arranque competitivo de la energía del hidrógeno y descentralizado.

Además de la necesidad de una producción competitiva frente a los actuales combustibles, debe de tratarse de un hidrógeno de pureza suficiente para ser empleado

en las pilas de combustible. El hidrógeno producido por OPC o RV se encuentra en una corriente mezcla, por lo que es necesaria su purificación. Existen diversas tecnologías implantadas en la industria para la purificación de gases, siendo el PSA (pressure swing adsorption) la más empleada. Esta técnica consiste en la separación de un compuesto gaseoso de una mezcla de gases adsorbiéndolo en un sólido por efecto de la presión. El coste de operación de esta técnica es elevado y es necesario disponer de dos unidades en paralelo para trabajar en continuo. Las membranas selectivas de hidrógeno basadas en Pd son sistemas avanzados para la purificación de hidrógeno de corrientes mezclas. Estas membranas presentan una selectividad infinita a hidrógeno, permitiendo producir una corriente de gran pureza.

El presente proyecto de tesis se encuadra en el escenario anteriormente descrito. Se analizó inicialmente la producción de hidrógeno a partir de gas natural para purificarla a continuación en un módulo dotado con una membrana de PdCu.

Para la producción de hidrógeno a partir de gas natural se prepararon tres catalizadores no convencionales de níquel soportado mediante impregnación húmeda. En estos catalizadores se analizó la influencia de soporte básico (MgO) y ácido ( $Al_2O_3$ ), así como el efecto de añadir distintas cantidades de níquel en el caso del básico (30 y 40%). El porcentaje real de metal activo en estos tres catalizadores se determinó mediante análisis químico y estos fueron entre un 2 y un 6% inferiores al nominal, pero dentro del rango experimental aceptable. Se tomaron imágenes de microscopía electrónica de los catalizadores para estudiar la dispersión del metal activo en los soportes. Se observó que el níquel se encontraba mejor disperso en el soporte básico MgO, de forma homogénea y en pequeñas partículas, que en el soporte de alúmina.

Las propiedades texturales de los catalizadores frescos se estudiaron mediante isotermas de adsorción y desorción de nitrógeno. El área superficial BET de los soportes empleados era bajo, especialmente el soporte de alúmina con  $6.2 \text{ m}^2/\text{g}$ . Tras la deposición de níquel el área superficial varió. Aumentó ligeramente en el soporte alúmina, dada su baja área superficial inicial, y disminuyó en los de MgO, probablemente debido al cierre de poros pequeños como se concluyó por el aumento de su tamaño promedio.

Se determinó también la capacidad reductora de los catalizadores mediante la técnica de reducción a temperatura programada. Los resultados obtenidos mostraban dos picos de reducción del níquel (II) a níquel metálico, que es la fase activa del proceso, alrededor de 698 y 898 K. El primer pico se debía principalmente al NiO libre y el de mayor temperatura al NiO que se encuentra interaccionando con el soporte. En los catalizadores de MgO no se detectaron picos de reducción. Esto se debe a la formación de la solución sólida de Ni/MgO detectada también en bibliografía y que explicaría tanto este efecto, como la buena dispersión observada en las imágenes de microscopía y los resultados de difracción de rayos X.

La actividad catalítica de los catalizadores en OPC, OPC-húmedo y RV se analizó a distintas temperaturas (1073 y 898 K) y velocidades espaciales de gas (600 y 1200 h<sup>-1</sup>). En las condiciones de OPC la conversión obtenida fue prácticamente la de equilibrio a 1073 K y superior a 898 K. En ambos casos la temperatura del lecho era superior a la de control de entrada debido a la exotermicidad del proceso para los tres catalizadores. Comparando a 1073 K los tres procesos de obtención de hidrógeno para cada catalizador y ambas velocidades espaciales, la actividad fue muy inferior en los procesos con presencia de agua. En OPC-húmeda, con bajo contenido en agua, la conversión disminuyó ligeramente hasta el 80 % mientras que el rendimiento a hidrógeno aumentó. En las condiciones de proceso empleadas la actividad de los catalizadores en RV fue baja.

Continuando con la caracterización de los catalizadores estos se analizaron mediante difracción de rayos X (DRX) y espectroscopía de rayos X (SPX) para determinar los principales compuestos que los formaban. En las muestras frescas-reducidas de los catalizadores de MgO se detectó NiO, pero en los mismos ángulos de difracción que el MgO. Esto reforzaba la hipótesis de la formación de solución sólida en este catalizador. Se analizó el tamaño promedio de partícula cristalina tras realizar ensayos de OPC-húmeda y RV y se observó la sinterización de partículas. Mediante los análisis de SPX se determinó la composición química de la superficie de los catalizadores. En las muestras frescas-reducidas los catalizadores de alúmina no se habían reducido completamente, probablemente debido a fuertes interacciones con el soporte. De la misma forma, en los catalizadores de MgO alrededor de la mitad del níquel se había reducido a Ni<sup>0</sup>. En las muestras analizadas tras ensayos de actividad se observó mayor

cantidad de Ni metálico en los catalizadores de Ni/MgO, indicando que si bien su reducción parece complicada por la formación de la solución sólida éste se va reduciendo a lo largo del proceso y se mantiene estable. En la muestra usada del catalizador de Ni/Al<sub>2</sub>O<sub>3</sub> se observó una rápida reoxidación del níquel metálico a NiO. Tal y como se esperaba en los catalizadores probados en OPC-húmeda y RV, no se detectó acumulación de coque que pudiera derivar en una desactivación del catalizador.

Tras los ensayos de actividad realizados con los catalizadores preparados se seleccionaron las condiciones de operación óptimas para posteriormente ser empleadas en la integración de los procesos de producción de hidrógeno seguido de su purificación en el módulo de membrana. Previamente a la integración de los procesos se procedió a preparar y caracterizar las membranas selectivas de hidrógeno.

Las membranas de PdCu se prepararon depositando el Cu mediante deposición no electrolítica sobre una membrana de Pd. Un vez depositado el cobre ambos metales se alearon para completar la mezcla, ya que es el Pd quien tiene la capacidad de disociar la molécula de hidrógeno en dos átomos capaces de difundirse a través de la capa metálica densa. La morfología y espesor de la capa metálica de las membranas se determinó mediante imágenes de microscopía electrónica (SEM) y se observaron superficies homogéneas y brillantes a la vista. Tras analizar imágenes SEM de membranas antes y después de realizar la aleación se concluyó que no era necesaria la completa aleación de los metales para obtener una membrana con alta y constante permeabilidad.

La permeabilidad de hidrógeno de las membranas se determinó mediante ciclos térmicos a 673 y/o 773 K en los que se realizaba un enfriamiento en gas inerte y otro en atmósfera de hidrógeno. La permeabilidad de las membranas se encontraba en el rango de las halladas en bibliografía. Los valores del exponente de presión calculados a partir de los datos de permeabilidad fueron superiores a 0.5, dado el pequeño espesor de la capa metálica de en torno a 1-2 micras. La permeabilidad de las membranas se mantuvo constante durante los ciclos térmicos, y no se detectó fragilización de la capa metálica durante los ciclos en hidrógeno.

La fase inicial de la integración en la planta piloto de la producción y purificación del hidrógeno supuso la optimización de dos parámetros con gran efecto en ambos

procesos: la presión de la alimentación y el caudal del gas de arrastre en la membrana. El mayor ratio de hidrógeno purificado y producido se obtuvo operando a 3.5 bar(g) de presión en la línea de alimentación y con un caudal de gas de arrastre igual al 20% del caudal de entrada al módulo de membrana. En estas condiciones se analizó la purificación de hidrógeno de corrientes complejas producidas en el primer reactor a partir de OPC y OPC-húmeda con los catalizadores preparados. En dichos ensayos el porcentaje de hidrógeno en la corriente producida en R1 varió en función de las condiciones de operación entre un 20 y un 30%. El hidrógeno recuperado en el módulo de membrana fue de en torno al 60-65% y no se observó una desactivación de la membrana como consecuencia del contacto con gases como el CO o CO<sub>2</sub>. La adición de agua pareció tener un efecto positivo en el comportamiento de la membrana.

Dos de las membranas ensayadas con mezclas complejas, M6 y M7, sufrieron enfriamientos incontrolados, algunos de ellos en presencia de hidrógeno. Tras 3500 y 1500 horas de operación, respectivamente, M6 y M7 dejaron de ser selectivas a hidrógeno. Durante el tiempo de operación de la membrana M6 el caudal de nitrógeno, la fuga, a través de la membrana se mantuvo constante, y fue disminuyendo el del hidrógeno. Tras el enfriamiento incontrolado la membrana dejó de ser selectiva y una vez fuera del módulo se observó que el metal se había desprendido del soporte cerámico. En imágenes de SEM se observó que los límites de grano se habían hecho más profundos, debido seguramente al estrés térmico. En la membrana M7 el flujo de hidrógeno se mantuvo hasta el segundo enfriamiento incontrolado momento en el que también el flujo de hidrógeno disminuyó. Tras el ensayo con estas dos membranas se concluyó que el estrés térmico debido a los enfriamientos incontrolados fue crítico para las membranas y que afectaba tanto a su permeabilidad como a la creación de poros.

Por último se realizaron ensayos con una membrana en mezclas de azufre con inerte y con mezclas complejas. Al añadir 100 o menos ppmv de H<sub>2</sub>S en una mezcla con hidrógeno puro, el porcentaje de hidrógeno recuperado en el módulo de membrana disminuía considerablemente, en torno a 75 puntos porcentuales. Pero al retirar el azufre del medio la membrana recuperaba la permeabilidad inicial, lo que implicaba que el azufre no se adsorbía de forma irreversible sobre la superficie metálica. Se analizó también el efecto de la adición de azufre en el proceso integrado de producción y purificación de hidrógeno mediante OPC y OPC-húmeda. En ambos casos 32-33 ppmv

de  $\text{H}_2\text{S}$  no afectaron la actividad del catalizador, si bien la purificación de hidrógeno disminuyó de un 80 % en OPC y un 60 % en OPC-húmeda iniciales a un 40 % al añadir  $\text{H}_2\text{S}$ . De nuevo, al retirar el compuesto de azufre la permeabilidad de la membrana se recuperó.

Durante los ensayos con azufre se observó que la fuga de la membrana aumentaba con el tiempo, lo que se puede justificar con un ataque preferente del azufre en los límites de grano o zonas débiles, llegando a crear poros en el metal. Las condiciones húmedas fueron especialmente críticas para la membrana. Al concluir las pruebas con azufre, y cuando la fuga de la membrana era ya muy elevada, ésta se retiró del módulo y se observó que la capa metálica no se había desprendido del soporte de la misma forma que en las dos membranas anteriores. La ruptura de la capa metálica se produjo en la zona de la membrana que trabajó a concentraciones mucho más elevadas a los 100 ppmv alimentados, ya que tras permear el hidrógeno al interior del tubo de la membrana la concentración de azufre al final de la membrana era mucho mayor. Sin embargo, no se observó azufre adsorbido en la superficie, corroborando la teoría de que el azufre no se adsorbió de forma irreversible en la membrana de PdCu.



# **1. STATE OF THE ART**

Hydrogen is foreseen as an important energy carrier in a future sustainable energy society. It can be produced by different sustainable ways, but there will be a transition between nowadays energy structure and the future sustainable situation. During this transition natural gas can be used for hydrogen production. It is the cleanest fossil fuel, and the highest  $H_2/(CO + CO_2)$  ratio can be obtained from its conversion. In most of the hydrogen applications high purity hydrogen is needed and hydrogen selective Pd alloy membranes can be used to fulfil this objective. An overview of the existing technologies for hydrogen production and the published research about  $H_2$  producing catalytic processes and PdCu membranes will be presented in this chapter.



The problems associated with petroleum use like pollution, global warming, oil spills and our increasing dependence on fossil fuels, have made it necessary to find new alternatives for the energy supply. The petroleum barrel production per year is already higher than the amount of petroleum that is discovered. Hydrogen is foreseen by many as an important energy carrier in the future. Today it is used in petroleum refinery, ammonium and fertilizers production and in fuel cells. The latest advances in fuel cells point to them as a very promising solution in the automobile sector to reduce air pollution. Hydrogen economy presents another important advantage: its decentralized production is possible. It can be generated from hydrocarbons, mainly from natural gas steam reforming; from water electrolysis, which requires energy that can be supplied from renewable sources like solar or wind; and from biomass or coal gasification. In most of these processes hydrogen is generated in a mixed stream. The main requirement of PEM fuel cells is that they need high purity hydrogen, so a purification unit is necessary. For this purpose there are different techniques: “pressure-swing adsorption” (PSA) which is widely used in industry and hydrogen selective membranes, which are a promising future technology mainly for decentralized production. Nowadays around half of the hydrogen is produced from natural gas, which is the hydrocarbon with the highest H:C ratio. Hydrogen production from natural gas is studied here as an option for the transition to a hydrogen economy. In the future the ideal situation would be hydrogen production from renewable energies to really have a green energy scenario.

## 1.1 Hydrogen uses

Nowadays the main uses of hydrogen are fossil fuel processing and ammonia production, but it is also interesting as an energy carrier. Hydrogen use in transportation, via fuel cells, would burn relatively cleanly without carbon emissions. It is years that prestigious motor companies like BMW, Toyota, Chrysler and Daimler Benz are working in the development of this system, and they have some prototypes. The energy conversion efficiency of fuel cells, defined as the fraction of the fuel’s energy that is available as mechanical energy at the wheel, is intrinsically higher than that of internal combustion engines since it is not limited by the Carnot cycle. The maximum theoretical electrical efficiency of the fuel cell stack can be 85 % [1], because of the internal resistance, etc. And the practical electrical efficiency of the fuel cell could be 50-70 % [2].

## 1.2 Hydrogen production from natural gas

### 1.2.1 Natural gas

Natural gas is formed from the decomposition of organic material trapped between rock layers. The composition of the natural gas varies depending on the origin of the reserve. Its average composition is 85 % CH<sub>4</sub>, 10 % C<sub>2</sub>H<sub>6</sub> and the rest is a mixture of C<sub>3</sub>H<sub>8</sub>, C<sub>4</sub>-C<sub>8</sub>, CO<sub>2</sub>, N<sub>2</sub>, H<sub>2</sub>S and He. The main gas reserves are located in the Middle East and in the Soviet Union, see Figure 1.1. One of the main advantages of natural gas is its high versatility. It can be used in the industry, for household use, in cogeneration, electric generation with combined cycle, etc.

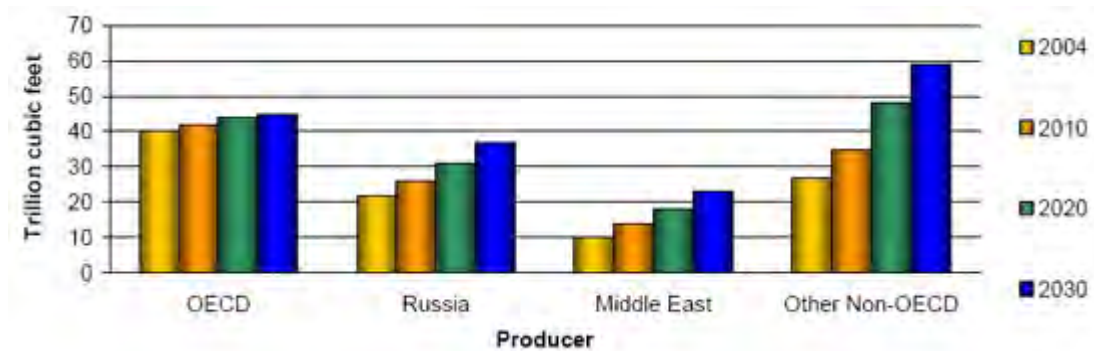
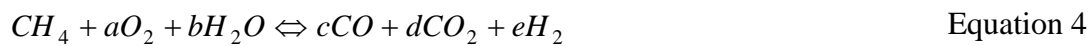


Figure 1.1. World natural gas production Source: Energy Information Agency (2007), International Energy Outlook 2007.

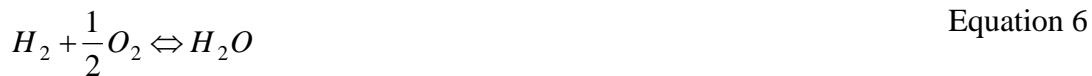
Natural gas is a less polluting fuel than coal or petroleum. Its combustion produces between 40 and 45 % less carbon dioxide than coal and 20-30 % less by-products than petroleum per energy unit. The emission of solid particles, nitrogen oxides, ashes and sulphur oxides is also smaller. As a consequence of all these environmental advantages the use of natural gas in countries with strict environmental regulations is encouraged. In Spain, natural gas demand in 2009 was 402.5 TWh, according to the Spanish energy regulator's annual report to the European Commission 2010. On the other hand, the main disadvantage of natural gas is that it has to be imported. In the European Union the demand is higher than the production, which also involves a necessity of source diversification and a high investment in new gas pipelines.

### 1.2.2 Chemical processes

The main processes for hydrogen production from natural gas are based on the following reactions: methane catalytic partial oxidation, CPO [Equation 1]; methane steam reforming, SR [Equation 2] and wet catalytic partial oxidation, wet-CPO [Equation 4] which is a combination of CPO and SR. Water gas shift process can also occur [Equation 3].



In these processes, oxidation side reactions can also occur:



Nowadays, methane SR is the main process for full-scale hydrogen production. It is a mature technology and operates close to its theoretical limits. Some of the disadvantages of SR are that it is highly endothermic [Equation 2] and that it is a slow reaction compared to CPO [Equation 1]. The advantages of CPO are that it is an exothermic and quick reaction (milliseconds [3]). And the main disadvantages are the catalysts' low stability, the possibility of coke deposition and hot spots formation on the catalysts' surface that can lead to sintering of active sites [4]. Regarding the wet-CPO, it has halfway conditions between SR and CPO with the positive point that it does not require so much energy supply, as it takes advantage of the heat generated from the CPO.

In processes for hydrogen production from methane processes, carbon can be deposited to various degrees according to the endothermic methane cracking, and the slightly exothermic Boudouard reaction or CO disproportionation.



The coke can be removed by steam gasification, Equation 9, or burnt off with oxygen, Equation 10.



Coking can lead to deactivation of both catalyst particles and hydrogen selective membranes due to surface covering. Thermodynamically, the methane steam reforming reaction is out of the region for carbon formation with a  $CH_4/H_2O$  ratio of 3 [5]. However when hydrogen selective membranes are involved, carbon deposition has been found to occur before the thermodynamic limit is reached as shown by Pieterse et al. [6]. De Groote et al. [7] modeled the partial oxidation of  $CH_4$  with steam addition on a  $Ni/MgO/Al_2O_3$  catalyst and found that operating at high pressures lowers the total amount of coke deposited on the catalyst surface. Operating the reactor at high pressure also implies a high partial pressure of oxygen. This leads to a faster combustion of methane, but also to a higher rate of coke burning by oxygen. Methane cracking is accelerated too, but to a lesser extent. Because of higher combustion rates more  $CO_2$  is produced, so that the rate of the reverse Boudouard reaction increases significantly. In methane reforming processes, an increase of pressure has been found to enhance the carbon deposition tendency [8, 9]. It has been suggested that carbon deposition can be attenuated when the metal is supported on a metal oxide with strong Lewis basicity. This occurs because the increase of the Lewis basicity of the support increases the ability of the catalyst to chemisorb  $H_2O$  and these species react with C to form CO, resulting in the reduction of coke formation [10].

Regarding the temperature influence on coke formation in methane catalytic partial oxidation with steam addition it was observed that the total carbon content decreases for higher temperatures [7]. The rate of methane cracking is less influenced by the temperature than the rates of the reverse Boudouard reaction and the coke gasification by oxygen. Wang et al. [11] analysed methanol reforming and observed a lower coke yield at high temperatures (1073 K > 973 K > 673 K > 473 K).

### 1.3 Catalysts

Methane conversion to hydrogen requires high temperature. Using catalysts with low activation energy, high conversions can be obtained at temperatures around 973-1073 K. The active phase present in a catalyst is responsible for the catalytic activity. This phase can be very expensive when using noble metals as platinum, rhodium or palladium. With an adequate support this active phase can be dispersed and stabilized while bringing good mechanical properties to the catalyst. Porous materials, with high surface area per catalyst weight, are normally used as supports. An operational limitation of the catalysts is their deactivation. The principal deactivation causes are:

- Poisoning of the catalytic surface by strongly adsorbed molecules.
- Carbon formation, coking.
- A decrease of the active surface due to thermal surface reconstruction, sintering. This can happen in the CPO due to hot spots in the catalyst surface.
- Loss of active phase due to catalyst erosion.

The employed active metals for methane conversion can be divided into two types, noble metal-based catalysts and “cheap” metal-based catalysts. The noble metal-based catalysts include Rh, Ru, Ir, Pt and Pd [12-14]. They show excellent catalytic performance, but their cost limits their applications in industry [15]. The “cheap” metal-based catalysts include Ni, Co and Cu. Among them, Ni-based catalysts exhibit similar catalytic performance than noble metal ones and have been studied extensively [16]. However, the Ni-based catalysts have been affected by deactivation due to carbon deposition [17] and sintering of Ni particles [18].

In order to improve the capability of Ni-based catalysts to resist carbon deposition, catalysts have been prepared with different methods [19], suitable supports have been selected [20], supports or catalysts have been modified with small amount of noble-metals [21], and promoters with basic properties have been added [22]. For solving the problem of the sintering of Ni particles at high reaction temperatures, noble metals or substances with high thermal conductivity were effective [23].

### 1.3.1 Supported Ni-based catalysts for CPO

#### Different supports.

Supported Ni catalysts have been the most commonly used and easily prepared catalysts. The most extensively investigated support has been  $\gamma$ -Al<sub>2</sub>O<sub>3</sub> [24, 25] due to its large specific surface area, thermal stability and cheap price.

The Ni/ $\gamma$ -Al<sub>2</sub>O<sub>3</sub> catalysts prepared by modified sol-gel method showed relatively high activity in CPO (80 % at 973 K, atmospheric pressure and 10<sup>5</sup> h<sup>-1</sup> GHSV ((volume of feed gas at STP/h)/(volume of the reactor))). However, the conversion of CH<sub>4</sub> decreased on Ni/ $\gamma$ -Al<sub>2</sub>O<sub>3</sub> catalysts prepared by the impregnation method in the long time stability test. In general, carbon deposited gradually on Ni/ $\gamma$ -Al<sub>2</sub>O<sub>3</sub> (10 wt% Ni) due to the acidic property of the support, which finally resulted in catalyst deactivation. Deactivation by carbon deposition was the lowest in Ni/MgO (10 wt% Ni) [26]. For this reason, supports other than  $\gamma$ -Al<sub>2</sub>O<sub>3</sub> have also been investigated, such as ZrO<sub>2</sub>, SiO<sub>2</sub>, La<sub>2</sub>O<sub>3</sub> and Y<sub>2</sub>O<sub>3</sub> [27].

The preparation methods of ZrO<sub>2</sub> affected the catalytic performance of Ni/ZrO<sub>2</sub> (14 wt% Ni) catalysts in CPO [28]. A Ni/ZrO<sub>2</sub> catalyst prepared by the precipitation method showed high catalytic activity (about 84 %), but it deactivated quickly in CPO owing to the large Ni particle sizes which favoured carbon deposition. On the contrary, a Ni/ZrO<sub>2</sub> (14 wt% Ni) catalyst prepared by hydrothermal method possessed small particle sizes, and was active (86 % conversion) and rather stable in life-test [28].

Guo et al. [29] illustrated that the catalytic performance of Ni/SiO<sub>2</sub> catalysts in CPO strongly depended on the size of Ni particles, and Takenaka et al. [30] reported that Ni/SiO<sub>2</sub> catalysts prepared by the impregnation method deactivated rapidly in CPO due to the large size of Ni particles and the weak interaction between Ni and SiO<sub>2</sub>.

Employing rare earth metal oxides as supports can be an effective way to decrease the carbon deposition tendency of catalysts. Fleys et al. [31] observed that Ni/La<sub>2</sub>O<sub>3</sub> (0.16-9.4 wt% Ni) was active and stable in CPO. Y<sub>2</sub>O<sub>3</sub> shows basic properties and could be a potential support for Ni in CPO with high capacity to resist carbon deposition [32].



### Promoters and redox properties

Promoters, mainly noble metals, can improve the catalytic performance of Ni-based catalysts in CPO. Berger-Karing et al. [33] observed that the addition of a small amount of Rh to a Ni/ $\gamma$ -Al<sub>2</sub>O<sub>3</sub> catalyst promoted the reduction of inactive NiAl<sub>x</sub>O<sub>y</sub> to Ni<sup>0</sup> species, which lead to a higher catalytic activity and selectivity. Cheng et al. [34] employed Ru-Ni/Mg(Al)O for converting hot coke oven gas to syngas and found that it exhibited good resistance to coking.

### Preparation methods

Preparation methods of catalysts would also influence the distribution of Ni particles, and affect their catalytic performance in CPO. Berrocal et al. [35] prepared Al-Zr supports by the precipitation method, and evaluated the impregnated Ni/Al-Zr (8 wt% Ni) in CPO. The results showed high activity and selectivity. Solid solutions of Ce-Zr and well dispersed Ni could be obtained by preparing Ni-Ce-Zr catalysts by the co-precipitation method [36]. With the sol-gel method, an efficient way of preparing catalysts, catalysts with elements mixed at molecular level could be obtained. In Ni-Al<sub>2</sub>O<sub>3</sub> (2 and 4 wt% of Ni) prepared by such a method the growth of Ni<sup>0</sup> particles was prevented and the catalysts presented a high resistance to carbon deposition [Song 2009] [37]. The hydrothermal method has been proved to be effective in preparing substances of high purity and good crystallization. ZrO<sub>2</sub> oxide hydrothermally prepared offered small particle size with uniform size distribution [28]. The activity, selectivity and solid solution formation of Ni/MgO catalyst were stronger when preparing them by wet impregnation than by mechanical mixing [38].

### Bimetallic catalysts

In order to improve the performance of catalysts, second active components can be employed, the most common ones are Cu and Co. Habimana et al. [39] prepared Ni/Cu/SBA-15 (5 to 15 wt% Ni) catalysts, and found that they presented better performance than the unmodified ones. The performance of Ni-Cu/Al<sub>2</sub>O<sub>3</sub> improved significantly compared to Ni/Al<sub>2</sub>O<sub>3</sub> and Cu/Al<sub>2</sub>O<sub>3</sub>, and the amount of carbon was negligible on Ni-Cu/Al<sub>2</sub>O<sub>3</sub> [40]. Ag, Fe, Pt and Pd were also applied to prepare bimetallic catalysts with 10 wt% of Ni [41]. Results indicated that Ni-Ag/CeZrO<sub>2</sub> exhibited the best performance and stability for 24 h in CPO. Methane conversions were also high on Ni-Pt/CeZrO<sub>2</sub> and Ni-Pd/CeZrO<sub>2</sub>, but not comparable to the Ag one.

### 1.3.2 Supported Ni-based catalysts for SR

The nickel-based catalysts are also much studied for methane steam reforming due to the relatively low price of nickel compared to other transition metals (Rh, Ru, Pt, Pd, Ir). The majority of the authors found that the most active metals for methane steam reforming are Rh and Ru [42, 43]. Wei and Iglesia recently reported a different relative reactivity of the transition metals: Pt>Ir>Ni>Rh>Ru [44].

Dan et al. [45] analysed the influence of metal addition (1 wt% of Ag and Au) and support modification (CeO<sub>2</sub> and La<sub>2</sub>O<sub>3</sub> 6 wt%) on the catalytic properties of Ni/Al<sub>2</sub>O<sub>3</sub> (7 wt% of Ni) prepared by the wet impregnation method. At 973 K and with a steam-to-carbon ratio of 4, S/C, they found no important effects of metal addition. Coke deposition was found in the Ni/La<sub>2</sub>O<sub>3</sub>-Al<sub>2</sub>O<sub>3</sub> and on the Ni/CeO<sub>2</sub>-Al<sub>2</sub>O<sub>3</sub> catalysts. The addition of Au and Ag has also been reported to reduce coke formation on nickel catalysts during hydrocarbon reforming [46, 47]. Cerium and lanthanum addition to alumina supported noble metal catalysts by the sol-gel method (Pt and Pd) was reported to improve the catalyst stability for methane SR [48, 49].

Other supports like ZrO<sub>2</sub> have also been experimentally analysed for SR [50]. In Co/CeO<sub>2</sub>-ZrO<sub>2</sub> catalyst prepared by wet impregnation and co-precipitation, Lin et al. [51] observed that they had similar physical properties, but impregnation showed the highest catalytic activity. Metal-support interactions were stronger in the impregnation, which allows only partial reduction of cobalt during the pre-reduction, but stronger and with higher activity.

Since MgO is an effective support in order to suppress the coke deposition [52, 53] it has been also used for methane reforming. When using MgO as a support with Ni, the interaction between Ni species and MgO is so strong that NiO-MgO solid solutions are formed. The reducibility of NiO-MgO is lower than that of Ni/ $\alpha$ -Al<sub>2</sub>O<sub>3</sub> and Ni/ $\gamma$ -Al<sub>2</sub>O<sub>3</sub> [52]. The interaction of Ni species with support materials such as Al<sub>2</sub>O<sub>3</sub> and MgO is much stronger than that of noble metals, and it can be related to the low reducibility of the supported Ni catalysts.

Ni/MgO catalysts prepared by the impregnation method and by mechanical mixture have been tested in the literature. Hu et al. [10] observed in the XRD patterns that a fraction of NiO formed a solid solution with MgO in the mechanical mixture calcined at 1073 K and that fraction increased with calcination time, whereas the entire NiO in the NiO/MgO catalyst prepared by impregnation and calcined at 1073 K for 1.5 h formed a solid solution with MgO. They concluded that the impregnation method is preferable to the precipitation and the mechanical mixture for NiO-MgO solid solution catalysts. The precipitation method provided a uniform NiO-MgO solid solution, hence a large amount of NiO was located in the bulk of the solid solution and was not available to the catalytic reaction.

In Ni/ $\gamma$ -Al<sub>2</sub>O<sub>3</sub> (10-13 wt% Ni) catalysts, surface area and pore volume of the one prepared by wet-impregnation were smaller than for the catalysts prepared by co-precipitation and sol-gel [54]. By the wet impregnation method yielded a larger particle size and Ni<sup>2+</sup> was easier to reduce.

Bimetallic catalysts have also been proposed to improve the performance in methane SR. Addition of small amounts of Rh to Ni/Al<sub>2</sub>O<sub>3</sub> (10 and 18 wt% Ni) catalysts increased the activity [55]. Rh-promoted Ni/ $\alpha$ -Al<sub>2</sub>O<sub>3</sub> (10 wt% Ni) catalysts prepared by co-impregnation were reported to show higher activity than Ni/ $\alpha$ -Al<sub>2</sub>O<sub>3</sub> and Rh/ $\alpha$ -Al<sub>2</sub>O<sub>3</sub> and excellent coke resistance in methane reforming with CO<sub>2</sub> [56]. Some other metals have also been tested in the literature. Foletto et al. [57] reported that the addition of small amounts of Pt to Ni/MgAl<sub>2</sub>O<sub>4</sub> (15 wt% Ni) promoted an increase in surface area of Ni metal and caused a considerable increase in methane conversion. The addition of Pt, Pd and Rh to Ni<sub>0.3</sub>Mg<sub>0.97</sub>O solid solution catalysts enhanced the activity and stability in methane reforming with CO<sub>2</sub> [58, 59].

As summarized in the previous sections, there has been a wide research done in the last decades about methane CPO and SR catalysts. In the current work nickel was used as the active metal in the prepared catalysts as it has been observed to have good activity both in methane CPO and SR processes, therefore it can also be expected to be a good choice for wet-CPO. Regarding the support, due to the fact that coke formation is favoured by acidic supports, metallic oxides with strong Lewis basic centres such as MgO were used together with alumina, which has also been widely employed due to its

high metal dispersion capacity.  $\alpha$ - $\text{Al}_2\text{O}_3$  is used instead of  $\gamma$ - $\text{Al}_2\text{O}_3$ , because it is thermally more stable, even if it has a lower surface area [60]. Both supports have been observed in the literature, and explained before, to strongly interact with nickel. This is important as phases that do not interact with the support are easily reducible to metallic nickel, but they also sinter and form carbonaceous structures more easily [61]. The preparation method chosen for the catalysts was the wet-impregnation. This is an easy method and is applied especially when a precursor-support interaction can be envisaged [62]. By wet-impregnation the solute ions may be taken up at the mouth of the pores, which can be desirable when the reaction occurs predominantly near the outer surface of the catalyst pellets as a result of quick reaction or pore diffusion limitation [60].

## 1.4 Hydrogen purification membranes

In most of the hydrogen applications high purity hydrogen is required. One of the most used technique for hydrogen purification is the pressure-swing adsorption (PSA). In the PSA technology hydrogen is separated from a mixture of gases under pressure according to its affinity for an adsorbent material. Different types of adsorbents such as zeolites [63] and activated carbons [64] are used. Hydrogen selective metallic membranes are viable and promising candidates for hydrogen purification processes due to their high hydrogen permeability. The main requirements for the implementation of membranes in a hydrogen purification unit is that they must show high hydrogen permeation and selectivity, appropriate mechanical resistance, chemical and thermal stability at the operating conditions, long and reliable performance and a cost / hydrogen production ratio better than other separation processes. Pd and Pd alloy membranes can be implemented as a hydrogen separation unit, or can be integrated in the reactor where hydrogen is produced, see Figure 1.2. If the catalyst is filled in the membrane reactor hydrogen is separated at the same time when it is produced, decreasing the hydrogen amount in the reactor and allowing to achieve higher conversions at lower temperature, as Le Chatelier law explains.

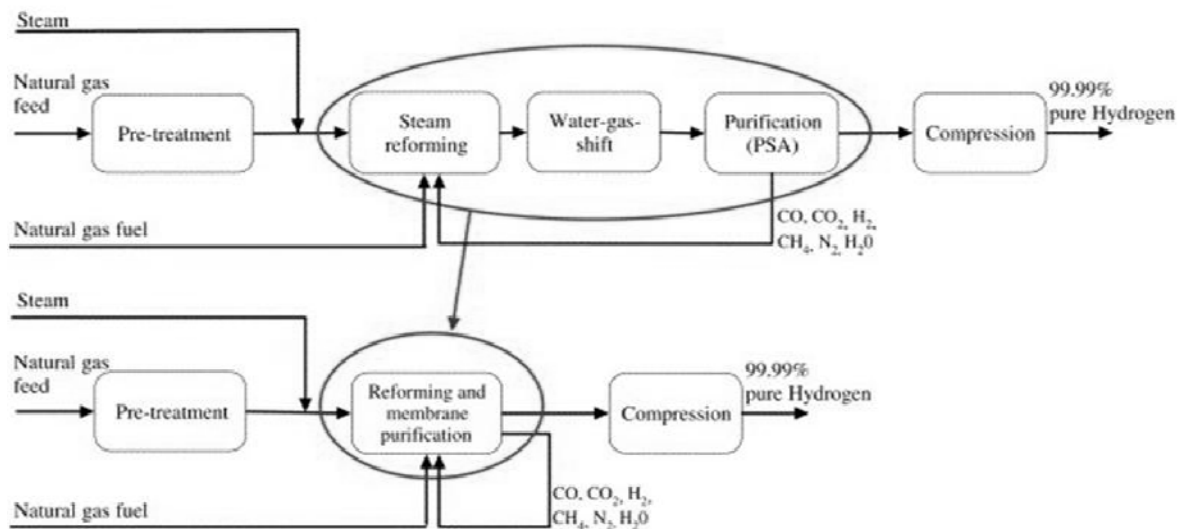


Figure 1.2. Diagram of hydrogen production from natural gas reforming integrating hydrogen selective membranes [65].

#### 1.4.1 Pd and PdCu membranes

Pd has the ability to dissociate hydrogen molecules into hydrogen atoms, whereby membranes separate hydrogen from other gases. Nevertheless, in practice, certain mechanical problems arise due to  $H_2$  embrittlement. At temperatures below 573 K, and pressures below 2.0 MPa [66] the  $\beta$  hydride may nucleate from the  $\alpha$  phase. This results in severe lattice strains (from the  $\alpha$  to  $\beta$  phases the lattice expands by about 4 %), and as a result pure palladium membranes become brittle after a few cycles of  $\alpha \leftrightarrow \beta$  transitions. The Pd-H  $\alpha$  system, depicted in Figure 1.3, has a low H/Pd concentration and the  $\beta$  phase a high hydrogen concentration ( $H/Pd \geq 0.57$  mol% at 298 K). Two phase region,  $\alpha + \beta$ , is also possible in between [67].

In order to improve the membranes resistance to hydrogen embrittlement, different Pd alloys have been studied, such as silver, gold, nickel and copper based ones. In general, the critical temperature for the  $\alpha/\beta$  phase transformation can be lowered considerably by alloying palladium with other metallic elements such as Ag, Cu, Fe and Ni [68-70]. The difference in lattice size between the  $\alpha$  and  $\beta$  phases also decreases in palladium-alloys so that less distortion occurs during hydrogen adsorption-desorption cycles [71, 72]. PdAg alloy membranes have received major attention as they often present higher hydrogen permeability than Pd over a wide temperature range [73]. The role of silver is

explained by its electron donating performance being similar to the one of the hydrogen atom in palladium. This makes the membrane more stable and increases its lifetime. The permeability of PdAg (23 wt% Ag) has been found in the literature to be higher than for pure Pd [74-76]. PdAg membranes with 23-25 % silver are produced commercially by Johnson Matthey [77], and there are other commercially available Pd based hydrogen separation modules today [78-80]. The PdCu alloy is being widely studied due to its better permeance compared to Pd, and its better resistance to hydrogen sulphide and sulphurous components. Kulprathipanja et al. [81] studied the effect of H<sub>2</sub>S addition to Pd and PdCu membranes. They observed that PdCu membranes show higher H<sub>2</sub> permeance than similar Pd membranes and also a higher resistance to H<sub>2</sub>S. Another advantage with respect to pure Pd membranes is the cost reduction due to replacement of Pd with less expensive Cu.

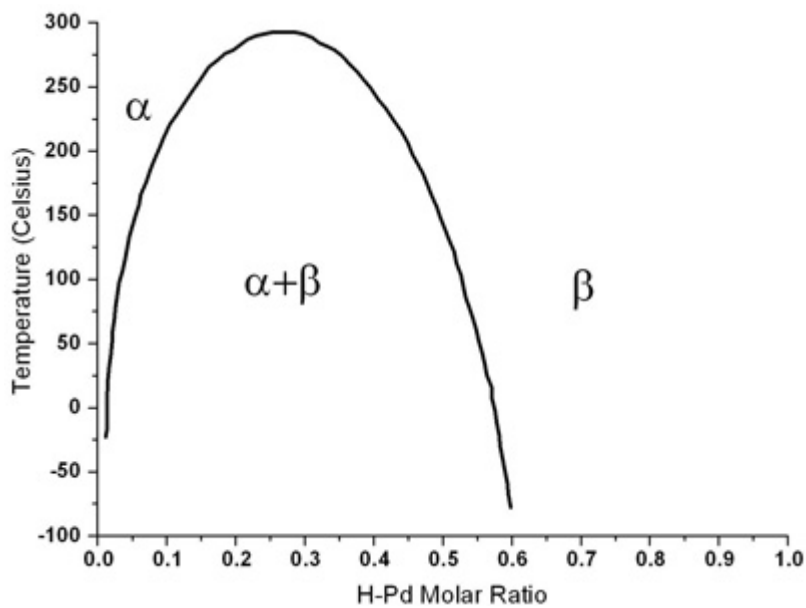


Figure 1.3. Phase diagram for Pd-H system at standard pressure [67].

#### 1.4.2 PdCu phase diagram

The phase diagram of the palladium-copper binary system has been reported in the literature [82]. The PdCu alloy can form two different crystal structures: bcc and fcc, shown in Figure 1.4.

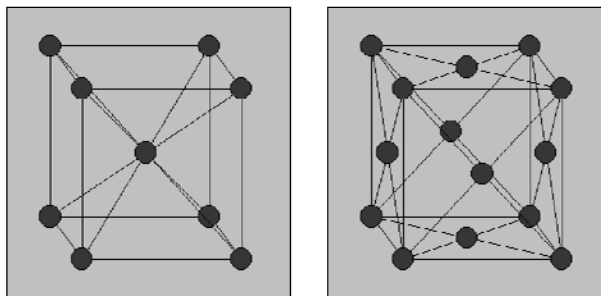


Figure 1.4. Crystal structure of the PdCu alloy. Body centred cubic (bcc) on the left, and face centred cubic (fcc) on the right [83].

As it can be seen in Figure 1.5, the ordered bcc structure is formed at temperatures below 873 K in the composition domain from 48 to 60 wt% of Pd. A two-phase domain is found in the neighbouring composition ranges. For composition lower than 40 wt% of Pd the phase boundary of ordered  $\text{Cu}_3\text{Pd}$  is shown ( $L1_2$  is  $\text{Pm}\bar{3}\text{m}$ , and 1D or 2D LPS are one or two dimensional long-period structures). The disordered fcc phase is formed for the other composition ranges. In general, bcc phase membranes are more permeable to hydrogen due to its tetrahedral configuration, as compared to the octahedral configuration of the fcc phase. The bcc lattice is less dense than the fcc one and the longer distance between the atoms could explain this observation of higher permeance [84]. When hydrogen is diffusing through the PdCu alloy several systems can be formed as: Pd-H, Cu-H, Pd-Cu and Pd-Cu-H. Huang et al. modelled the thermodynamics of these systems to analyse hydrogen diffusion through them [85].

The influence of the PdCu alloy composition on its hydrogen permeance has been widely studied. The structure change of the PdCu alloy means a restructuring of Pd and Cu atoms, which affects membrane permeability. In most of the references the maximum hydrogen permeability was measured with a Pd percentage of 47 mol% or 60 wt%. Hydrogen permeation through dense metal membranes is influenced by the thickness of the metal layer, temperature, alloy composition, pressure difference across the membrane and support, amongst others. A lot of works are based on a patent from McKinley and Nitro in 1969 [87], where they tested PdCu alloy foils of 25  $\mu\text{m}$  at 623 K. Since this study a lot of studies have been published and a more selective comparison can be made nowadays.

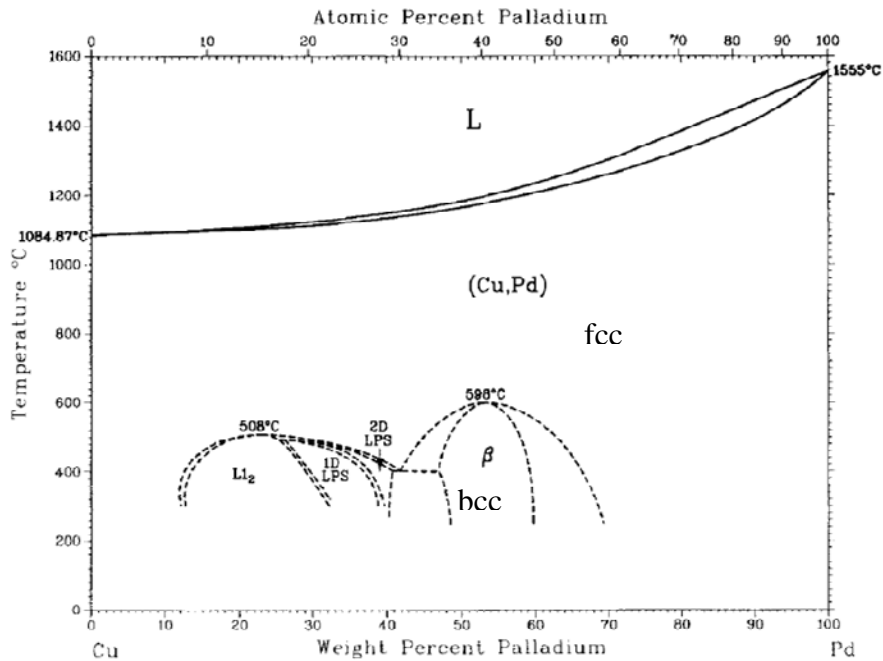


Figure 1.5. Phase diagram of the PdCu alloy [86].

Figure 1.6 shows hydrogen permeability data from the literature related to membrane composition and measured at temperatures in the range 623-773 K. The data depicted with full rhombus is from PdCu membranes over ceramic supports with between 1 and 27  $\mu\text{m}$  thickness [81, 87-92]. The permeability data in open triangles are from McKinley and Nitro [87] performed with 25.4  $\mu\text{m}$  foils. In the data from McKinley the highest permeability was obtained with 60 wt% of Pd, but there are more recent values in the range of higher Cu content, obtained with ceramic support, which also show quite high permeability. This gives a glimpse about the fact that it is not so easy to assume that the Pd<sub>60</sub>Cu<sub>40</sub> composition is always the one with the highest permeability. Nevertheless, it must be taken into account that the possible differences in composition and in thickness of the electroless plated membranes make more difficult to compare their permeability results with those from foil membranes.



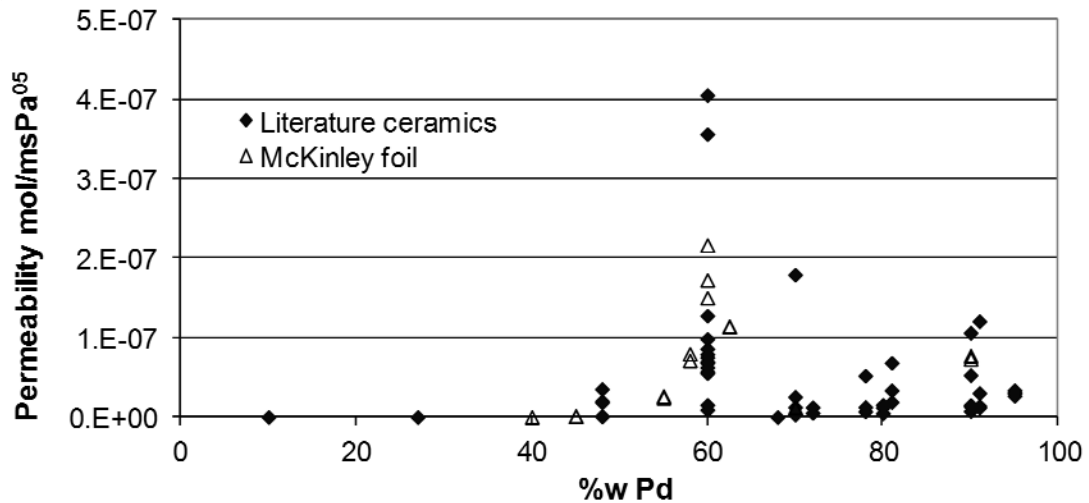


Figure 1.6. Hydrogen permeability data of PdCu membranes over ceramic supports with between 1-27  $\mu\text{m}$  thickness from the literature [81, 87-92].

As it has been explained before, all the metal phase, the thickness and the support influence membranes hydrogen permeance. Figure 1.7 shows a relation between the three most important variables for membranes: temperature, composition and permeability (proportional to the sphere diameter). Temperature and composition are represented by the centre of the circles. These data have been obtained from data reported in the literature for ceramics-supported PdCu membranes with a metal layer thickness between 1 and 13  $\mu\text{m}$  at different temperatures [87-91, 94]. By means of this figure the influence of the metal phase in the recorded permeability value can be easily studied. In order to differentiate the results from McKinley and Nitro [87] their data are shown in darker coloured circles. From the data shown in the figure it can be again observed that, apart from the composition, there are other variables affecting membranes permeability, as for example the metal layer microstructure, which can affect the hydrogen diffusion process and consequently the permeability.

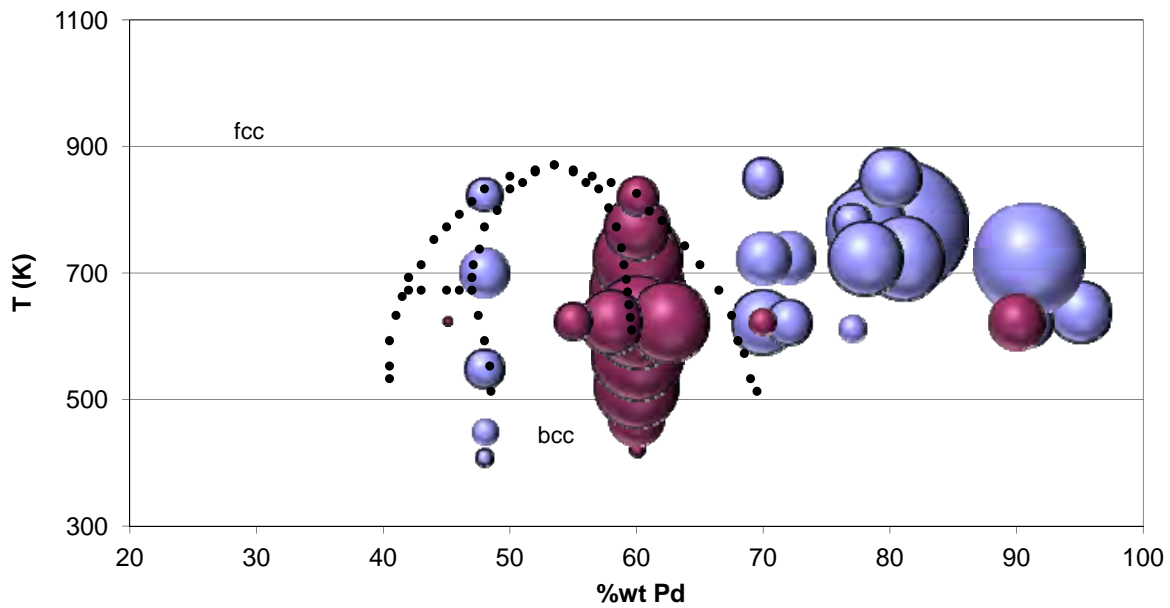


Figure 1.7. Hydrogen permeability values (proportional to circle diameter) of PdCu membranes over ceramic supports with metal thickness of 1-13  $\mu\text{m}$  from the literature at different temperatures and with different compositions. In blue colour [88-91, 94] and in purple colour McKinley and Nitro [87].

The structure of most of the tested membranes in the literature is bcc+fcc or fcc. Howard et al. [93] made PdCu alloy foils (100  $\mu\text{m}$ ) with different compositions and they checked the effect of temperature on permeance (Figure 1.8). The permeability values shown in this figure are calculated from the permeance data depicted and the thickness given in the paper. As it can be observed, permeability of the 60 and 53 wt% Pd membranes decreases at temperatures that coincide with the phase change area. There is no phase change in the 80 wt% Pd membrane, and its permeability therefore increases constantly. As a conclusion it can be said that if the membrane is going to operate just at a temperature below 775 K, the bcc phase is more appropriate, but otherwise, if temperature changes are going to take place, the fcc phase can present a better performance. The adjustment of the atoms during the phase change has a negative effect on the permeability of the membrane.

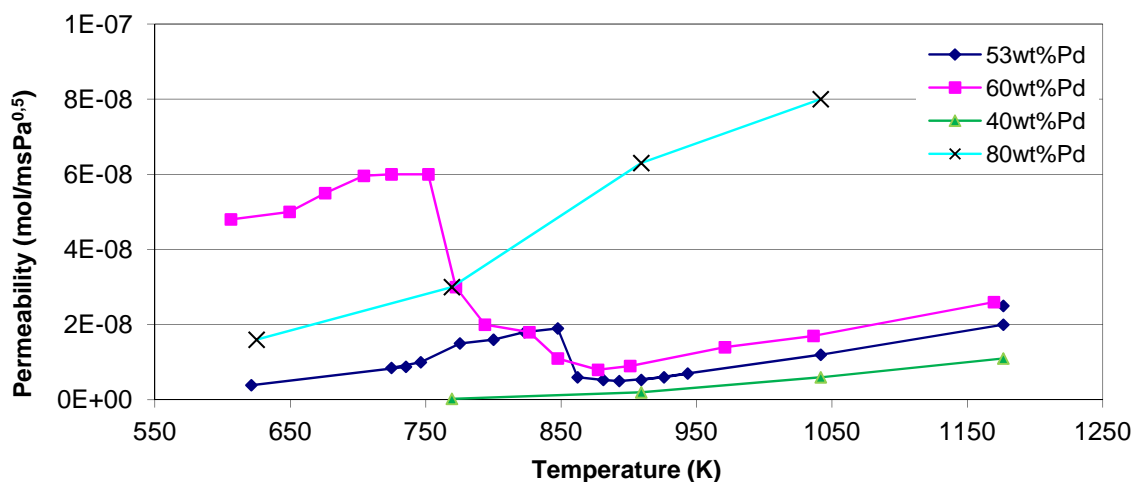


Figure 1.8. Effect of the temperature change on the hydrogen permeability of PdCu membranes with different composition. Estimated data from [93].

### 1.4.3 Electroless plating

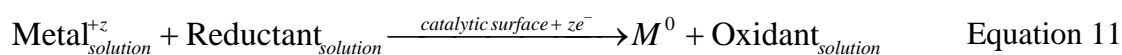
There are different ways of producing PdCu membranes such as: electroless plating, electroplating, physical vapour deposition (PVD or sputtering) and chemical vapour deposition (CVD). From all these techniques electroless plating is the most researched one, since it requires minimal equipment, no exotic precursors and can be performed on any appropriately activated surface [95]. The disadvantages of this technique are the slow kinetics and the possible membrane contamination with the elements from the bath. Metals can be either co-plated or sequentially plated and then alloyed by increasing the temperature [96, 97].

The support, where the metal layer will be plated, influences the stability and permeability of the membrane. Frequently studied supports are porous stainless steel (PSS), Vycor glass and ceramics. The main differences between them are the minimal thickness needed to obtain dense metal layers, and the temperature and pressure range at which membranes can operate. Some advantages of porous steel are that it increases the robustness due to the similar thermal expansion coefficients of Pd and PSS, resulting in better mechanical properties during thermal cycling. The minimum thickness required to obtain a dense Pd film depends strongly on the morphology, roughness, and size of the largest pores of the support surface. As an example, in a symmetric ceramic support (99.8 % alfa-alumina) with 200 nm particles 10  $\mu\text{m}$  thickness was enough. Whereas, in

an asymmetric alfa-alumina support (particle size between 1 and 70 nm) the needed minimum thickness was around 1-2  $\mu\text{m}$  [98]. Ceramics can be synthesized with a smoother surface layer than the steel support, containing very uniform small pore systems, and they are commercially available.

### Theoretical background

The main characteristic of the electroless plating is that a controlled metal deposition occurs on an active surface without any power supply. The plating only occurs on this catalytic surface and the minimum necessary components are a metal salt and an adequate reducing agent. The reducing agent supplies the electrons that the oxidizing agent uses. The overall reaction of the electroless metal deposition is:



The catalytic surface for electroless plating can be the substrate itself or catalytic nuclei of a metal dispersed on a non-catalytic substrate surface. For the Cu plating Pd seeds are usually needed. The reducing or oxidizing behaviour of a metal depends always on the potential of other components present in the solution. The standard electrode potential ( $E^0$ ) is the electromotive force of a cell in which the cathode electrode is a standard hydrogen electrode and the anode is the electrode in question, measured with a concentration of 1 mol/L for aqueous species and 1 atm for gaseous ones. In general, an agent with lower electrode potential will reduce an agent with higher electrode potential, as illustrated in Figure 1.9.

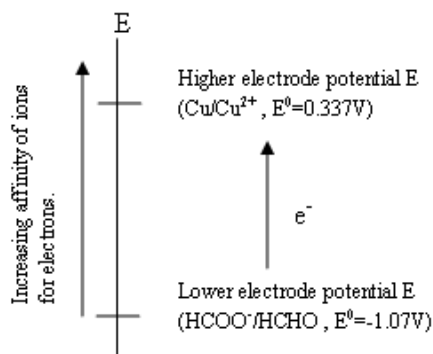
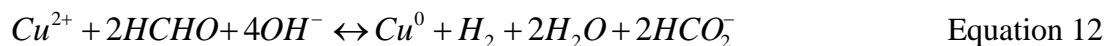


Figure 1.9. An electrode with lower electrode potential ( $E^0$ ) will reduce ions of an electrode with higher electrode potential [99].

#### 1.4.4 Electroless deposition of Cu on Pd membrane

The overall electroless copper plating reaction, when using formaldehyde, is theoretically given as follows, see Equation 12.



Each deposited copper atom will consume four hydroxide ions and two molecules of formaldehyde, but some side reactions can also take place. The most common side reaction is the Cannizzaro reaction (disproportionation of formaldehyde), which consumes additional caustic and formaldehyde, see Equation 13.



The rate of this side reaction increases with increasing pH and temperature [100]. Other side reactions can also occur, consuming formaldehyde and producing unwanted by-products such as cuprous oxide, which can lead to bath instability.

#### Cu electroless plating recipe

As mentioned before, the main components of the plating solution are a Cu containing reactant and a reducing agent, but other additives are normally added such as complexing agents and stabilizers. Some Cu plating recipes used in the literature are shown in Table 1.1. No conclusion about the precursor Cu (II) salt effect on the copper plating could be obtained from the literature, as the electroless plating processes were performed using different recipes and at different conditions, making a comparative discussion very difficult. Copper sulphate seems to produce more uniform surfaces than other copper salts according to Bennett et al. [101].

The type of deposited copper and its physical and morphological properties depend, to a great extent, on the first deposited layers. The complex (ligand) dissociation rate and the deposition rate are closely related. But a deep study of this rate is complex as, for example, at pH higher than 11 there are at least three simultaneously existing complexes in solutions of Cu(II) ions and EDTA: CuEDTA, Cu(OH)EDTA and Cu(H<sub>2</sub>O)EDTA [102].

The reducing agents used in the Cu plating industry are formaldehyde, dimethylamine borane, borohydride, hypophosphite, hydrazine, sugars and dithionite [103]. However, in practice, formaldehyde is the most common one due to the combination of cost, effectiveness and ease of control, despite the health concerns regarding the exposure. Since  $\text{OH}^-$  ions are reactants in the charge-transfer step of the electroless plating, the effect of pH is significant and its value has to be around 12-14.

Complexing or chelating agents, such as tartrate salts, alkanol amines or EDTA compounds, are required in the plating solution due to the fact that simple copper salts are insoluble at pH above 4 and the operating pH is around 12-14. Salts can be easily separated from the plating solution with pH adjustment. The saccharose has also been studied as copper (II) ligand for electroless copper plating solutions. Norkus et al. [104] showed that although with the sucrose the deposition rate was similar, the Cu roughness was higher than with the EDTA. Lin et al. [105] performed a comparison using EDTA, TEA and ethylenediamine (En) as additives or chelating agents in electroless copper plating with formaldehyde as reduction agent and  $\text{CuSO}_4$  as Cu source. They observed that EDTA played an important role of chelating and the plated Cu grain size was more uniform than with TEA and En.

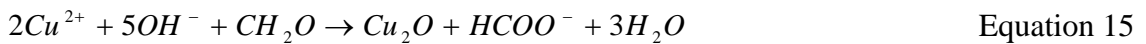
Some other additives can also be present in the electroless plating solution. They are supposed to control parameters such as initiation, plating rate, stability, colour, ductility, etc. Some rate promoters can be: ammonium salts, nitrates, chlorides, chlorates and perchlorates. Examples of components used as stabilizers are mercaptobenzothiazole, thiourea and methyl butynol. Surfactants can also be added to improve deposit characteristics. Some additives, such as 2,2-bipyridyl, have different effects depending on the temperature at which they are used, or the quantity that is added.

### The stability of the plating solution

Formation of metal in the plating solution is hindered by energy barriers; the activation barrier of homogeneous reactions between metal ions and reducing agent, and the barrier of the new phase formation. The stability of plating solutions decreases with the increase of the reactant concentration, the increase of temperature, the decrease in metal ion complexes stability and with the presence of solid foreign particles in the solution.

The most effective solution stabilization method is the introduction of special additives [106].

Due to the plating solution characteristics,  $\text{Cu}(\text{OH})_2$  precipitation can be one of the most important aspects for the bath stability. This precipitation is strongly related with  $\text{Cu}_2\text{O}$  formation, which can also influence the properties of the Cu deposits. There are different suggested reactions leading to  $\text{Cu}_2\text{O}$  formation:



### pH influence in the Cu plating

Electroless copper deposition is affected by the pH in two different ways. Firstly,  $\text{OH}^-$  ions are reactants in the overall reaction. Secondly, it affects various phenomena associated with the structure and composition of the metal-solution interphase. If experimentally observed plating rates are plotted against pH, an initial increase, a maximum value, and finally a decrease of the rate can be observed. The pH value at which the maximum rate is achieved depends on the plating conditions. As an example, the results obtained in an EDTP (ethylenedinitrilo-tetra-2-propanol) type electroless copper bath, where the oxygen was removed by bubbling argon through the solution, are shown in Figure 1.10. The pH values used in the literature for the Cu electroless plating vary from 12 to 14.

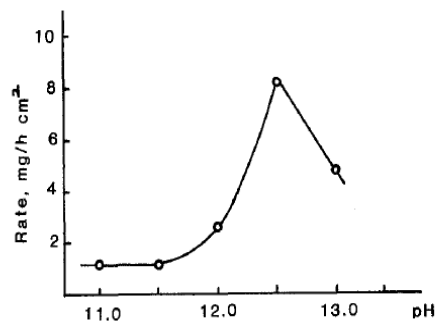


Figure 1.10. Electroless copper deposition rate as a function of pH [112, 113].

Table 1.1. Review of some recipes for electroless plating of Cu used in the literature.

Reagents \ [Ref.] support	[107] Al <sub>2</sub> O <sub>3</sub>	[98] Ceramic	[92] Al <sub>2</sub> O <sub>3</sub>	[88] Al <sub>2</sub> O <sub>3</sub>	[94] Ceramic	[108] Ceramic	[109] PSS	[82] PSS	[110]	[111]	[103] (general recipe)
CuCl <sub>2</sub> ·2H <sub>2</sub> O (g/L)	8.6										
CuSO <sub>4</sub> ·5H <sub>2</sub> O (g/L)		7.8	6.23			8.69	20	25	7.49	12.5	
Cu(NO <sub>3</sub> ) <sub>2</sub> ·2H <sub>2</sub> O (g/L)				9.6	9.6						
Cu salt as Cu(II)*											2.0 g/L
KNaC <sub>4</sub> H <sub>4</sub> O <sub>6</sub> (g/L)	11.3										
NaOH (g/L)	18.0	16	20	11	11	17.78		pH12	pH12	pH12.9	7
(C <sub>2</sub> H <sub>5</sub> ) <sub>2</sub> NCS <sub>2</sub> Na·3H <sub>2</sub> O							5 ppm	5 ppm			
K <sub>4</sub> Fe(CN) <sub>6</sub> ·3H <sub>2</sub> O	400 mg/L			50 mg/L	50 mg/L		35 ppm	35 ppm			
2,2-bypyridyl (mg/L)	80	10	5	20	2	9.6			0-500	150-156	
N,N,N',N'-tetramethylethylenediamine	320 mg/L										
HCHO (>37 %) (mL/L)	14	16	14.0	125	124	15.3	14	25	6.24	6.0	3.9
Na <sub>2</sub> EDTA·2H <sub>2</sub> O (g/L)	19.2						30	47.5			42
Na <sub>2</sub> EDTA (g/L)		40	20.1	29.8	23.3	44.44				37.2	
EDTA (g/L)									8.76		
EDA							100 ppm	112 ppm			
Glycine (g/L)		5									
Tryton X-100 (mg/L)		50	25			0.62					
Tryton X-114 (mL/L)										0.1-0.3	
Additives (in general)											<2g/L
T (K)	303	315-325	338	329	330	323	293-298	293-298	303-343	333	318

\* 2 g/L of Cu (II) = 7 g/L of CuSO<sub>4</sub>·5H<sub>2</sub>O.



### Temperature influence in Cu plating

The temperature range used in the literature is between 293 and 343 K, as reported in Table 1.1. The deposition rate of Cu is remarkably affected by the bath temperature as explained by Oita et al. [110]. Morphology and Cu<sub>2</sub>O precipitation were also influenced by temperature, as co-deposited Cu<sub>2</sub>O on the copper film was observed at 303 K with fine grain structure; while at 343 K there was not Cu<sub>2</sub>O and a coarse grain structure was observed. Varying the temperature from 303 to 353 K the colour of the copper films varied from blue to copper-bright, being the strength of the copper-bright film superior to that of the blue one.

#### 1.4.5 Mechanism of Cu electroless plating

The electroless plating of Cu on Pd membranes can be considered an autocatalytic process. These type of processes are highly complex. They contain many reactions and their mechanism is not yet understood in detail. The reduction reaction and metal deposition on the metal surface is usually attributed to the requirement of a catalytic surface for one or more stages of the process. In accordance with one of the theories, an active intermediate product is obtained on the catalytic surface, which then reduces the metal ions [114]. Firstly, atomic hydrogen, and later a negative hydrogen ion were considered to be the intermediate products [115]. This reaction scheme gives a good explanation of the relationship observed in nickel and copper plating processes. A more versatile explanation of the catalytic mechanism in these processes is based on electrochemical reactions [116]. It is suggested that reducing agents are oxidized on the catalyst surface and the electrons obtained are transferred to metal ions, which are reduced. According to this theory electrons are the active intermediate product. The electrons may be easily transferred along the catalyst without mass transfer resistance, and for this reason, the catalytic reaction occurs because of the exchange of electrons via the metal surface.

Another theory is the mixed potential theory. During the simultaneous oxidation and reduction process on the metal surface, a steady state in the catalytic system of electroless plating is obtained. In that moment, the rates of both electrochemical reactions are equal, and the metal catalyst acquires a mixed potential ( $E_m$ ). This theory was developed by Wagner and Traud (1938) for the purpose of interpreting metal

corrosion processes and it was years after applied to the interpretation of the electroless deposition of copper [117].

After analysing the possible theories of the Cu deposition first steps, the next stage is the thin film formation ( $< 3 \mu\text{m}$ ). This mechanism is characterized by three simultaneous crystal building processes: nucleation (formation), growth, and coalescence of three dimensional crystallites (TDC) [118]. According to this work, in the initial stages the nucleation is the predominant process, and the average density of TDCs increases with time of deposition. Later, the average density of TDCs reaches a maximum and then decreases with time. In the TDC density decreasing stage, the coalescence is the predominant crystal-building process. A continuous electroless film is formed by lateral growth and coalescence of TDC. The process of coalescence deserves special attention, since many physical properties of the deposit depend on the type of coalescence. There are two types of TDC coalescence. Coalescence without the proper filling of the space between TDC results in the incorporation of impurities or additives, generation of stress, voids, and dislocations (Figure 1.11b). Coalescence with filling of the space between TDC, favourably generates joined crystallites (Figure 1.11a) and results in copper films of better quality than in the first type. The process type of coalescence depends to a great extent on the type and concentration of additives in the solution.

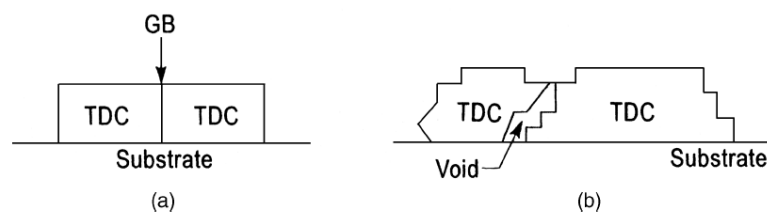


Figure 1.11. Two types of coalescence of the three dimensional crystallites (TDC): (a) coalescence with proper filling and (b) coalescence without proper filling [99].

As a conclusion it could be said that the type of coalescence that takes place during the deposition will influence the roughness of the sample (Figure 1.11b is rougher than Figure 1.11a), and the roughness can give us an idea of the quality of the metal layer. An easy, but approximate way, of analysing the roughness of the sample is the brightness of the deposited Cu. The brightness of a surface is defined as the optical

reflecting power of the surface and it is measured by the amount of light specularly reflected, as depicted in Figure 1.12. In case of the electroless plating deposition there is a direct relationship between the logarithm of the amount of light specularly reflected by a surface and the fraction of the surface having a roughness of less than 1500 Å [119]. As prepared membrane samples can be visually analysed and this can give a hint to its expected performance and leak tests results.

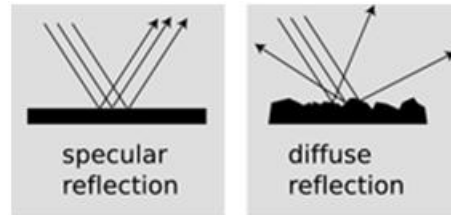


Figure 1.12. Effect of the surface roughness in the light reflection [99].

#### 1.4.6 Alloying of PdCu membranes

When PdCu membranes are prepared by sequential plating of Pd and Cu, it is necessary to alloy the metals in order to obtain high hydrogen permeance, since Pd dissociates hydrogen molecules into two atoms. If Cu is on the outside of the metal layer hydrogen will not diffuse through it. In some references the alloying is stopped when a constant permeance is obtained, but there are also some theoretical methods. In the work by Khanuja et al. [67] the alloying was studied analysing the  $d$  value (distance between identical lattice planes) of alloyed PdCu samples. These values were between the ones of pure Cu and pure Pd. As the Vegard' Law states, the expansion of the crystal structure upon substitution of smaller atoms by larger ones is reflected by increasing lattice constants, and vice versa. As a consequence, the  $d$  value can represent the mixture between Cu and Pd atoms.

Palladium and copper have melting points of 1828 and 1358 K, corresponding to Tamann temperatures of about 913 and 679 K, respectively. The so-called Huttig and Tamman temperatures indicate the temperature at which sintering starts. The following semi-empirical relations for Huttig and Tamman temperatures are the more common ones:

$$T_{Huttig} = 0.3T_{melting}$$

Equation 16

$$T_{\text{Tamman}} = 0.5T_{\text{melting}}$$

Equation 17

The temperature at which the solid phase becomes mobile depends on several factors such as texture, size and morphology of the metal crystallites. For small particles this temperature may be much lower than that indicated by Tamman or Huttig. The effect of the size can be clearly observed in the literature, as the alloying temperature is influenced by the thickness of the metal layer. In Table 1.2 some alloying methods found in the literature are listed.

Table 1.2. Alloying methods for some PdCu membranes used in the literature.

Ref.	Support	Gas	T(K)	Time (h)	wt% Pd	Thick (μm)
[120]	Alumina	H <sub>2</sub>	623-823			
[92]	Alumina	H <sub>2</sub>	623		70, 80, 90	15
[94]	Alumina	H <sub>2</sub>	853	12	60, 76, 60, 10	6-7
[121]	Alumina	5% H <sub>2</sub> /N <sub>2</sub>	623-723	120/240		5
[81]	Alumina	5% H <sub>2</sub> /He	623-723	120	35, 30, 70, 80, 90	
[88]	Alumina	H <sub>2</sub> and N <sub>2</sub>	573*(N <sub>2</sub> ) and to 773*(H <sub>2</sub> )	Until constant permeance		15
[122]	Alumina	He	873			
[89]	Alumina	Inert	623	8	99, 70, 60, 10	1-5
[108]	Alumina	N <sub>2</sub>	673* / 898*	120	54-100	2.5-6
[123]	Foil	H <sub>2</sub>	623	72	60	8
[82]	Porous SS	H <sub>2</sub>	773	120		5
[124]	Metal	H <sub>2</sub>	523-823 (50 K 12-24h)		95	7
[112]	Porous SS	N <sub>2</sub>	723	5 (alternative Pd, Cu layers)	63	2

\* The slope used in the heating was 1 K/min, in the other references it is not specified.

The mechanism of PdCu alloying has been widely studied, but unlike most Pd systems, PdCu is uncertain: theory and experiments are equally divided with respect to the choice of which metal diffuses through the other one. Based on the Tamman temperature Cu

atoms will start to be mobile before the Pd ones. Therefore, Cu will be expected to diffuse in the Pd crystal structure [112]. Some models have been performed in the literature about the tendency of the Cu to diffuse into or from the Pd surface. Some Cu segregation to the outer surface was observed in Pd-Cu systems calcined in air at 673 K, and then reduced in hydrogen at 623 K [125]. Preferential segregation of Cu was experimentally detected in 100 nm  $\text{Cu}_x\text{Pd}_{1-x}$  films at temperatures  $\geq 700$  K [126], and was also predicted using a density-functional band-structure formalism [127]. On the contrary, some recent theoretical studies found reversal diffusion for  $\text{Cu}_x\text{Pd}_{1-x}$  disordered alloys, meaning that the diffusing species varies with composition at 300 K [128] and at room temperature [129]. Diffusion has not only been observed during the alloying, but also during the  $\text{H}_2$  permeation experiments. After performing hydrogen permeance tests in 3-7  $\mu\text{m}$  PdCu membranes the Pd composition in the surface was enriched from 88-91 at% to 98.7-99.2 at% [107].

During the alloying process Pd and Cu atoms mix, and this involves that the Pd:Cu ratio changes. The phase formation during alloying of a 100 nm ( $\text{Pd}_{50}\text{Cu}_{50}$ ) film has been studied in the literature [130]. It was observed that the interdiffusion that occurred during alloying was accompanied by sequential formation of  $\text{Cu}_3\text{Pd}$  and then PdCu, and that it led to a little increase in the average grain size. Alloying had also influenced the residual stress of the studied metal layers. In the as-deposited conditions, the stress in the Pd layer was compressive and in the Cu layer was tensile, while after the alloying the average stress was tensile and increased with increasing alloying time and temperature.

A computational technique (breadth-first search, BFS) can be used to study the energy of the different superficial PdCu (100) and PdCu (110) alloys formation, based on the energy difference between the alloy and each component separately [131]. With this technique it was concluded that the preferred ways for the surface structure in which the energy was minimised are the configurations represented in Figure 1.13.

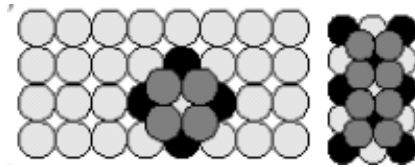


Figure 1.13. Energetically favoured surface structure of PdCu. White: Cu (100) surface. Grey: Cu atoms. Black: Pd atoms. [131].

### 1.4.7 Hydrogen transport in dense Pd alloy membranes

Membranes can be defined as a material layer designed to separate or filter. The use of dense metal membranes for hydrogen separation gives to the process a theoretically infinite selectivity.  $H_2$  permeation process through dense metal membranes has different steps: diffusion of the  $H_2$  molecules to the membrane, adsorption of hydrogen molecules, dissociation from  $H_2$  into H, diffusion of atomic H through interstitial sites in the membrane, recombination of the H atoms and, finally, desorption of the  $H_2$  molecules and diffusion to the permeate flow as illustrated in Figure 1.14.

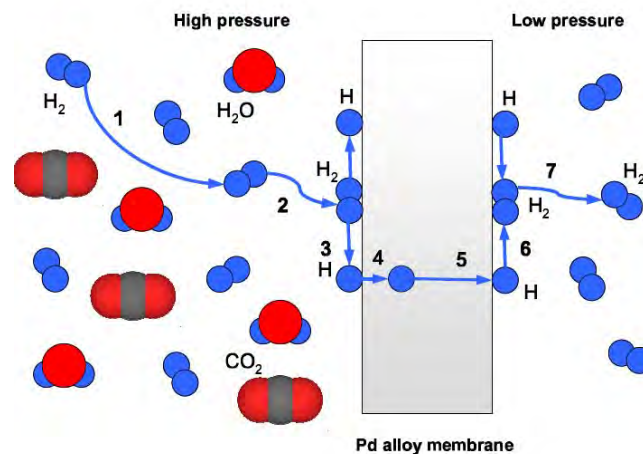


Figure 1.14.  $H_2$  transport in dense Pd alloy membranes.

The simplest description of gas diffusion through a nonporous structure is Fick's first law [132]:

$$J = -D \frac{dc}{dx}$$

Equation 18

Where,  $J$  is the molar flux through the membrane ( $\text{mol}/\text{cm}^2\text{s}$ ),  $D$  is the diffusion coefficient ( $\text{cm}^2/\text{s}$ ), and the driving force is the concentration gradient across the membrane,  $dc/dx$ .

Under these conditions, the thermodynamic equilibrium between the hydrogen molecules in the gas phase and hydrogen atoms dissolved at the interface can be established by the following formula [133]:

$$c = SP_1^n \quad \text{Equation 19}$$

Where  $S$  is the hydrogen solubility and  $P_1$  the hydrogen partial pressure.

The hydrogen permeation at constant temperature through a dense palladium membrane is described by the following general expression:

$$J_{H_2} = \frac{P_{H_2} (P_{i,feed}^n - P_{i,perm}^n)}{l} \quad \text{Equation 20}$$

Where  $J_{H_2}$  is the hydrogen flux through the membrane,  $P_{H_2}$  the hydrogen permeability,  $l$  the membrane thickness and  $n$  the dependence factor of the hydrogen flux on the hydrogen partial pressure, experimentally determined in the range 0.5-1 [133]. When  $n$  is 0.5 the hydrogen flux follows the so-called Sieverts' law, which applies only when the limiting step of the hydrogen permeation process is the bulk diffusion through the metal.

Concerning the influence of temperature on hydrogen permeability, the relationship between the hydrogen permeation rate and the temperature can be described by an Arrhenius law:

$$P_{H_2} = P_{H_2}^0 \exp\left[\frac{-E_a}{RT}\right] \quad \text{Equation 21}$$

Where  $P_{H_2}^0$ ,  $E_a$ ,  $R$  and  $T$  are the pre-exponential factor, the apparent activation energy, the universal gas constant, and the absolute temperature, respectively.

The rate of bulk transport is inversely proportional to the membrane thickness, while the combination of surface characteristics and operating conditions determine the surface reaction rate. The value of  $n=0.5$  has been the most widely used for permeability data in the literature allowing the comparison. In the last years metal membrane preparation techniques are improving, reducing membrane thickness and increasing the importance of the surface reaction and of the  $H_2$  mass transport resistance on the overall performance of a membrane.

It is expected that as the membrane thickness decreases, the pressure exponent will vary, indicating that the limiting step of the permeation process changes. In the literature it is generally accepted that if the pressure exponent is close to 1 the surface reactions become rate-limiting in hydrogen transport [134]. This  $n$  approaching to 1 is also generally related to thin membranes,  $\ll 10 \mu\text{m}$ . But the hydrogen diffusion process is affected by many things, such as the material (grain boundaries, pores and voids), the temperature (the higher the temperature the lower the limitation of the surface reactions) and the thickness (the higher the thickness the higher the diffusion limitation through the metal layer). This could be the explanation for different  $n$  values found in the literature for membranes of similar thickness. With a  $2 \mu\text{m}$  thick membrane using a mesoporous SS support, the  $n$  value was close to 1 at 723 K in a study by Nam et al. [112], while an unsupported  $2 \mu\text{m}$  Pd-23 %Ag membrane showed an  $n$  value equal to 0.54 at 673 K [135]. Caravela et al. [136] performed a correlation between the permeation steps and the obtained  $n$  value with a theoretical model and compared it to experimental data from two different membranes in the literature. They concluded that the  $n$  value is dependent on the operating conditions, thickness and material, making it impossible to assume that an  $n$  value tending to 1 would always indicate that the surface reactions are rate-limiting.

When a hydrogen containing mixture is fed to a membrane, the concentration polarization (CP) phenomenon contributes to the resistance of hydrogen permeation through the membrane, as summarized in Figure 1.15. It consists of a driving force decrease of hydrogen from the bulk gas to the membrane surface in the presence of non permeable species due to counter diffusion of  $H_2$  and the non-permeating species. This phenomenon will also occur inside the porous support and from the support surface to the permeate side gas. As it has been explained before, the mass transfer resistance can





that can react with the surface. The ones that react can be categorised depending on the degree of reversibility of their effect. Compounds are classed as inhibitors if the system is recovered when the compound is removed, as for example CO, CO<sub>2</sub>, H<sub>2</sub>O, O<sub>2</sub> and H<sub>2</sub>S. Compounds which effect is irreversible are known as poisons. Some compounds, as CO and H<sub>2</sub>S can show both tendencies depending on the concentration and the exposure time. The adsorption energy of the inert gases is negligible and the H<sub>2</sub> flux decrease is principally due to hydrogen dilution. On the contrary, inhibitors adsorb on the membrane surface. In this case, H<sub>2</sub> flux reduction is caused by the dilution and the adsorption of inhibitors on the surface. The removal of inhibitor gases from the membrane surface stores their efficiency. Poisonous gases are expected to adsorb and also react with membrane surface atoms. Temperature has a strong influence on the effect of feed contaminants as, in general, adsorption is unfavoured at high temperatures.

### The effect of H<sub>2</sub>O, CO and CO<sub>2</sub>

Gases such as H<sub>2</sub>O, CO and CO<sub>2</sub> can have an inhibitive effect on the hydrogen permeation through dense membranes due to their competitive adsorption with hydrogen on the metallic surface [137]. Steam and CO were found to have significant effects at temperatures lower than 623 K, and at 2 bar, whereas, CO<sub>2</sub> displayed only a slightly inhibitive effect on a PdAg membrane studied by Hoe et al. [138]. At 548 K, with 5 % of H<sub>2</sub>O, CO and CO<sub>2</sub> alternatively, the hydrogen permeation rate decreased by 70 % with steam, 10 % with CO<sub>2</sub> and 40 % with CO. They also observed that the effect increased with the amount of steam, CO or CO<sub>2</sub> in the feed, and decreased with temperature. At temperatures higher than 673 K very slight effects were recorded. For a 6 µm thick PdCu membrane the hydrogen permeation decrease was higher in contact with 10 % of H<sub>2</sub>O (75 %) than with 10 % of CH<sub>4</sub> (67 %) or 10 % of CO<sub>2</sub> (67 %) at 623 K [139]. Delamination of the metal film was even observed for a PdCu membrane after 60 min in contact with 10 % of steam [121]. It was also found that the height of micron-scale hillocks and the size of defects increased after the addition of CO and CO<sub>2</sub> [121].

### The effect of O<sub>2</sub>

The positive or negative effect of air purges on hydrogen permeance has been widely studied. Paglieri et al. [140] observed a recovery of the hydrogen flux in 9, 10 and 15 µm thick Pd membranes after introducing an air purge between H<sub>2</sub> permeation tests.

Their explanation was that some Pd will oxidize to palladium (II) oxide (PdO), and in contact with H<sub>2</sub> it will reduce again resulting in nano-crystallites of Pd with higher activity or surface area for hydrogen dissociation. The surface of the metal layer changed after being in contact with air, or oxygen. Aggarwal et al. [141] annealed some 40-200 nm thick Pd films in vacuum and oxygen and observed that the morphology of the metal layer annealed in oxygen had completely changed (Figure 1.16). This shape changing can be a consequence of the Pd film deformation due to the PdO crystallites.

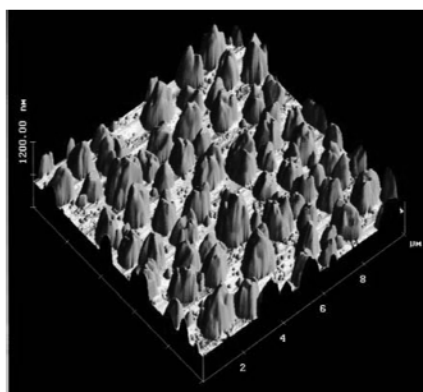


Figure 1.16. Atomic Force Microscopy (AFM) image published in [141] showing the result of annealing a 80 nm Pd film in oxygen at 1173 K for 1 h.

PdCu membranes tested with air or O<sub>2</sub> purge showed the same behaviour observed for the Pd ones. Air exposure of Pd alloy thin films can make them rearrange in conical-shaped structures, and with higher surface area more H<sub>2</sub> can permeate. Air would also clean the surface from contaminants. Additional contribution to the permeation rate could come from the pinholes generated during the rearrangement of the film, but with negative effects on the selectivity. It is noticed that the oxidation of metallic Pd is accompanied by an experimentally observed volume change of 38 %, as can be seen in Figure 1.17 [98]. After air exposure at 723 K a lot of pores, of around 5 nm diameter, were formed. After being one week in H<sub>2</sub> atmosphere, the holes and features developed during the air purge were covered and levelled off [98]. This reversible effect, after being in contact with hydrogen, has also been observed in damaged membranes with CO or CO<sub>2</sub>.

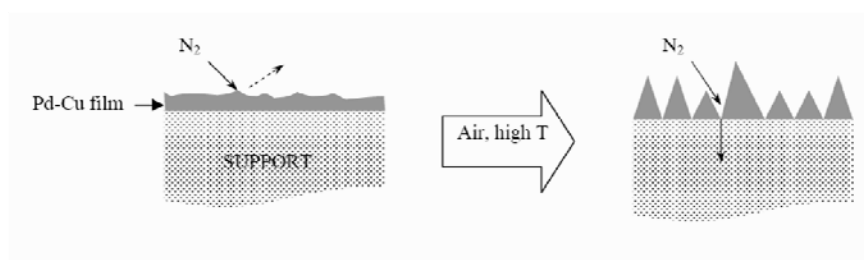


Figure 1.17. Air purge representation and implications for nitrogen leakage and surface area increase [98].

### The effect of sulphur compounds

Products like H<sub>2</sub>S are very common in process streams derived from natural gas, coal gasification or oil refinery operations. It is not easy to estimate the percentage of sulphur in natural gas as it strongly depends on the source, but it can be around 8000 ppmv [142] or 15000 ppmv [143]. Most of the sulphur is generally removed before entering to a process but some ppm are always left. In the case of the household natural gas sulphur compounds are added in the pipelines to odorize the gas and make possible leaks easily detectable. Sulphur components are poisonous for a lot of catalysts and they can deactivate metal membranes and reduce their hydrogen permeation and selectivity. Some studies have shown that Pd alloy membranes, such as PdCu and PdAu, have a better H<sub>2</sub>S resistance than the Pd ones [144, 145]. The present work is focused on PdCu alloy membranes. In a study by Kulprathipanjan et al. [81] H<sub>2</sub> permeation was totally inhibited with 300 ppmv of H<sub>2</sub>S for a PdCu membrane and with 100 ppmv for a Pd membrane. In general it can be said that the effect of H<sub>2</sub>S on PdCu membranes is related to the working temperature, concentration of H<sub>2</sub>S and time of exposure. These parameters will determine also the reversibility of the contamination.

PdCu membranes with different metal compositions have been studied in contact with H<sub>2</sub>S. Pomerantz et al. [82] observed an 80 % decrease in H<sub>2</sub> permeance when adding 45-55 ppmv of H<sub>2</sub>S in a H<sub>2</sub>S/H<sub>2</sub> mixture, at 723 K. They reintroduced a pure H<sub>2</sub> stream and observed that some of the H<sub>2</sub>S poisoning was reversible. The amount of irreversible poisoning increased as the H<sub>2</sub>S exposure time increased and the exposure temperature decreased, because of the exothermic nature of H<sub>2</sub>S adsorption. In the work by Ishteiwy et al. [120] H<sub>2</sub> permeance decreased by 32-36 percentage points when exposing the PdCu membrane to 1 ppmv of H<sub>2</sub>S, and by 52-63 points with 10 ppmv at 523 K. The hydrogen permeance was recovered after introducing a pure H<sub>2</sub> feed, while with 250

ppmv of H<sub>2</sub>S it totally failed. In the work of Way et al. [122] a 40 percentage point reduction of the hydrogen flux occurred when adding 100 ppmv of H<sub>2</sub>S to a 50/50 H<sub>2</sub>/N<sub>2</sub> mixture.

Some other studies showed good performance of PdCu membranes in the presence of H<sub>2</sub>S. Iyoha et al. [142] found that when adding H<sub>2</sub>S below the H<sub>2</sub>S/H<sub>2</sub> threshold ratio required to form thermodynamically stable sulphides (molar ratio H<sub>2</sub>S/H<sub>2</sub>=0.0011), both Pd and Pd<sub>80</sub>Cu<sub>20</sub> membranes kept their mechanical integrity and H<sub>2</sub> selectivity, but with a big deactivation of the catalytic surface. They tested a mixture of 90 % H<sub>2</sub> with 1000 ppmv of H<sub>2</sub>S and He with both Pd and Pd<sub>80</sub>Cu<sub>20</sub> membranes, and there were no changes in the H<sub>2</sub> permeance. But when working under WGS conditions with H<sub>2</sub>S addition, the Pd<sub>80</sub>Cu<sub>20</sub> membrane had no problems along 6 days, while in the Pd membrane pinhole defects were formed in the third day. Increasing the H<sub>2</sub>S/H<sub>2</sub> ratio made membranes fail within minutes and they broke. SEM analysis of the samples suggested that at high H<sub>2</sub>S/H<sub>2</sub> ratios, the H<sub>2</sub>S compromised the mechanical integrity by preferentially attacking the grain boundary region. Morreale et al. [146] tested a 50 μm Pd<sub>60</sub>Cu<sub>40</sub> at 773 K with 1000 ppmv during 14 days and hydrogen flux was almost constant at around  $1.6 \cdot 10^{-3} \text{ molm}^{-2}\text{s}^{-1}\text{Pa}^{-0.5}$ .

The effect of the PdCu phase on the resistance to H<sub>2</sub>S has been also studied. Mundschau et al. [147] studied 0.1 mm foils of different compositions (Pd<sub>80</sub>Cu<sub>20</sub>, Pd<sub>60</sub>Cu<sub>40</sub>, Pd<sub>53</sub>Cu<sub>47</sub>) at temperatures from 603 to 1123 K. They saw that the permeance of the fcc crystalline structure did not change when adding 1000 ppmv of H<sub>2</sub>S at any temperature, while that of the bcc phase was two orders of magnitude lower (Figure 1.18). So they suggested that the fcc phase was resistant to H<sub>2</sub>S, but not the bcc one.

As it has been explained in previous sections, the structure of the PdCu membranes depends not only on the composition, but also on the temperature. To check the claim that the fcc phase is resistant to sulphur, Table 1.3 shows a comparison of some literature results. It can be noticed that not all the experiments carried out with H<sub>2</sub>S and fcc structure membranes were successful. The thickness of the tested membranes could have been an important factor in the results as well.

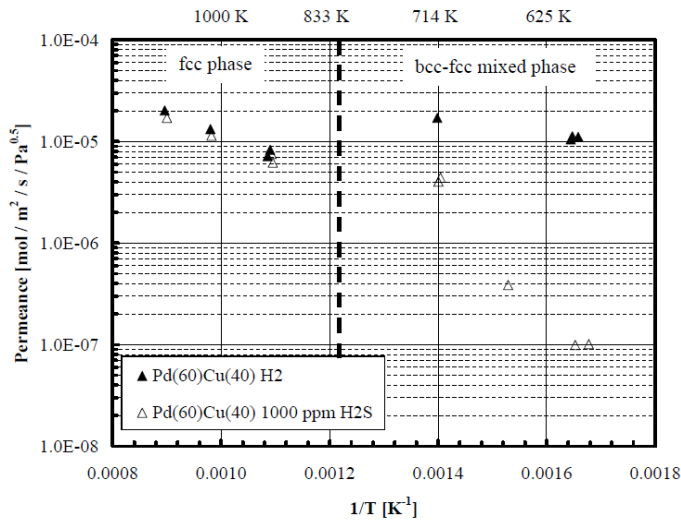


Figure 1.18. Hydrogen permeance results for 60 wt% Pd – 40 wt% Cu alloy membranes as a function of temperature. Reported in Morreale et al. [147].

Table 1.3. Comparison of the H<sub>2</sub>S effect on PdCu membranes.

Ref.	Pd <sub>x</sub> Cu <sub>y</sub>	T (K)	Phase	Metal layer (μm)	[H <sub>2</sub> S] (ppmv)	Effect in the H <sub>2</sub> permeance
[82]	Pd <sub>92</sub> Cu <sub>8</sub> Pd <sub>82</sub> Cu <sub>18</sub> Pd <sub>81</sub> Cu <sub>19</sub>	623-723	fcc fcc fcc	20	45-55	80 % loss
[120]	ns	623	ns	2	1-50	Decrease 32-63 %
[122]	Pd <sub>60</sub> Cu <sub>40</sub>	723	bcc+fcc	1-25	100	40 % decrease
[81]	Pd <sub>35</sub> Cu <sub>65</sub> Pd <sub>27</sub> Cu <sub>73</sub>	723	fcc fcc	3-10	115-630	Decrease 10-30 %
					160-250	Decrease 70-90 %
	Pd	723	ns	ns	20 115	Decrease 30 % Failed
[146]	Pd <sub>60</sub> Cu <sub>40</sub>	773	bcc+fcc	25-50	1000	No decrease after 14 days
[142]	Pd <sub>80</sub> Cu <sub>20</sub>	1173	fcc	ns	1000	No decrease
	Pd	1173	ns	ns	1000	No decrease
[147]	Pd <sub>80</sub> Cu <sub>20</sub>	625-1000	fcc	100 – 1000	1000	Decrease <10 %
	Pd <sub>60</sub> Cu <sub>40</sub>		bcc		1000	Decrease 80-90 %
	Pd <sub>53</sub> Cu <sub>47</sub>					

ns: not specified

The H<sub>2</sub>S can be thermally decomposed, yielding hydrogen and elemental sulphur as primary products. In the presence of a catalytic element this can be a very fast reaction, but it will just proceed to 10-20 % conversion of the H<sub>2</sub>S, for thermodynamic equilibrium limitations, at 973 K. Thermal decomposition of H<sub>2</sub>S can be the reason for

the good results from [142] in Table 1.3. The elemental sulphur can be combined with the elements of the membrane: Pd membranes form Pd<sub>4</sub>S in the bulk, PdAg membranes Ag<sub>5</sub>Pd<sub>10</sub>S<sub>5</sub> and PdCu ones Pd<sub>4</sub>S. PdCu membranes show better tolerance to H<sub>2</sub>S and the surface remains with the original alloy composition, but some Pd<sub>4</sub>S is formed in the bulk [148]. In the membranes prepared for the present work the Pd percentage is around 40-80 % and the temperature will range between 673 K and 773 K, so no H<sub>2</sub>S thermal decomposition can be expected.

The mechanism by which the hydrogen permeance decreases in Pd alloy membranes when being in contact with sulphur compounds is not yet completely understood. At low H<sub>2</sub>S concentrations H<sub>2</sub> dissociation sites are blocked. Wilke et al. [149] made a theoretical study and found that low sulphur surface coverage ( $\theta_s < 0.25$ ) reduces hydrogen adsorption energy at sites close to adsorbed sulphur, while at higher surface coverage ( $\theta_s = 0.5$ ) strong repulsive H-S interactions strictly block the adsorption of hydrogen in the vicinity of sulphur adsorbed atoms. When high H<sub>2</sub>S concentrations are used, a sulphur surface layer does not allow H<sub>2</sub> to even penetrate to the PdCu surface. They set out two hypotheses: firstly, the decrease in hydrogen flux can be attributed to the formation of a sulphide surface scale with low hydrogen transport, and secondly, there is a competitive adsorption between adsorbed S and H atoms.

## 1.5 Membrane reactor

With the implementation of hydrogen selective membranes in reactors it is possible to overcome the thermodynamic equilibrium conversion of methane reforming processes, resulting in less severe operating conditions. The selective removal of hydrogen from the reaction side enables methane reforming to proceed towards completion. Moreover, high purity hydrogen could be produced via dense Pd-based membrane reactors (MR), which allows the simultaneous performance of both chemical reaction and mixture gas separation in the same device.

Several works can be found in the literature where Pd or PdAg membranes are integrated in a MR in processes producing hydrogen. Pd membranes reactors have been tested for methane reforming with Ni/Al<sub>2</sub>O<sub>3</sub> catalyst [150]. They simulated the effect of granular or structured catalyst beds and found that the structured catalytic bed could

noticeably raise the yield of hydrogen. Uemiya et al. [151] employed a MR with Pd membranes of 20  $\mu\text{m}$  at 773 K and 10 bar obtaining 80 % conversion in methane steam reforming. A methane conversion of 84-98 % was achieved by Tong et al. [152] with a 6  $\mu\text{m}$  thick Pd membrane. The good performance was mainly ascribed to the better separation efficiency of the membrane and optimum operating parameters. A higher methane conversion of 98.8 % was reported by Che et al. [153] with a 4  $\mu\text{m}$  thick Pd membrane at 823 K,  $P_{\text{feed}}=9$  bar,  $\text{GHSV}=4000 \text{ mL}/(\text{g}_{\text{cat}}\text{h})$ , and with a steam to methane ratio of 3.0. The high conversion was attributed to the high membrane permeance, good catalyst activity and the counter current design.

MR with Pd membranes have also been tested for the WGS reaction. Li et al. [154] employed a multi-tube membrane reactor with 5.6  $\mu\text{m}$  thick membranes to perform WGS with a simulated pre-reformed mixture ( $\text{CO}$ ,  $\text{CO}_2$ ,  $\text{H}_2$ ,  $\text{CH}_4$  and  $\text{H}_2\text{O}$ ) at 673 K with 20-35 bar of feed pressure and 15 bar of permeate pressure. They observed that the overall hydrogen permeation dropped by 20 % compared to a  $\text{H}_2/\text{N}_2$  mixture with the same  $\text{H}_2$  concentration.

As explained in previous sections Pd alloys have been widely studied as their hydrogen permeance is close or sometimes even higher than that of Pd membranes and because they minimize embrittlement problems. Membrane reactors with PdAg membranes have been analysed during the last years in different processes. A conversion of 63 % in methane steam reforming was obtained using a PdAg with 23 wt% of Pd and 0.1 mm thickness in a MR adding pure  $\text{CH}_4$  at  $0.5 \text{ LNCH}_4/(\text{g}_{\text{cat}}\text{h})$ , 773 K,  $P_{\text{feed}}=10$  bar and  $P_{\text{sweep}}=0.5$  bar [155]. 51 %  $\text{CH}_4$  conversion was derived by Shu et al. [156] with a 10.3  $\mu\text{m}$  thick PdAg membrane at 773 K,  $P_{\text{feed}}=1.36$  bar, a steam-to-carbon ratio of 3, and in presence of a  $\text{Ni}/\text{Al}_2\text{O}_3$  catalyst, exceeding the calculated equilibrium  $\text{CH}_4$  conversion of 40 %. 56 % conversion was obtained by Basile et al. [157] at 723 K,  $P_{\text{feed}}=3$  bar,  $P_{\text{sweep}}=1$  bar with a 50  $\mu\text{m}$  PdAg membrane with co-current system and a  $\text{Ni}/\text{ZrO}$  catalyst. Gallucci et al. [158] obtained 70 %  $\text{CH}_4$  conversion with a 50  $\mu\text{m}$  thick PdAg membrane at 723 K,  $P_{\text{feed}}=1.22$  bar, far beyond the  $\text{CH}_4$  conversion of 25 % in the traditional reactor.

As a consequence of the improvement in PdCu alloy preparation, obtaining membranes with hydrogen permeance values in the ranges of the Pd ones, PdCu membranes have



started to be tested in membrane reactors for different processes. The amount of works found in the literature testing PdCu membranes in real conditions is still quite low compared to Pd or PdAg ones. Membrane reactors for ethanol steam reforming with PdCu membranes have been tested. Lim et al. [159] obtained better conversion and hydrogen yield with a PdCu MR for ethanol steam reforming at 1-10 atm and 623 K than in a conventional reactor. Yun et al. [160] observed an ethanol conversion enhancement of 22 % in ethanol steam reforming in a 2  $\mu\text{m}$  PdCu MR at 733 K compared to a conventional packed bed reactor.

PdCu membrane reactors have also been tested in water gas shift reactions. Hwang et al. [161] performed WGS with Pt/CeO<sub>2</sub> catalysts in a 4  $\mu\text{m}$  PdCu MR at 773 K. They observed that the presence of CO and other gases reduced the H<sub>2</sub> permeation by more than 50 %. The CO conversion was improved by 65 % compared to the catalyst without any membrane, and the CH<sub>4</sub> formed by an undesired side reaction was significantly reduced. The system was operated for 60 h without membrane defect or carbon deposition. With thick-walled tubes (125  $\mu\text{m}$ ) Iyoha et al. [142] obtained higher conversion with the MR than without the membrane in CO WGS at 1173 K. Comparing Pd and PdCu MR they observed higher conversion in the Pd one, most probably because of a higher permeability of this membrane. In another work from the same authors [162] they observed that after 8 days operating in CO WGS conditions at 1173 K with 241 kPa trans-membrane pressure differential and in the absence of heterogeneous catalyst particles both in Pd and PdCu (125  $\mu\text{m}$  thick) the environment caused pinhole formation in the retentate surface.

No studies have been found in the literature about the application of PdCu membranes to methane steam reforming or catalytic partial oxidation processes, which are the processes studied in the present thesis. As not too much work has been done on the testing of PdCu membranes under real mixtures, in the present work the hydrogen production from methane and the purification with PdCu membranes has been performed in separate units. This configuration has a number of advantages. (1) Many different operating conditions can be tested and many catalysts can be evaluated with easy substitution without damaging the membrane. (2) Operating at lower temperatures in the membrane module increases membrane stability, allowing to operate with thinner metal layers.

## Reference List

- [1] Y. Hou, M. Zhuang, G. Wan, *Renewable Energy* **2007**, *32*, 1175.
- [2] Matthew Huang, *Vehicle Crash Mechanics*, CRC Press **2002**, USA.
- [3] V. R. Choudhary, A. S. Mamman, *Fuel Process. Technol.* **1999**, *60*, 203.
- [4] Y. Ji, W. Li, H. Xu, Y. Chen, *Appl. Catal. A* **2001**, *213*, 25.
- [5] H. Li, J. A. Z. Pieterse, J. W. Dijkstra, W. G. Haije, H. Y. Xu, C. Bao, R. W. van den Brink, D. Jansen, *J. Membr. Sci.* **2011**, *373*, 43.
- [6] J. A. Z. Pieterse, J. Boon, Y. C. van Delft, J. W. Dijkstra, R. W. van den Brink, *Catal. Today* **2010**, *156*, 153.
- [7] A. M. De Groot, G. F. Froment, *Catal. Today* **1997**, *37*, 309.
- [8] J. N. Armor, *Appl. Catal. A* **1999**, *176*, 159.
- [9] J. H. Edwards, A. M. Maitra, *Fuel Process. Technol.* **1995**, *42*, 269.
- [10] Y. H. Hu, E. Ruckenstein, *Catal. Rev. - Sci. Eng.* **2002**, *44*, 423.
- [11] J. Wang, H. Chen, Y. Tian, M. Yao, Y. Li, *Fuel* **2012**, *97*, 805.
- [12] H. Tanaka, R. Kaino, K. Okumura, T. Kizuka, Y. Nakagawa, K. Tomishige, *Appl. Catal. A* **2010**, *378*, 175.
- [13] N. Perkas, D. P. Minh, P. Gallezot, A. Gedanken, M. I. Besson, *Appl. Catal. B* **2005**, *59*, 121.
- [14] L. S. F. Feio, C. E. Hori, L. V. Mattos, D. Zanchet, F. B. Noronha, J. M. C. Bueno, *Appl. Catal. A* **2008**, *348*, 183.
- [15] S. Freni, G. Calogero, S. Cavallaro, *J. Power Sources* **2000**, *87*, 28.
- [16] J. Requies, M. A. Cabrero, V. L. Barrio, J. F. Cambra, M. B. Guemez, P. L. Arias, V. La Parola, M. A. Pena, J. L. G. Fierro, *Catal. Today* **2006**, *116*, 304.
- [17] V. R. Choudhary, V. H. Rane, A. M. Rajput, *Catal. Lett.* **1993**, *22*, 289.
- [18] B. Li, K. Maruyama, M. Nurunnabi, K. Kunimori, K. Tomishige, *Appl. Catal. A* **2004**, *275*, 157.
- [19] H. H. Ibrahim, P. Kumar, R. O. Idem, *Energy Fuels* **2007**, *21*, 570.
- [20] A. F. Lucrecio, J. M. Assaf, E. M. Assaf, *Appl. Catal. A* **2011**, *400*, 156.
- [21] F. Basile, G. Fornasari, F. Trifiro, A. Vaccari, *Catal. Today* **2001**, *64*, 21.
- [22] A. Nandini, K. K. Pant, S. C. Dhingra, *Appl. Catal. A* **2005**, *290*, 166.
- [23] J. A. C. Dias, J. M. Assaf, *J. Power Sources* **2004**, *137*, 264.
- [24] Y. Kobayashi, J. Horiguchi, S. Kobayashi, Y. Yamazaki, K. Omata, D. Nagao, M. Konno, M. Yamada, *Appl. Catal. A* **2011**, *395*, 129.
- [25] H. W. Kim, K. M. Kang, H. Y. Kwak, *Int. J. Hydrogen Energy* **2009**, *34*, 3351.
- [26] H. Oezdemir, O. Faruk, G. Ali, *Int. J. Hydrogen Energy* **2010**, *35*, 12147.
- [27] H. Liu, D. He, *Catal. Surv. Asia* **2012**, *16*, 53.
- [28] Y. Q. Song, D. H. He, B. Q. Xu, *Appl. Catal. A* **2008**, *337*, 19.
- [29] J. Guo, Z. Hou, J. Gao, X. Zheng, *Energy Fuels* **2008**, *22*, 1444.
- [30] S. Takenaka, H. Umebayashi, E. Tanabe, H. Matsune, M. Kishida, *J. Catal.* **2007**, *245*, 392.
- [31] M. Fleys, Y. Simon, D. Swierczynski, A. Kiennemann, P. M. Marquaire, *Energy Fuels* **2006**, *20*, 2321.
- [32] H. Liu, D. He, *Int. J. Hydrogen Energy* **2011**, *36*, 14447.

- [33] C. Berger-Karin, J. Radnik, E. V. Kondratenko, *J. Catal.* **2011**, *280*, 116.
- [34] H. Cheng, X. Lu, X. Liu, Y. Zhang, W. Ding, *J. Nat. Gas Chem.* **2009**, *18*, 467.
- [35] G. P. Berrocal, S. Da, J. M. Assaf, A. Albornoz, M. d. C. Rangel, *Catal. Today* **2010**, *149*, 240.
- [36] L. Jalowiecki-Duhamel, H. Zarrou, A. D'Huysser, *Catal. Today* **2008**, *138*, 124.
- [37] Y. Song, H. Liu, S. Liu, D. He, *Energy Fuels* **2009**, *23*, 1925.
- [38] E. Ruckenstein, Y. Hang Hu, *Appl. Catal. A* **1999**, *183*, 85.
- [39] F. Habimana, X. Li, S. Ji, B. Lang, D. Sun, C. Li, *J. Nat. Gas Chem.* **2009**, *18*, 392.
- [40] C. R. B. Silva, C. da, N. F. P. Ribeiro, M. M. V. M. Souza, *Catal. Commun.* **2011**, *12*, 665.
- [41] S. C. Dantas, J. C. Escritori, R. R. Soares, C. E. Hori, *Chem. Eng. J.* **2010**, *156*, 380.
- [42] J. R. Rostrup-Nielsen, J. H. B. Hansen, *J. Catal.* **1993**, *144*, 38.
- [43] G. Jones, J. G. Jakobsen, S. S. Shim, J. Kleis, M. P. Andersson, J. Rossmeisl, F. Abild-Pedersen, T. Bligaard, S. Helveg, B. Hinnemann, J. R. Rostrup-Nielsen, I. Chorkendorff, J. Sehested, J. K. Nørskov, *J. Catal.* **2008**, *259*, 147.
- [44] J. Wei, E. Iglesia, *J. Catal.* **2004**, *224*, 370.
- [45] M. Dan, M. Mihet, A. R. Biris, P. Marginean, V. Almasan, G. Borodi, F. Watanabe, A. S. Biris, M. D. Lazar, *React. Kinet., Mech. Catal.* **2012**, *105*, 173.
- [46] Y. H. Chin, D. L. King, H. S. Roh, Y. Wang, S. M. Heald, *J. Catal.* **2006**, *244*, 153.
- [47] N. V. Parizotto, R. F. Hernandez, C. M. P. Marques, J. M. C. Bueno, *Stud. Surf. Sci. Catal.* **2007**, *167*, 421.
- [48] J. C. S. Araujo, D. Zanchet, R. Rinaldi, U. Schuchardt, C. E. Hori, J. L. G. Fierro, J. M. C. Bueno, *Appl. Catal. B* **2008**, *84*, 552.
- [49] W. H. Cassinelli, L. S. F. Feio, J. C. S. Araujo, C. E. Hori, F. B. Noronha, C. M. P. Marques, J. M. C. Bueno, *Catal. Lett.* **2008**, *120*, 86.
- [50] J. G. Jakobsen, M. Jakobsen, I. Chorkendorff, J. Sehested, *Catal. Lett.* **2010**, *140*, 90.
- [51] S. S. Y. Lin, H. Daimon, S. Y. Ha, *Appl. Catal. A* **2009**, *366*, 252.
- [52] O. Yamazaki, K. Tomishige, K. Fujimoto, *Appl. Catal. A* **1996**, *136*, 49.
- [53] Y. g. Chen, K. Tomishige, K. Yokoyama, K. Fujimoto, *J. Catal.* **1999**, *184*, 479.
- [54] G. Li, L. Hu, J. M. Hill, *Appl. Catal. A* **2006**, *301*, 16.
- [55] E. C. Luna, A. M. Becerra, M. I. Dimitrijewits, *React. Kinet. Catal. Lett.* **1999**, *67*, 247.
- [56] Z. Hou, T. Yashima, *Catal. Lett.* **2003**, *89*, 193.
- [57] E. L. Foletto, R. W. Alves, S. L. Jahn, *J. Power Sources* **2006**, *161*, 531.
- [58] Y. g. Chen, O. Yamazaki, K. Tomishige, K. Fujimoto, *Catal. Lett.* **1996**, *39*, 91.
- [59] Y. g. Chen, K. Tomishige, K. Yokoyama, K. Fujimoto, *Appl. Catal. A* **1997**, *165*, 335.
- [60] Julian R.H.Ross, *Heterogeneous Catalysis. Fundamentals and Applications*, Elsevier **2011**, Great Britain.

- [61] J. Barbero, M. A. Peña, J. M. Campos-Martín, J. L. G. Fierro, P. L. Arias, *Catal. Lett.* **2003**, 87, 211.
- [62] F. Pinna, *Catal. Today* **1998**, 41, 129.
- [63] M. Bastos-Neto, A. Moeller, R. Staudt, J. Böhm, R. Gläser, *Sep. Purif. Technol.* **2011**, 77, 251.
- [64] F. V. S. Lopes, C. A. Grande, A. r. E. Rodrigues, *Chem. Eng. Sci.* **2011**, 66, 303.
- [65] M. Sjardin, K. J. Damen, A. P. C. Faaij, *Energy* **2006**, 31, 2523.
- [66] J. Shu, B. P. A. Grandjean, A. van Neste, S. Kaliaguine, *Can. J. Chem. Eng.* **1991**, 69, 1036.
- [67] M. Khanuja, B. R. Mehta, S. M. Shivaprasad, *J. Chem. Sci.* **2008**, 120, 573.
- [68] Y. S. Cheng, K. L. Yeung, *J. Membr. Sci.* **1999**, 158, 127.
- [69] K. J. Bryden, J. Y. Ying, *J. Membr. Sci.* **2002**, 203, 29.
- [70] C. S. Jun, K. H. Lee, *J. Membr. Sci.* **2000**, 176, 121.
- [71] K. Ohira, Y. Sakamoto, T. B. Flanagan, *J. Alloys Compd.* **1996**, 236, 42.
- [72] Y. Sakamoto, K. Ohira, N. Ishimaru, F. L. Chen, M. Kokubu, T. B. Flanagan, *J. Alloys Compd.* **1995**, 217, 226.
- [73] G. Zeng, A. Goldbach, L. Shi, H. Xu, *Int. J. Hydrogen Energy* **2012**, 37, 6012.
- [74] S. Yun, S. Ted Oyama, *J. Membr. Sci.* **2011**, 375, 28.
- [75] G. Q. Lu, J. C. niz da Costa, M. Duke, S. Giessler, R. Socolow, R. H. Williams, T. Kreutz, *J. Colloid Interface Sci.* **2007**, 314, 589.
- [76] W. M. Tucho, H. J. Venvik, M. Stange, J. C. Walmsley, R. Holmestad, R. Bredesen, *Sep. Purif. Technol.* **2009**, 68, 403.
- [77] T. H. Hsiung, D. D. Christman, E. J. Hunter, A. R. Homyak, *AIChE J.* **1999**, 45, 204.
- [78] Hysep Hydrogen Separation Modules powered by the Energy Research Centre of the Netherlands (ECN) <http://hysep.com> accessed May, 2012.
- [79] Johnson Matthey, Gas Purification Technology Products information available at <http://www.jmgpt.com> accessed May 2012.
- [80] REB Research, Hydrogen Purifier products information available at <http://www.rebresearch.com/catalog.html> accessed May, 2012.
- [81] A. Kulprathipanja, G. k. O. Alptekin, J. L. Falconer, J. D. Way, *J. Membr. Sci.* **2005**, 254, 49.
- [82] N. Pomerantz, Y. H. Ma, *Ind. Eng. Chem. Res.* **2009**, 48, 4030.
- [83] <http://ecee.colorado.edu/>
- [84] C. Decaux, R. Ngameni, D. Solas, S. Grigoriev, P. Millet, *Int. J. Hydrogen Energy* **2009**, 35, 4883.
- [85] W. Huang, S. M. Opalka, D. Wang, T. B. Flanagan, *Calphad* **2007**, 31, 315.
- [86] P. R. Subramanian, D. E. Laughlin, *J. Phase Equilib.* **1991**, 12, 231.
- [87] D. L. McKinley, United States Patent 3439474, **1969**.
- [88] L. Yuan, A. Goldbach, H. Xu, *J. Phys. Chem. B* **2007**, 111, 10952.
- [89] F. Roa, J. D. Way, *Ind. Eng. Chem. Res.* **2003**, 42, 5827.
- [90] F. Roa, M. J. Block, J. D. Way, *Desalination* **2002**, 147, 411.
- [91] F. Roa, J. D. Way, *Fuel Chemistry Division Preprints* **2003**, 48, 335.

- [92] F. Roa, J. D. Way, R. L. McCormick, S. N. Paglieri, *Chem. Eng. J.* **2003**, *93*, 11.
- [93] B. H. Howard, R. P. Killmeyer, K. S. Rothenberger, A. V. Cugini, B. D. Morreale, R. M. Enick, F. Bustamante, *J. Membr. Sci.* **2004**, *241*, 207.
- [94] L. Yuan, A. Goldbach, H. Xu, *J. Membr. Sci.* **2008**, *322*, 39.
- [95] P. T. Liu, Y. T. Chou, C. Y. Su, H. M. Chen, *Surf. Coat. Technol.* **2010**, *205*, 1497.
- [96] J. Shu, B. P. A. Grandjean, E. Ghali, S. Kaliaguine, *J. Membr. Sci.* **1993**, *77*, 181.
- [97] Ø. Hatlevik, d, S. K. Gade, M. K. Keeling, P. M. Thoen, A. P. Davidson, J. D. Way, *Sep. Purif. Technol.* **2010**, *73*, 59.
- [98] F. Roa, Palladium/copper composite membranes. Influence of support specifications, alloy composition and air treatment on hydrogen permeation, PhD Thesis, **2003**, Colorado School of Mines.
- [99] M. Schlesinger, M. Paunovic, *Modern Electroplating*, John Wiley & Sons, **2000** USA.
- [100] J. W. Walker, *Formaldehyde. Third edition*, ACS Monograph No. 159, Reinhold, New York **1964**.
- [101] Harry Bennett, *Two Thousand Formulas, Recipes and Trade Secrets* **2004**.
- [102] M. Paunovic, *J. Electrochem. Soc.* **1997**, 349.
- [103] J. R. Davis, *Copper and copper alloys. ASM specialty handbook*, ASM International **2001**.
- [104] E. Norkus, K. Prusinskas, A. Vaskelis, J. Jaciauskiene, I. Stalnioniene, D. L. Macalady, *Carbohydr. Res.* **2007**, *342*, 71.
- [105] Y. M. Lin, S. C. Yen, *Appl. Surf. Sci.* **2001**, *178*, 116.
- [106] A. A. Tracton, *Coatings technology handbook. Third edition*, Taylor and Francis Group, Boca Raton **2005**.
- [107] X. Zhang, W. Wang, J. Liu, S. Sheng, G. Xiong, W. Yang, *Thin Solid Films* **2008**, *516*, 1849.
- [108] E. A. N. Tesselaar, Ontwikkeling van een gedragen palladium/koper membraan middels electroless platen, ECN The Netherlands **2005**.
- [109] Y. H. Ma, B. C. Akis, M. E. Ayturk, F. Guazzone, E. E. Engwall, I. P. Mardilovich, *Ind. Eng. Chem. Res.* **2004**, *43*, 2936.
- [110] M. Oita, M. Matsuoka, C. Iwakura, *Electrochim. Acta* **1997**, *42*, 1435.
- [111] P. Andricacos, S. H. Boettcher, F. R. McFeely, M. Paunovic, US Patent 6416812 B1, **2002**.
- [112] S. E. Nam, K. H. Lee, *J. Membr. Sci.* **2001**, *192*, 177.
- [113] J. Duffy, L. Pearson, M. Paunovic, *J. Electrochem. Soc.* **1983**, 876.
- [114] A. Brenner, G. E. Riddell, *J. Res. Natl. Bureau Standards* **1946**, *37*, 31.
- [115] K. M. Gorbunova, M. V. Ivanov, V. P. Moiseev, *J. Electrochem. Soc.* **1973**, *120*, 613.
- [116] C. H. Minjer, *Electrodep. Surf. Treat.* **1975**, *3*, 261.
- [117] M. Paunovic, *Plating* **1968**, *55*, 1161.
- [118] M. Paunovic, C. Stack, *Electrocrystallization*, Electrochemical Society, Pennington **1981**.
- [119] R. Weil, R. Paquin, *J. Electrochem. Soc.* **1960**, *107*, 87.

- [120] O. Ishteiwy, P. M. Thoen, F. Roa, J. D. Way, DOE University Coal Research Contractor's Review Meeting **2005**.
- [121] A. Kulprathipanja, G. O. Alpekin, J. L. Falconer, J. D. Way, *Ind. Eng. Chem. Res.* **2004**, *43*, 4188.
- [122] J. D. Way, R. L. McCormick, F. Roa, S. N. Paglieri, *Proceedings of the 6<sup>th</sup> International Conference on Inorganic Membranes*, **2000**.
- [123] W. Juda, C. Krueger, R. T. Bombard, U S Patent 6238465, **2001**
- [124] F. Guazzone, E. E. Engwall, I. P. Mardilovich, Y. H. Ma, *Preprint Papers - American Chemical Society, Division of Fuel Chemistry* **2005**, *50*, 609.
- [125] S. p. Lambert, B. é. Heinrichs, A. Brasseur, A. Rulmont, J. P. Pirard, *Appl. Catal. A* **2004**, *270*, 201.
- [126] D. Priyadarshini, P. Kondratyuk, Y. Picard, B. D. Morreale, A. J. Gellman, J. B. Miller, *J. Phys. Chem. C* **2011**, *115*, 10155.
- [127] O. M. Løvvik, *Surf. Sci.* **2005**, *583*, 100.
- [128] L. Yang, *Philos. Mag. A* **2000**, *80*, 1897.
- [129] G. Bozzolo, J. E. Garcés, R. D. Noebe, P. Abel, H. O. Mosca, *Progress in Surf. Sci.* **2003**, *73*, 79.
- [130] J. Chakraborty, U. Welzel, E. J. Mittemeijer, *J. Appl. Phys.* **2008**, *103*, 113512.
- [131] J. E. Garcés, H. O. Mosca, G. H. Bozzolo, *Surf. Sci.* **2000**, *459*, 365.
- [132] M. Mulder, *Basic Principles of Membrane Technology*. Second Edition, Kluwer Academic Publishers **2000**, The Netherlands.
- [133] F. Galluci, M. De Falco, S. Tosti, L. Marrelli, A. Basile, *Int. J. Hydrogen Energy*, **2007**, *32*, 4052.
- [134] A. Li, C. J. Lim, J. R. Grace, *Chem. Eng. J.* **2008**, *138*, 452.
- [135] T. A. Peters, M. Stange, H. Klette, R. Bredesen, *J. Membr. Sci.* **2008**, *316*, 119.
- [136] A. Caravella, F. Scura, G. Barbieri, E. Drioli, *J. Phys. Chem. B* **2010**, *114*, 6033.
- [137] G. Barbieri, F. Scura, F. Lentini, G. De Luca, E. Drioli, *Sep. Purif. Technol.* **2008**, *61*, 217.
- [138] K. Hou, R. Hughes, *J. Membr. Sci.* **2002**, *206*, 119.
- [139] X. Zhang, G. Xiong, W. Yang, *Stud. Surf. Sci. Cat.* **2007**, *167*, 219.
- [140] S. N. Paglieri, K. Y. Foo, J. D. Way, J. P. Collins, D. L. Harper-Nixon, *Ind. Eng. Chem. Res.* **1999**, *38*, 1925.
- [141] S. Aggarwal, A. P. Monga, S. R. Perusse, R. Ramesh, V. Ballarotto, E. D. Williams, B. R. Chalamala, Y. Wei, R. H. Reuss, *Science* **2000**, *287*, 2235.
- [142] O. Iyoha, R. Enick, R. Killmeyer, B. Howard, M. Ciocco, B. Morreale, *J. Membr. Sci.* **2007**, *306*, 103.
- [143] J. D. Way, *Palladium/Copper alloy composite membranes for high temperature hydrogen separation from coal-derived gas streams* report **2002**.
- [144] A. Shamsi, *Catal. Today* **2009**, *139*, 268.
- [145] S. K. Gade, S. J. DeVoss, K. E. Coulter, S. N. Paglieri, G. k. O. Alptekin, J. D. Way, *J. Membr. Sci.* **2011**, *378*, 35.
- [146] D. Edlund, *Advanced coal-fired power systems '96 review meeting*, Morgantown, West Virginia, **1996**.

- 
- [147] B. D. Morreale, M. V. Ciocco, B. H. Howard, R. P. Killmeyer, A. V. Cugini, R. M. Enick, *J. Membr. Sci.* **2004**, *241*, 219.
- [148] M. V. Mundschau, X. Xie, C. R. Evenson IV, A. F. Sammells, *Catal. Today* **2006**, *118*, 12.
- [149] S. Wilke, M. Scheffler, *Surf. Sci.* **1995**, *329*, L605-L610.
- [150] A. B. Shigarov, V. A. Kirillov, *Theor. Found. Chem. Eng.* **2012**, *46*, 97.
- [151] S. Uemiya, T. Matsuda, E. Kikuchi, *J. Membr. Sci.* **1991**, *56*, 315.
- [152] J. Tong, Y. Matsumura, H. Suda, K. Haraya, *Ind. Eng. Chem. Res.* **2005**, *44*, 1454.
- [153] Y. Chen, Y. Wang, H. Xu, G. Xiong, *J. Membr. Sci.* **2008**, *322*, 453.
- [154] H. Li, J. W. Dijkstra, J. A. Z. Pieterse, J. Boon, R. W. van den Brink, D. Jansen, *Energy Procedia* **2011**, *4*, 666.
- [155] S. Lægsgaard Jørgensen, P. E. H. Nielsen, P. Lehrmann, *Catal. Today* **1995**, *25*, 303.
- [156] J. Shu, B. P. A. Grandjean, S. Kaliaguine, *Appl. Catal. A* **1994**, *119*, 305.
- [157] A. Basile, S. Campanari, G. Manzolini, A. Iulianelli, T. Longo, S. Liguori, M. De Falco, V. Piemonte, *Int. J. Hydrogen Energy* **2011**, *36*, 1531.
- [158] F. Gallucci, L. Paturzo, A. Fama, A. Basile, *Ind. Eng. Chem. Res.* **2004**, *43*, 928.
- [159] H. Lim, Y. Gu, S. T. Oyama, *J. Membr. Sci.* **2012**, *396*, 119.
- [160] S. Yun, H. Lim, S. Ted Oyama, *J. Membr. Sci.* **2012**, *409-410*, 222.
- [161] K. R. Hwang, S. K. Ihm, J. s. Park, *Korean J. Chem. Eng.* **2010**, *27*, 816.
- [162] O. Iyoha, R. Enick, R. Killmeyer, B. Howard, M. Ciocco, B. Morreale, *J. Membr. Sci.* **2007**, *306*, 103.





# **2. SCOPE AND OBJECTIVES**

The goals and scope of the research work are defined in this chapter.



Nowadays hydrogen is foreseen as an important energy carrier for the future as it presents advantages such as available technologies for its decentralized production, low pollution via fuel cell utilization and diverse production sources, among others. In a green hydrogen economy this fuel will be generated from renewable energy sources or materials. In order to decrease the relatively high hydrogen storage and transport costs the production must be planned close to the consumption places.

Before a green hydrogen economy is reached the required infrastructures have to be built. In the meanwhile, the easiest and cheapest way of producing hydrogen with the present available technologies is from methane via its catalytic conversion. The most extended industrial technology for hydrogen production from methane is steam reforming (SR). But for its decentralized generation more compact technologies are needed, such as catalytic partial oxidation (CPO) or wet catalytic partial oxidation (wet-CPO). Using methane, which is the main component of natural gas and biogas, hydrogen production and price would be adequate to start with the development of the infrastructure required for a hydrogen economy, while greener technologies are optimized and their use generalized.

It is not only important to produce hydrogen, but its quality is also critical for its use in fuel cells, as this is one of the most promising hydrogen applications to solve the pollution problems created in the cities by internal combustion engine vehicles. In order to purify hydrogen from a mixture different techniques can be employed. The most spread one in industry is pressure swing adsorption (PSA) which operates under pressure and implies high investment, making it economic only at large scale. For decentralized hydrogen production smaller scale economic purification technologies will be required, such as hydrogen selective Pd based membranes. They have theoretically infinite hydrogen permselectivity and will allow performing hydrogen production and purification in an integrated unit.

As a consequence, both compact technologies for hydrogen production and small-scale technologies for its purification are key areas of research on the road to decentralized hydrogen production. This development, starting with natural gas as raw-material, will prepare the infrastructures that will facilitate later on hydrogen production from renewable sources. As renewable energies are available at smaller scales and spread

over large areas, and as hydrogen storage and transportation costs are high, the decentralized strategy is a very promising alternative.

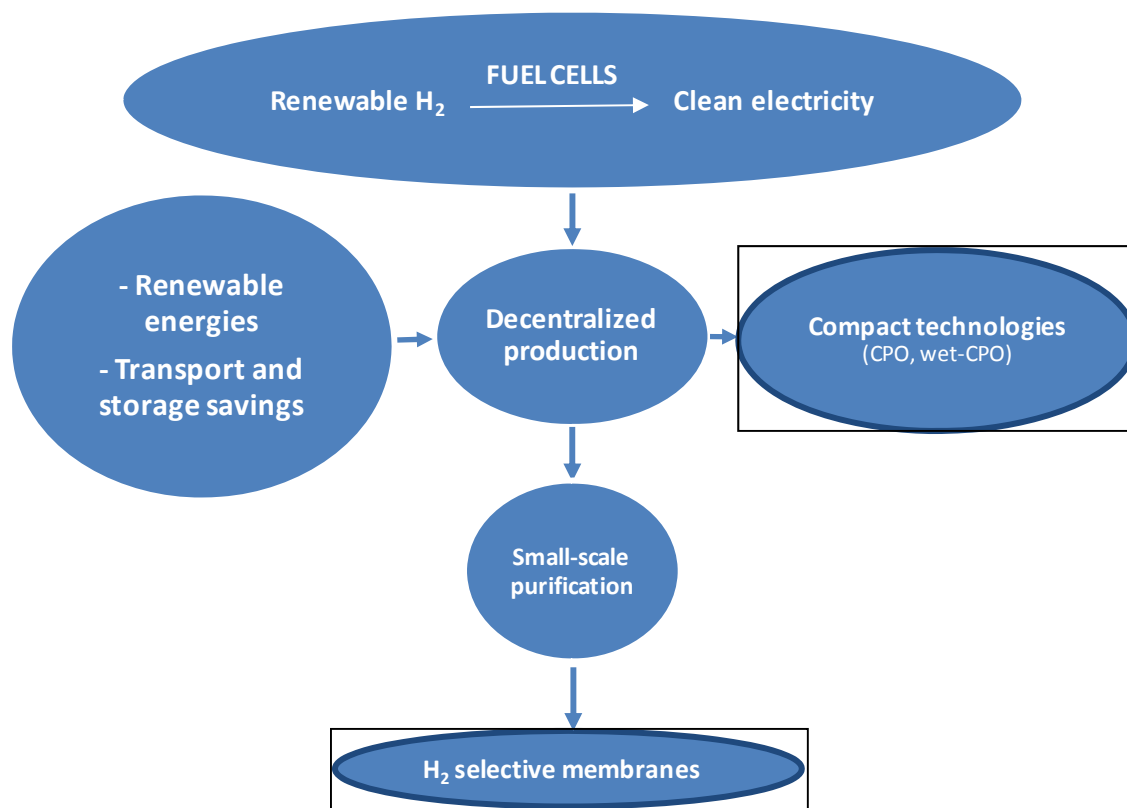


Figure 2.1. Main research areas of this Ph.D. thesis.

The main objective of the thesis is focused on the previously summarized scenario: to improve the knowledge about hydrogen selective PdCu membranes when operating in complex mixtures produced from methane CPO or wet-CPO using Ni-based catalysts and also in the presence of H<sub>2</sub>S. An outline of the main research areas of this Ph.D. Thesis is shown in Figure 2.1.

Works about hydrogen production via CPO or wet-CPO with Ni-based catalysts have been previously published in the literature, but further knowledge about the effects of the generated complex mixtures on PdCu membranes performance is needed. In order to achieve this main objective the following steps will be executed:

1. Catalysts preparation. Ni based catalysts will be prepared over basic and acidic supports via wet impregnation method. Different Ni percentages will be

incorporated to analyse the influence of the support and the active metal amount on catalyst activity and stability.

2. Characterization of the prepared catalysts. The prepared catalysts will be characterized using textural and physicochemical techniques in order to establish correlations between catalysts characterization and activity results.
3. Set-up of a bench-scale pilot plant. This plant will allow testing of catalysts and membranes in the same reactor or in consecutive stages with the adequate control of temperatures, pressures, flows and gas compositions.
4. Activity tests of the prepared catalysts. The catalysts will be tested at different temperatures, space velocities and in CPO, wet-CPO and SR processes. The aim of this part will be to choose the most promising catalyst and the optimal conditions to be used in the integrated hydrogen production plus purification system.
5. Membrane preparation. As one of the aims of this work was to test the influence of small concentrations of H<sub>2</sub>S, it was decided to prepare Pd membranes alloyed with Cu. The method for Cu electroless plating over Pd ceramic membranes will be optimized. Several PdCu membranes with different compositions will be prepared to be later employed in hydrogen purification tests.
6. Membranes characterization. The prepared membranes surface and metal layer will be characterized and measured, and their permeability in pure hydrogen will be measured at different pressures and with thermal cycles to analyse if embrittlement problems appear.
7. Membrane performance tests. Membrane permeability will be measured purifying hydrogen from complex mixtures produced via CPO or wet-CPO from methane with the developed catalysts. The optimal feed pressure and sweep gas flow for the integration will be analysed and the effect that compounds other than hydrogen have on membrane surface and performance will be studied.

8. Membrane permeability tests treating H<sub>2</sub>S containing mixtures. Hydrogen sulphide addition effect on membrane performance and stability will be analysed. Less than 100 ppmv of H<sub>2</sub>S will be used trying to simulate realistic conditions.
9. Integration of hydrogen production and purification when H<sub>2</sub>S is added. The integrated process, hydrogen production and purification, will be tested operating with H<sub>2</sub>S addition. The tests will allow studying catalyst activity with H<sub>2</sub>S addition and membranes hydrogen permeability when purifying hydrogen from complex mixtures containing H<sub>2</sub>S.
10. Analysis of membrane lifetime. The hydrogen and nitrogen flow variation along time-on-stream of the membranes tested with complex mixtures and with H<sub>2</sub>S addition will be checked to obtain information about the effect of the operating conditions on the membrane performance.
11. Characterization of the used membranes. The ones used with complex mixtures and with H<sub>2</sub>S addition will be characterized at the end of their lifetime using SEM and XRD techniques in order to explain how the membrane performance evolved.

# **3. EXPERIMENTAL PROCEDURES**

In this chapter the bench-scale pilot plants where catalyst and membrane tests were performed are explained, together with the activity and stability tests carried out with them. Then, catalyst and membrane preparation methods, wet impregnation and electroless plating respectively, are described. And finally, catalyst and membrane characterization techniques are presented.





### 3.1 Bench-scale pilot plants description

Two different bench-scale pilot plants were used to carry out catalyst and membrane tests. The catalysts activity and stability tests were performed in a bench-scale pilot plant (PP) (PID Eng&Tech) using a stainless steel fixed-bed reactor (1.15 cm i.d. and 30 cm length). The PP is illustrated in Figure 3.1. The reactor and the lines were inside a hot box (at 413 K) that kept the water in the vapour phase to avoid flooding problems during system operation. Feed gas flows were controlled with massflow controllers, and water was fed to the system with a liquid pump (Gilson 307). The desired gases entered the hot box and were mixed with the water steam. This mixture entered the reactor from the top, the reaction occurred and products went out through a condenser. The effluent stream was cooled down, thus condensed water was collected and weighed, and the gas phase was analysed on-line by a GC (HP 5890) equipped with FID and TCD detectors. Two columns, Porapak Q and Molecular Sieve 5A, were used in a series/bypass arrangement for the complete separation of  $H_2$ ,  $CH_4$ ,  $CO$  and  $CO_2$  in the GC. The outflows were manually measured with a soap bubble-flowmeter.

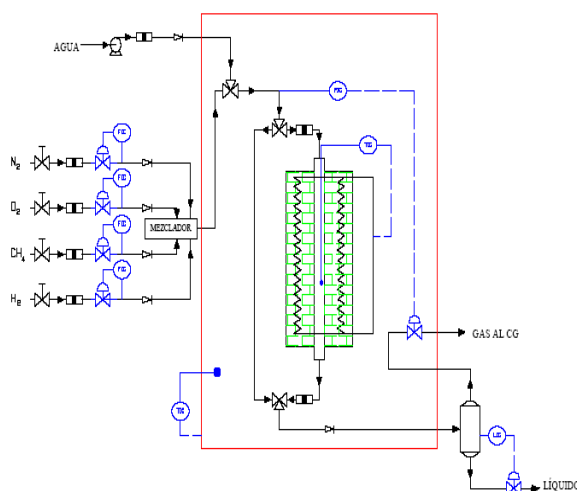


Figure 3.1. Diagram and image of the bench-scale pilot plant PP for catalysts activity tests.

Membranes were tested in a bench-scale Membrane Plant (MP) (PID Eng&Tech). The diagram of this plant is shown in Figure 3.3. Feed gases were pre-heated and mixed with the water steam produced in an evaporator. This mixture entered the first oven,

with a stainless steel fixed-bed reactor (1.22 cm i.d. and 30 cm length), and the generated products entered the membrane module. Membranes (around 15 cm long and with 1.4 cm outer diameter) were located in this module, and Ar was fed as sweep gas. Retentate gases could enter a second reactor with the same characteristics as the first one, if further reaction tests were to be performed with them (for example water gas shift reaction). Finally, the gases went out through a condenser. This MP was connected on-line to a mass spectrometer (OmniStar Pfeiffer Vacuum). By means of a six lines valve, the composition of the outlet gas from the first reactor, both permeate and retentate flows from the membrane module, and the outlet flow from the second reactor can be analysed. The membrane module was operated in counter-current mode, which allowed a higher hydrogen partial pressure difference throughout the membrane. Figure 3.2. depicts the nomenclature of the streams involved in the membrane module. As it can be observed in this figure, the membranes used in this work were dead end type. The main advantage of this MP is the different test options that it offers, making it possible to test different reactions and hydrogen separation configurations in order to identify the most suitable one.

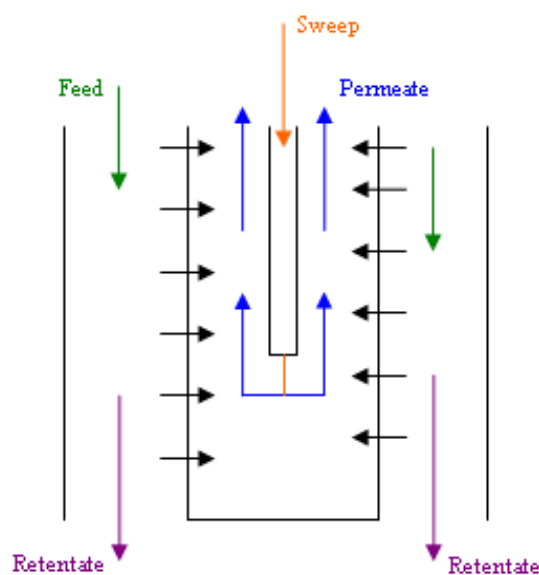


Figure 3.2. Nomenclature of the flows involved in the membrane reactor.

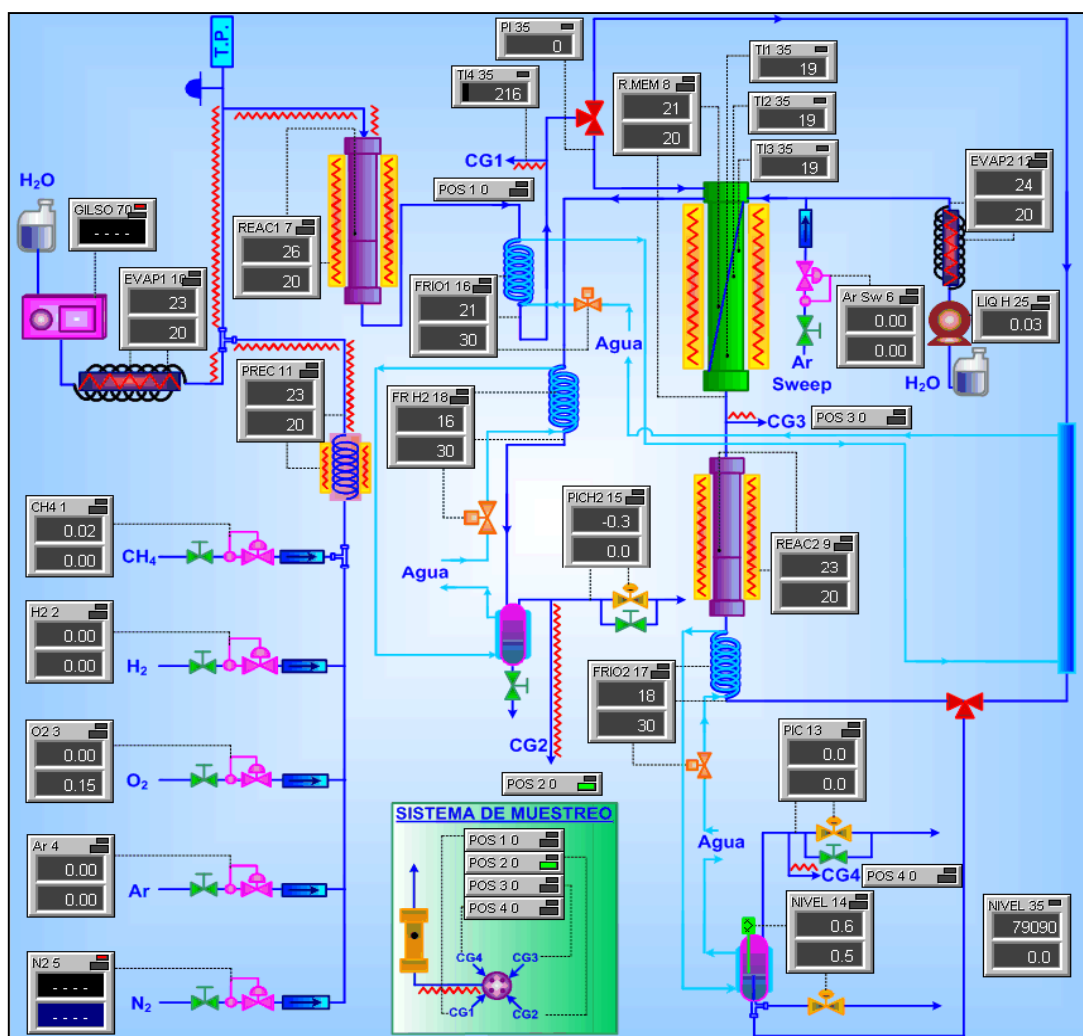


Figure 3.3. Diagram of the membrane plant.

## 3.2 Catalyst preparation

Three Ni catalysts were prepared for the CPO, SR and wet-CPO tests: 30 and 40 wt% Ni over MgO (30Ni/MgO, 40Ni/MgO) and 40 wt% Ni over Al<sub>2</sub>O<sub>3</sub> (40Ni/Al<sub>2</sub>O<sub>3</sub>). All of them were prepared by the wet impregnation method. For the catalysts with basic support Ni(NO<sub>3</sub>)<sub>2</sub>·6H<sub>2</sub>O (Sigma Aldrich, 99.999 %) was used as the active phase precursor and MgO (Sigma Aldrich, >98 %, BET-specific area 27.09 m<sup>2</sup>/g, pore volume 0.1583 cm<sup>3</sup>/g) as the support precursor. The impregnation was made in a rotary evaporator.

Firstly, the required amount of the Ni salt was dissolved in about 120-150 mL of distilled water. When the salt was completely dissolved, the solution was added to the rotary cylinder, where the adequate amount of MgO suspension had been previously

located. The mixture was kept stirring for 30 min at 293 K, and then the excess water was evaporated to dryness in the rotary evaporator at 323 K and 0.4 bar total pressure. Samples were dried in a drying oven at 383 K during 24 h, and finally they were calcined in air atmosphere at 1073 K for 4 h, with 3 K/min. In order to avoid extremely high pressure drops in the catalytic fixed-bed reactor the catalysts were pressed, crushed and sieved to obtain a homogeneous particle size of  $0.42 < d_p < 0.50$  mm.

The Ni/Al<sub>2</sub>O<sub>3</sub> catalyst was prepared using the same method. In this case, nickel acetate Ni(CH<sub>3</sub>CO<sub>2</sub>)<sub>2</sub>·4H<sub>2</sub>O was used as precursor (Sigma Aldrich, 99.99 %) and α-Al<sub>2</sub>O<sub>3</sub> (Alfa Aesar 99.9 %, 20-50 μm, BET-specific area 6.17 m<sup>2</sup>/g, pore volume 0.0110 cm<sup>3</sup>/g) as support. The nickel acetate was dissolved in distilled water, and it was mixed with an alumina suspension (the alumina dust had been previously calcined at 1073 K for 4 h). The mixture was stirred in the cylinder and the pH value was measured before establishing the vacuum and the temperature at 323 K. In the preparation of this catalyst the pH value is an important parameter, it has to be neutral. The rest of the preparation method was the same as used for the Ni/MgO catalysts: dry, calcine, press, crush and sieve.

### 3.3 Catalyst characterization

#### 3.3.1 Elemental chemical analysis

The metal nominal composition of the prepared catalysts was measured with an inductively coupled plasma unit, ICP (Perkin Elmer ICP-AES 2000-DV). Samples are nebulised and injected in an argon plasma. The plasma, at 7273 K, excites thermally the electrons from the external layer of the elements contained in the sample. The excitation causes sample atomization, and therefore, the emission of the energy beams. A spectrometer scatters the beam dividing the characteristic wavelength of each element. The selected emission is then directed, through different lenses, to the photomultiplier-detector. This detector sends an electric signal to the computer where it is transformed into a concentration value. There were some requirements that catalysts samples had to satisfy in order to be analysed by ICP:

- Samples needed to be in aqueous solution and without precipitates or suspended solids.
- Ni concentration had to be lower than 20 ppmv, if not the samples had to be diluted.
- The calibration patterns and samples had to be prepared in the same way and in each analysis. In addition to the samples two patterns and a sample blank had to be prepared each time.

Due to the conditions explained before, the solid catalysts (samples around 30-50 mg) were broken down in a digester with 4.5 mL of HF, 4.5 mL of HNO<sub>3</sub> and 3.0 mL of HCl. Before the analysis in the ICP the liquid samples were diluted with deionised water to fulfil the detection limits of the equipment.

### 3.3.2 X-Ray diffraction

With the non-destructive X Ray diffraction method the qualitative and quantitative determination of the crystalline phases of the sample components can be performed. Every crystalline substance gives always the same pattern; therefore, the X-ray diffraction pattern of pure substances is like a fingerprint. The main use of powder diffraction is to identify components in a sample. Furthermore, the areas under the diffractogram peak are related to the amount of each phase present in the sample. Due to the nature of the technique just the crystalline solids can be characterized with XRD.

The equipment employed for the X-ray diffraction analysis was a Philips PW 1710 diffractometer using Cu K $\alpha$  radiation. The XRD patterns had been represented with the  $2\theta$  angle value where diffraction maximum appeared. Identification of the phases was done using the Powder Diffraction File (PDF-2,4) database from the International Centre for Diffraction Data (ICDD).

The particle average size of the crystalline phases present in the samples can be calculated with the Scherrer equation. In this equation the full-width half maximum (B) is related to the effective crystal size (d) by the relation:

$$d = \frac{K \cdot \lambda}{B \cdot \cos \theta}$$

Equation 22

Where:

K: Sphericity factor of the particles (0.9).

$\lambda$  : Wavelength of the used radiation (Cu line 1.54 Å).

B: Full-width half maximum.

$\theta$ : Angular position of the maximum diffraction line.

d: The average crystallite size.

The Scherrer equation states that narrow diffraction peaks correspond to big and crystalline particles, whereas wide peaks correspond to amorphous or small particles.

The previous equation assumes that the only factor that affects the broadening of the diffraction line is the crystallite size. In small particles the number of available parallel planes is not high enough to obtain a sharp diffraction line and the peaks widen. Nevertheless, there are more factors that contribute to line widening, such as instrumental factors and the fact that crystals are not completely ideal. As a consequence of this difficulty to establish the actual particle size, the values obtained for the catalysts in this work were used more in a qualitative than in a quantitative way.

### 3.3.3 Electron microscopy

In the electron microscopy technique an electronically-magnified image of the sample is generated. The microscopes use an electron beam to illuminate the specimen and create a magnified image of it. The Transmission electron microscope (TEM) uses high voltage electrons to create the image. The electrons are emitted, accelerated by an anode, focused by lenses and transmitted through the specimen that is in part transparent to electrons and in part scatters them out of the beam. These electrons carry information about the structure of the specimen.

Unlike the TEM, the SEM does not carry a complete image of the specimen at any time. SEM produces images by probing the specimen with a focused electron beam that is scanned across a rectangular area of the specimen. At each point on the specimen the

incident electron beam loses some energy, and the lost energy is converted into other forms, such as heat, emission of low-energy secondary electrons, light emission or x-ray emission. The display of the SEM maps the varying intensity of any of these signals into the image in the position of the beam on the specimen when the signal was generated.

SEM analyses of the catalysts were performed using a JEOL JSM-6400 equipment with W filament and a maximum resolution of 3.5 nm. The resolution is given by the manufacturer and means that under optimum operational conditions points separated by 3.5 nm can be differentiated. The TEM analyses were performed in a Philips CM200. SEM provided information about the morphology of the sample and TEM allowed studying the internal structure.

### 3.3.4 Nitrogen adsorption isotherms (BET)

The texture of the catalysts was evaluated using nitrogen adsorption isotherms. Gas adsorption represents the most used technique to evaluate the specific surface and to characterize porous textures. Porosity can be characterised by adsorption isotherms, usually with nitrogen. In addition to the specific surface, total pore volume and pore size distribution can be measured. The size distribution is often important to ensure efficient transport of reactants and products to and from the active surface.

The equipment used for this technique was a Micromeritics TPR/TPD 2900. Firstly samples were degassed at 423 K for 24 hours, until the physisorbed gases were taken out. Then, the nitrogen pressure was increased in the sample chamber at 77 K until saturation. The surface area was determined with the physisorption of nitrogen through the B.E.T. method. The equation for the adsorption in different layers is the following one:

$$\frac{1}{V_a \cdot (P/P_0 - 1)} = \frac{1}{c \cdot V_m} + \frac{c-1}{c \cdot V_m} \cdot \frac{P}{P_0} \quad \text{Equation 23}$$

Where:

$P/P_0$ : The nitrogen partial pressure.

$V_a$ : The adsorbed volume.

$V_m$ : The adsorbed volume of the first monolayer.

c: The B.E.T. constant that is related to the adsorption enthalpy of the first layer.

When representing the  $1/V_a(P/P_0-1)$  values as function of the  $P/P_0$ , for  $P/P_0$  values lower than 0.3, a straight line is obtained. From its slope,  $V_m$  can be calculated, and, knowing the area that a nitrogen molecule covers ( $0.162 \text{ m}^2$ ), it is possible to estimate the surface area of the sample.

### 3.3.5 Temperature programmed reduction (TPR)

This technique is very interesting for the characterization of supported metals in catalysts. It provides information about the redox properties and the metal-metal and metal-support interactions. The tests were performed subjecting the oxidized catalytic materials to a programmed heating in a reducing atmosphere and registering the consumed hydrogen. This hydrogen consumption is due to the reduction of the oxidized phases with the following stoichiometry.



The employed equipment was an Autosorb 1C-TCD. The analysis conditions were: reduction mixture: 5 % of  $H_2$  in Ar, mixture flow: 50 NmL/min, temperature range: 323-1273 K, heating rate: 10 K/min. The measurements were made using approximately 1 g of catalyst. The outlet gas went through a cold trap that maintained a temperature of 185 K during the experiments in order to condense the water provided from the reduction. After the cold trap the remaining gas went through the detector (TCD).

### 3.3.6 X-ray photoelectron spectroscopy (XPS)

This technique has been used to determine the chemical state and the surface composition of fresh and used catalysts. XPS spectra are obtained by irradiating a material with a beam of X-rays while simultaneously measuring the kinetic energy and number of electrons that escape from the top 1 to 10 nm of the material being analysed. The area of the analysed catalysts sample is a circle of 720  $\mu\text{m}$  diameter, which allows to obtain information about the metal and the supports. The equipment where the samples were analysed was a VG ESCALAB 200R spectrometer with an X-ray



emission source of Mg. The kinetic energy of the electrons is related to the bond energies of each atom at each level following the equation:

$$E_C = h\nu - BE - \Phi_s \quad \text{Equation 25}$$

In this equation  $h\nu$  is the energy of the X-ray photons being used,  $BE$  is the kinetic energy of the electron as measured by the instrument and  $\Phi_s$  is the work function of the spectrometer (not the material).

In addition to element identification, surface atomic ratios were calculated. The intensity of the obtained peak was calculated by integrating each peak and subtracting the background signal.

### 3.4 Catalyst activity tests

The activity of the developed catalysts was tested at 1073 K, atmospheric pressure and two different gas space velocities: 600 h<sup>-1</sup> and 1200 h<sup>-1</sup> (WHSV, g<sub>gas</sub>g<sub>cat</sub><sup>-1</sup>h<sup>-1</sup>). The reaction temperature was controlled with a K type thermocouple. Prior to the corresponding activity measurement, the catalysts were activated to obtain the metal active phase. For the Ni catalysts used in this work, the active phase is the metallic nickel. To obtain the metallic phase, the catalysts were reduced at 1073 K, using 0.015 Nm<sup>3</sup>/h of a 3:1 N<sub>2</sub>:H<sub>2</sub> mixture, during 4 h. The catalyst weight (0.18 g) was diluted with SiC at 1:9 ratio in order to minimize temperature gradients in the bed. The rest of the reactor was filled with SiC to improve the mixture of the feed gases.

In the CPO tests the feed molar ratio was: CH<sub>4</sub>/O<sub>2</sub>/N<sub>2</sub>=2/1/3.8. These ratios are thermodynamically the most adequate ones [1]. In the wet-CPO and SR experiments different steam-to-carbon (S/C) ratios were used: 0.5, 2.0, 2.5 and 3.0. Working with water excess the coke formation in the Ni catalysts is minimized [2, 3].

The parameters used for evaluation of the performance of the catalysts were conversion, yield and selectivity, which are defined as follows:

$$\text{Methane conversion (\%): } CH_4 \text{ conv} = \frac{\text{mol } CH_4 \text{ in} - \text{mol } CH_4 \text{ out}}{\text{mol } CH_4 \text{ in}} \quad \text{Equation 26}$$

$$\text{Hydrogen selectivity (\%): } H_2 \text{ select} = \frac{\text{mol } H_2 \text{ out}}{\text{mol } H_2 \text{ out} + \text{mol } H_2O \text{ out}} \quad \text{Equation 27}$$

$$\text{Hydrogen yield: } H_2 \text{ yield} = \frac{\text{mol } H_2 \text{ out}}{\text{mol } CH_4 \text{ in}} \quad \text{Equation 28}$$

### 3.5 Membrane preparation

The tested PdCu membranes were prepared in the Energy Research Centre of the Netherlands (ECN), in the Efficiency and Infrastructure unit during a six month internship. PdCu membranes were prepared by sequential electroless plating. The initial membranes used in this work were ECN's Pd membranes. These membranes consisted of Pd over an alumina tubular support, with an outside diameter of 14 mm and a wall thickness of 3 mm. The support consists of a multiple layer structure with a top layer of  $\alpha$ -Al<sub>2</sub>O<sub>3</sub> with 90 nm pore size. Pd membranes were prepared following the procedure reported by Hou et al. [4].

The reactants used for the copper plating metal and reducing solutions are shown in Table 3.1 and Table 3.2. A simplified recipe based on suggestions found in the literature was used [5]. In case of Cu electroless plating on a Pd membrane, the Pd layer itself is the active surface. When using formaldehyde as the reducing agent, the effect of pH is significant; with its optimum value between 12 and 14, and also the plating bath temperature [6]. The amount of solution was prepared according to the membrane length, so that the entire surface was covered. The solution volume per membrane surface area was between 6 and 7 cm<sup>3</sup>/cm<sup>2</sup>, which varied due to the different length of the Pd membranes that were Cu plated.

Table 3.1. Recipe of the metal solution for Cu plating.

Reagent	Quantity
CuSO <sub>4</sub> 5H <sub>2</sub> O	8.69 g/L
Na <sub>2</sub> EDTA	44.44 g/L
NaOH	17.77 g/L
Triton X-100	0.617 mg/L

Table 3.2. Recipe of the reducing solution for Cu plating.

Reagent	Quantity (for 100 mL of Cu bath)
Formaldehyde (37 %)	1,53 mL
2,2-bypirydyl	0,96 mg
Ultrapure water	9,58 mL

The necessary equipment for the Cu plating was an electroless plating bath (placed in a fume hood) with a heating unit, a filter cylinder, filter papers, Teflon plugs to seal the membranes inside, and a drying oven. The Pd and Cu layers were on the outside of the tubular membrane, so the inside of the membrane had to be hermetically sealed during the plating time. In the plating process the membranes and the solution were carefully manipulated to avoid any dust deposition or damage. The metal solution was put into a plating bath equipped with a heating unit that kept the temperature constant at 323 or 318 K. The solution was carefully shaken by hand during plating to prevent the exhaustion of the metal solution near the membrane as well as bubble adhesion to the membrane that could result in film defects.

When the desired plating time (0.5, 1.0, 1.5 or 2.0 h) had elapsed, the membranes were rinsed and dried at 333 K. Membranes were weighed before and after the plating process to measure the weight increase with a view to estimating the amount of deposited copper. PdCu layers were then alloyed in an inert atmosphere at 673 K for 150 h, according to the procedure proposed in [7]. To verify the optimum alloying time, two of the prepared membranes were alloyed in a gas permeation system. This experiment simulated the alloying conditions, the same heating rate and in inert atmosphere, but allowed to measure hydrogen permeation to check how the permeation changed with alloying time.

All the prepared membranes were checked with a simple nitrogen test to detect metal layer defects that could influence membrane permeance and selectivity results. This test was conducted before and after Cu plating, after alloying and after the hydrogen permeance tests in order to control the effect of the steps on membrane morphology (defect formation). For the leak tests, the ends of the membranes were sealed and the membranes were then filled with nitrogen at 3 bar(g).

### 3.6 Membrane characterization

#### Thickness of the metal layers

The easiest technique for measuring the PdCu metal layers thickness is the weighing difference before and after the metal plating. The Cu layer thickness values obtained using the weight difference technique were compared to the ones determined by SEM. Membranes SEM analyses were performed with a JEOL JSM 6550F equipment with a field emission cathode and with 8 nm of resolution. To measure the metal layer thickness by SEM images, membrane rings were cut and these rings were broken to measure the thickness perpendicularly.

#### Membrane Composition

The composition was calculated from the metal layer thicknesses measured with Field-Emission SEM after the Cu plating. Due to the fact that membranes are not completely regular, the thickness of the Pd and Cu was measured at different points on a cut ring, and the average of these values was calculated. With the obtained thickness values the composition of the membranes was estimated. EDX measurements were also performed after the alloying of some of the membranes.

#### Morphology of the metal layer

It is important to check the morphology of the prepared membranes, as it has been observed in the literature that the strength of the metal layer is directly related to the performance and selectivity of the membrane. Membrane morphology was analysed using SEM images. These images were obtained after Cu plating, after alloying and after the permeance tests, in order to check how the surface changed throughout the entire process.

### 3.7 Membrane permeance measurements in pure H<sub>2</sub>

The hydrogen permeance ( $\text{molH}_2 \text{ m}^{-2}\text{s}^{-1}\text{Pa}^{-n}$ ) of some of the prepared PdCu membranes was measured at ECN facilities, during the internship period, in a Gas Permeation System (GPS). The others were tested in the MP previously explained in section 3.1. The GPS system, which includes a dead end module with bleed flow, can control feed and permeate pressure, temperature, and the feed gas type and flow. The procedure to

measure the permeance was the same in the GPS (ECN) and in the MP (Bilbao) systems. Before starting the hydrogen permeance tests, a leak test was conducted with N<sub>2</sub> at 298 K, as a reference, and then the membranes were heated in N<sub>2</sub> to 673 K. Once at the desired temperature, another N<sub>2</sub> leak test was carried out. The membranes were then kept in hydrogen followed by permeation readings, at 9, 7, 5 and 3 bar(g) feed pressure with 2 bar of pressure difference across the membrane. These measurements were repeated three times. The membranes were then cooled to 423 K and subsequently heated again to 673 K in N<sub>2</sub> followed by three permeance measurements in a hydrogen atmosphere. The next step involved cooling and heating the membranes again, but this time in H<sub>2</sub>. Finally, before the last cooling, three hydrogen permeance measurements were taken at different feed pressures.

### 3.8 Membrane permeation measurements in complex mixtures

In the bench-scale pilot membrane plant in Bilbao, MP, membrane integration in hydrogen production and purification process was analysed. In the MP, methane catalytic CPO and wet-CPO with subsequent hydrogen separation in the membrane module were performed in order to analyse the membrane performance when purifying hydrogen from complex mixtures. Methane was converted to hydrogen in the first fixed bed reactor. The product flow, from here on the complex mixture, generated in this first reactor was then fed to the membrane module for hydrogen purification.

In CPO and wet-CPO reactions hydrogen production is favoured by high temperature and low pressure. However, the second part of the process, hydrogen purification, is favoured by high pressure difference over the membrane. In order to select the optimum operating pressure for both processes, hydrogen production followed by purification tests were performed at different feed pressures. The hydrogen pressure difference over the membrane, and therefore hydrogen recovery, can also be improved by adding a sweep gas on the permeate side of the membrane. The sweep gas can decrease the partial pressure of hydrogen on this side increasing the hydrogen pressure difference across the membrane. Several sweep gas flows were employed at two pressure differences across the membrane, 2 and 3.5 bar, in order to analyse its effect on hydrogen recovery. Argon was used in these tests as sweep gas for reasons of

simplicity, but steam can also be used, obtaining a pure hydrogen flow simply by cooling the hydrogen/water permeate flow.

Once the main process parameters had been set, hydrogen production and subsequent purification tests were performed at different reaction conditions in the first reactor. Both CPO and wet-CPO processes were carried out in the catalytic reactor at a space velocity of  $600 \text{ h}^{-1}$  ( $\text{g}_{\text{gas}} \cdot \text{h}^{-1} \cdot \text{g}_{\text{cat}}^{-1}$ ) with 0.35 g of catalyst, diluted with SiC at a 1:9 ratio. Prior to the reaction tests, the catalyst was reduced at 1073 K using  $0.015 \text{ Nm}^3/\text{h}$  of a 3:1  $\text{N}_2:\text{H}_2$  mixture for 4 h. In the wet-CPO process, steam-to-carbon ratios (S/C) were varied from 0.02 to 2.5. The membrane module operated at 673 K. By means of a six-port valve, the outlet gas from the first reactor and both permeate and retentate outlet flows from the membrane module compositions were analysed on-line by the mass spectrometer. The performance of the process was analysed in terms of methane conversion, Equation 26. Hydrogen recovery, Equation 29, was calculated to analyse hydrogen purification in the membrane module.

$$\text{Hydrogen recovery: } H_2 \text{ recovery} = \frac{\text{mol } H_2 \text{ feed} - \text{mol } H_2 \text{ retentate}}{\text{mol } H_2 \text{ feed}} \quad \text{Equation 29}$$

### 3.9 Membrane permeation measurements with $\text{H}_2\text{S}$ addition

The  $\text{H}_2\text{S}$  addition effect on the membrane performance was analysed through different kinds of tests. First of all hydrogen permeance tests were performed in  $\text{H}_2:\text{H}_2\text{S}$  mixtures with 40, 60 and 100 ppmv of  $\text{H}_2\text{S}$ . With these tests it was possible to study the influence of  $\text{H}_2\text{S}$  addition and compare it with the hydrogen permeance recorded with pure hydrogen at the same pressure difference. Sulphur compounds are interesting as they appear in the natural gas. Therefore, some process integration tests with hydrogen production from methane in the first reactor followed by purification in the membrane module were performed adding 32 ppmv of  $\text{H}_2\text{S}$ . Two different hydrogen production processes were performed, CPO and wet-CPO with  $\text{S}/\text{C}=0.5$ . Finally, hydrogen permeance recovery tests were carried out. As observed in the literature hydrogen permeance will be affected by sulphur addition, and maintaining the membrane in hydrogen atmosphere at high temperature can restore its permeance. In order to try to recover the permeance and selectivity, the membrane was kept in hydrogen at temperatures around 773-898 K.

## Reference List

- [1] B. Christian Enger, R. Lødeng, A. Holmen, *Appl. Catal. A* **2008**, 346, 1.
- [2] A. Djaidja, A. Kiennemann, A. Barama, *Stud. Surf. Sci. Catal.* **2006**, 162, 945.
- [3] B. C. Michael, A. Donazzi, L. D. Schmidt, *J. Catal.* **2009**, 265, 117.
- [4] K. Hou, R. Hughes, *J. Membr. Sci.* **2002**, 206, 119.
- [5] F. Roa, J. D. Way, *Ind. Eng. Chem. Res.* **2003**, 42, 5827.
- [6] M. Oita, M. Matsuoka, C. Iwakura, *Electrochim. Acta* **1997**, 42, 1435.
- [7] A. Kulprathipanja, G. k. O. Alptekin, J. L. Falconer, J. D. Way, *J. Membr. Sci.* **2005**, 254, 49.





# **4. EXPERIMENTAL RESULTS. CATALYSTS**

Prior to performing activity tests with the prepared catalysts, some theoretical studies were carried out. The Aspen Plus software was employed to choose the optimum operating conditions taking into account the three hydrogen production processes: CPO, wet-CPO and SR. Diffusional studies were done to identify if the catalytic processes were limited by the diffusional steps or by the reactions. The selected operational variables were: 1073 K and atmospheric pressure, knowing that they imply some diffusional limitations. The three prepared catalysts were characterized before and after the activity tests. A good dispersion of the Ni over the low BET surface supports was observed in SEM and TEM images. By XRD and TPR it was concluded that a solid-solution was formed in the Ni/MgO catalysts. No carbon formation was observed by XPS in the used catalyst samples and sintering could be the main reason for the deactivation observed in some of the activity tests.



## 4.1 Thermodynamic and diffusion studies of hydrogen production processes

The operating variables for hydrogen production process have to be selected in order to obtain high hydrogen production with low catalyst deterioration. The variables that most influence the process are temperature, pressure, steam-to-carbon ratio (S/C), and feed space velocity. Low temperatures would be thermodynamically favourable for the CPO reaction and high temperatures for SR. About the pressure, the process is favoured at low pressures, as explained by Le Chatelier's Law. Hydrogen production will be enhanced increasing the steam-to-carbon ratio in SR and wet-CPO processes, minimizing also coke production.

The Aspen Plus software, with the UNIQUAC model, was used to carry out a sensitivity analysis of temperature, pressure and steam-to-carbon ratio influence on methane conversion and select the most appropriate operating conditions for the experimental tests. The S/C and O/C ratios of the simulated conditions are shown in Table 4.1. The effect of temperature on methane conversion and hydrogen yield was analysed at 1 bar and with constant composition, varying the temperature from 723 to 1123 K, see Figure 4.1, Figure 4.2, Figure 4.3 and Figure 4.4. At around 1073 K methane conversion is around 95 % in CPO and almost 100 % in wet-CPO and SR with an S/C value higher than 2. As it can be observed in the figures, when all the possible reactions between CH<sub>4</sub>, CO, CO<sub>2</sub>, H<sub>2</sub>O and O<sub>2</sub> are considered in CPO, the methane equilibrium conversion increases with temperature. Methane conversion is lower than 50 % in SR with S/C=0.5 even at high temperatures, as depicted in Figure 4.2. This is due to water stoichiometric limitation and is not reflecting the thermodynamics. Hydrogen yield increases when increasing the amount of water added to the process, as expected. Working at temperatures higher than 1073 K will only imply higher energy consumption with no significant increase of methane conversion.

Table 4.1. S/C and O/C ratios of the CPO and wet-CPO conditions.

Process	CPO	wet-CPO			
S/C ratio	0	0.5	2.0	2.5	3.0
O/C ratio	1.0	1.4	2.5	2.8	3.2

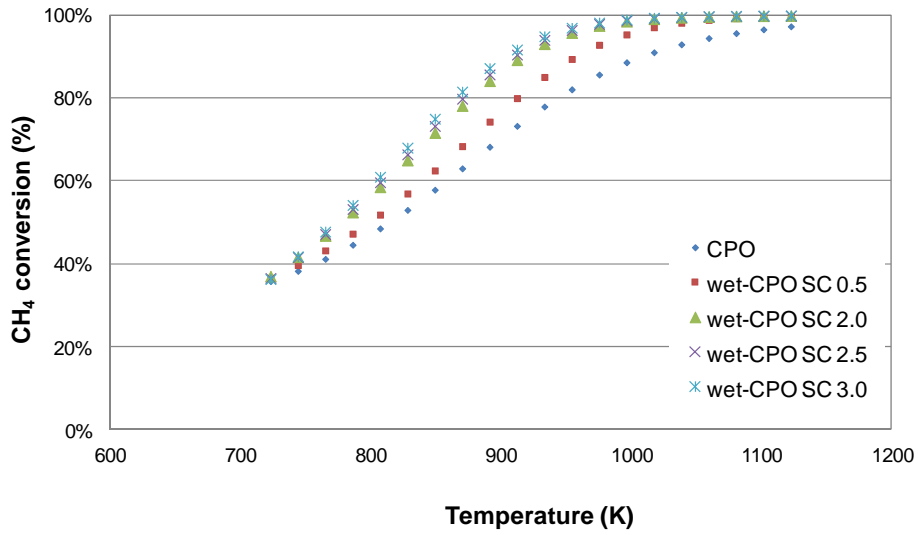


Figure 4.1. Thermodynamic effect of temperature on methane conversion with CPO and wet-CPO processes with S/C ratio from 0.5 to 3 at 1 bar.

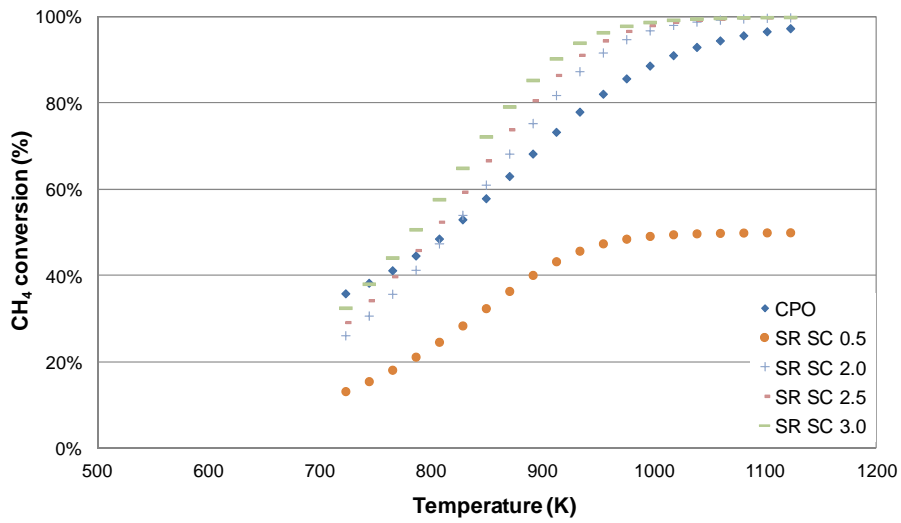


Figure 4.2. Thermodynamic effect of temperature on methane conversion with CPO and SR processes with S/C ratio from 0.5 to 3 at 1 bar.

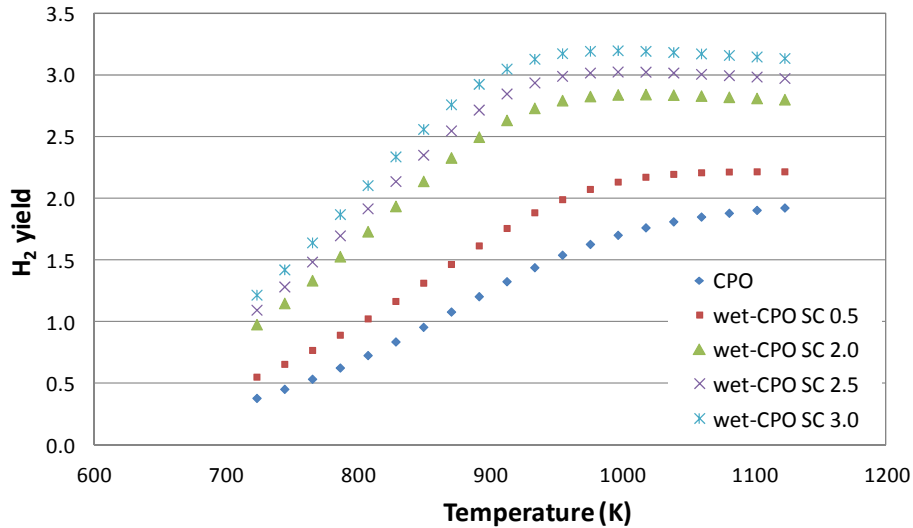


Figure 4.3. Thermodynamic effect of temperature on hydrogen yield with CPO and wet-CPO processes with S/C ratio from 0.5 to 3 at 1 bar.

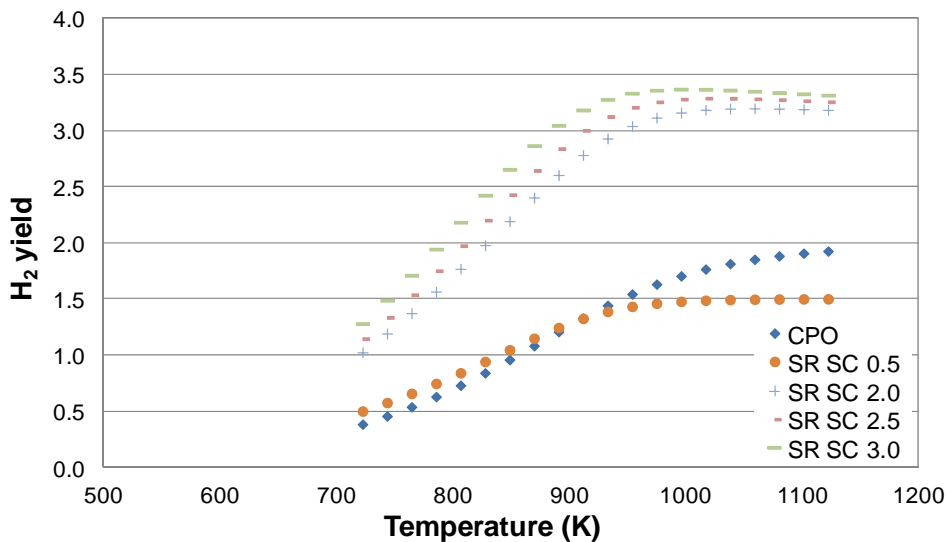


Figure 4.4. Thermodynamic effect of temperature on hydrogen yield with CPO and SR processes with S/C ratio from 0.5 to 3 at 1 bar.

When simulating the effect of increasing pressure at constant temperature, see Figure 4.5 and Figure 4.6, it was observed that it unfavoured all three processes, as it is thermodynamically expected, due to the fact that in the main reactions the product moles are more than the reactant moles. The addition of water to the process, at 1 bar and 1073 K, increases methane conversion to almost 100 % with S/C=0.4 in wet-CPO and with S/C=1.2 for SR process as illustrated in Figure 4.7. Hydrogen yield also

increases with water addition to 2.3 and 3.2 at S/C=2 in wet-CPO and SR respectively, see Figure 4.8.

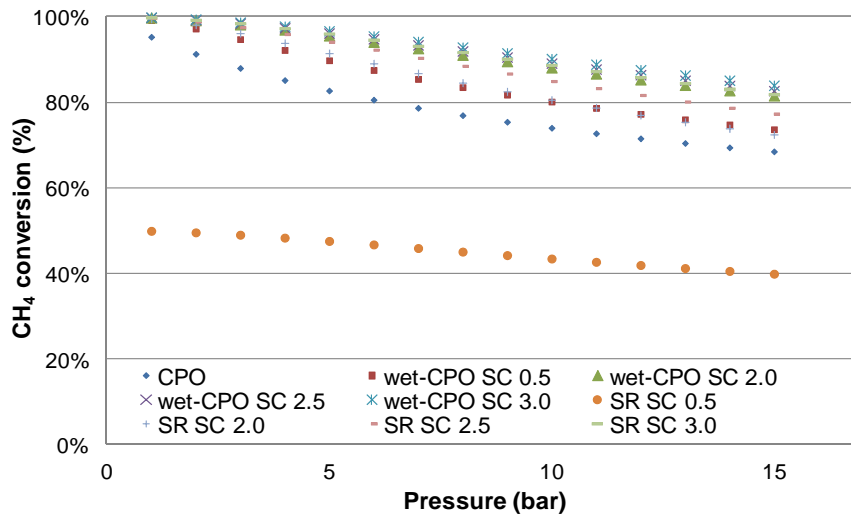


Figure 4.5. Thermodynamic effect of pressure on methane conversion in CPO, wet-CPO and SR processes at 1073 K.

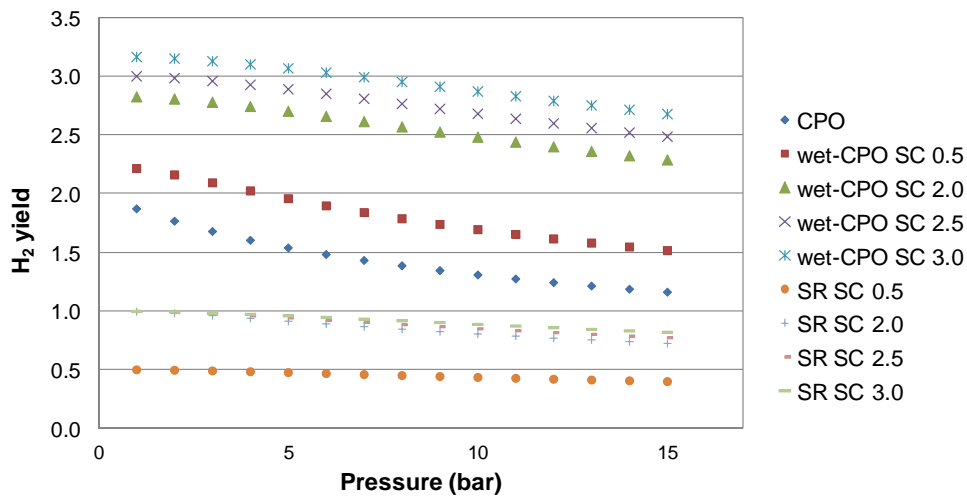


Figure 4.6. Thermodynamic effect of pressure on hydrogen yield in CPO, wet-CPO and SR processes at 1073 K.

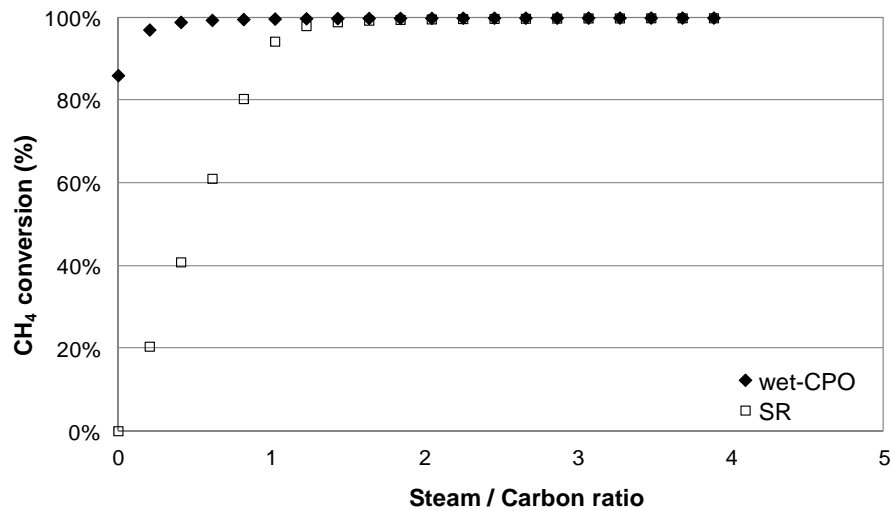


Figure 4.7. Thermodynamic effect of S/C ratio on methane conversion in wet-CPO and SR processes at 1 bar and 1073 K.

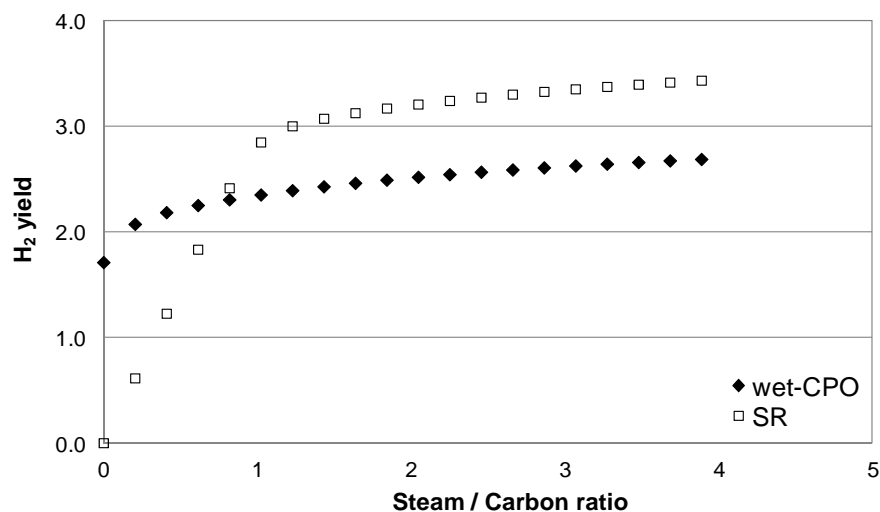


Figure 4.8. Thermodynamic effect of S/C ratio on hydrogen yield in wet-CPO and SR processes at 1 bar and 1073 K.

With the previous simulations the thermodynamic influence of the main parameters was studied. According to the thermodynamic simulation results the operating conditions for CPO, SR and wet-CPO will preferably be atmospheric pressure, temperature between 1023 and 1073 K, and S/C ratio between 2 and 3 for wet-CPO.

Nevertheless, the real process is catalytic, so the thermodynamic values are just the maximum conversion that could be reached. A theoretical study of diffusional

limitations was performed taking into account that the real process needs catalyst to operate at moderate temperatures with high methane conversion. Hydrogen production from methane is a heterogeneous catalytic process that can be divided in different stages:

1<sup>st</sup>. Mass transport of reactants from the bulk fluid phase to the outer surface of the catalyst particles.

2<sup>nd</sup>. Reactant diffusion from the outside of the pores to the active centres that can be inside the porous structure.

3<sup>rd</sup>. Reactant adsorption at an active centre of the catalyst.

4<sup>th</sup>. Reaction at an active centre of the catalyst.

5<sup>th</sup>. Desorption of the products.

6<sup>th</sup>. Diffusion of the products from the inside of the pores to the outside.

7<sup>th</sup>. Mass transport of the products from the outer surface of the catalysts particles to the bulk fluid phase.

The overall reaction rate depends on the resistance of all the stages involved in the catalytic process and it is controlled by the slowest stage. In the case of porous catalysts, as in this case, it is necessary to analyse separately the reaction influence and the possible internal (inside the catalysts pores) and external (in the fluid boundary layer around the catalytic particles) diffusional limitations. When the reaction occurs in, or close to, the catalyst active centres usually the adsorption and desorption stages are quick enough as to be considered in quasi equilibrium.

The preferred operational situation is the one where the reaction limits the catalytic process, so that the conversion will be conditioned by the catalyst performance and not by diffusional problems. The external and internal mass transport resistances can be analysed with the Mears and Weisz-Prater criteria [1] in order to determine if they are influencing the overall process. According to the Mears criterion the external mass transport effects can be neglected if the relation shown in Equation 30 is confirmed.

$$\frac{-r'_A(obs) \cdot \rho_b \cdot R \cdot n}{k_c \cdot C_{Ab}} < 0.15 \quad \text{Equation 30}$$



Where:

$-r'_A$  (obs): observed reaction rate, mol CH<sub>4</sub> per catalyst kg and second

$\rho_b$ : catalyst bed bulk density (kg/m<sup>3</sup>)=  $(1 - \varepsilon_b)\rho_c$

$\varepsilon_b$ : bed porosity

$\rho_c$ : catalyst density

R: catalyst particle radius (m)

n : reaction order

$k_c$  : external mass transport coefficient, related to the catalyst bed volume (m/s)

$C_{Ab}$  : bulk volumetric concentration (kmol/m<sup>3</sup>)

It was assumed that the reaction order was 1 and the global mass transport coefficient,  $k_c$ , was calculated using the Colburn J factor ( $J_D$ ) as a function of the Reynolds number, see Equation 31, Equation 32, Equation 33 and Equation 34.

$$J_D = \frac{Sh}{Sc^{1/3} Re} \quad \text{Equation 31}$$

$$\text{Sherwood number: } Sh = \frac{k_c d_p}{D_A} \quad \text{Equation 32}$$

$$\text{Schmidt number: } Sc = \frac{\nu}{D_A} \quad \text{Equation 33}$$

$$\text{Reynolds number: } Re = \frac{\rho d_p U}{\mu} = \frac{d_p U}{\nu} \quad \text{Equation 34}$$

Where:

$k_c$  : external mass transport coefficient (m/s)

$d_p$  : catalyst particle diameter (m)

$D_A$  : diffusivity of methane in the mixture (m<sup>2</sup>/s), estimated by ASPEN PLUS software

$\nu = \frac{\mu}{\rho}$  : kinematic viscosity (m<sup>2</sup>/s)

$\mu$  : fluid viscosity (g/sm)

$\rho$  : fluid density (g/m<sup>3</sup>)

U: superficial gas velocity (m/s)

The mixture density and viscosity were calculated simulating the operating conditions in the Aspen Plus software.

The  $J_D$  factor was calculated from the Dwidevi and Upadhayay [2] mass transport correlation for packed beds, see Equation 35, that is applicable for low Re numbers ( $>1$ ).

$$\varepsilon_b J_D = 0.4548 \text{Re}^{-0.4069} \quad \text{Equation 35}$$

To analyse if the internal diffusion inside the pores limited the catalytic rates the Weisz-Prater criterion (Equation 36) was used [1], employing experimentally observed reaction rates,  $-r'_A(\text{obs})$ .

$$C_{WP} = \eta \phi^2 = \frac{-r'_A(\text{obs}) \cdot \rho_c \cdot R^2}{D_e \cdot C_{AS}} \quad \text{Equation 36}$$

If  $C_{WP} \ll 1$  there is no internal diffusion limitation

If  $C_{WP} \gg 1$  the internal diffusion limits the catalytic process

Where:

A : methane

$$-r'_A(\text{obs}): \frac{\text{mol } CH_4 \text{ react}}{\text{kg cat} \cdot \text{s}}$$

$D_e$  : effective diffusivity, see Equation 37 ( $\text{m}^2/\text{s}$ ).

$$D_e = \frac{D_A \cdot \varepsilon_p \cdot \sigma}{\tilde{\tau}} \quad \text{Equation 37}$$

Where:

$D_A$  : methane diffusivity in the gaseous mixture ( $\text{m}^2/\text{s}$ )

$\varepsilon_p$  : catalyst particle porosity (typical value of 0.4)

$\sigma$  : constriction factor (typical value of 0.8)

$\tilde{\tau}$  : tortuosity (typical value of 3)

$C_{AS}$  : methane concentration on the catalyst outer surface

The methane diffusivity was calculated with the Aspen Plus software, and for the calculation of the reaction rate the experimentally obtained conversion at the operating conditions was used. The rest of the values were known.

During the experimental work two different catalytic systems were employed: pilot plant (PP) (section 4.2) and the first reactor R1 in the membrane plant (MP) (sections 6.2 and 6.3). As the reactors dimensions were different, the external and internal mass transport influence was analysed for both of them separately. The mass transport limitation criteria were calculated for both, the equilibrium conversion at the set point temperature and pressure and the observed conversion for the 30Ni/MgO catalyst.

When operating in CPO in the PP, see Table 4.2, there are both external and internal mass transport limitations. The observed conversion was close to the equilibrium one even with the mass transport limitations, which meant that the process was not kinetically controlled. At 898 K the experimental conversion was higher than the corresponding equilibrium conversion, due to a higher temperature in the catalytic bed, which will be discussed in section 4.2. Thus, the qualitative nature of the data shown in Table 4.2 should be taken into account when diffusion limitations at different space velocities are compared. The uncertainties arise from: I) the temperature at the bed exit was not measured; II) not all the catalyst particles might be required when the lowest space velocity was used, as equilibrium conversions could be reached before the end of the bed. This implies that weight based specific reaction rates are underestimated, resulting in higher values of the parameters used to determine if diffusion limitations must be taken into account.

Table 4.2. Results of the external and internal mass transport criteria for the PP with the equilibrium (Eq conv) and the experimentally observed (Obs conv) conversions for 30Ni/MgO at CPO and 1 bar.

<b>PP</b>		<b>CPO</b>			
		1073		898	
Temperature (K)					
Space velocity (h <sup>-1</sup> )		600	1200	600	1200
Mears, external < 0.15	Eq conv	0.23	0.29	0.16	0.21
	Obs conv	<b>0.22</b>	<b>0.30</b>	<b>0.19</b>	<b>0.29</b>
Weisz-Prater, internal < 1	Eq conv	3.54	7.10	2.76	5.52
	Obs conv	<b>3.51</b>	<b>7.02</b>	<b>3.31</b>	<b>7.56</b>

When operating in wet-CPO or SR conditions in the PP the observed conversion was much lower than the equilibrium one at 1073 or 898 K. With the lower conversions, wet-CPO with S/C 2 and 3 and SR, there was no external mass transport limitation, see Table 4.3. Regarding the internal diffusion results in most of the conditions there is still internal mass transport limitation, which means that the Ni deposited inside the pores will not be 100 % effective. This is partially solved by incorporating the active phase mostly over the surface of the catalyst particles and on the outer part of the pores.

Table 4.3. Results of the external and internal mass transport criteria for the PP with the equilibrium (Eq conv) and the experimentally observed (Obs conv) conversions for 30Ni/MgO at wet-CPO and SR at 1 bar.

<b>PP</b>		Wet-CPO						SR					
Temperature (K)		1073						1073					
WHGV (h <sup>-1</sup> )		600			1200			600			1200		
S/C ratio		0.5	2	3	0.5	2	3	0.5	2	3	0.5	2	3
Mears, external < 0.15	Eq conv	0.23	0.25	0.25	0.30	0.32	0.33	0.12	0.25	0.26	0.16	0.33	0.35
	Obs conv	<b>0.21</b>	<b>0.14</b>	<b>0.09</b>	<b>0.26</b>	<b>0.14</b>	<b>0.05</b>	<b>0.05</b>	<b>0.07</b>	<b>0.08</b>	<b>0.03</b>	<b>0.03</b>	<b>0.02</b>
Weisz-Prater, internal < 1	Eq conv	3.69	4.55	4.66	7.34	8.56	9.32	1.97	4.45	4.83	3.96	8.92	9.67
	Obs conv	<b>3.38</b>	<b>2.54</b>	<b>1.62</b>	<b>6.23</b>	<b>3.60</b>	<b>1.38</b>	<b>0.79</b>	<b>1.27</b>	<b>1.53</b>	<b>0.79</b>	<b>0.91</b>	<b>0.45</b>

In the MP bench-scale pilot plant when CPO and wet-CPO process were carried out there was still high internal mass transport limitation, see Table 4.4, but the external limitation was less severe than in the PP due to a better reactor design.

Table 4.4. Results of the external and internal mass transport criteria for the PM with the equilibrium (Eq conv) and the experimentally observed (Obs conv) conversions for 30Ni/MgO tested with M8 membrane in CPO and wet-CPO at 3.5 bar(g).

<b>PM</b>		CPO	Wet-CPO		
Temperature (K)		1073	1073		
Space velocity (h <sup>-1</sup> )		600	600		
S/C ratio		0	0.5	1.5	2.5
Mears, external < 0.15	Eq conv	0.14	0.17	0.17	0.17
	Obs conv	<b>0.12</b>	<b>0.15</b>	<b>0.16</b>	<b>0.16</b>
Weisz-Prater, internal < 1	Eq conv	2.60	2.92	3.64	3.45
	Obs conv	<b>2.19</b>	<b>2.59</b>	<b>3.42</b>	<b>3.17</b>

## 4.2 Catalysts performance in methane CPO, wet-CPO and SR

The Ni-based catalysts prepared for hydrogen production from methane in CPO, wet-CPO and SR were analysed at different temperatures and space velocities in the bench-scale pilot plant PP. First of all, the three of them were tested in CPO at 1073 K with 600 h<sup>-1</sup> and 1200 h<sup>-1</sup> of space velocity, followed by the same test at 898 K. The catalysts were changed after the tests at 1073 K and fresh catalysts were used for the tests at 898 K. The dotted lines indicate the change of working day. During the nights the reactor was cooled down to room temperature and heated before next day operation at 3 K/min under nitrogen. Only fresh catalysts were activated, heating them at 3 K/min in N<sub>2</sub>:H<sub>2</sub> 3:1 and maintained 4 h at the desired temperature. Catalysts were activated at the operation temperature, 1073 or 898 K.

The reactor temperature was controlled with a thermocouple located just before the catalytic bed. A second thermocouple was also placed around the middle of the catalytic bed in order to get qualitative knowledge about the temperature profile inside it. From the analysis of these temperature measurements it can be concluded that: I) for the CPO tests an increase of around 100 to 200 K was measured; II) for wet-CPO tests with S/C ratios higher than 2, temperature differences lower than 10 K were recorded, and III) for SR reaction decreases of 50-100 K were detected.

Table 4.5. Deviations, (inlet-outlet)/inlet in %, of C, O and H material balances during the CPO tests with 30Ni/MgO, 40Ni/MgO and 40Ni/Al<sub>2</sub>O<sub>3</sub> at 1 bar.

		1073 K 600 h <sup>-1</sup>	1073 K 1200 h <sup>-1</sup>	898 K 600 h <sup>-1</sup>	898 K 1200 h <sup>-1</sup>
30NiMgO	C	6.2	0.4	5.6 6.0	1.5
	O	14.9	13.0	1.2 8.3	3.8
	H	2.5	3.6	9.4 6.5	2.0
40NiMgO	C	6.5	2.6	0.3 2.0	2.0
	O	0.2	2.9	0.3 0.2	4.7
	H	7.3	3.5	4.8 4.6	0.9
40NiAl <sub>2</sub> O <sub>3</sub>	C	7.8	4.3	6.8	5.4
	O	2.0	1.4	5.3	3.3
	H	9.6	6.9	9.9	4.5

In Table 4.5 a summary of the deviation on the C, O and H material balances during the CPO tests performed with the three catalysts (Figure 4.9, Figure 4.10 and Figure 4.11)

are shown. C, O and H mol differences between the inlet (feed flows) and the outlet (measured out flow and composition) was calculated for each measured point. In the table the average value of the C, O and H deviation obtained at each condition is shown. Differences were usually below 10 %, which is considered acceptable taking into account the experimental procedure (i.e. liquid water determined by weight and flows measured by manual bubble flow-meter).

The 40Ni/MgO catalyst showed high methane conversion, around 94 %, close to the equilibrium conversion, when operating at 1073 K and 600 h<sup>-1</sup>, see Figure 4.9. The increase of the space velocity from 600 h<sup>-1</sup> to 1200 h<sup>-1</sup> at 1073 K had a negative effect on the conversion. The conversion had a slightly decreasing tendency, being 88 % at the end of the test. The conversion decrease indicates that the catalytic bed is not enough to achieve the equilibrium conversion. At both space velocities the temperature inside the catalytic bed was higher than the set point, as explained in previous section.

When the catalyst was activated and operated at 898 K, the conversion at 600 h<sup>-1</sup> was continuously increasing for around 7 hours. Ni/MgO catalysts are known to form solid solutions, impeding the metal reduction, which will be discussed in section 4.3. Most probably, the activation at 898 K (heating at 3 K/min till 898 K and maintained for 4 h) was not enough to activate the catalyst. The hydrogen produced during the reaction together with the fact that the real temperature in the bed was higher than 898 K, will have allowed further activation of the catalyst during the test, obtaining higher conversion. The obtained conversion was above the equilibrium one at 898 K, due to the higher temperature in the catalytic bed due to the exothermic CPO reaction. Increasing the space velocity at 898 K the conversion increased to around 90 %. With more feed gas, more reaction occurred, more heat was generated, and higher was the bed temperature.

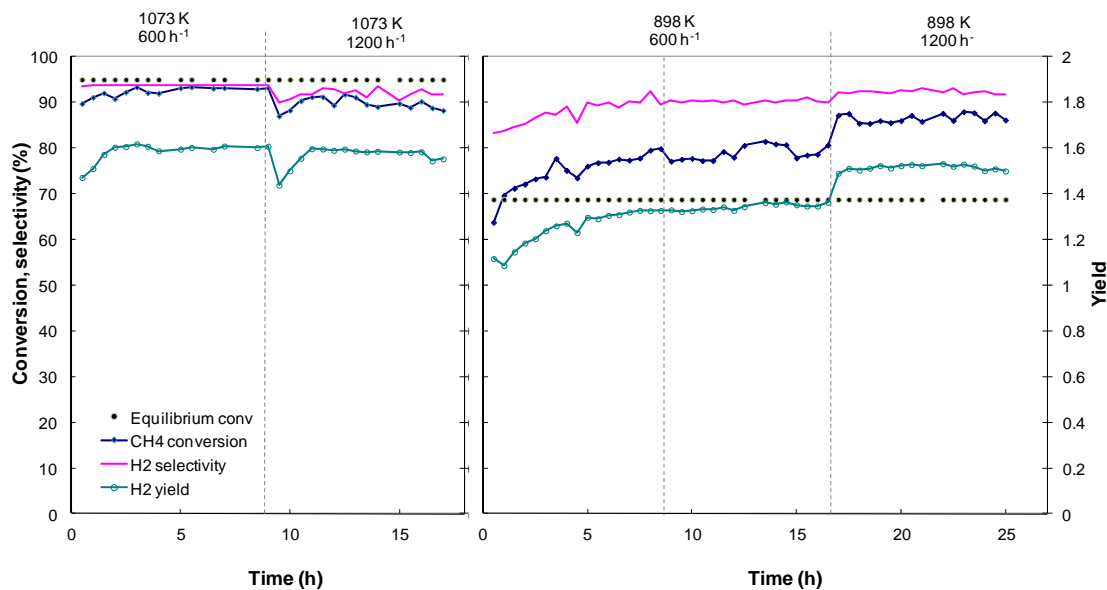


Figure 4.9. Activity results of 40Ni/MgO catalyst in CPO conditions at 1 bar in the PP.

The 30Ni/MgO catalyst showed, in general, the same behaviour as the 40Ni/MgO one as illustrated in Figure 4.10. Conversion at 1073 K was around 95 % at  $600 \text{ h}^{-1}$  and around 93 % at  $1200 \text{ h}^{-1}$ , near the equilibrium conversion in both cases.

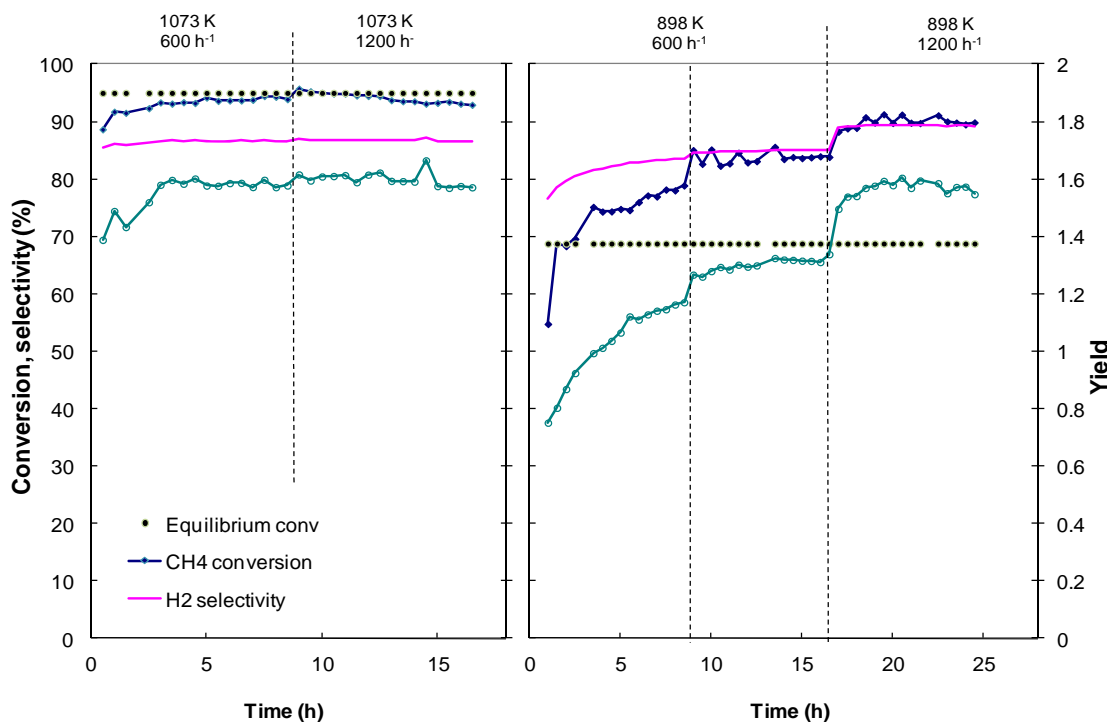


Figure 4.10. Activity results of 30Ni/MgO catalyst in CPO conditions at 1 bar in the PP.

As observed in the 40Ni/MgO catalyst, the conversion of the 30Ni/MgO was continuously increasing when operating at 898 K and 600 h<sup>-1</sup>. Comparing the tendencies of the two Ni/MgO catalysts, a bigger increase was observed for 30Ni/MgO. This can be due to the fact that as it had less nickel, it needed more time to achieve its highest activity. At 898 K the observed conversion, higher than the theoretical one at 898 K is explained by the bed temperature, higher than 898 K.

The conversion obtained for the 40Ni/Al<sub>2</sub>O<sub>3</sub> catalyst at 1073 K was also high and close to the equilibrium one, see Figure 4.11. The main difference between the Ni/Al<sub>2</sub>O<sub>3</sub> and the Ni/MgO catalysts was recorded when operating at 898 K. The conversion at 898 K and 600 h<sup>-1</sup> for the 40Ni/Al<sub>2</sub>O<sub>3</sub> was stable, unlike the Ni/MgO ones that needed 6 or more hours to stabilize. The main reason for stable conversion with 40Ni/Al<sub>2</sub>O<sub>3</sub> can be the reducibility of the catalyst, as it will be discussed in section 4.3. Most probably the catalyst was activated enough during the activation step prior to reaction.

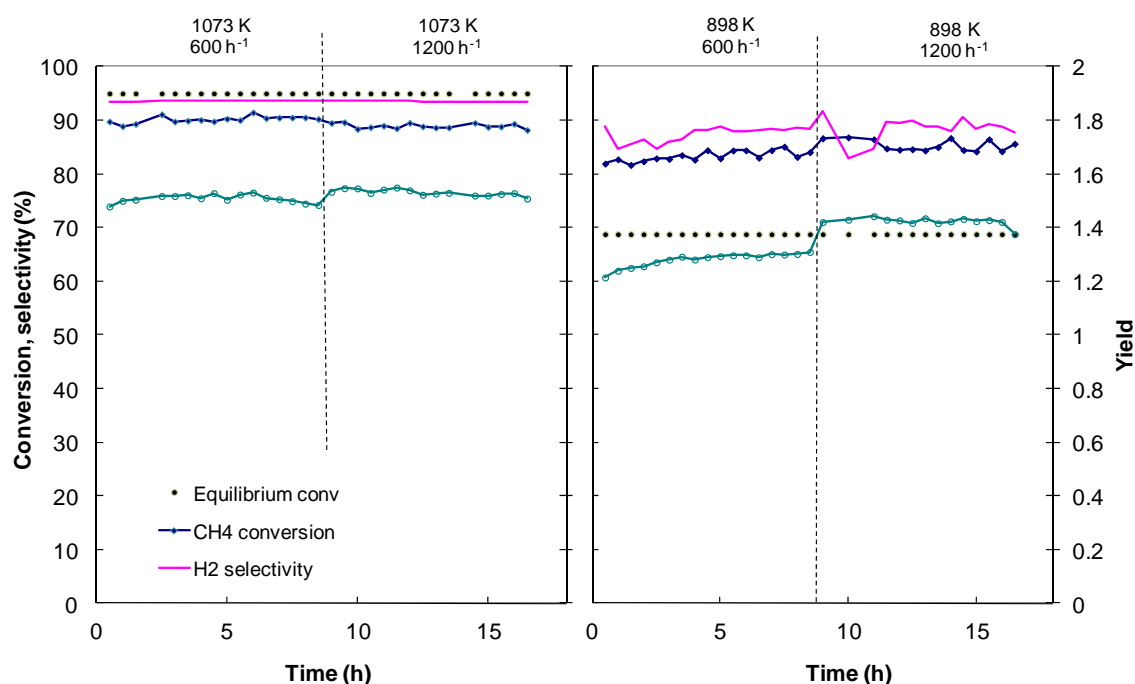


Figure 4.11. Activity results of 40Ni/Al<sub>2</sub>O<sub>3</sub> in CPO conditions at 1 bar in the PP.

After the analysis of the temperature and space velocity effects on CPO for the three catalysts, the catalytic performance of each catalyst in wet-CPO and SR conditions was tested. The selected temperature for these tests was 1073 K, and they were tested at two



space velocities: 600 and 1200 h<sup>-1</sup>. Before testing each process (CPO, wet-CPO and SR) fresh catalyst was charged and reduced in the reactor at 1073 K. After the wet-CPO and SR tests at S/C 2 the reactor was cooled to room temperature during night at 3 K/min under nitrogen. Before the tests at S/C 2.5 the catalysts were reactivated heating them to 1073 K at 3 K/min with N<sub>2</sub>:H<sub>2</sub> 3:1 mixture and maintained for 4 h.

As observed before, in CPO conditions all the catalysts presented high and stable methane conversion, between 90 and 94 % at 600 h<sup>-1</sup> and 1073 K, depicted in Figure 4.12. The Ni/MgO catalysts were the ones which presented the best activities and H<sub>2</sub> yields. Regarding the hydrogen yield, all the catalysts reached similar value, around 1.6. The catalysts presented high methane conversion in wet-CPO conditions with a S/C ratio of 0.5, but the activity decreased with the addition of water. In general the 40Ni/Al<sub>2</sub>O<sub>3</sub> presented better behaviour than the Ni/MgO ones operating with water addition. Under wet-CPO operation with S/C 2 and 3 the external mass transport limitation with the observed conversion was negligible, due to the low observed conversions. Therefore, the low activity of the catalysts was due to a kinetic limitation.

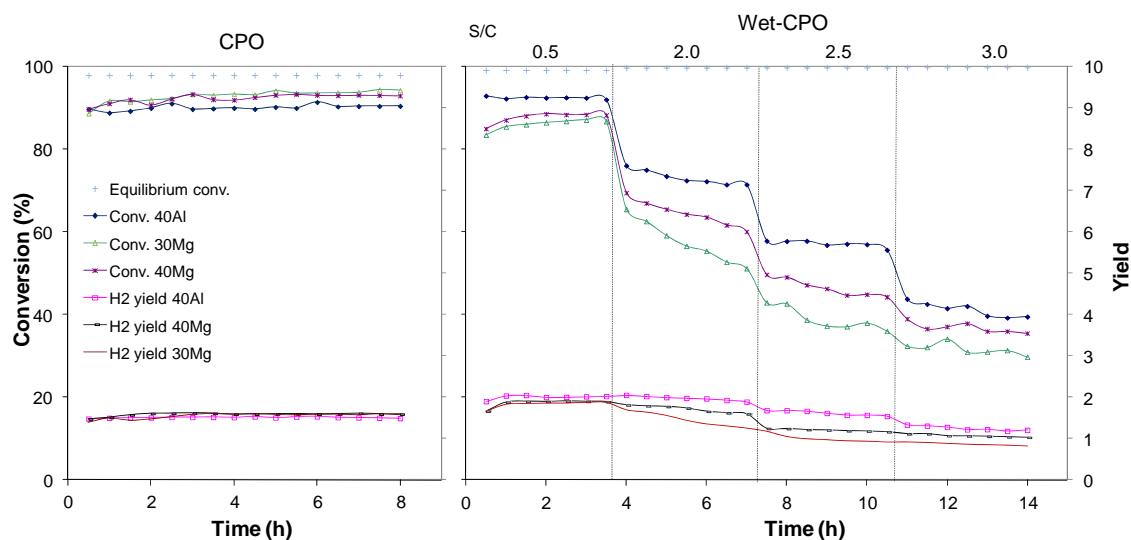


Figure 4.12. Activity results of 30Ni/MgO, 40Ni/MgO and 40Ni/Al<sub>2</sub>O<sub>3</sub> at 1 bar, 600 h<sup>-1</sup> and 1073 K in CPO and wet-CPO conditions in the PP.

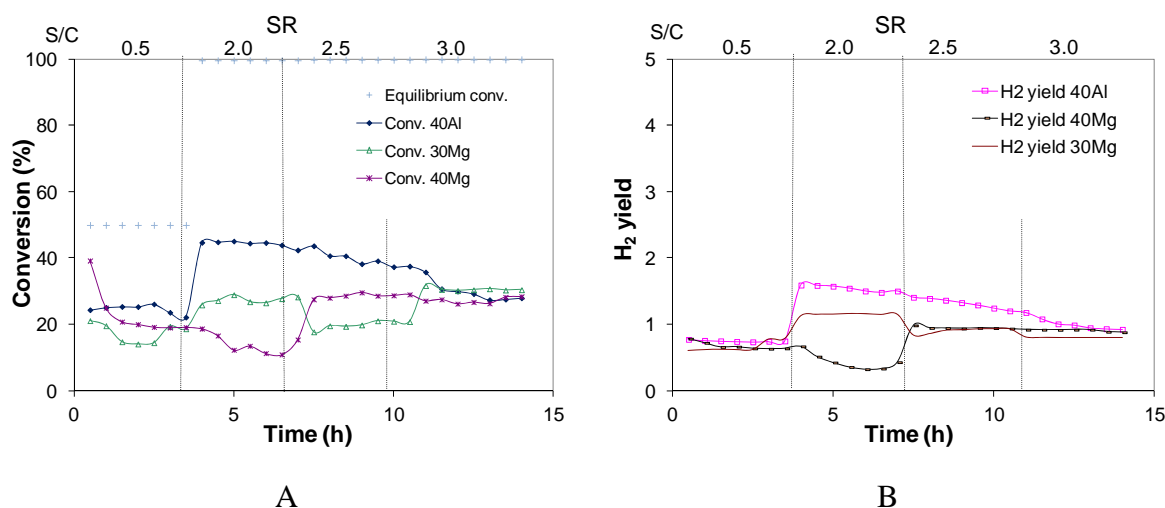


Figure 4.13. Activity results of 30Ni/MgO, 40Ni/MgO and 40Ni/Al<sub>2</sub>O<sub>3</sub> in the PP at 1 bar, 600 h<sup>-1</sup> and 1073 K in SR conditions. A: methane conversion results, B: H<sub>2</sub> yield results.

In SR experiments the activity of the catalysts was very low (see Figure 4.13). At S/C 0.5 the conversion was limited by the water amount fed to the system. At S/C 2.0 the activity of 40Ni/Al<sub>2</sub>O<sub>3</sub> increased, reflecting the stoichiometric limitation at S/C 0.5. With further water addition catalyst activity was negatively affected. Regarding the Ni/MgO catalysts, the addition of water seemed to improve their activity. The low water amount fed during the initial operating time could have affected their behaviour. Coke could have been formed initially due to methane decomposition and then have been gradually removed with higher water addition.

In Figure 4.14 the activity results of the three catalysts in CPO and wet-CPO at 1073 K when the space velocity was doubled from 600 h<sup>-1</sup> to 1200 h<sup>-1</sup> is depicted. The theoretical equilibrium conversion at 1073 K and 1 bar for each reaction condition is also shown. In CPO the conversion was again high for all the catalysts, close to the theoretical one, being the 30Ni/MgO the most active catalyst. When operating in wet-CPO conditions with S/C 0.5, they all maintained quite high conversions, but lower than at 600 h<sup>-1</sup>. This indicated that the catalytic bed was not enough to reach the equilibrium conversion with this space velocity. When the S/C ratio was further increased, from 0.5 to 3.0, the 30Ni/MgO and 40Ni/Al<sub>2</sub>O<sub>3</sub> the conversion continuously dropped from 80 % to 20 %. The 40Ni/MgO catalyst presented conversion values slightly higher than the ones reported for 600 h<sup>-1</sup>, which can be an indicator of external mass transport limitation

improvement due to the higher feeding flow. The  $H_2$  yield, that was very stable under CPO operation, decreased for the  $40Ni/Al_2O_3$  and  $30Ni/MgO$ . As observed at  $600\text{ h}^{-1}$ , the hydrogen yield at CPO conditions was very similar for all the catalysts and its value was around 1.6.

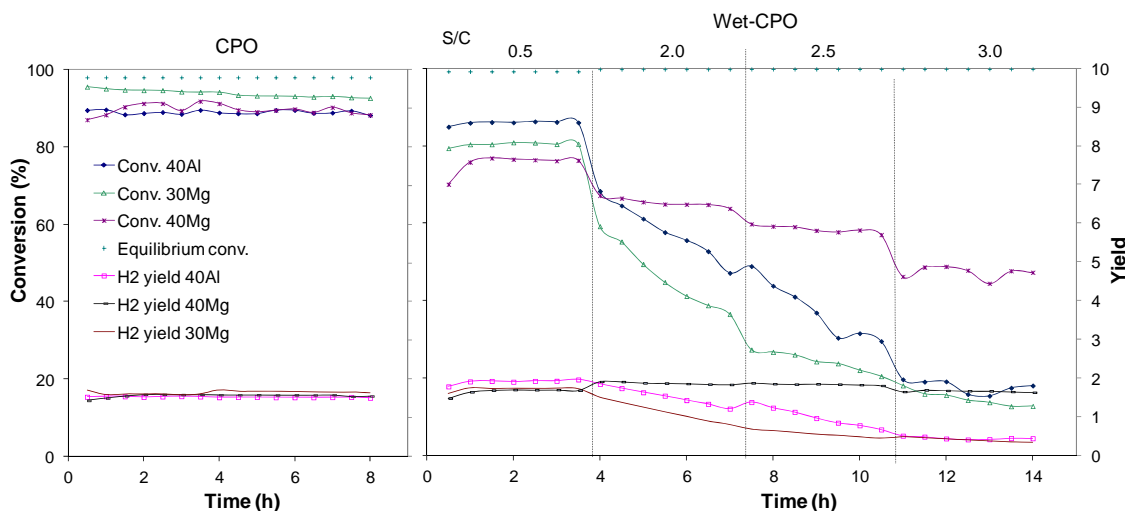


Figure 4.14. Activity results of  $30Ni/MgO$ ,  $40Ni/MgO$  and  $40Ni/Al_2O_3$  at 1 bar,  $1200\text{ h}^{-1}$  and  $1073\text{ K}$  in CPO and wet-CPO conditions in the PP.

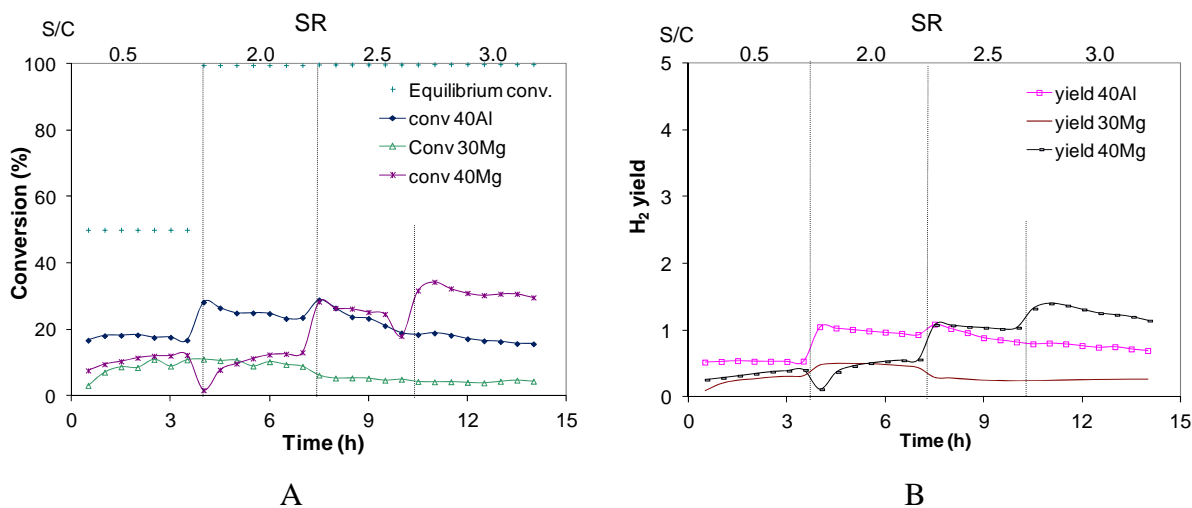


Figure 4.15. Activity results of  $30Ni/MgO$ ,  $40Ni/MgO$  and  $40Ni/Al_2O_3$  at 1 bar,  $1200\text{ h}^{-1}$  and  $1073\text{ K}$  in SR conditions. A: methane conversion results, B:  $H_2$  yield results in the PP.

At SR conditions, see Figure 4.15, the  $40Ni/MgO$  and  $40Ni/Al_2O_3$  catalysts performance was in general similar to the one observed at  $600\text{ h}^{-1}$ , but with lower

conversions. The 30Ni/MgO catalyst seemed to be much damaged after operation at S/C 0.5, and the conversion was lower than 10 % even with the addition of water. The low activity of these catalysts can be attributed to the high space velocity used in the activity tests. The SR reaction rate is known to be slower than the CPO one, which occurs in milliseconds [3, 4]. These tests were carried out at a higher space velocity than the ones that can be found in the literature [5-8]. At wet-CPO and SR conditions, the hydrogen yield was higher than in CPO. Therefore, at this space velocity a part of the fed water was converted to hydrogen.

### 4.3 Catalysts characterization

#### 4.3.1 Chemical analysis (ICP)

In order to check the real metal amount in the prepared catalysts chemical analyses were carried out. The nominal and measured metal values of fresh Ni catalysts were very close, see Table 4.6. Nominal values are used to identify them, in order to simplify the nomenclature.

Table 4.6. Real Ni content of the catalysts prepared for hydrogen production measured with ICP.

	Ni measured (wt%)
30Ni/MgO	29.38
40Ni/MgO	37.74
40Ni/Al <sub>2</sub> O <sub>3</sub>	38.20

#### 4.3.2 Scanning electron microscopy (SEM) and transmission electron microscopy (TEM)

With the main objective of trying to obtain information about the Ni dispersion on the supports surface, SEM analyses in back scattered electrons mode were carried out for the three Ni freshly-calcined catalysts. In these images it can be observed how the Ni was distributed on the samples in a different way, mainly depending on the support. The bright areas are the Ni particles and the dark ones the support. In the Ni/MgO catalysts, see Figure 4.16, the colour of the SEM images was more homogeneous compared to the

40Ni/Al<sub>2</sub>O<sub>3</sub> one (Figure 4.17). This means that the Ni was apparently better dispersed initially in the MgO support. Regarding the Ni/MgO catalysts, no high nickel dispersion differences were observed between them.

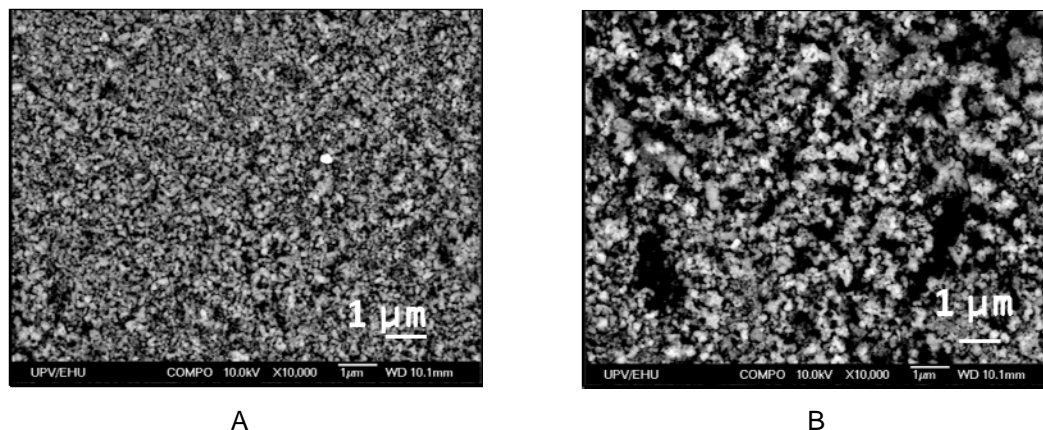


Figure 4.16. SEM images of the Ni/MgO catalysts. A: 30Ni/MgO. B: 40Ni/MgO.

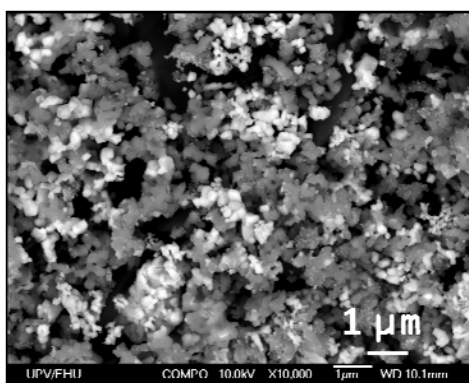


Figure 4.17. SEM image of the 40Ni/Al<sub>2</sub>O<sub>3</sub> catalyst.

For a deeper analysis of the Ni dispersion in the catalysts, TEM images were taken. In the two MgO samples, see Figure 4.18, there were some darker areas that correspond to Ni. Analysing the composition of the samples with the Energy-dispersive X-ray spectroscopy (EDX) at different points, it was found that there was Ni everywhere. This can be due to a solid solution formation between the nickel and the support. On the other hand, for the 40Ni/Al<sub>2</sub>O<sub>3</sub> catalyst, see Figure 4.19, it can be clearly seen in the image that there were some Ni particles dispersed on the surface of the support. Apparently, the Ni dispersion in the 40Ni/Al<sub>2</sub>O<sub>3</sub> was not as good as in the MgO ones.

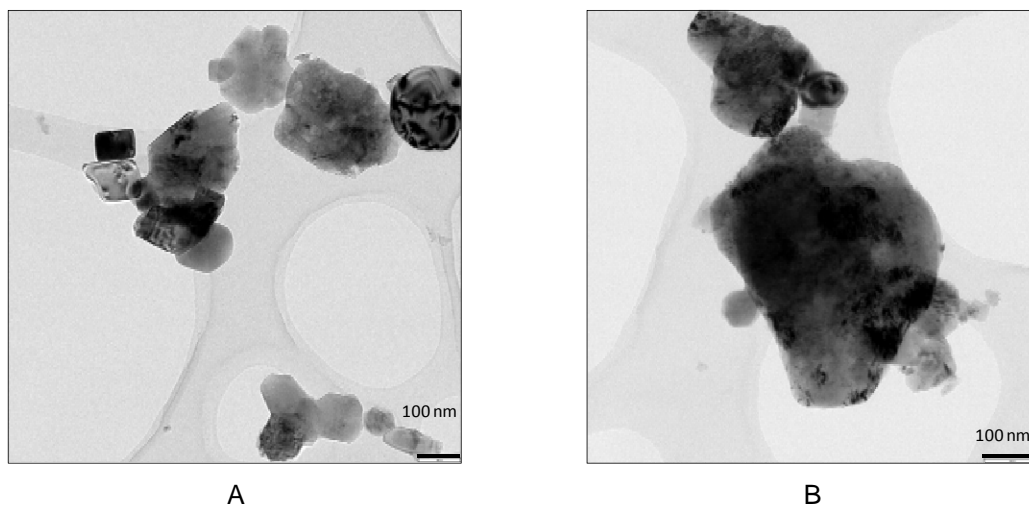


Figure 4.18. TEM images of the Ni/MgO catalysts: A: 30Ni/MgO. B: 40Ni/MgO.

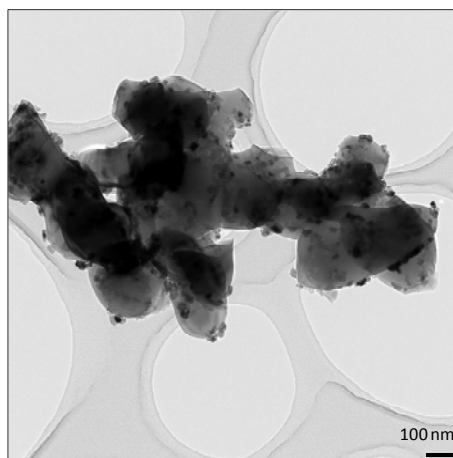


Figure 4.19. TEM image of the 40Ni/Al<sub>2</sub>O<sub>3</sub> catalyst.

### 4.3.3 X ray diffraction

Through XRD measurements the crystalline structure and crystallite size of the fresh and calcined catalysts was analysed. Some of the catalyst samples used in wet-CPO and SR processes were also analysed. The XRD patterns for the fresh 30Ni/MgO and 40Ni/MgO were the same, given in Figure 4.20. Two solid phases were observed: NiO (as they were fresh catalyst samples the metal was not yet reduced to Ni) and MgO. The reflexion angles of both compounds are the same, but the intensity is different as the elements are different. The intensity of the catalyst sample (111) reflexion at position 37 (2 $\theta$ ) and the (200) at 43 (2 $\theta$ ) indicated that it was a mixture of MgO and NiO.

The presence of NiO and MgO at the same diffraction angle indicates structural similarities that facilitate the solid-solution formation between them, which has been widely studied [9-10]. In the work of Hu et al. [11] three double peaks were observed in catalysts prepared by mechanically mixing of NiO and MgO at  $2\theta$  positions: 63, 75 and 79. On the other hand, double peaks were not observed in the samples prepared by wet impregnation, concluding the solid solution formation between them. For the two Ni/MgO catalysts prepared in this work single peaks were obtained by XRD, indicating that all the NiO was probably forming solid solution with the MgO. In the 40Ni/Al<sub>2</sub>O<sub>3</sub> catalyst, see Figure 4.21, the signals of NiO and Al<sub>2</sub>O<sub>3</sub> could easily be distinguished [12].

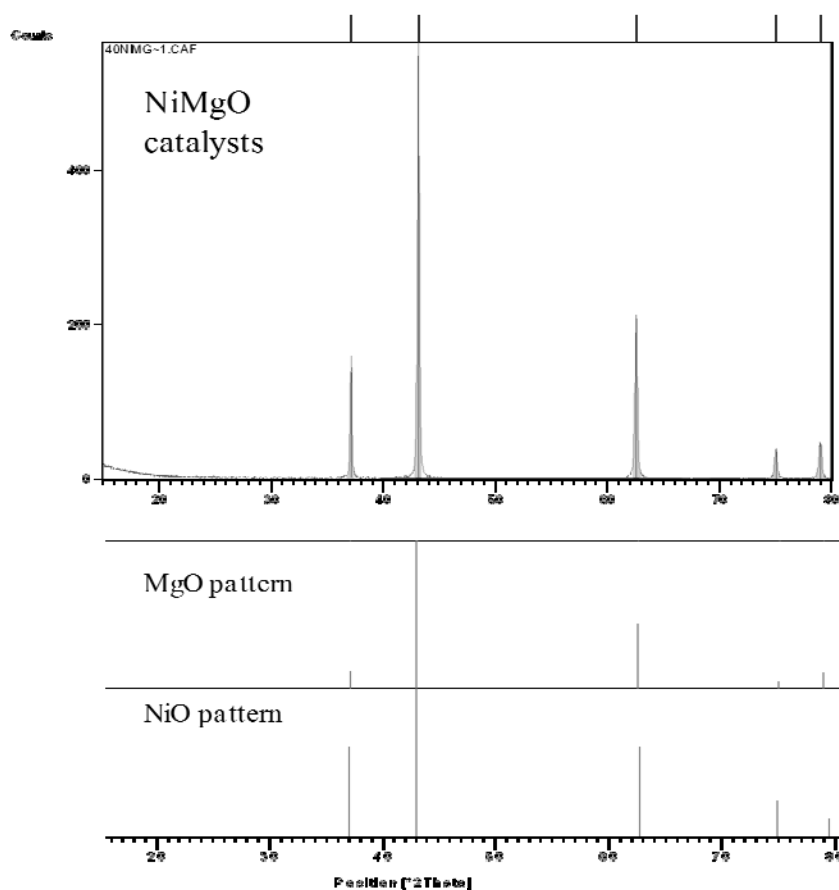


Figure 4.20. XRD diffraction spectra of the freshly-calcined 30Ni/MgO and 40Ni/MgO catalysts with the NiO and MgO diffraction patterns.

In both MgO and Al<sub>2</sub>O<sub>3</sub> catalysts NiO was observed, but it was a different phase. In the Ni/MgO catalysts the NiO was the phase with JCPDS (International Centre for Diffraction Data) card number 00-001-1239 and in the 40Ni/Al<sub>2</sub>O<sub>3</sub> the card number of the NiO was 00-044-1159. The NiO formed in the MgO catalysts was a cubic crystal system, from the space group Fm-3m and the NiO formed in the Al<sub>2</sub>O<sub>3</sub> catalyst was rhombohedral with a space group R-3m. The density of both NiO phases was very similar, 6.8 and 6.81 respectively, but the volume was quite different: 72.56 and 54.66 respectively, which could influence the performance of the active metal or its reduction ability [13, 14].

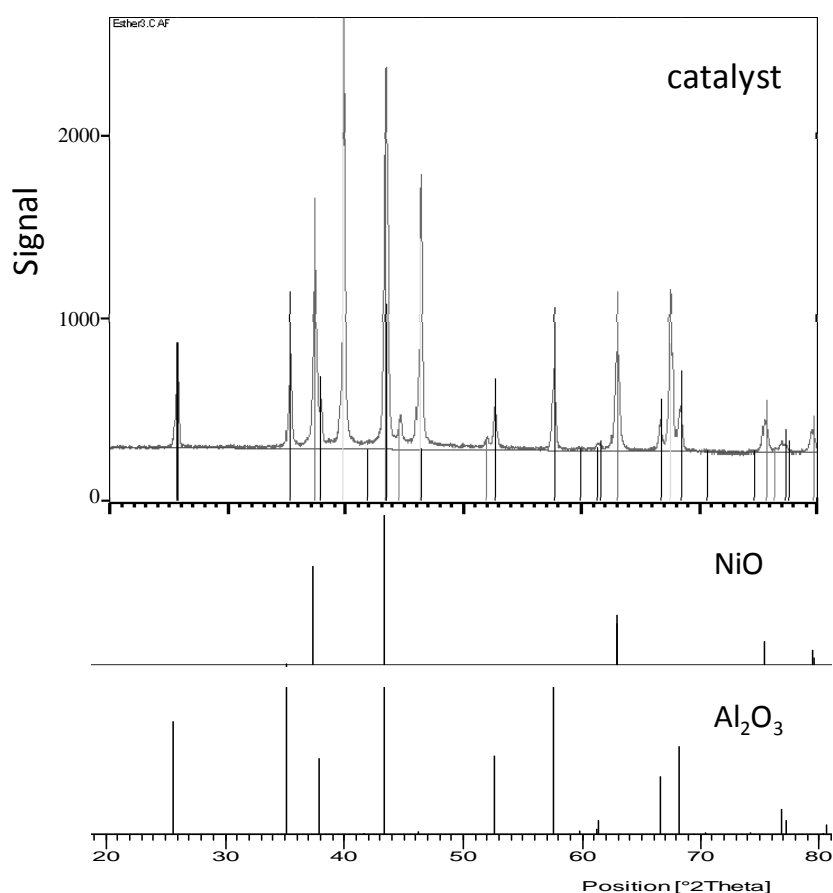


Figure 4.21. XRD diffraction patterns of the freshly-calcined 40Ni/Al<sub>2</sub>O<sub>3</sub> catalyst with the NiO and Al<sub>2</sub>O<sub>3</sub> diffraction patterns.

An estimation of the catalysts crystallite size was made by measuring the line broadening of the most intense reflection line by the SCHERRER calculator of the X'Pert HighScore software. For the Ni/MgO catalysts the size was an average of the



solid solution crystallites. The results shown in Table 4.7 were calculated using the peak at position around 44 ( $2\theta$ ). The largest crystallites appeared in the 30Ni/MgO catalyst (0.115  $\mu\text{m}$ ) and a similar value was obtained in the 40Ni/MgO (0.099  $\mu\text{m}$ ). Most probably solid solution formation influences the Ni/MgO particle structure and they can be more dispersed over the catalyst surface, but as bigger crystallites. The 40Ni/Al<sub>2</sub>O<sub>3</sub> presented the smallest crystallite size.

Table 4.7. Average crystallite size of the fresh and calcined catalysts.

Fresh catalysts	Crystallite size ( $\mu\text{m}$ )
30Ni/MgO	0.115
40Ni/MgO	0.099
40Ni/Al <sub>2</sub> O <sub>3</sub>	0.069

Extensive XRD measurements of the reduced and used 40Ni/Al<sub>2</sub>O<sub>3</sub> catalyst were recorded, see Table 4.8. The crystallite size was estimated using the X'pert HighScore software with peaks at position 44 ( $2\theta$ ) for Ni, 35 ( $2\theta$ ) for Al<sub>2</sub>O<sub>3</sub> and 37 ( $2\theta$ ) for NiO. After reduction, the metallic Ni content observed using XRD was very low (2.2 %). This can be due to a quick Ni re-oxidation during the handling of the sample or to the fact that the nickel was difficult to reduce due to a strong interaction between the NiO and the alumina support. This strong interaction could indicate the formation of nickel aluminates [15, 16] which are difficult to reduce. Consequently, only a small amount of the Ni present as NiO is expected to be reduced and to form small metallic nickel particles on the surface of the catalyst. The increase in the Ni crystallite size for the used catalysts can be due to Ni sintering, being the NiO particles undetectable in the used catalysts samples, probably because of a further reduction under reaction conditions [17].

Comparing the crystallite size of the 40Ni/Al<sub>2</sub>O<sub>3</sub> after wet-CPO and after SR with the fresh-calcined samples, it can be observed that the Ni crystallites were bigger. They rose from 48 nm to 93 nm after the wet-CPO test at 600 h<sup>-1</sup>, and to 122 nm after SR at 600 h<sup>-1</sup>. This means that sintering phenomena took place during the tests [18], which could have influenced the activity observed during the tests at wet-CPO and SR.

Table 4.8. Al<sub>2</sub>O<sub>3</sub>, NiO and Ni crystallite sizes in the fresh, reduced and used 40Ni/Al<sub>2</sub>O<sub>3</sub> catalyst.

40Ni/Al <sub>2</sub> O <sub>3</sub>	Al <sub>2</sub> O <sub>3</sub>	NiO	Ni
Fresh (μm)	0.199	0.112	nd
Fresh-reduced (%)	64.5	33.3	2.2
Fresh-reduced (μm)	0.074	0.044	0.048
Used in wet-CPO, 600 h <sup>-1</sup> (μm)	0.199	nd	0.093
Used in SR, 600 h <sup>-1</sup> (μm)	0.333	nd	0.122

nd: not detected

#### 4.3.4 Nitrogen adsorption isotherms (BET)

The textural properties of the prepared catalysts were examined by nitrogen adsorption-desorption isotherm measurements. Figure 4.22 depicts the nitrogen isotherms of the MgO support and the two Ni/MgO catalysts. All the samples exhibited type IV isotherms, according to the IUPAC classification [19], indicating well-developed mesopores (pores of between 2 nm – 50 nm diameter). Adsorption on mesoporous solids proceeds via multilayer adsorption followed by capillary condensation. Therefore, the adsorption process is initially similar to that on macroporous solids, but at higher pressures the adsorbed amount rises very steeply due to the capillary condensation in mesopores. After these pores are filled, the adsorption finishes. Capillary condensation and evaporation do not take place at the same pressure, which leads to the appearance of hysteresis loops. In the Ni/MgO catalysts the adsorption at  $p/p_0$  close to 0 was not very high, indicating a small amount of micropores [20].

The adsorption process on mesoporous solids is often accompanied by adsorption-desorption hysteresis. The hysteresis is usually attributed to the thermodynamic or network effects or the combination of these two effects. Namely, if larger pores have access to the surrounding only through narrower pores; the former cannot be emptied at the relative pressure corresponding to the capillary evaporation in the smaller connecting pores. The MgO support and Ni/MgO catalysts presented isotherms with H3 type hysteresis loops, indicating the existence of narrow slit-shaped pores. The isotherms show a hysteresis loop at relatively high pressures, between 0.8 and 1.0, reflecting larger pores formed between plate-like particles [21, 22]. In the Ni/MgO catalysts the addition of Ni decreased the adsorption volume, compared to the support.

But the adsorption volume in the hysteresis region increased when increasing the Ni amount from 30 to 40 wt%. This can be due to the creation of new volume due to the metal addition.

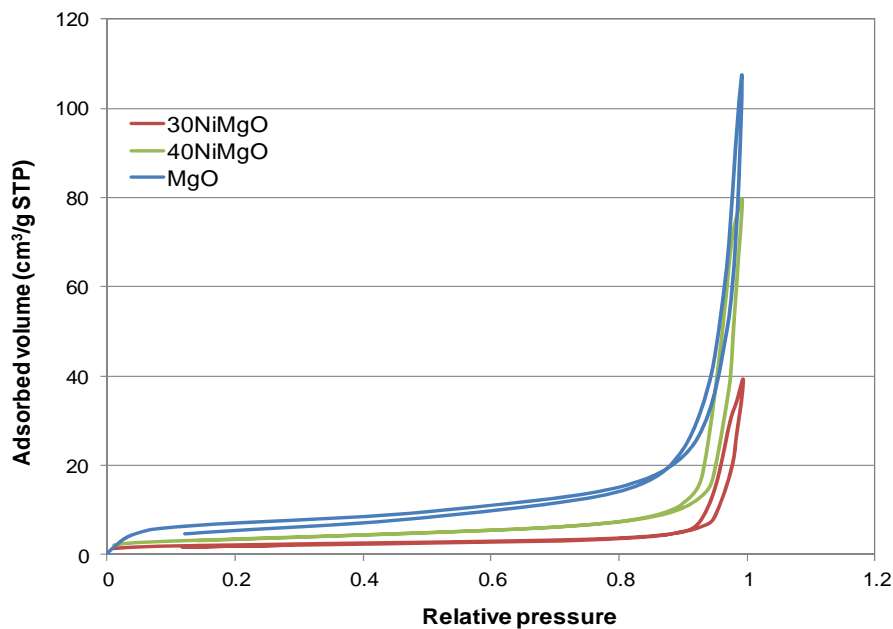


Figure 4.22. Nitrogen adsorption-desorption isotherms of the MgO support and Ni/MgO catalysts.

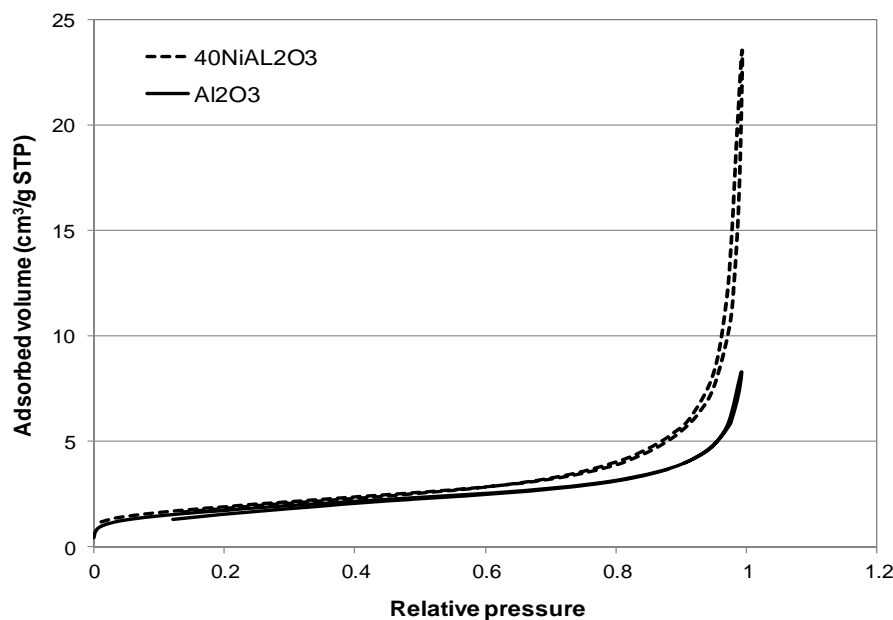


Figure 4.23. Nitrogen adsorption-desorption isotherms of the  $\alpha$ -Al<sub>2</sub>O<sub>3</sub> support and the Ni-Al<sub>2</sub>O<sub>3</sub> catalyst.

In the case of the  $\alpha$ -Al<sub>2</sub>O<sub>3</sub> support it exhibited a type-II isotherm without hysteresis loop, whereas the Ni/Al<sub>2</sub>O<sub>3</sub> catalyst presented isotherm type IV with H3 loop as illustrated in Figure 4.23. In the literature, isotherms type-IV [23, 24] and type-V [25] were observed for Ni/Al<sub>2</sub>O<sub>3</sub> catalysts. The change in surface area after the impregnation process with Ni can be explained based on the increase of the particle size and the decrease of the contact area among them, which consequently increases the pore sizes of the materials, also shown in Table 4.9 [26].

In Table 4.9 the BET results of the supports and catalysts are summarized. All the supports presented low BET area, as all of them were materials with low surface area: 7.4 m<sup>2</sup>/g for the 30Ni/MgO, 12.1 m<sup>2</sup>/g for the 40Ni/MgO and 6.8 m<sup>2</sup>/g for the 40Ni/Al<sub>2</sub>O<sub>3</sub>. As a consequence of the  $\alpha$ -Al<sub>2</sub>O<sub>3</sub> support low area, observed in Figure 4.23, a small increase of the BET area was measured when nickel was deposited on it. On the other hand, the BET area of the Ni/MgO catalysts decreased after the nickel deposition, probably due to blocking of some pores, but it increased with further addition of Ni from 7.4 to 12.1 m<sup>2</sup>/g. The increase of the surface area could be due to a roughening of the surface due to Ni incorporation, which has also been found in the literature [27, 28]. A higher Ni content and higher exposure area (m<sup>2</sup>/g) implies a higher amount of nickel with low interaction with the support, which can facilitate the reducibility of 40Ni/MgO compared to 30Ni/MgO. This easier reduction was observed operating at 898 K, see Figure 4.13. To have more Ni available on the surface of the catalyst could have also been responsible for the better behaviour shown under kinetic controlled wet-CPO and SR tests of the 40Ni/MgO catalyst compared to the 30Ni/MgO one.

Table 4.9. Surface area and pore data of the prepared catalysts and supports.

	MgO	30Ni/MgO	40Ni/MgO	$\alpha$ -Al <sub>2</sub> O <sub>3</sub>	40Ni/Al <sub>2</sub> O <sub>3</sub>
BET surface area (m <sup>2</sup> /g)	27.1	7.4	12.1	6.2	6.8
Vol. of pores between 17.0 and 3000.0 Å diameter (cm <sup>3</sup> /g)	0.16	0.06	0.12	0.01	0.04
Average pore diameter (4V-A) (Å)	341	449	410	118	250

### 4.3.5 Temperature programmed reduction (TPR)

The TPR profiles obtained for the three prepared catalysts in the same conditions (0.1 g of sample with heating rate of 10 K/min) are shown in Figure 4.24. With this technique the reduction temperature required for the nickel deposited over the supports can be evaluated. In the 40Ni/Al<sub>2</sub>O<sub>3</sub> catalyst a major peak and two other overlapped peaks at higher temperatures were observed. The lower temperature peak appeared at 695 K and it was due to the bulk NiO particles without interaction with the support,  $\alpha$ -Al<sub>2</sub>O<sub>3</sub>. The second peak, at around 790 K, was attributable to the NiO strongly interacting with the support. The last peak, at around 840 K, could be related to the reduction of the stable NiAl<sub>2</sub>O<sub>4</sub> species [29, 30].

For the Ni/MgO catalysts no significant temperature peak was observed, which could be due to the known Ni<sub>x</sub>Mg<sub>1-x</sub>O solid-solution formation in these catalysts [31, 32]. This involves a difficulty to reduce the NiO to Ni<sup>0</sup> in these catalysts. In order to further analyse their reducibility, the reduction conditions used before the reaction tests in the PP and PM were reproduced in the TPR measurement. This second profile, shown in Figure 4.25, was performed at 3 K/min and then maintaining 1073 K during 4 h with 1 g of 30Ni/MgO. In this case, some reduction peaks were observed, which indicates that under these conditions nickel was reduced. Comparing the signals of the 30Ni/MgO reduction peaks at 3 K/min to those obtained for 40Ni/Al<sub>2</sub>O<sub>3</sub> at 10 K/min it can be concluded that the 40Ni/Al<sub>2</sub>O<sub>3</sub> is more easily reducible. The easier reduction of the 40Ni/Al<sub>2</sub>O<sub>3</sub> catalyst corroborates the conclusion obtained from the activity tests at 898 K in section 4.2. In Figure 4.9 and Figure 4.10 the Ni/MgO catalysts increased their activity during the first hours of the tests, whereas the 40Ni/Al<sub>2</sub>O<sub>3</sub> in Figure 4.13 had almost stable conversion since the beginning.

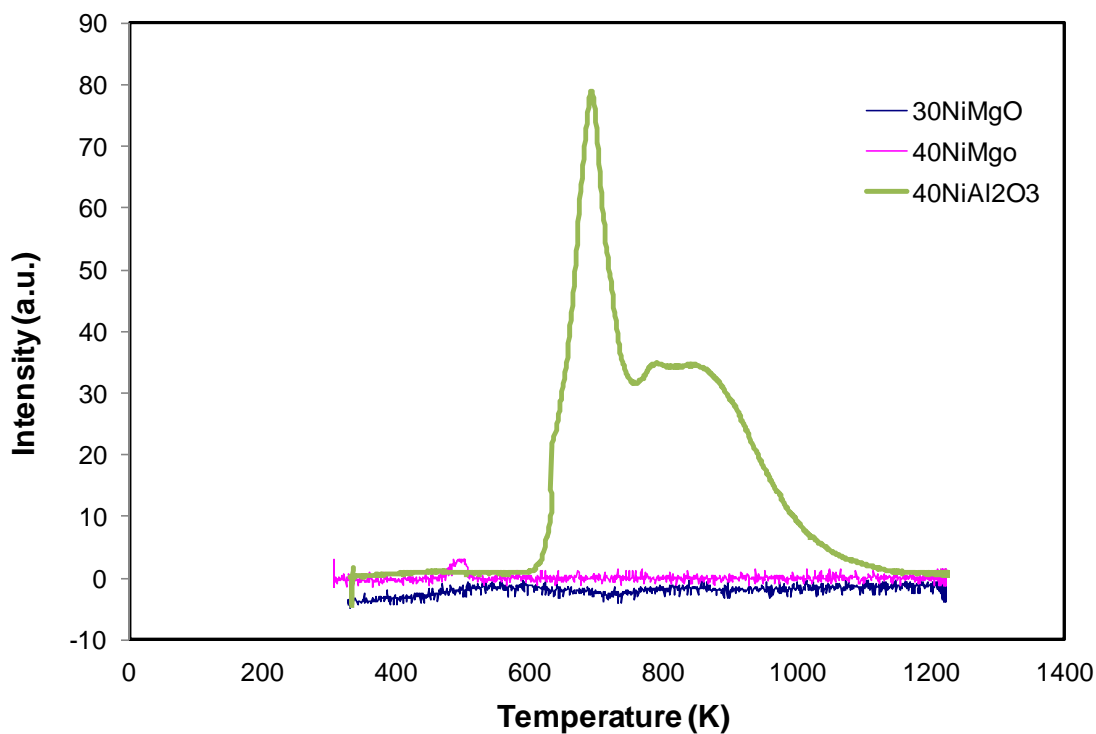


Figure 4.24. TPR profiles of the 30Ni/MgO, 40Ni/MgO and 40Ni/Al<sub>2</sub>O<sub>3</sub> catalysts with 0.1 g of sample and heated at 10 K/min.

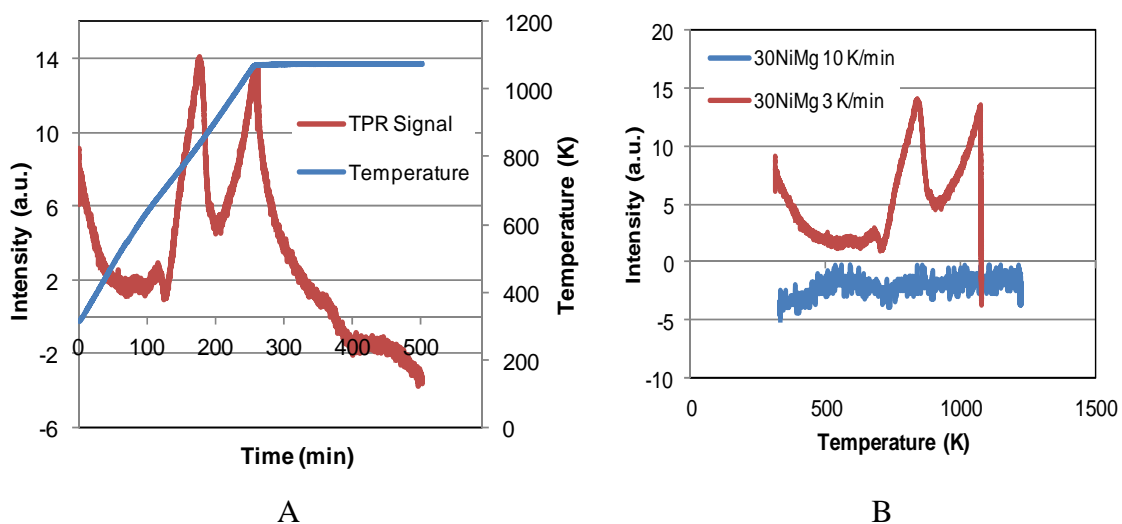


Figure 4.25. TPR profiles of 30NiMgO. A: heated with 3 K/min and maintained at 1073 K 4 h, and the temperature variation in time. B: heated at 3 K/min and 10 K/min.

#### 4.3.6 X-ray photoelectron spectroscopy (XPS)

XPS analysis was used to determine the chemical composition of the catalyst surface and to better understand the nature of interactions between the dispersed Ni species and the supporting oxides. This technique was employed to analyse the surface characteristics of the freshly-reduced catalysts and catalysts used in wet-CPO at  $1200 \text{ h}^{-1}$  with S/C ratios from 0.5 to 3.0. All the samples were collected in isooctane after taking them out from the reactor to prevent metal oxidation. For each sample C1s, O1s, Ni2p and Mg2p or Al2p internal electronic levels were analysed. For comparison of the freshly-reduced and the used catalysts only the Ni2p<sub>3/2</sub> is presented.

The freshly-reduced Ni/MgO catalysts showed the shoulder peaks of Ni2p<sub>3/2</sub> identified as Ni<sup>0</sup> (852.8-852.9 eV), in addition to the peaks at 854.9-857.2 eV corresponding to Ni<sup>2+</sup> spectra [33, 34]. The shake-up satellite peak of the Ni<sup>2+</sup> was observed in binding energy (BE) values between 859.65-862.34 eV [35], see Figure 4.26. Furthermore, deconvolution of Ni 2p<sub>3/2</sub> peaks was carried out and relative percentage areas of Ni<sup>0</sup> and Ni<sup>2+</sup> were calculated. As it can be observed in Table 4.10 the main peak was attributed to the Ni<sup>0</sup> in the fresh Ni/MgO catalysts: 57.8 % in the 30Ni/MgO and 48.8 % in the 40Ni/MgO. The BE values of Ni<sup>0</sup> could indicate that the Ni electron state was intermediate between bulk Ni metal (852 eV) and NiO (854 eV) [36]. The binding energy of the largest Ni<sup>2+</sup> peak in the fresh Ni/MgO catalysts was high as compared to the pure NiO (854 eV). This could be due to the Ni<sup>2+</sup> ions forming part of the NiO-MgO solid solution as revealed by the XRD and TPR characterization [27, 37, 38].

For the freshly-reduced Ni/Al<sub>2</sub>O<sub>3</sub> catalyst the Ni2p<sub>3/2</sub> peak showed a peak at 852.4 eV, identified as Ni<sup>0</sup>, the Ni<sup>2+</sup> peaks at 854.9 eV and 856.9 eV, and the satellite peak of the Ni<sup>2+</sup> at 861.1 eV. The XPS spectra of the used 40Ni/Al<sub>2</sub>O<sub>3</sub> did not show the Ni<sup>0</sup> characteristic peak. The energy recorded for the Ni<sup>2+</sup> species in the used 30Ni/Al<sub>2</sub>O<sub>3</sub> catalyst was 855.2 and 856.7 eV with the shake-up satellite broad peak at 861.9 eV.

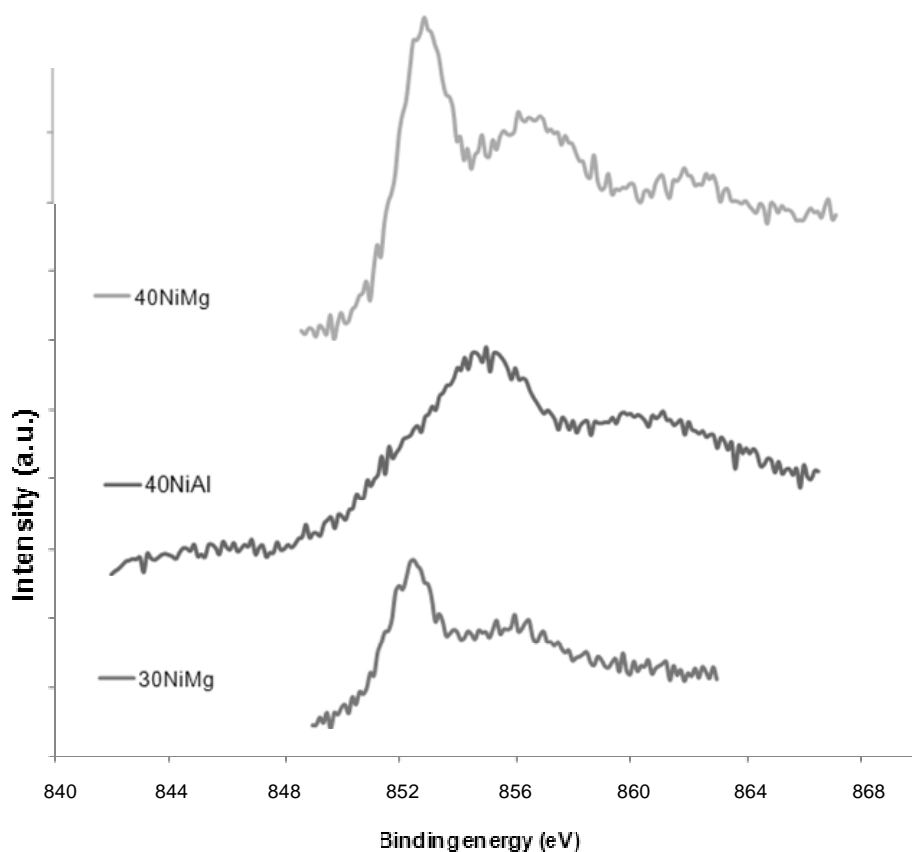


Figure 4.26. XPS spectra of the fresh-reduced Ni-based catalysts.

In the comparison between the freshly-reduced and the used catalysts it could be observed that in the Ni/MgO catalysts the binding energies moved to higher energies in the used catalyst samples. The main peak in the used 30Ni/MgO catalyst, see Figure 4.27, was at 855.2 eV, which is referred to the Ni<sup>2+</sup> and it was a 52 % of the area, at higher energy than the fresh sample (852.8 eV a 57.8%). The performance of the 40Ni/MgO catalyst was similar. The main peak for the fresh sample was the Ni<sup>0</sup>, 48.8 %, whereas in the used sample it was 18.9 %. In the used 40Ni/MgO the binding energies moved also to higher energies, see Figure 4.28.



Table 4.10. XPS spectra peaks and their relative atomic percentage area of the freshly-reduced and used catalysts in wet-CPO at  $1200 \text{ h}^{-1}$  and S/C 0.5-3.0.

Catalyst	Peak position	Area (%)
30Ni/MgO freshly-reduced	852.8	57.8
	854.9	9.2
	856.6	27.4
	859.6	5.6
30Ni/MgO used	852.9	3.7
	855.2	52.0
	861.2	44.3
40Ni/MgO freshly-reduced	852.9	48.8
	855.5	15.0
	857.2	25.0
	860.3	4.5
40Ni/MgO used	862.3	6.7
	852.5	18.9
	854.4	46.2
	859.6	27.3
40Ni/MgO used	861.8	7.6
	852.4	18.5
	854.9	34.1
	856.9	24.0
40Ni/Al <sub>2</sub> O <sub>3</sub> freshly-reduced	861.1	23.4
	855.2	53.8
	856.7	15.5
40Ni/Al <sub>2</sub> O <sub>3</sub> used	861.9	30.7

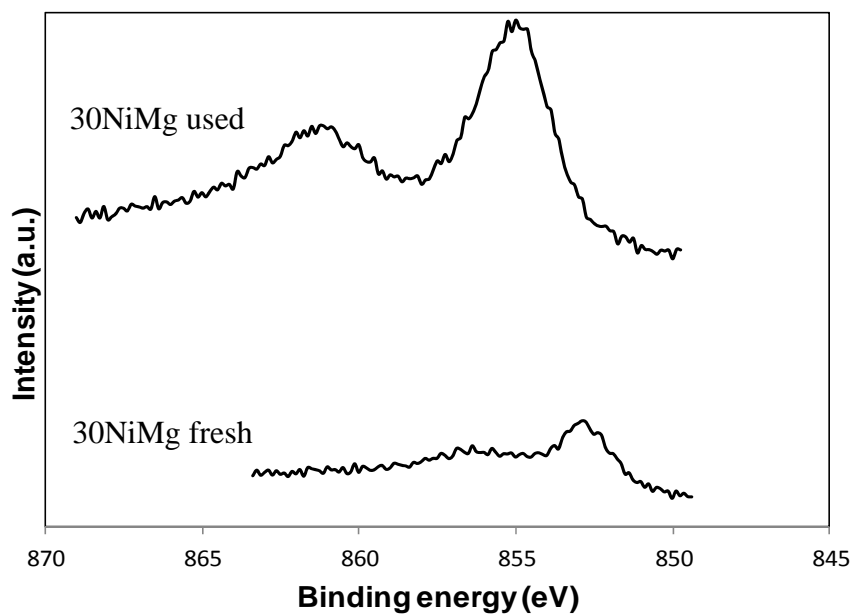


Figure 4.27. XPS for 30Ni/MgO catalyst fresh-reduced and used in wet-CPO at  $1200 \text{ h}^{-1}$  with S/C=0.5-3.

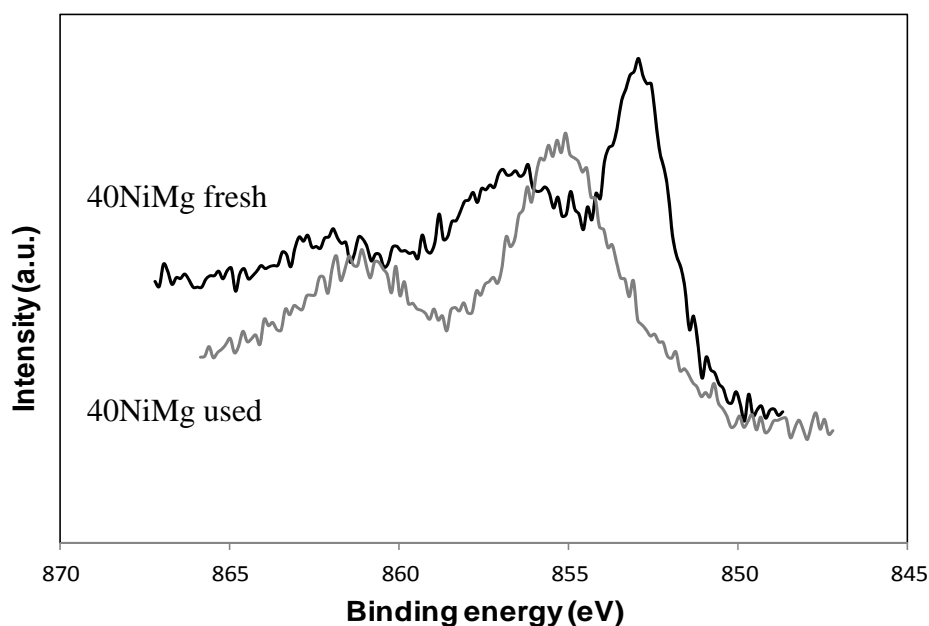


Figure 4.28. XPS for 40Ni/MgO catalyst fresh-reduced and used in wet-CPO at  $1200 \text{ h}^{-1}$  with S/C=0.5-3.

The high amount of  $\text{Ni}^{2+}$  in the used Ni/MgO could be due to the reoxidation of the outer Ni atoms with low interaction with the support during the handling. There was more metallic nickel in the used sample of 40Ni/MgO than in 30Ni/MgO which supports the quicker reduction observed in the test at 898 K (see Figure 4.9 and Figure 4.10).

In the 40Ni/ $\text{Al}_2\text{O}_3$  used catalyst sample, see Figure 4.29, the binding energies shifted to higher energies, compared to the fresh samples, but only  $\text{Ni}^{2+}$  peaks were observed at 855.2 and 856.7 eV, with the satellite peak at 861.9 eV. Binding energy of the  $\text{Ni}^0$  was not observed in the XPS analysis of the used catalyst sample. This suggested that a quick re-oxidation of the outer metallic nickel layer could have happened during the handling of the sample before putting it in isooctane, or that the signal of  $\text{Ni}^{2+}$  species could be due to  $\text{NiAl}_2\text{O}_4$ , which is more difficult to reduce [39]. Aluminate species were not detected by XRD, which could be due to a crystal size not big enough to be detected. The fact that  $\text{Ni}^0$  was not observed in the used 40/Ni $\text{Al}_2\text{O}_3$  catalyst corroborates the easier reducibility/reoxidation of the Ni/ $\text{Al}_2\text{O}_3$  compared to the Ni/MgO observed in the activity tests and in the TPR.

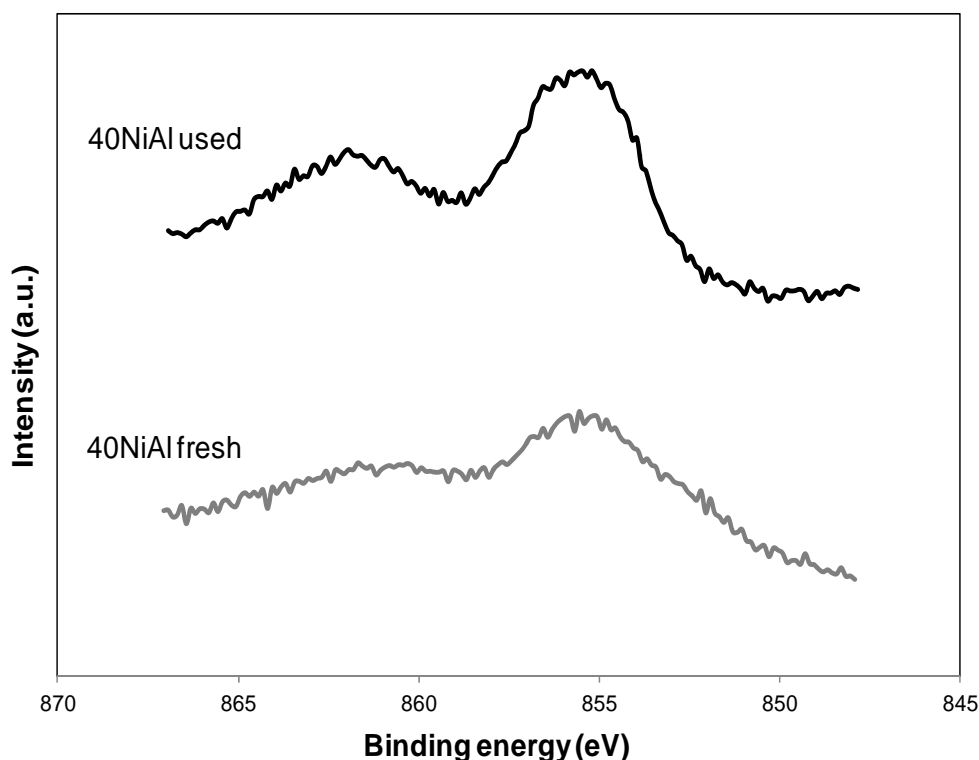


Figure 4.29. XPS for 40Ni/Al<sub>2</sub>O<sub>3</sub> catalyst fresh-reduced and used in wet-CPO at 1200 h<sup>-1</sup> with S/C=0.5-3.

As it can be observed in Table 4.11 carbon signals were detected in the XPS analysis of the freshly-reduced and used catalysts samples. For the three freshly-reduced catalysts the main peak in the spectra of the C1s was at 284.7 eV (81 % in the 30Ni/MgO), 284.2 eV (65 % in the 40Ni/MgO) and 284.9 eV (68.9 % in the 40Ni/Al<sub>2</sub>O<sub>3</sub>) that are attributed to the sp<sup>2</sup> of graphitized carbon [40]. The origin of this carbon in the fresh catalysts can be the catalyst preparation method. In the used catalysts the main peak was also the one from the graphitized carbon. The C/Ni ratio in the freshly-reduced and used catalysts did not change considerably in the Ni/MgO catalysts, whereas in the alumina sample the ratio was very high in the freshly-reduced sample. This could be explained taking into account that the Ni/Al<sub>2</sub>O<sub>3</sub> catalyst was prepared using nickel acetate, whereas the Ni/MgO catalysts were prepared using nickel nitrate. The reduction step seemed to be not severe enough for degrading these carbon-containing compounds in the 40Ni/Al<sub>2</sub>O<sub>3</sub> catalysts, but after 16 hours under testing conditions the C/Ni ratio strongly decreased to values similar to the other two catalysts. The low C/Ni ratios after the tests were expected as the samples operated under wet-CPO conditions with S/C ratios that were supposed to minimize coke production.

Table 4.11. Atomic element ratios determined by XPS for fresh and used catalysts in wet-CPO at 1200 h<sup>-1</sup> with S/C=0.5-3.

Catalyst	Atomic Ni/Mg or Ni/Al ratio	Atomic C/Ni ratio	Atomic C/Mg or C/Al ratio
30Ni/MgO fresh	0.17	3.33	0.57
30Ni/MgO used	0.32	3.14	1.00
40Ni/MgO fresh	0.18	4.09	0.74
40Ni/MgO used	0.31	4.05	1.24
40Ni/Al <sub>2</sub> O <sub>3</sub> fresh	0.14	21.34	2.92
40Ni/Al <sub>2</sub> O <sub>3</sub> used	0.25	3.06	0.77

With respect to the atomic Ni/Mg and Ni/Al ratios, they were very similar, regardless the Ni content. This could imply that the Ni amount accessible to the XPS technique was similar in all of them. The Ni/support ratio measured with the XPS increased after the tests in wet-CPO conditions in a proportion between 1.7 and 1.9. This can indicate a diffusion of the nickel to the outer surface during reaction time [41]. From the catalysts weight composition measured by ICP the Ni/support values can be calculated and compared to the surface values obtained by XPS, see Table 4.12. The diffusion of the metal particles to the outer surface of the catalysts can also be observed from this comparison. In the used catalyst samples there was more Ni in the outer surface accessible to the XPS than present in the fresh samples before the catalytic process.

Table 4.12. Catalysts Ni/Mg or Ni/Al ratio calculated from the ICP composition and compared to the XPS results.

Catalyst	Ni/Mg or Ni/Al ratio (ICP)	Ni/Mg or Ni/Al ratio (XPS)
30Ni/MgO fresh	0.29	0.17
30Ni/MgO used		0.32
40Ni/MgO fresh	0.41	0.18
40Ni/MgO used		0.31
40Ni/Al <sub>2</sub> O <sub>3</sub> fresh	0.54	0.14
40Ni/Al <sub>2</sub> O <sub>3</sub> used		0.25

## 4.4 Discussion

The prepared catalysts showed high performance in CPO and wet-CPO at S/C 0.5 at 600 and 1200 h<sup>-1</sup> despite their low specific surface area. The corresponding reaction rates were high enough to reach the equilibrium. This indicated that the dispersion was adequate in the three catalysts and stable during the operation time. Ni/MgO and Ni/Al<sub>2</sub>O<sub>3</sub> catalysts presented all good activity and stability in the CPO tests. Methane conversion and hydrogen yield were very close to the equilibrium values. This good performance was maintained in wet-CPO at low S/C ratio, while at higher ratios in wet-CPO and SR processes the activity and stability decreased considerably as compared to CPO. During CPO at 898 K the catalytic bed temperature was always much higher than 898 K, which explained the conversions higher than the equilibrium one at 898 K that were obtained. Apparently, the reactor temperature in CPO mode was affected by both the heat of the exothermic reaction and the heat flow from the furnace.

Operating at wet-CPO with S/C higher than 0.5 and in SR the catalytic processes were kinetically controlled. The experimentally obtained conversions were far from the equilibrium, with no external mass transport limitation and lower internal diffusion limitation. The crystallite size increase observed in XRD could indicate that the activity decrease could be due to sintering of the nickel. However, it is known from literature that SR is a slower reaction compared to CPO. Coke formation was not observed by XPS in the samples used at wet-CPO.

Due to the low conversion observed in wet-CPO and SR processes the theoretically estimated external mass transport limitation was negligible and internal diffusion limitation was also lower than in CPO mode. Therefore, the low activity of the catalysts was due to a kinetic limitation. This indicated that the space velocity was too high, or that the catalyst bed was not enough

When NiO was incorporated to the MgO support, a solid-solution was formed between them during calcination. This solid-solution was detected by same diffraction angles in XRD, good dispersion in SEM and TEM, higher surface Ni/Mg ratio than Ni/Al and low reoxidation by XPS. As a consequence of this strong interaction Ni/MgO catalysts

were more difficult to reduce. This slow reducibility was observed by TPR and during the activity tests at 898 K.

Ni/MgO catalysts had higher BET surface areas than the Ni/Al<sub>2</sub>O<sub>3</sub> one. This, together with the solid-solution formation, could explain a better dispersion of Ni over the support observed by SEM and TEM in the Ni/MgO catalysts. Comparing the 40Ni/MgO with the 30Ni/MgO catalyst, a higher Ni percentage (ICP), together with a higher surface area (BET) allowed a higher Ni availability at the catalyst surface (XPS), which implied that there was more Ni with low metal-support interaction, allowing a better reducibility of the 40Ni/MgO catalyst as observed in a quicker stabilisation of the activity at 898 K and a quicker reoxidation detected in the used samples by XPS.

With the same amount of Ni and lower BET surface, Ni particles were formed over the Al<sub>2</sub>O<sub>3</sub> surface, whereas solid solution between NiO and MgO was observed by TEM images for the 40Ni/MgO. This implies a worse dispersion of Ni in Al<sub>2</sub>O<sub>3</sub> and can be the reason for the lower amount of Ni in the outer layer measured by XPS.

In the case of the 40Ni/Al<sub>2</sub>O<sub>3</sub> there was also a part of the Ni<sup>2+</sup> which could be highly interacting with the support forming aluminates (XPS). In wet-CPO at 1200 h<sup>-1</sup> and S/C from 0.5 to 3, the 40Ni/MgO catalyst showed better performance than the 30Ni/MgO one, which can be explained by a higher amount of metallic nickel (by ICP and also in the surface by XPS), with larger surface area (BET) which implies a larger amount of accessible Ni being more easily reducible.

In wet-CPO process, at the lowest S/C ratio, only 40Ni/Al<sub>2</sub>O<sub>3</sub> catalyst presented an activity increase as compared to CPO. The presence of water in the feed avoided coke formation, as observed in the C/Ni ratios in XPS, but at the same time the deactivation rate increased. After reaction, in wet-CPO conditions, the crystallite size calculated from XRD results was bigger than in the freshly-reduced catalyst, indicating that some sintering had taken place. At higher water concentration in the feed flow (SR conditions) the crystallite size was bigger than in wet-CPO conditions, which could support the idea of catalyst deactivation due to nickel agglomeration.

## Reference list

- [1] H. S. Fogler, *Elements of Chemical Reaction Engineering*, Prentice Hall **2003**.
- [2] P. N. Dwidevi, S. S. Upadhyay, *Ind. Eng. Chem. Process Des. Dev.* **1977**, *16*, 157.
- [3] L. Chen, Q. Hong, J. Lin, F. M. Dautzenberg, *J. Power Sources* **2007**, *164*, 803.
- [4] J. D. Grunwaldt, M. Beier, B. Kimmerle, A. Baiker, M. Nachttegaal, B. Griesebock, D. Lützenkirchen-Hecht, J. Stötzel, R. Frahm, *Phys. Chem. Chem. Phys.* **2009**, *11*, 8770.
- [5] A. Djaidja, A. Kiennemann, A. Barama, *Stud. Surf. Sci. Catal.* **2006**, *162*, 945.
- [6] B. C. Michael, A. Donazzi, L. D. Schmidt, *J. Catal.* **2009**, *265*, 117.
- [7] P. Wu, X. Li, S. Ji, B. Lang, F. Habimana, C. Li, *Catal. Today* **2009**, *146*, 82.
- [8] Q. H. Zhang, Y. Li, B. Q. Xu, *Catal. Today* **2004**, *98*, 601.
- [9] F. Basile, G. Fornasari, F. Trifiro, A. Vaccari, *Catal. Today* **2001**, *64*, 21.
- [10] P. Malet, M. Martin, M. Montes, J. A. Odriozola, *Solid State Ionics* **1997**, *95*, 137.
- [11] Y. H. Hu, E. Ruckenstein, *J. Catal.* **1999**, *184*, 298.
- [12] E. Acha, J. Requies, V. L. Barrio, J. F. Cambra, M. B. Güemez, P. L. Arias, *Int. J. Hydrogen Energy* **2010**, *35*, 11525.
- [13] S. A. El-Safty, Y. Kiyozumi, T. Hanaoka, F. Mizukami, *Appl. Catal. B* **2008**, *82*, 169.
- [14] I. Hotovy, J. Huran, L. Spiess, *J. Mater. Sci.* **2004**, *39*, 2609.
- [15] T. Shishido, M. Sukenobu, H. Morioka, M. Kondo, Y. Wang, K. Takaki, K. Takehira, *Appl. Catal. A* **2002**, *223*, 35.
- [16] J. T. Richardson, B. Turk, M. V. Twigg, *Appl. Catal. A* **1996**, *148*, 97.
- [17] B. C. Enger, R. Lodeng, A. Holmen, *Appl. Catal. A* **2009**, *364*, 15.
- [18] F. B. Rasmussen, J. Sehested, H. T. Teunissen, A. M. Molenbroek, B. S. Clausen, *Appl. Catal. A* **2004**, *267*, 165.
- [19] K. S. W. Sing, D. H. Everett, R. A. W. Haul, L. Moscou, R. A. Pierotti, J. Rouquerol, T. Siemieniewska, "IUPAC recommendations. Reporting physisorption data for gas/solid systems", **2008**.
- [20] D. Gulková, O. Solcová, M. Zdrzil, *Microporous and Mesoporous Mater.* **2004**, *76*, 137.
- [21] M. Kruk, M. Jaroniec, *Chem. Mater.* **2001**, *13*, 3169.
- [22] J. Zhou, S. Yang, J. Yu, *Colloids Surf. A* **2011**, *379*, 102.
- [23] S. M. Morris, P. F. Fulvio, M. Jaroniec, *J. Am. Chem. Soc.* **2008**, *130*, 15210.
- [24] Y. S. Seo, Y. S. Jung, W. L. Yoon, I. G. Jang, T. W. Lee, *Int. J. Hydrogen Energy* **2011**, *36*, 94.
- [25] Y. Kobayashi, J. Horiguchi, S. Kobayashi, Y. Yamazaki, K. Omata, D. Nagao, M. Konno, M. Yamada, *Appl. Catal. A* **2011**, *395*, 129.
- [26] L. S. Neiva, H. M. C. Andrade, A. C. F. M. Costa, L. Gama, *Braz. J. Pet. Gas* **2009**, *3*, 83.
- [27] J. Requies, M. A. Cabrero, V. L. Barrio, M. B. Güemez, J. F. Cambra, P. L. Arias, F. J. Perez-Alonso, M. Ojeda, M. A. Pena, J. L. G. Fierro, *Appl. Catal. A* **2005**, *289*, 214.

- [28] M. A. Goula, A. A. Lemonidou, W. Grünert, M. Baerns, *Catal. Today* **1996**, 32, 149.
- [29] Z. Hou, O. Yokota, T. Tanaka, T. Yashima, *Appl. Catal. A* **2003**, 253, 381.
- [30] R. Yang, X. Li, J. Wu, X. Zhang, Z. Zhang, Y. Cheng, J. Guo, *Appl. Catal. A* **2009**, 368, 105.
- [31] Y. H. Wang, H. M. Liu, B. Q. Xu, *J. Mol. Catal. A* **2009**, 299, 44.
- [32] J. M. Requies, Oxidación parcial catalítica de gas natural para la obtención de gas de síntesis, Thesis **2005**, University of the Basque Country.
- [33] M. S. Fan, A. Z. Abdullah, S. Bhatia, *Appl. Catal. B* **2010**, 100, 365.
- [34] K. Sato, F. Sago, K. Nagaoka, Y. Takita, *Int. J. Hydrogen Energy* **2010**, 35, 5393.
- [35] R. Yang, J. Wu, X. Li, X. Zhang, Z. Zhang, J. Guo, *Appl. Catal. A* **2010**, 383, 112.
- [36] K. Y. Koo, H. S. Roh, Y. T. Seo, D. J. Seo, W. L. Yoon, S. B. Park, *Appl. Catal. A* **2008**, 340, 183.
- [37] E. Ruckenstein, Y. Hang Hu, *Appl. Catal. A* **1999**, 183, 85.
- [38] C. E. Daza, S. Moreno, R. Molina, *Int. J. Hydrogen Energy* **2011**, 36, 3886.
- [39] S. Natesakhawat, O. Oktar, U. S. Ozkan, *J. Mol. Catal. A* **2005**, 241, 133.
- [40] L. Zhang, F. Li, *Appl. Clay Sci.* **2010**, 50, 64.
- [41] Y. H. Wang, H. Wang, Y. Li, Q. M. Zhu, B. Q. Xu, *Top. Catal.* **2005**, 32, 109.



# **5. EXPERIMENTAL RESULTS. MEMBRANES**

The electroless plating recipe for PdCu alloy membranes preparation was optimized and a kinetic study of the Cu deposition was carried out. Alloying is a required step for PdCu membranes preparation, and it was observed that even if no complete alloying was achieved, 15-20 h were enough to obtain a high and stable hydrogen permeance with a thin metal layer of less than 2  $\mu\text{m}$ . Membrane preparation steps influenced the membrane surface. The calculated experimental  $n$  value was higher than 0.5 as expected, due to the thin metal layer. During the performed thermal cycles in inert and hydrogen atmospheres embrittlement problems were not detected.



## 5.1 Membrane preparation

### 5.1.1 Plating recipe

PdCu membranes were prepared by Cu electroless plating over Pd membranes. The first two PdCu membranes were prepared with the recipe from Tesselaar et al. [1] listed in Table 5.1. Membranes were plated for 1 h and then thickness and surface morphology were analysed with SEM images. As the 2,2-bipyridyl (2,2-bpd) compound used in the recipe could have a negative influence on the Cu deposition rate [2], a simplified recipe was also used. In the work by Li et al. [3] it can be observed that with more 2,2'-bipyridyl the deposited copper was brighter and less rough, but the plating rate was slower (at 343 K and with hypophosphite,  $\text{H}_2\text{PO}_2^-$ , instead of formaldehyde). 2,2-bipyridyl is also known to be a ductility promoting additive. The brittleness of the electroless plated copper is mainly determined by the formation of small voids and small gas bubbles containing hydrogen. Another two membranes were prepared without the 2,2-bpd and some bigger Cu particles were observed, so temperature was decreased from 323 to 318 K trying to improve the surface morphology by decreasing the deposition rate. As a result three different procedures were used to prepare PdCu membranes: with 2,2-bpd at 323 K, without 2,2-bpd at 323 K and without 2,2-bpd at 318 K.

Table 5.1. Recipe for PdCu membrane electroless plating, [1].

Metal solution		Reducing solution	
Reagent	Quantity	Reagent	Quantity (for 100 mL Cu bath)
$\text{CuSO}_4 \cdot 5\text{H}_2\text{O}$	8.69 g/L		
$\text{Na}_2\text{EDTA}$	44.44 g/L	Formaldehyde (37 %)	1.53 mL
NaOH	17.77 g/L	2,2-bypirydyyl	0.96 mg
Triton X-100	0.617 mg/L	Ultrapure water	9.58 mL

A comparison of the metal surface morphology using the original recipe and the simplified recipe at 318 K is shown in Figure 5.1. As it can be observed, using the third recipe the surface was more homogeneous and the metal particles were smaller. The main negative effect of the new recipe was that the plating rate was a bit slower. It decreased from 1.22 to 1.05 mg Cu/(h·cm<sup>2</sup>).

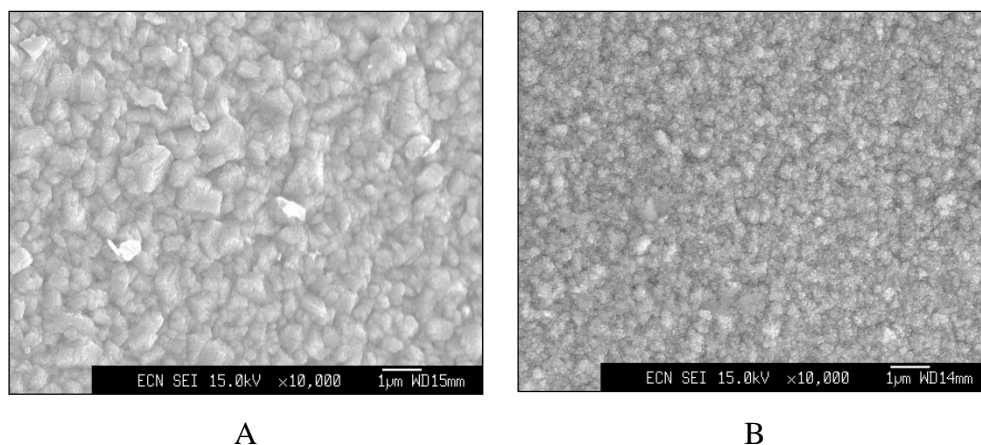


Figure 5.1. SEM surface image of membranes plated with the original recipe at 323 K (A), and with the simplified recipe at 318 K (B).

After this initial work it was decided that all the membranes to be characterized and tested in this work would be prepared with the recipe shown in Table 5.1 without 2,2-bpd and at 318 K. In Figure 5.2 the conditions studied by Shu et al. [4] for the  $\text{Cu}(\text{OH})_2$  precipitation are represented. The  $[\text{EDTA}]/[\text{CuSO}_4]$  and  $[\text{NaOH}]/[\text{CuSO}_4]$  ratios of this recipe are represented in Figure 5.2 with a grey spot. All the plating solutions used for Cu plating were stable, no precipitation was observed, as their concentration was lower than the  $[\text{CuSO}_4] = 0.05 \text{ M}$  line.

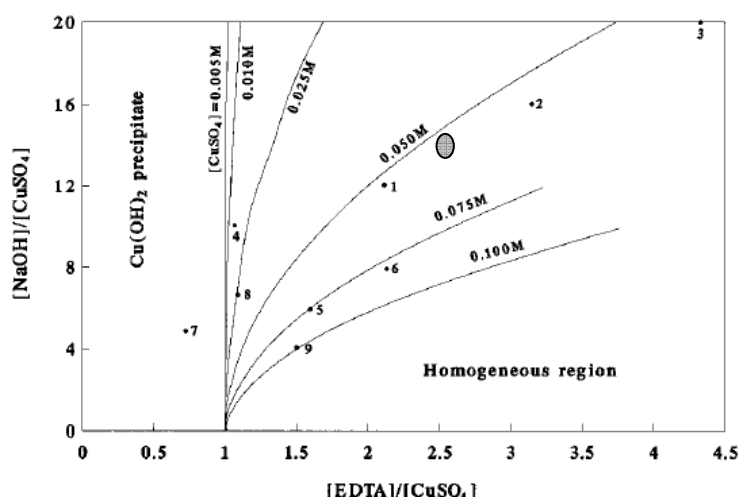


Figure 5.2.  $\text{Cu}(\text{OH})_2$  precipitate formation probability in electroless copper baths [4].

### 5.1.2 Kinetic study of Cu plating

It is important to know the amount of Cu that will be deposited in a fixed period of time, in order to predict the final alloy composition. The thickness of the Cu plated was measured using two different techniques, namely, weight analysis and SEM analysis. Figure 5.3 shows the Cu thickness calculated with both methods after different Cu plating times of the Pd membranes. There was not a clear correlation between time and thickness. Even though, there was a general tendency for the thickness calculated from weight differences: the plating rate increased at the beginning, then stabilized and, finally, prolonged plating times did not result in further Cu deposition.

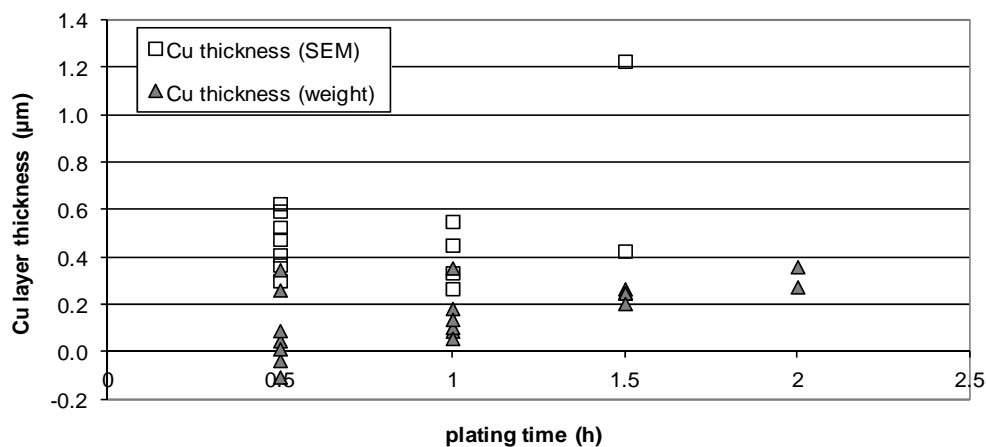


Figure 5.3. Comparison of the Cu thickness obtained at different plating times.

Both methods used for the estimation of the layer thickness had major experimental limitations, even leading to the recording of negative values using the weight method. This was probably due to humidity and to the fact that the gained weight was very small compared to the membranes total weight. In Figure 5.3 it can be observed that results of the thickness measurements by SEM, for the same plating time, are more spread than the ones calculated by the weight method. This may be a consequence of the thin metal layer of Pd and Cu, which implies high measuring errors by SEM, and to the fact that just a ring from the whole membrane is taken for this purpose and the electroless plating can be heterogeneous. Differences between the thickness calculated with the weight difference method and the SEM images have also been reported in the literature [5]. Some authors use the weight method [6, 7] and others SEM images [8-10] to determine the Pd alloy composition. The thickness calculated with the SEM images was the

average of three or four measurements, with a standard deviation lower than 0.2  $\mu\text{m}$ . Regarding the weight values, an error of 1 mg in the measured weight would involve a standard deviation of 0.018  $\mu\text{m}$ . In the present work, as the Pd was already on top of the membrane, metal thicknesses measured by SEM images were used for the composition estimation of the prepared membranes.

With respect to Cu plating rates, the calculated ones from the SEM Cu thicknesses can be compared to a kinetic equation from the literature [11], see Equation 38, being T the temperature in Kelvin. Introducing in this equation the compound concentrations used in this work at 318 K, the obtained initial Cu plating rate with the initial concentrations would be 1.955  $\mu\text{m}/\text{h}$ . The observed global plating rates of the prepared membranes in this work varied from 0.267 to 1.25  $\mu\text{m}/\text{h}$  of Cu. Taking into consideration that the kinetic equation from the literature was obtained in a non-stirred bath and that the substrate and catalytic surface can influence the kinetic parameters, it can be concluded that the experimental values were in the same order of magnitude than the ones estimated with the equation.

$$r_p = 2.81 \frac{[\text{Cu}^{2+}]^{0.43} [\text{HCHO}]^{0.16}}{[\text{OH}^-]^{0.70} [\text{EDTA}]^{0.04}} \exp \left[ 11.5 \frac{(T-313)}{T} \right] \quad \text{Equation 38}$$

### 5.1.3 Membrane alloying

After Cu deposition, Pd and Cu were alloyed to obtain the desired composition and  $\text{H}_2$  permeance characteristics. Diffusion of the metals was visually monitored as the colour changed from Cu colour, before the alloying, to Pd colour after the alloying, see Figure 5.4.

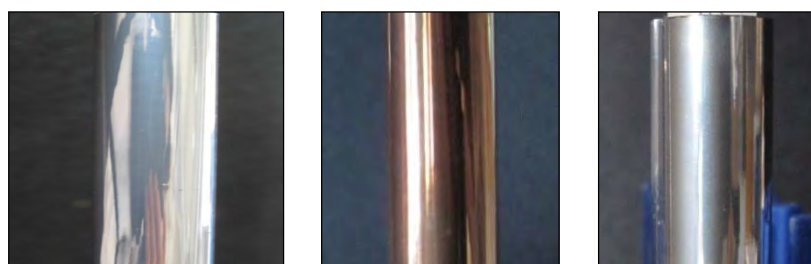


Figure 5.4. Membrane colour before the Cu plating (left), after Cu plating (middle) and after alloying (right).

For the alloying process membrane samples were kept in a reactor for 150 h at 673 K under nitrogen atmosphere. Membranes were alloyed in three different batches, but even if all batches were alloyed under the same conditions they looked different after this process. Membranes from the first batch were bright and homogeneous, the ones in the second batch had no homogeneous colour, and in the third the membranes got dark as shown in Figure 5.5. Most probably there was a set-up problem resulting in oxygen presence during the alloying.

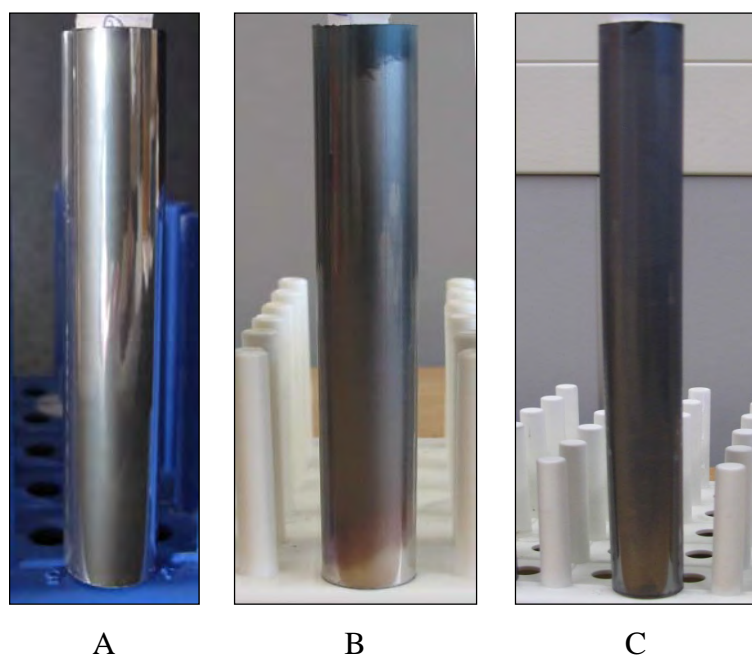


Figure 5.5. Comparison of membranes alloyed in the three different batches: in the first one (A), in the second one (B) and in the third one (C).

The composition of the outside and inside area of the alloyed metal layer of some of the membrane rings was analysed by EDX to study metal diffusion during alloying. PdCu composition was measured from a metal layer cross-section. Figure 5.6 shows the SEM image of a metal layer after alloying. The outside, the darkest area, contains more Cu than the inside. This is due to incomplete alloying.

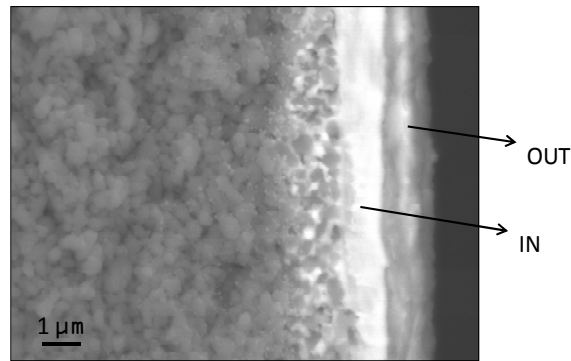


Figure 5.6. Membrane ring piece for the EDX composition measurement after the alloying.

Figure 5.7 shows the EDX results for two of the prepared and alloyed membranes with different Cu plating times, 0.5 and 1.0 h. Before alloying, all the Cu was on the outside and the Pd was on the inside of the metal layer. Although after alloying there still was more Cu on the outside of the membrane (23 and 14 %) than inside (18 and 9 %), metal diffusion throughout the alloying could be monitored. All the prepared and analysed membranes followed the same pattern when EDX compositions before and after alloying were compared.

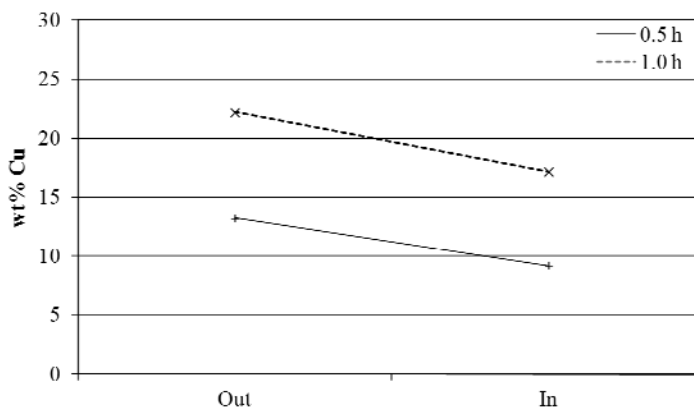


Figure 5.7. EDX composition of two membranes with different plating times (0.5 and 1.0 h) on the outside and inside of the metal layer after alloying at 673 K for 150 h in the first batch.

Two of the prepared membranes were alloyed in a gas permeation system (GPS) with hydrogen tests in between to check the increase in permeance and the required alloying time. The results are illustrated in Figure 5.8. The membranes were heated at 1 K/min in nitrogen and once at 673 K they were maintained in nitrogen except when hydrogen was



introduced to measure the H<sub>2</sub> permeance. The hydrogen permeance was zero at the beginning of both tests, when all Cu was outside, and after a sharp increase at around 15 h of alloying it continued increasing, albeit much more slowly. As no permeance occurs when Cu is on the top of the metal layer, the beginning of H<sub>2</sub> permeance could be attributed to the presence of some Pd on the surface. Therefore, around 20 h in an inert atmosphere and 673 K were enough in order to reach a 1-2 μm partially alloyed thickness.

Another important conclusion of this test is that PdCu membranes prepared by sequential electroless plating can be directly placed in the reactors. If they are heated in inert atmosphere at 1 K/min and maintained at 673 K, after around 15-20 hours high hydrogen permeance can be obtained. With this, the alloying step can be taken out from the membrane production process.

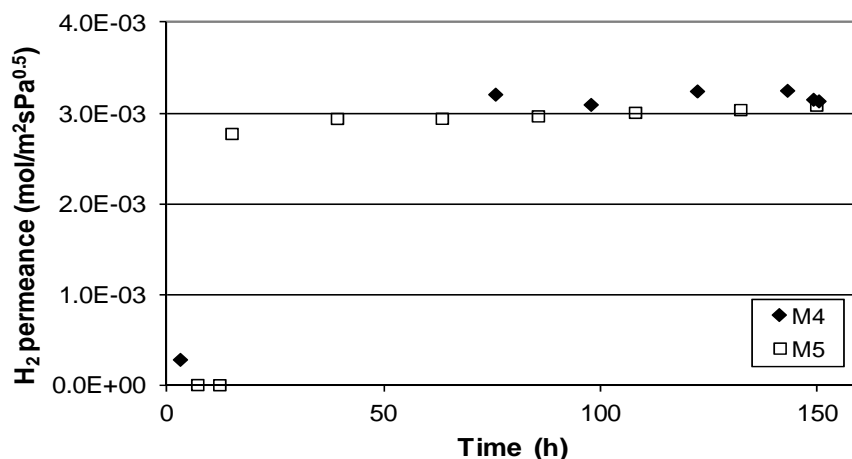


Figure 5.8. Hydrogen permeance in the membranes while alloying in nitrogen gas at 673 K.

## 5.2 Visual analysis

It is very important to perform visual analysis of membranes during all the preparation process. As it is not always possible to analyse membrane morphology, non-destructive methods, such as leak tests and visual analysis, are needed to select good membranes from a batch. In the prepared membranes visual changes happened after the plating and after the alloying, as illustrated previously in Figure 5.4. Pd membranes showed Pd colour, bright and homogeneous. After the Cu plating the colour changed to the Cu one

and after the diffusion occurred during the alloying the colour was again the one of Pd, see Figure 5.4.

In one of the prepared membranes delamination of the metal layer occurred and was detected by visual analysis, see Figure 5.9. Differences between membranes from the three alloying batches were also visually observed, see Figure 5.5. Membranes from the first alloying batch looked bright and homogeneous. The ones from the second one showed no homogeneous colour, and the membranes from the third one were dark. Two membranes, one prepared like the ones alloyed in the second batch and the other like the ones from the third batch, were alloyed in the GPS instead of the oven. After their in situ alloying in the GPS, both looked bright and homogeneous. Therefore, something changed in the alloying reactor from the first to the third batch. Most probably there was a leak in the system and some oxygen entered during the alloying. A membrane from the third alloying batch was analysed by SEM technique and will be studied in the next section. In principle, even if the colour of the third alloying batch was darker they were not dull, so most probably the differences had more to do with the composition than with the morphology of the metal layer.



Figure 5.9. Delamination problems could be visually predicted in the membranes before and after Cu plating.

### 5.3 Gas permeation measurements

In this section the influence of hydrogen feed pressure variation on the membrane permeation performance will be discussed. Hydrogen permeation of the prepared membranes was tested at different feed pressures after H<sub>2</sub> activation and with cooling cycles. A summary of the main characteristics of the compared membranes is shown in Table 5.2.

Table 5.2. Hydrogen permeation performance of PdCu and Pd membranes reported in literature and in this work.

	Pd wt%	PdCu or Pd layer ( $\mu\text{m}$ )	Temperature (K)	Permeability mol/smPa <sup>0.5</sup>	Selectivity	n	Ref.
M1	63	1.0	673	$1.6 \cdot 10^{-8}$	>300	0.65 <sup>a</sup>	c
M2	65	1.4	673	$1.7 \cdot 10^{-8}$	>400	0.64 <sup>a</sup>	c
M3	44	0.9	673	$3.3 \cdot 10^{-9}$	>100	0.75 <sup>a</sup>	c
M4	60	1.0	673	$7.8 \cdot 10^{-9}$	>450	nm	c
M5	77	0.9	673	$1.2 \cdot 10^{-8}$	>1000	nm	c
M6	82	1.7	673	$7.1 \cdot 10^{-9}$	>600	0.63 <sup>a</sup>	c
M6	82	1.7	773	$9.9 \cdot 10^{-9}$	>750	0.71 <sup>a</sup>	c
M7	74	0.7	673	$7.5 \cdot 10^{-9}$	>550	0.76 <sup>a</sup>	c
M7	74	0.7	773	$1.4 \cdot 10^{-8}$	>1700	0.80 <sup>a</sup>	c
M8	69	0.9	673	$3.2 \cdot 10^{-9}$	>750	0.76 <sup>a</sup>	c
M8	69	0.9	773	$7.8 \cdot 10^{-9}$	>1000	0.89 <sup>a</sup>	c
PdCu/PSS	68	20	623	$4.9 \cdot 10^{-9}$	$\infty$	0.6	[12]
PdCu/PSS	64.2	16.7	723	$4.7 \cdot 10^{-9}$	123	0.8	[13]
PdCu/PSS	60	25.4	673	$2.1 \cdot 10^{-8}$	ns	0.5	[14]
PdCu/Al <sub>2</sub> O <sub>3</sub>	92	5.0	753	$1.1 \cdot 10^{-8}$	>1000	1	[15]
PdCu/Al <sub>2</sub> O <sub>3</sub>	95	7.0	753	$1.2 \cdot 10^{-8}$	900	1	[15]
PdCu/Al <sub>2</sub> O <sub>3</sub>	50	3	750	$5.3 \cdot 10^{-9}$	150	ns	[16]
Pd	100	0.35	673	$7.6 \cdot 10^{-10}$	1140	1	[17]
Pd	100	10	740	$2.1 \cdot 10^{-8b}$	970	0.65	[18]
Pd	100	20	623	$6.0 \cdot 10^{-9}$	$\infty$	0.6	[12]
Pd	100	5	723	$1.1 \cdot 10^{-8b}$	3700	ns	[19]

<sup>a</sup>: average n value calculated from the experimental data.

<sup>b</sup>: permeability value calculated from the data in the article assuming standard conditions and n value of 0.5.

c: this work.

ns: not specified

nm: not measured

The composition of the membranes was calculated from Pd and Cu metal layer thicknesses measured by SEM at different points of one ring of each membrane. As explained previously, SEM measurements were not very accurate due to the thin metal layer thicknesses. This implies that the calculated composition is also not very accurate. In Table 5.3 the standard deviations of the calculated Pd wt% in each membrane are shown. The number of points employed to measure the thickness in each membrane ring is also given. As it can be concluded from the deviation values, the real composition of membranes M8, M2 and M1 could differ significantly from the estimated ones.

Table 5.3. Standard deviation of the Pd wt% calculated for membranes composition by metal layer thicknesses measured by SEM and the number of points analysed in each membrane ring.

	M1	M2	M3	M4	M5	M6	M7	M8
Standard deviation (%)	6.3	7.7	--	5.5	2.9	2.4	1.4	8.2
Measured points	4	4	1	4	3	3	3	3

The hydrogen flux values of membranes M1, M2, M3, M6, M7 and M8 measured at 673 K in pure hydrogen at 2 bar pressure difference across the membrane are shown in Figure 5.10. The experimentally estimated  $n$  value was used in the  $\Delta P^n$  calculation. Richardson's equation (Equation 20) was followed at all the tested feed pressures. This can be observed from the correlation index values obtained from linear regression, close to 1 (Table 5.4).

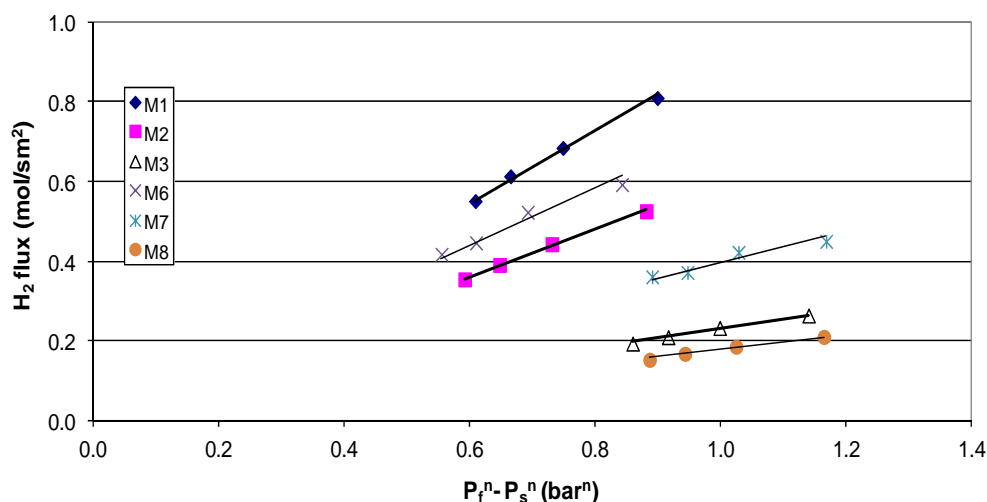


Figure 5.10. Hydrogen permeance results for PdCu membranes at 673 K using the experimental  $n$  value at 2 bar of pressure difference.

Table 5.4. Correlation index values obtained in the hydrogen permeance results at 673 K.

Membrane	M1	M2	M3	M6	M7	M8
Correlation index value ( $R^2$ )	0.996	0.998	0.989	0.947	0.912	0.978

The highest hydrogen flux,  $0.81 \text{ mol}^1\text{s}^{-1}\text{m}^{-2}$ , was obtained for the M1 membrane at 3 bar(g) on the feed side and 1 bar(g) on the permeate side of the membrane, but a correlation between flux, thickness or composition was not observed. When the metal

bulk diffusion limits the hydrogen purification process of the membranes, a hydrogen flux increase should be observed for thinner membranes, but there is not a direct correlation in the obtained results. Looking at the experimentally calculated  $n$  values they are between 0.5 and 1, which implies that the limiting step should probably be a mixture of metal bulk diffusion and surface adsorption and desorption steps. External mass transport step should be almost negligible as the tests were done with pure hydrogen and without sweep gas. The thin metal layer of the prepared membranes, the low accuracy in the SEM measurements, the surface reactions implication in the hydrogen diffusion process and the known membrane composition effect on hydrogen diffusion make difficult to find an explanation to the different fluxes observed for the membranes. Also the amount of Pd deposited inside the pores structure or the support may play an important role in hydrogen diffusion through the membrane. These differences in Pd incorporation to the membranes are analysed in section 5.4.

Three of the membranes were also tested at 773 K in pure hydrogen, with the same feed pressures and submitting them to the cooling and heating cycles under  $N_2$  and  $H_2$  as the ones performed at 673 K. In Figure 5.11 a comparison of the data obtained for the M6, M7 and M8 membranes at 673 and 773 K is shown. At both temperatures Richardson's Law was followed, as it can be concluded from the correlation index values, see Table 5.5. In this case, the correlation index of the M8 membrane tested at 773 K was quite low, probably due to experimental error.

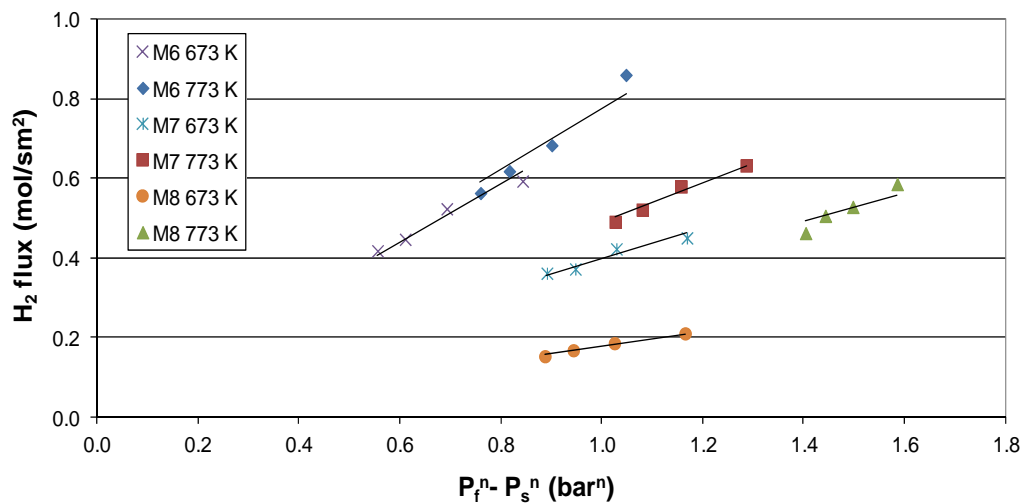


Figure 5.11. Hydrogen flux results for PdCu membranes with the experimental  $n$  value tested at 673 K and 773 K.

Table 5.5. Correlation index values obtained in the hydrogen permeance results at 673 K and 773 K.

Membrane	M6		M7		M8	
	673 K	773 K	673 K	773 K	673 K	773 K
Correlation index value ( $R^2$ )	0.947	0.933	0.912	0.9687	0.978	0.775

From Arrhenius plot of the hydrogen permeance data at different temperatures, the global activation energy of the hydrogen permeation process can be calculated. In the present work the estimated activation energies are not accurate, as just two temperatures were tested. In Table 5.6 the estimated activation energies of M6, M7 and M8, from permeability data with  $n=0.5$ , are shown together with some data from the literature for PdCu, Pd, PdAg and PdAu membranes. The activation energies estimated for M6, M7 and M8 are different, but in the range of the PdCu membranes from the literature with similar thickness. The metal composition, the limiting step in the hydrogen diffusion process, the metal surface structure and the thickness could influence the activation energy value. This could also explain the differences in the  $E_a$  values found in the literature.

The hydrogen permeation performance of the PdCu membranes tested in the GPS (M1, M2, M3, M4 and M5) and in the MP (M6, M7 and M8) systems are summarized in Table 5.2. The permeability data shown in this table for the prepared membranes were obtained at 673 K and/or 773 K with 2 bar pressure difference and using a pure hydrogen atmosphere. As observed in Table 5.2, the prepared membranes showed good permeation performance as compared to the reported values for PdCu and Pd membranes. The selectivity of the tested membranes was high, at least  $>100$  mL  $H_2$ /mL  $N_2$ , and the thickness of the metal layers was around 0.7 – 1.7  $\mu\text{m}$ . The calculated  $n$  coefficient values, from the correlation between permeance values and pressure differences across membranes, were between 0.628 and 0.891. The  $n$  values were calculated from 36 points for the M1 to M7 membranes and with 12 points for the M8. The standard deviation of the  $n$  values calculated from flux data obtained in the GPS (M1 to M3) was between 0.9 and 1.7 %, whereas for the membranes tested in the MP (from M6 to M8) it was higher, between 3.0 and 8.8 %. The reason for this accuracy

difference is that the GPS is a smaller and more optimized system for characterizing membranes, whereas the MP is a bigger system, optimized for chemical processes.

Table 5.6. Activation energies calculated for M6, M7 and M8 membranes and for some PdCu, Pd, PdAg and PdAu reported in the literature.

Membrane	Pd wt%	Support	Thickness ( $\mu\text{m}$ )	$E_a$ (kJ/mol)	Ref.
M6	82	$\text{Al}_2\text{O}_3$	1.7	14.3	<sup>a</sup>
M7	74	$\text{Al}_2\text{O}_3$	0.7	27.8	<sup>a</sup>
M8	69	$\text{Al}_2\text{O}_3$	0.9	38.3	<sup>a</sup>
PdCu	57	PSS	25.4	9.5	[14]
PdCu	Ns	PSS	20	13.2-16.5	[12]
PdCu	76	<sup>b</sup>	16.7	9.3	[13]
PdCu	61	$\text{Al}_2\text{O}_3$	2	10.3	[8]
PdCu	81	PSS	2	33.3	[20]
PdCu	58	$\text{ZrO}_2/\text{PSS}$	1	15.4	[21]
PdCu	85	$\text{ZrO}_2/\text{PSS}$	0.6	14.5	[21]
Pd	100	Foil	100-150	23.7	[22]
Pd	100	$\gamma\text{Al}_2\text{O}_3/\alpha\text{Al}_2\text{O}_3$	15	10	[23]
Pd	100	$\text{CeO}_2\text{-PSS}$	13	16.2	[24]
PdAg	76	PSS	20-26	8-15	[25]
PdAg	90	$\text{Al}_2\text{O}_3/\text{PSS}$	16	12.3	[26]
PdAu	84	Foil	100-150	21.3	[22]
PdAu	50	Foil	100-150	35.2	[22]
PdAu	Ns	PNS	4	14.6	[27]

PSS: Porous Stainless Steel Support, PNS: Porous Nickel Support

<sup>a</sup>: this work

<sup>b</sup>: the membrane film was deposited directly on a micro-channel plate

ns: not specified

As membrane thickness decreases, the pressure exponent is expected to be higher than 0.5, meaning that bulk metal diffusion is not the only limiting step. In the membranes prepared in this work all the  $n$  values were higher than 0.5, which most probably implies that surface reactions influenced the overall hydrogen diffusion process due to the thin metal layer. As the measurements were made in pure hydrogen, external mass transport phenomena could be neglected. The hydrogen transport through Pd-based membranes occurs via a solution and diffusion mechanism, including several surface processes and bulk diffusion. Both processes could be the rate-determining step for hydrogen permeation [28]. If the pressure exponent is close to 1, this indicates that the surface

reactions or mass transport become rate-limiting in hydrogen transport [20, 29]. For  $n$  values between 0.5 and 1, both surface, mass transport and bulk diffusion processes can be responsible for hydrogen flux resistance. Rothenberger et al. [30] compared Pd membrane thicknesses and  $n$  values and found that for thicknesses of less than 10  $\mu\text{m}$  the  $n$  value was higher than the theoretical one of 0.5. In Table 5.2 it can be observed that for thicker membranes the  $n$  value is closer to 0.5, indicating metal bulk diffusion limitation.

The  $n$  value is not only affected by the thickness of the metal layer, but also by, amongst others, the preparation method, surface composition, mass transport resistance and experimental conditions [15]. In the work by Li et al. [3] a 2  $\mu\text{m}$  Pd membrane was analysed and they observed that  $n$  value gradually decreased from 1.0 to 0.68 when temperature and pressure were increased. They worked with pure  $\text{H}_2$ , so the change of the rate-limiting step was suggested to be the main reason for the fluctuation of  $n$  value, as there were no polluting agents. In the membranes tested in the MP the  $n$  value also varied when increasing temperature, as the relative importance of surface processes and bulk diffusion changes with temperature. Moreover, membranes may undergo structural changes such as grain coarsening, segregation and grain boundary excretion with increasing temperature.

Hydrogen flux through the membranes, measured in pure  $\text{H}_2$  with 2 bar pressure difference, increased when increasing temperature in the three tested membranes. In the M6 it varied from 0.33 to 0.42  $\text{mol}/(\text{sm}^2)$ , in the M7 from 0.28 to 0.50  $\text{mol}/(\text{sm}^2)$  and in the M8 from 0.20 to 0.59  $\text{mol}/(\text{sm}^2)$ . This increase is also observed in the permeability, with  $n=0.5$ , data presented in Table 5.2. The selectivity obtained in measurements made at 773 K was higher than 750 mL  $\text{H}_2$ /mL  $\text{N}_2$  and it increased with temperature. The experimentally calculated  $n$  values were high at 773 K, between 0.713 and 0.891 highlighting the relative importance of the surface step in the permeance process.

As explained before, PdCu membranes permeance depends on a lot of parameters as composition, temperature and crystalline phase. Figure 5.12 shows a qualitative comparison of the permeance values obtained in this work (darker circles) with some from the literature for PdCu alloys on ceramic supports and with metal layer thickness  $< 5\mu\text{m}$  (lighter colour), as a function of membrane composition and temperature.



Permeance values are proportional to circle diameters and were calculated with the theoretical  $n=0.5$  value. The permeance values of the membranes reported in this work were consistent with the ones from literature. At the same temperature membranes with composition around 60 wt% of Pd were the ones with the highest permeance values, as expected from the literature [14, 31]. Nevertheless, permeance is influenced by so many variables that it is not easy to establish a maximum permeance just based on membrane composition. At 673 K and with the composition calculated from the SEM images, the membranes with the highest theoretical permeance values seemed to have bcc+fcc structure. The membrane with the lowest Pd percentage (44.4 wt% Pd) was also the one with the lowest permeance value, even if it also seemed to have bcc+fcc structure.

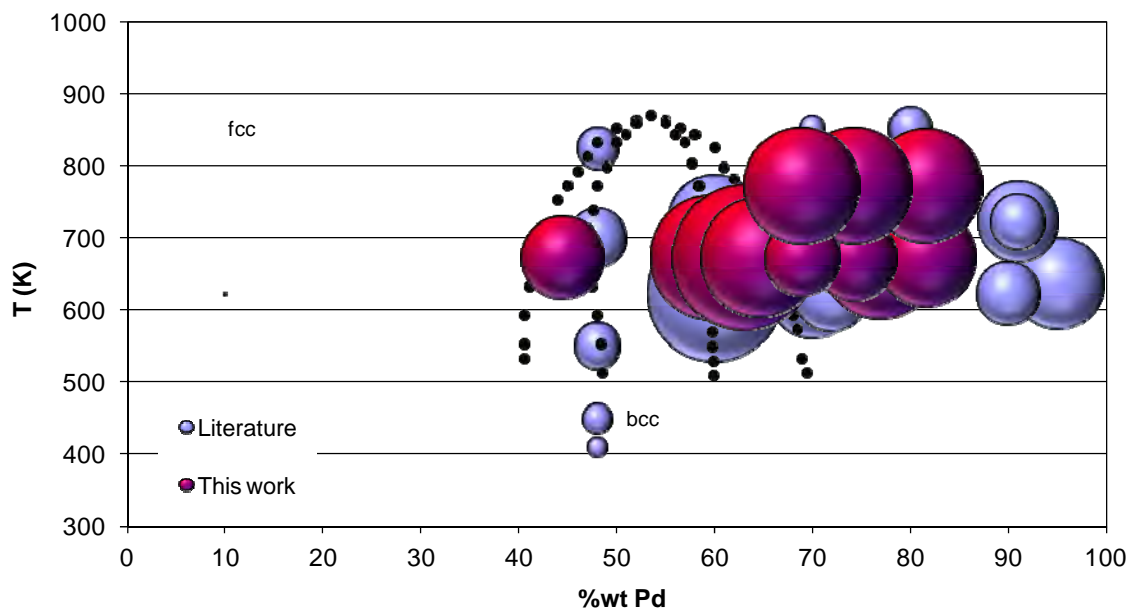


Figure 5.12. Comparison of the prepared PdCu membranes permeance values with some reported in the literature [8, 32-35]. Circle diameter is proportional to permeance. Small points represent phase limits.

Temperature cycles were carried out to test the stability of the prepared PdCu membranes by cooling them under inert and hydrogen atmospheres. Figure 5.13 shows the calculated permeability values of the tested membranes in the GPS (M1, M2 and M3) and in the MP (M6, M7 and M8) at 673 K. Between the first and the second group of data, membranes were cooled to 423 K and heated again to 673 K in an inert atmosphere. Between the second and the third group of data, the same thermal cycle was performed, but this time in a hydrogen atmosphere. As it can be observed,

membrane permeability was stable after the temperature cycles, even after the one in hydrogen. According to Miller et al. [36] the reason could be that the H atoms in the Pd alloys travel through the Pd-X lattice, but are not incorporated into the structure, thereby minimising embrittlement problems. This test showed that membranes were stable and did not become brittle, but longer thermal cycle tests should be carried out to gain more information about permeability evolution with thermal cycles.

The membranes with the highest permeability were M1 and M2 that had a calculated composition close to the optimum 60 wt% of Pd and metal thicknesses of 1.0 and 1.4  $\mu\text{m}$  respectively. The lowest permeabilities were measured for M3 and M8 and both had 0.9  $\mu\text{m}$  of metal layer thickness. The reason for the low permeability of M3 could be its low Pd concentration, 44 wt%. In the case of M8, the calculated composition was 69 wt% of Pd, but the standard deviation of this value was very high as presented before, being more difficult to find an explanation for the low permeability.

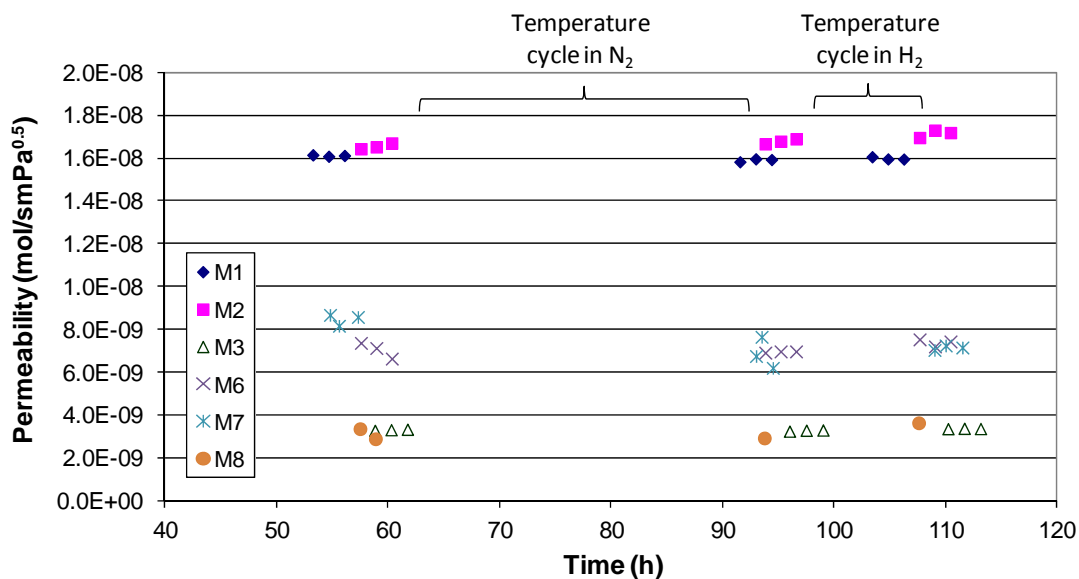


Figure 5.13. Hydrogen permeability,  $n=0.5$ , with temperature cycles in inert and hydrogen atmospheres at 673 K.

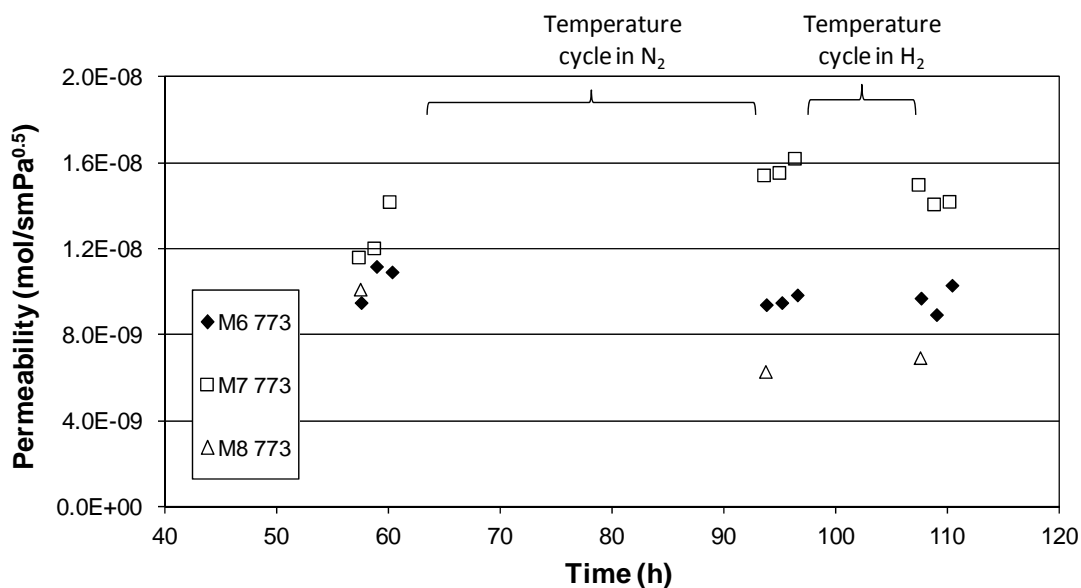


Figure 5.14. Hydrogen permeability test,  $n=0.5$ , with temperature cycles in inert and hydrogen atmospheres at 773 K at 2 bar of pressure difference.

The same thermal cycle was also performed at 773 K with three of the membranes in the MP, see Figure 5.14. The three membranes showed stable permeability with similar values. With these tests it was again observed that the membranes were stable and that they did not suffer from embrittlement along the tests carried out. At 773 K the membrane with the highest permeability was the thinnest one, M7, but due to the uncertainty of the thickness measurements and therefore, the calculated composition, it was not possible to obtain an explanation for the differences in the permeability values.

#### 5.4 Membrane morphology

In order to analyse the effect of Cu plating, alloying and hydrogen permeance tests on the membrane metal layer, SEM images were taken. In these SEM images the dark rough area on the left is the alumina support. Moving to the right there is an area where the Pd is anchored to the support, the next bright area is the Pd and the last and darkest one is the Cu layer. Figure 5.15 illustrates SEM images of the M2 membrane after Cu plating (A), after alloying in an inert atmosphere (B) and after the hydrogen permeance test at 673 K over 5 days with two temperature cycles in between: in inert and in hydrogen atmospheres (C). Metal diffusion during alloying was not clearly detectable in the SEM images. Comparing A and B images from Figure 5.15, the difference originated by Pd and Cu mixing cannot clearly be observed, even though the high

permeability value of the alloyed membrane implied that there was some Pd in the surface. In image C, after the hydrogen permeance and temperature cycles, it was still possible to differentiate the Cu layer, but the PdCu mixture was more extended.

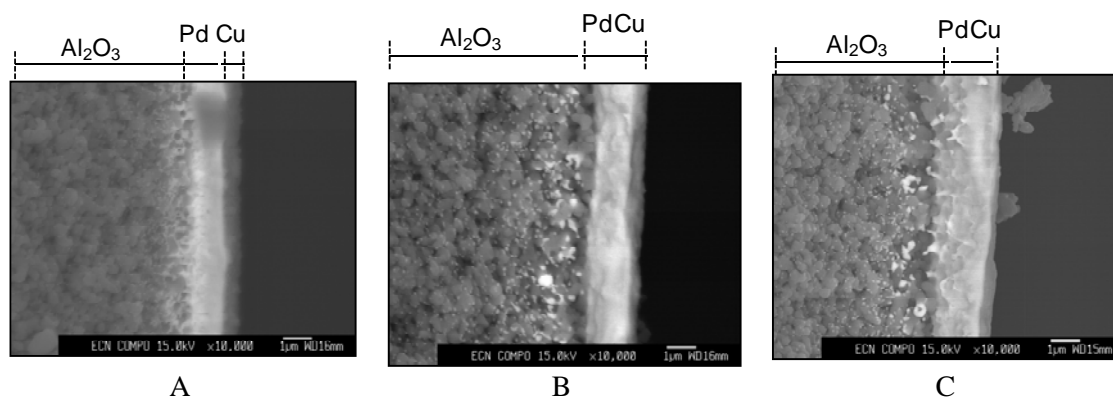


Figure 5.15. SEM image of the M2 after Cu plating (A), after alloying (B), and after the hydrogen permeance test at 673K (C).

Figure 5.15 also shows the previously mentioned differences in Pd amount diffused into the alumina support. This Pd deposition inside the pores could contribute to different hydrogen fluxes despite similar apparent membrane thickness.

The membrane composition was measured after alloying and after hydrogen testing to check if alloying continued during the hydrogen diffusion. Table 5.7 presents the composition values measured by EDX in the M2 and M1 membranes after alloying and after the hydrogen permeance test, calculated as an average from four measured points. Even if no clear conclusions can be obtained from these data, it seems that metals continued mixing during the hydrogen permeance test as in the “In” the area Cu concentration increased after the H<sub>2</sub> test. Based on SEM images, EDX values, alloying tests in the GPS and permeation measurements performed with the membranes, it can be concluded that from a certain point onwards, alloying has no substantial influence on permeance, even if it has not been completed to full homogeneity [37].

Table 5.7. EDX composition of two membranes on the outside (Out) and inside (In) of the metal layer after alloying and after the hydrogen permeance test.

		Out	In
		Cu wt%	Cu wt%
M2	After alloying	5.10	2.31
	After H <sub>2</sub> test	5.28	5.57
M1	After alloying	7.82	2.17
	After H <sub>2</sub> test	6.43	3.84

The metal appearance of most of the prepared membranes was not completely homogeneous after Cu plating. To check the differences between areas such as white spots and blackish areas, examples are given in Table 5.8, SEM images were taken to analyse their morphology. According to these images no big surface differences were observed. In Table 5.8 the average surface, representative of the overall membranes' surface morphology, is shown. Only the white or clearer spots seemed to have a rougher or more opened surface as shown in Table 5.9. The M9, M10 and M11 membranes' metal layer was peeled off, that could be correlated to the roughness and/or heterogeneity of the surface.

Table 5.8. Images of blackish and whitish area and spots observed in some membranes after Cu plating.

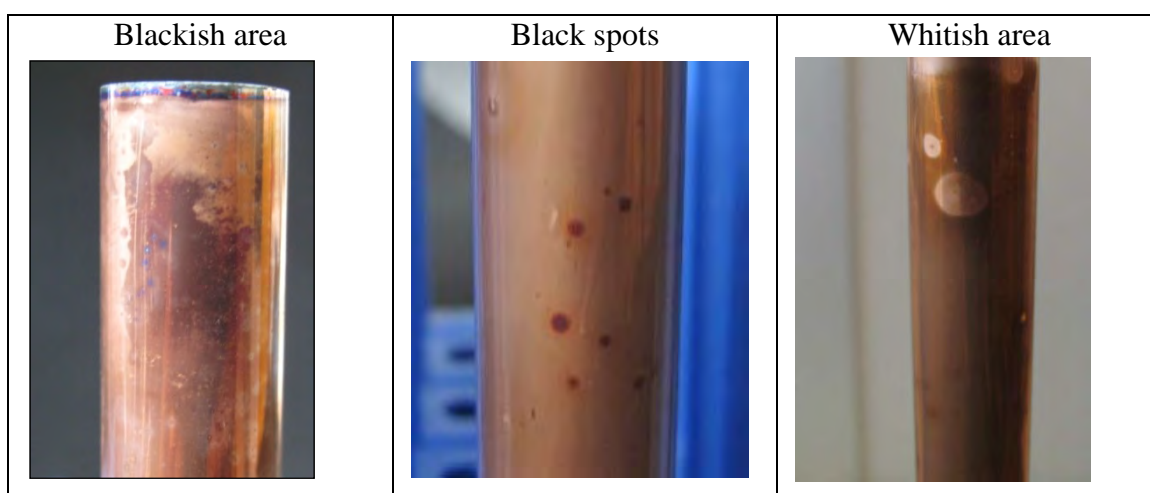
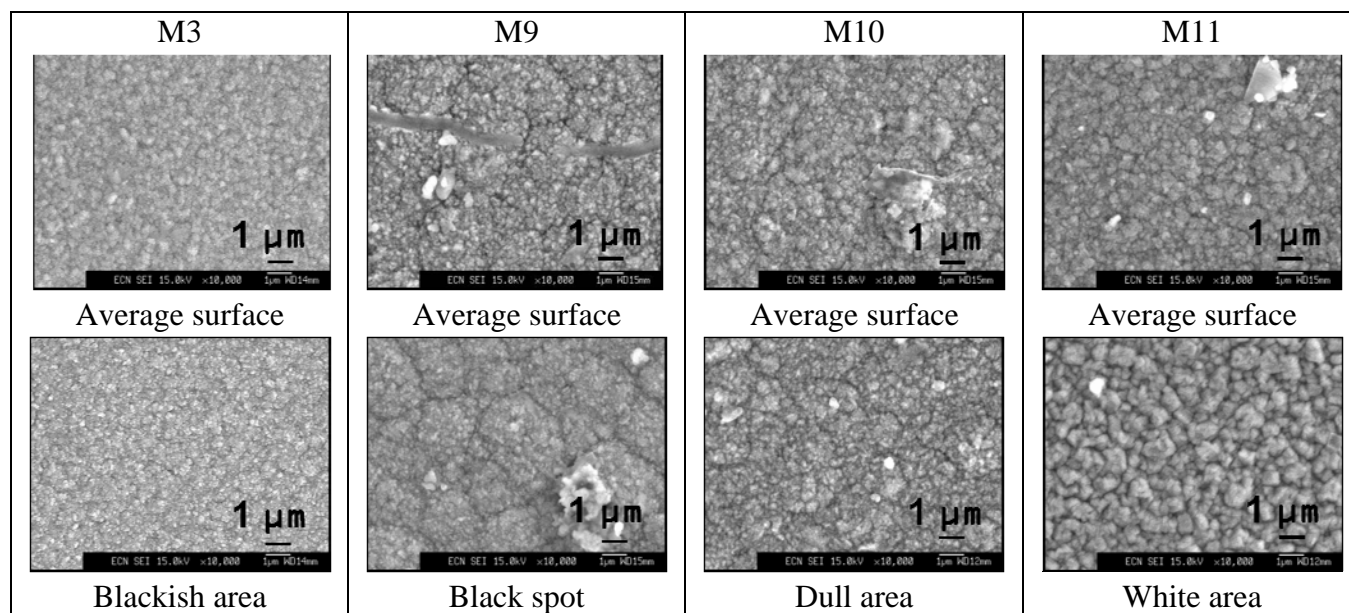


Table 5.9. Comparison of the average surface morphology with the black, dull and white areas of membranes after Cu plating.

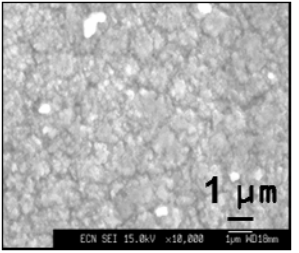
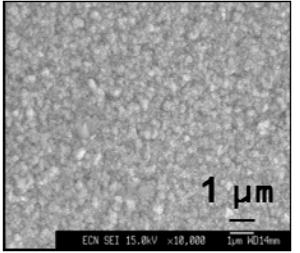
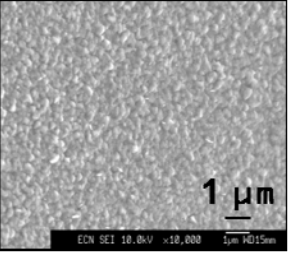
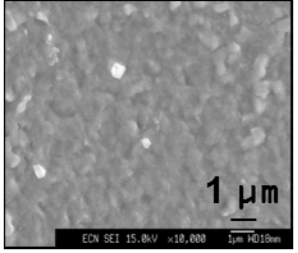
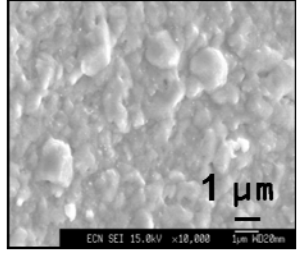
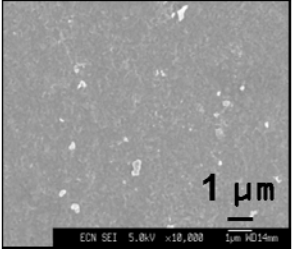
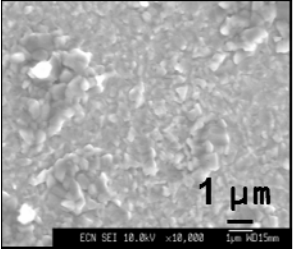
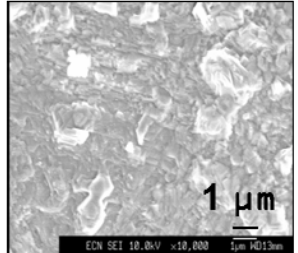
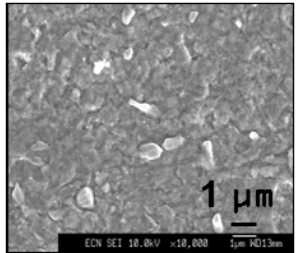


SEM images were also taken to analyse the influence the membrane preparation steps had on the surface morphology. Table 5.10 compares the membrane surface after Cu plating, after alloying and after the H<sub>2</sub> test and temperature cycles in the GPS/MP. After hydrogen tests the appearance of the PdCu membranes was homogeneous. Areas such as whitish, blackish or spots, detected after Cu plating, were not observed. The white particles observed in the images were probably alumina particles from membrane cutting prior to SEM analysis. After alloying the surface was rougher and there were larger metal particles in the surface due to grain growth. Nevertheless, after the hydrogen permeance tests, the large metal particles tended to disappear.

The third batch of alloyed membranes was especially interesting, as they were going to be tested with gas mixtures from hydrogen production processes from methane and also in the presence of a sulphur compound (Chapter 6). As explained before, the visual appearance of these membranes was darker and the SEM image showed that the surface was rougher and with bigger particles. The surface of one of these membranes, M7, was analysed with both SEI and COMPO images, shown in Figure 5.16. In the SEI images the colour differences are due to morphologic differences, and in the COMPO ones the colour can be related to composition. The morphology of the membrane was quite homogeneous, but rough (see Figure 5.16 A). Regarding the composition, it could be

clearly observed that it was not homogeneous (see Figure 5.16 B). The irregular areas observed in the morphologic analysis had different compositions compared to the smooth areas.

Table 5.10. Comparison of the average surface morphology of the membranes after the Cu plating, the alloying and the H<sub>2</sub> permeance tests.

M1	M2	M3	M7
	 <p data-bbox="555 875 780 909">After Cu plating.</p>	 <p data-bbox="893 875 1118 909">After Cu plating.</p>	 <p data-bbox="1232 875 1457 909">After Cu plating.</p>
 <p data-bbox="212 1173 450 1249">After alloying, 2<sup>nd</sup> batch.</p>	 <p data-bbox="550 1173 788 1249">After alloying, 2<sup>nd</sup> batch.</p>	 <p data-bbox="888 1173 1126 1249">After alloying, 1<sup>st</sup> batch.</p>	 <p data-bbox="1227 1173 1465 1249">After alloying, 3<sup>rd</sup> batch.</p>
 <p data-bbox="193 1518 469 1552">After permeance test.</p>	 <p data-bbox="531 1518 807 1552">After permeance test.</p>		

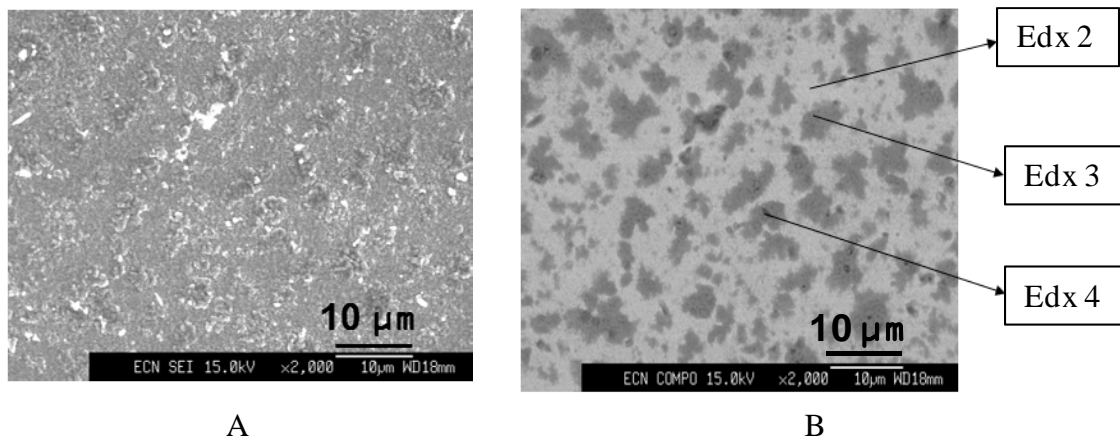


Figure 5.16. SEM images of the M7 membrane from the third alloying batch. (A) SEI image, (B) COMPO image.

Surface composition in three different areas of the membrane was analysed with EDX. The results are listed in Table 5.11. As it can be observed, in the darker areas, EDX 3 and EDX 4, there was high oxygen content. The alumina detected in the EDX 4 could be due to ceramic particles in the surface from the cutting. The hypothesis of a leak in the alloying reactor system seemed to be right, and the effect on the membrane performance can be critical. The morphologic roughness could also be explained by a shape change as a consequence of Pd deformation due to PdO crystallite formation shown in Figure 1.16. This rearrangement of the film could lead to pinholes generation, but the surface could also be levelled off while being under hydrogen atmosphere.

Table 5.11. Surface composition study of the M7 membrane from the third batch.

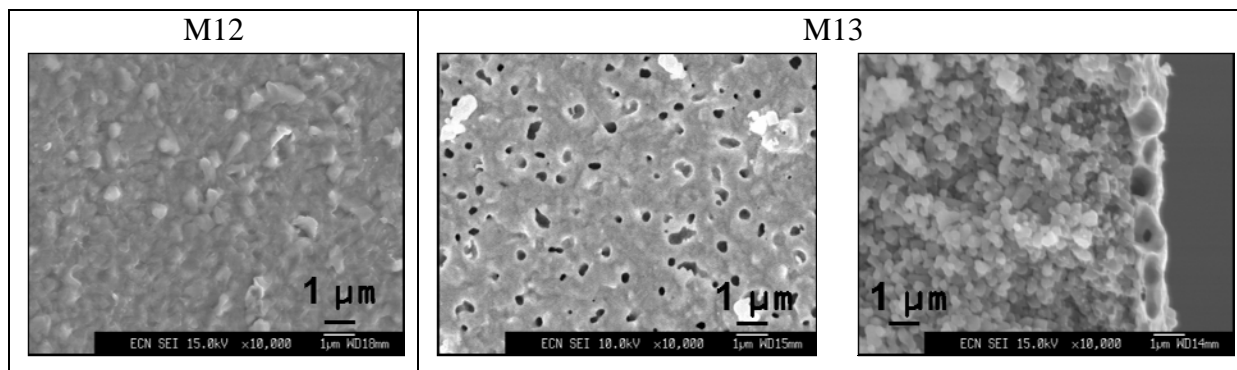
Wt%	EDX 2	EDX 3	EDX 4
C	2.9	1.6	1.7
O	4.6	13.9	24.9
Pd	83.7	31.9	39.4
Cu	8.8	52.6	19.2
Al	-	-	14.8

Some membrane defects could be detected with SEM, such as pinholes in the membranes as shown in Table 5.12. Both membranes, M12 and M13, were found to be not dense after the alloying step. There were some small holes and open surfaces in the M12 membrane, but the metal surface in M13 was completely porous with open pore sizes between 0.2-0.5  $\mu\text{m}$ . These defects have also been observed in the literature, as the



bcc/fcc mixed phase morphology is prone to defect formation along the grain boundary [16]. Large holes were also observed in the bulk metal layer. These results observed for the defective membranes highlight the importance of the leak tests performed before testing membranes in the GPS.

Table 5.12. SEM images of the membranes that were not dense after alloying.



## 5.5 Discussion

The electroless plating method was suitable for thin PdCu metal layer membrane preparation. The Cu plating recipe for PdCu membranes preparation was optimized. The electroless solutions were stable, without precipitation, and allowed to prepare thin and dense PdCu membranes that showed high permeability. The weight increase and SEM images were compared as methods to estimate the metal layer thickness and to calculate the composition, but SEM was not accurate enough for the thin prepared membranes. The alloying step could be reduced to around 20 h for the metal layer thickness of the prepared membranes, 1-2 μm. In addition, a sequentially plated PdCu membrane can be also alloyed insitu in the reactor, obtaining high permeability without the alloying step in a separate unit. Therefore, the manipulation of membranes is reduced decreasing the risk of damages before delivery and utilization.

The prepared membrane composition was between 44 and 82 wt% Pd and all of the membranes followed Richardson's Law. The experimental values of the pressure exponent  $n$  were higher than the theoretical one, 0.5, measured under pure hydrogen atmosphere. This indicates that in the prepared thin membranes both surface and bulk diffusion processes were limiting the hydrogen flux. The hydrogen flow increased with

increasing temperature in the tested membranes, but as the hydrogen diffusion steps are differently affected by the temperature, different  $n$  values were detected.

A direct correlation between the thickness of the metal layer and the permeability was not observed. This can be due to the low accuracy when measuring thin metal layers with SEM images. The membrane with the highest permeance value at 673 K had an estimated composition close to 60 wt% of Pd and, therefore, according to the phase diagram it should present the bcc+fcc structure. The tested membranes showed stable permeances throughout the temperature cycles, even after the one in hydrogen, and their selectivity was high.

The characterization of the membranes using SEM images provided valuable information about the influence of the metal alloying and the hydrogen permeance processes on the surface morphology. The membrane surface presented bigger particles after alloying and was less rough after the permeance tests. This can be due to hydrogen diffusion through the metal affecting its morphology. Based on the cross-sectional metal layer composition measurements taken with EDX it was concluded that a full alloying was not required to obtain a PdCu membrane with high and stable permeance.

## Reference list

- [1] E. A. N. Tesselaar, Ontwikkeling van een gedragen palladium/koper membraan middels electroless platen, report , ECN The Netherlands **2005**.
- [2] M. Oita, M. Matsuoka, C. Iwakura, *Electrochim. Acta* **1997**, *42*, 1435.
- [3] J. Li, H. Hayden, P. A. Kohl, *Electrochim. Acta* **2004**, *49*, 1789.
- [4] J. Shu, B. P. A. Grandjean, S. Kaliaguine, *Ind. Eng. Chem. Res.* **1997**, *36*, 1632.
- [5] S. N. Paglieri, K. Y. Foo, J. D. Way, J. P. Collins, D. L. Harper-Nixon, *Ind. Eng. Chem. Res.* **1999**, *38*, 1925.
- [6] X. Zhang, W. Wang, J. Liu, S. Sheng, G. Xiong, W. Yang, *Thin Solid Films* **2008**, *516*, 1849.
- [7] M. E. Ayturk, Y. H. Ma, *J. Membr. Sci.* **2009**, *330*, 233.
- [8] L. Yuan, A. Goldbach, H. Xu, *J. Phys. Chem. B* **2007**, *111*, 10952.
- [9] Y. H. Ma, B. C. Akis, M. E. Ayturk, F. Guazzone, E. E. Engwall, I. P. Mardilovich, *Ind. Eng. Chem. Res.* **2004**, *43*, 2936.
- [10] K. Hou, R. Hughes, *J. Membr. Sci.* **2002**, *206*, 119.
- [11] F. M. Donahue, K. L. M. Wong, R. Bhalla, *J. Electrochem. Soc.* **1980**, *127*, 2340.
- [12] W. H. Chen, P. C. Hsu, *Int. J. Hydrogen Energy* **2011**, *36*, 9355.
- [13] M. S. Islam, M. M. Rahman, S. Ilias, *Int. J. Hydrogen Energy* **2012**, *37*, 3477.
- [14] D. L. McKinley, United States Patent 3439474, **1969**.
- [15] X. Zhang, W. Wang, J. Liu, S. Sheng, G. Xiong, W. Yang, *Thin Solid Films* **2008**, *516*, 1849.
- [16] A. Goldbach, L. Yuan, H. Xu, *Sep. Purif. Technol.* **2010**, *73*, 65.
- [17] L. Q. Wu, N. Xu, J. Shi, *Ind. Eng. Chem. Res.* **2000**, *39*, 342.
- [18] A. Li, W. Liang, R. Hughes, *Catal. Today* **2000**, *56*, 45.
- [19] X. Hu, W. Chen, Y. Huang, *Int. J. Hydrogen Energy* **2010**, *35*, 7803.
- [20] T. A. Peters, M. Stange, H. Klette, R. Bredesen, *J. Membr. Sci.* **2008**, *316*, 119.
- [21] H. Gao, S. Lin, Y. Li, B. Zhang, *J. Membr. Sci.* **2005**, *265*, 142. [22] T. B. Flanagan, D. Wang, *J. Phys. Chem. C* **2011**, *115*, 11618.
- [23] R. Dittmeyer, V. Höllein, K. Daub, *J. Mol. Catal. A:* **2001**, *173*, 135.
- [24] J. Tong, Y. Matsumura, H. Suda, K. Haraya, *Ind. Eng. Chem. Res.* **2005**, *44*, 1454.
- [25] M. a. L. Bosko, J. B. Miller, E. A. Lombardo, A. J. Gellman, L. M. Cornaglia, *J. Membr. Sci.* **2011**, *369*, 267.
- [26] M. L. Bosko, D. Yepes, S. Irusta, P. Eloy, P. Ruiz, E. A. Lombardo, L. M. Cornaglia, *J. Membr. Sci.* **2007**, *306*, 56.
- [27] K. R. Hwang, C. B. Lee, S. K. Ryi, J. s. Park, *Int. J. Hydrogen Energy* **2012**, *37*, 6626.
- [28] F. Gallucci, F. Chiaravalloti, S. Tosti, E. Drioli, A. Basile, *Int. J. Hydrogen Energy* **2007**, *32*, 1837.
- [29] A. Li, C. J. Lim, J. R. Grace, *Chem. Eng. J.* **2008**, *138*, 452.
- [30] K. S. Rothenberger, A. V. Cugini, B. H. Howard, R. P. Killmeyer, M. V. Ciocco, B. D. Morreale, R. M. Enick, F. Bustamante, I. P. Mardilovich, Y. H. Ma, *J. Membr. Sci.* **2004**, *244*, 55.

- [31] C. Decaux, R. Ngameni, D. Solas, S. Grigoriev, P. Millet, *Int. J. Hydrogen Energy* **2009**, *35*, 4883.
- [32] F. Roa, M. J. Block, J. D. Way, *Desalination* **2002**, *147*, 411.
- [33] F. Roa, J. D. Way, *ACS Fuel Chemistry Division Preprints* **2003**, *48*, 335.
- [34] F. Roa, J. D. Way, *Ind. Eng. Chem. Res.* **2003**, *42*, 5827.
- [35] L. Yuan, A. Goldbach, H. Xu, *J. Membr. Sci.* **2008**, *322*, 39.
- [36] J. B. Miller, B. D. Morreale, A. J. Gellman, *Surf. Sci.* **2008**, *602*, 1819.
- [37] E. Acha, Y. C. van Delft, J. Overbeek, P. L. Arias, J. F. Cambra, *Int. J. Hydrogen Energy* **2011**, *36*, 13114.

# **6. EXPERIMENTAL RESULTS. PROCESS INTEGRATION**

Membrane performance separating hydrogen from complex mixtures was evaluated in this chapter. Hydrogen production was carried out in a first reactor (R1) using the previously developed and tested catalysts at the operating conditions used in chapter 4 and the outgoing complex mixtures were fed into the membrane module (MM). Hydrogen recovery in the MM was analysed varying the hydrogen production process in R1 and therefore, varying the composition of the mixture fed to the membrane. Both catalysts and membranes were finally tested operating with H<sub>2</sub>S addition. Membrane lifetime was analysed and SEM and XRD techniques were employed to characterize the used membranes.



## 6.1 Coke formation in the membrane plant (MP)

In order to test the membrane performance separating hydrogen from complex mixtures, a mixture was produced in the catalytic reactor (R1) and then the product mixture was fed to the membrane module (MM), see Figure 6.1. In the first process integration tests performed with hydrogen production in R1 and purification in MM coke formation was detected in the membrane module, see Figure 6.2. The membrane located in the module was completely covered by coke and it cracked and separated from the metallic header tube.

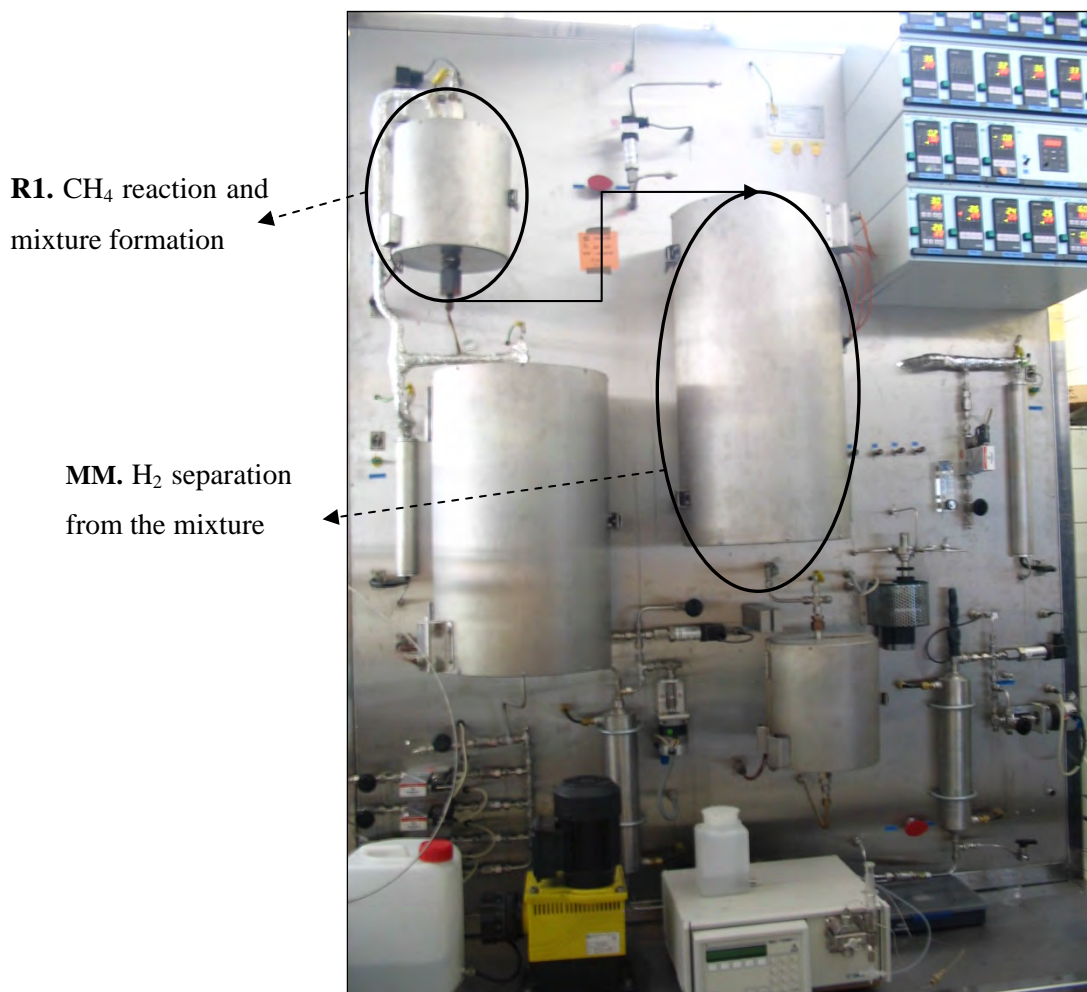


Figure 6.1. Membrane plant (MP) scheme for hydrogen production in R1 followed by hydrogen purification in MM.



Figure 6.2. Coke formation in the membrane module during the initial tests with complex mixtures.

In order to search what was the reason for coke formation, a stainless steel tube was located instead of the membrane, as illustrated in Figure 6.3. With this purpose different process configurations and conditions were tested. Coke formation occurred in the membrane module, even if no catalyst was used here because just hydrogen separation was carried out. Different reaction conditions were tested in the R1 to analyse if water addition could prevent coke formation in MM. Methane CPO, wet-CPO and SR were performed in R1 at 1073 K and  $1000 \text{ h}^{-1}$  with different S/C ratios, as summarised in Table 6.1. In this table, the obtained methane conversion in R1 and the collected coke weight in the MM at the end of the test are also shown. Water addition in the hydrogen production process in R1 had a positive effect avoiding coke formation in MM. When the CPO process was carried out in R1 a lot of coke was generated in the MM, but operating in SR conditions with S/C ratios of 2 and 3, the coke formation was almost negligible. Even though a way of minimizing coke formation was found, further investigation was needed for the CPO and wet-CPO scenarios.

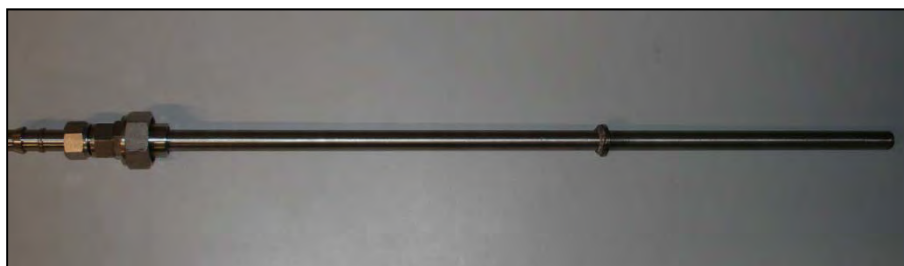


Figure 6.3. Stainless steel tube located in the MM.



Table 6.1. Reaction conditions in R1 and their effect in coke formation in MM.

	SR		Wet-CPO						CPO		
S/C	3.0	2.0	2.0	1.9	1.7	1.5		1.3	1.0	0	
CH <sub>4</sub> conversion (%)	45	40	78	77	90	89	80	88	87	88	84
Coke in MM (g)	0.08	nd	0.10	0.11	0.98	1.41	0.08	0.11	1.33	1.33	8.65

nd: not detected

One of the possibilities for coke formation was that the Boudouard reaction took place in MM, Equation 39. In order to analyse this possibility, two different tests were carried out. First of all a CO:N<sub>2</sub> mixture, with 15 % of CO, was fed to the system at 1073 K and at the same space velocity as the previous tests from Table 6.1, 1000 h<sup>-1</sup>.



The composition of the inlet and outlet gas from MM was measured with the mass spectrometer. The consumed CO amount was calculated throughout a material balance. If all the CO would have reacted in Boudouard reaction, 0.012 g of coke should have been formed in the MM during the testing time. When the test was finished, the generated coke amount was measured. In the MM there was 1.26 g of coke, 0.14 g in the last reactor and big coke pieces were collected from the R1. Then, the test was repeated but feeding CO<sub>2</sub> to the system instead of CO. In this case, no coke was generated in the R1, neither in the R2 and 0.21 g in the MM. From these tests it was concluded that Boudouard reaction was occurring in the MM, but the CO was not the only carbon source.

Three coke samples were analysed by XRD to determine their composition and C, NiCr<sub>2</sub>O<sub>4</sub> and Fe<sub>2</sub>O<sub>3</sub> were detected. In Table 6.2 the overall composition of the 316 stainless steel used in the bench-scale plant is shown. The reactors and the membrane module are made of this material. Comparing the composition of the coke samples and steel it can be observed that coke formation was linked to the steel as the only source of Ni, Cr and Fe in the system was the steel. The MM steel tube appearance after doing some tests at 1073 K is shown in Figure 6.4. The 316 stainless steel was damaged by the aggressive operating conditions. Most probably the steel was even decomposed in

contact with the complex mixtures produced in the R1. This can be related to the “metal dusting” phenomenon, which can take place under reducing atmospheres with high levels of  $\text{CH}_4$  and  $\text{CO}$ . Metal dusting is a severe form of corrosive degradation of metals and alloys at high temperatures (300-850 °C) in carbon-supersaturated gaseous environments [1]. The suspected mechanism is firstly the deposition of a graphite layer on the surface of the metal, and then it forms metastable  $\text{M}_3\text{C}$  species (where M is the metal) which migrate away from the metal surface [2].

Table 6.2. Average composition of the 316 Stainless steel (wt%).

C max.	Si max.	Mn max.	P max.	S max.	Cr	Ni	Mo	Fe
0.08	1.00	2.00	0.045	0.030	16-18	10-14	2-3	62-68



Figure 6.4. The steel tube of the membrane module after tests at 1073 K.

As metallic elements from the steel were found in the coke, it was concluded that most probably those metals, especially the Ni and Fe, could be promoting coke formation in the MM. The higher reactor volume, compared to the R1, which implies a lower gas space velocity and therefore, more time to react, could also have enhanced coke formation in the MM. In order to analyse the steel effect on coke formation, a membrane module tube with the inside covered by a thick chromium layer was prepared, see Figure 6.5. This hard chrome plating is an electrolytic process used in the industry for deposition of a layer of chromium onto a metallic object with the objective of improving properties like the corrosion resistance.



Figure 6.5. Membrane module with the hard chrome plating inside.

To check if the chromium plated tube was suitable for the system, the CPO process was performed in R1 with the new tube in the membrane module. When the test finished the MM was opened and the “stainless steel membrane” was taken out of it. It was clearly observed that the chromium plated tube was coke free, but the steel tube was completely covered by coke, see Figure 6.6.

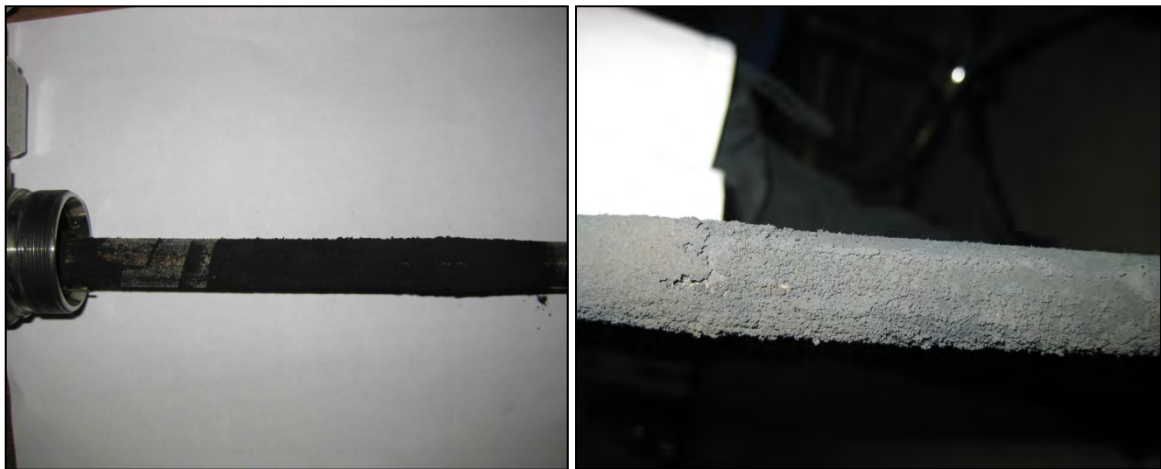


Figure 6.6. Coke formed in the “stainless steel membrane” inside the hard chrome plated tube.

When operating with membranes, the steel surface exposed to the mixtures was going to be lower than with the “stainless steel membrane”, but even then, there were some steel areas (i.e. the end caps of the membranes). A special high temperature tape was used to cover the exposed steel (69 Glass Cloth Electrical Tape, 3M). Using this tape no coke was detected in the membrane module after carrying out CPO in R1 as shown in Figure 6.7. During all the tests that will be explained in this chapter, where complex mixtures were fed to the MM, the hard chrome plated tube was used in the MM and the stainless

steel areas of the membrane were covered with the special tape. In a real process a more suitable metallic material for the membrane holder should be used to avoid coke formation in this area if operating in similar conditions.



Figure 6.7. Hard chrome plated tube and the “stainless steel membrane” covered with a high temperature tape after performing CPO.

## 6.2 Process integration parameters selection

### 6.2.1 Feed pressure

Once the coke formation problem was solved, the most appropriate hydrogen production (in R1) followed by purification (in MM) process parameters were selected. From an economic point of view there is clear indication to avoid the incorporation of a gas compressor between reactor and membrane module. Therefore, in order to get the optimal feed pressure, the effect of this feed pressure on both the CPO reaction and hydrogen separation was tested. Figure 6.8 shows the effect of increasing pressure on the hydrogen flow produced by CPO in the catalytic reactor R1 and on the hydrogen amount purified in the MM at 673 K. The sweep/permeate side pressure was atmospheric and the feed/retentate side pressure was increased varying the pressure difference across the membrane. As expected from the thermodynamics of the CPO reaction, there was a decrease in the produced hydrogen amount when the feed pressure increased. At around 4 bar of feed pressure, it decreased by 30 %. The test conditions are summarised in Table 6.3, and an overview of the mixture composition produced in the CPO reactor is shown in Table 6.4. The composition of the mixture changed along

time with the feed pressure as it affected the CPO process. Table 6.4 shows the average composition of the process for some of the tested feed pressures. The rest of the flow to 100 % was Ar.

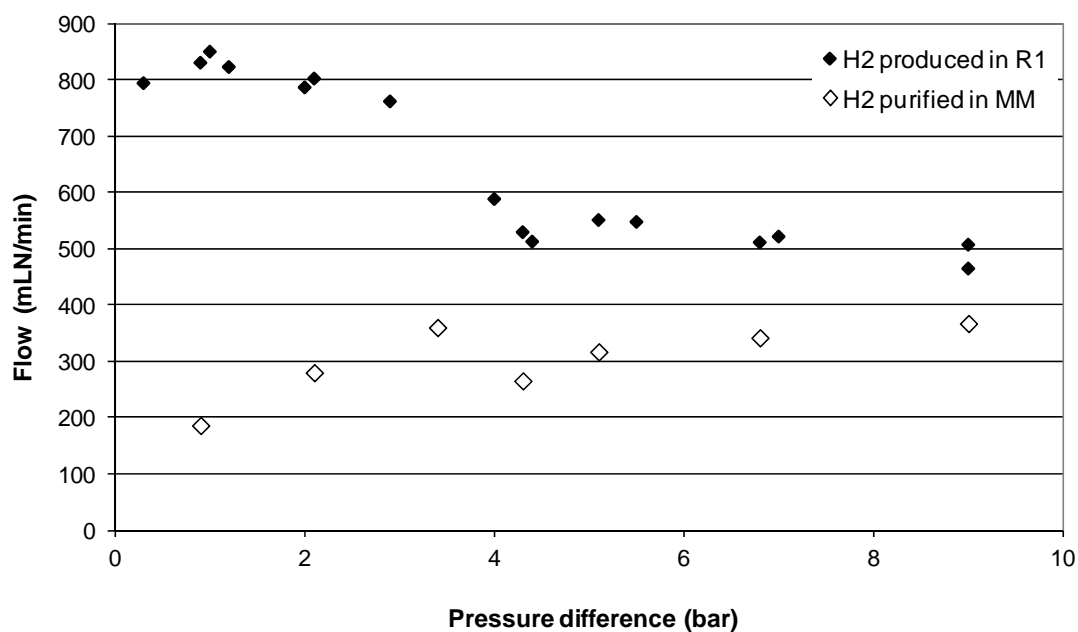


Figure 6.8. Feed pressure effect on the amount of hydrogen produced by CPO in the catalytic reactor (reactor temperature 1073 K and methane feed flow 700 NmL/min) and on the purified H<sub>2</sub> flow in the MM at 673 K.

Table 6.3. Test conditions in the catalytic reactor and in the membrane module for the analysis of the optimal feed pressure.

	Catalytic reactor	Membrane module
T (K)	1073	673
Flow in (NL/min)	2.3	2.9 – 2.5
Sweep flow (NL/min)	-	0 / 0.55 / 1.7
Feed pressure (barg)	0-9	0-9
Permeate pressure	-	atmospheric
Process	Hydrogen production by methane CPO	Hydrogen purification with M6 PdCu membrane

Table 6.4. Average composition produced in the catalytic reactor and fed to the membrane module.

	H <sub>2</sub>	CO <sub>2</sub>	CO	CH <sub>4</sub>	O <sub>2</sub>
With feed pressure = 1.0 bar(g)	29.0	1.8	17.1	3.8	nd
With feed pressure = 3.5 bar(g)	26.7	2.2	16.3	4.7	nd
With feed pressure = 5.5 bar(g)	21.5	3.7	12.9	9.0	nd
With feed pressure = 9.0 bar(g)	18.1	4.3	12.1	9.9	nd

nd: not detected

A decrease in the hydrogen production in the reactor R1 due to an increase of the feed pressure directly affected the hydrogen recovery in the membrane module. There are two simultaneous processes in the system with an opposite effect on membrane performance. Less hydrogen is produced when the feed pressure increases, decreasing the hydrogen pressure difference across the membrane and hence decreasing the hydrogen recovery in the MM. However, the hydrogen partial pressure in the retentate increases as the feed pressure increases, increasing the hydrogen pressure difference across the membrane. Figure 6.9 shows the effect of the feed pressure on the hydrogen recovery at a constant atmospheric pressure on the permeate side. The hydrogen recovery in the membrane module is calculated with Equation 29. It is increased as the feed pressure increases even though the feed hydrogen percentage decreased, due to a higher hydrogen pressure difference across the membrane. The selected operating feed pressure was 3.5 bar(g), as it was the value with the highest hydrogen recovery/production ratio.

Figure 6.9 also shows the effect of the sweep gas flow variation on the hydrogen recovery with the M6 membrane in the MM. Sweep gas flow addition had a positive effect on the process due to the increase of the hydrogen partial pressure difference across the membrane. With 550 NmL/min of sweep gas, the hydrogen recovery was approximately doubled, but with 1700 NmL/min no further improvement of any significance was observed.

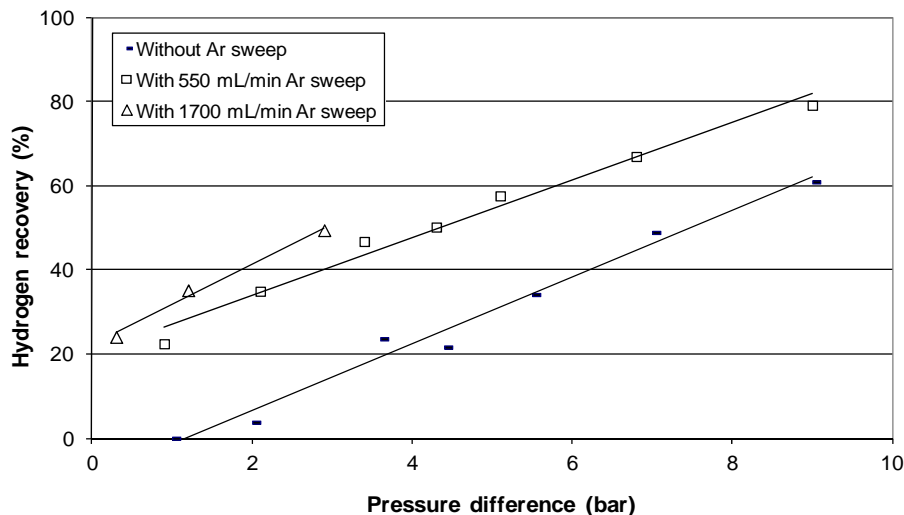


Figure 6.9. Feed pressure effect on hydrogen recovery at different sweep gas flows (M6 membrane at 673 K).

### 6.2.2 Sweep gas flow

As explained before hydrogen production is thermodynamically favoured at low pressures and hydrogen purification at high feed pressures. Apart from the feed pressure effect analysed before, the sweep gas flow is also an important parameter. Higher sweep gas flow implies lower hydrogen partial pressure in the permeate side of the membrane, increasing the hydrogen pressure difference across the membrane. Another disadvantage of increasing the pressure to increase the hydrogen pressure difference, apart from the fact that it decreases the produced amount of hydrogen, is that gases different from hydrogen could go through the membrane [3]. Even though the use of sweep gas is beneficial for the overall process, it is also an expensive part of it, which makes indispensable to optimize the required flow. The hydrogen dilution in the retentate, or feed, side of the membrane is another critical factor for the hydrogen permeation across the membrane. In the integrated hydrogen production plus purification process, the hydrogen concentration in the feed flow to the membrane depends on the conversion and feed dilution of the previous R1, thus, it can change with time on stream.

In order to obtain an optimal sweep gas flow, hydrogen permeation tests were performed with different hydrogen dilutions and using different sweep gas flows. In the tests, the hydrogen amount was maintained constant and it was diluted by varying the added Ar amount. The main experimental error was the flow measurement with the

manual flow-meter. Measurements were repeated until differences between them were lower than 3 %.

Figure 6.10 illustrates hydrogen recovery tests performed at 3.5 bar(g) in the feed side and atmospheric pressure in the sweep side with the M7 membrane at 773 K. The solid lines are guides. The hydrogen flow was kept constant at 0.54 NL/min and it was diluted with Ar to obtain different feed gas compositions. Eight different hydrogen dilutions in inert gas were tested, between 20 and 70 %. For each dilution the hydrogen flow across the membrane was measured at different sweep gas flows. The sweep gas flow used in each measurement was fixed as a percentage of the feed gas that was added to the membrane module.

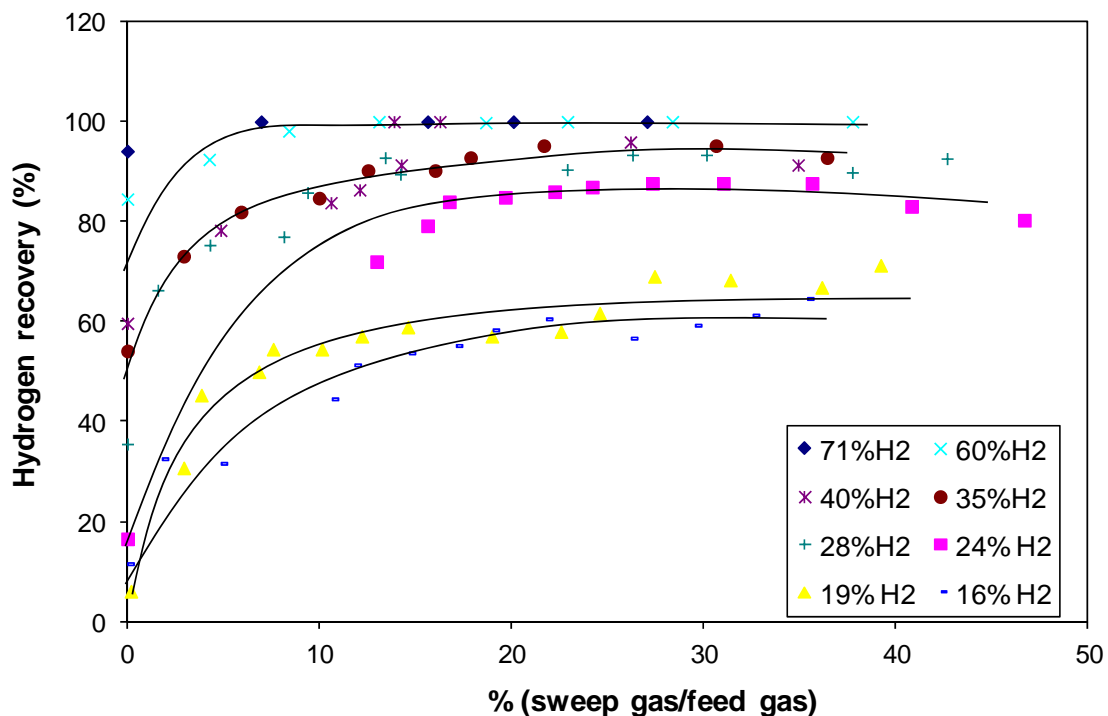


Figure 6.10. Hydrogen recovery of M7 (membrane area of 53.7 cm<sup>2</sup>) in the membrane module with 0.54 NL/min of H<sub>2</sub> diluted with Ar to obtain different feed gas compositions and using different sweep gas flows at 3.5 bar pressure difference across the membrane and 773 K.

It can be observed that when the hydrogen percentage was high, 70 %, even with no sweep gas the hydrogen recovery was very high, more than 90 %. But for lower hydrogen percentage cases, around 20-25 %, the recovery without sweep gas flow was



lower than 20 %. When using a sweep flow around 15-20 % of the total flow fed to the MM, the hydrogen recovery levelled off. Larger sweep gas flow, and therefore higher economical cost, will not imply higher efficiency of the process.

Hydrogen recovery versus sweep gas flow at different hydrogen compositions was also studied at 2.0 bar(g) of feed pressure and 773 K. The corresponding results are shown in Figure 6.11. The solid lines are guides. The hydrogen flow was kept constant at 0.54 NL/min and it was diluted with Ar to obtain different feed gas compositions. The aim of this second test was to check the dependence of the optimal sweep gas flow percentage, calculated from the results given in Figure 6.10, on the feed pressure. The tested hydrogen dilutions were in the range of the ones used in the previous test at 3.5 bar(g), between 16 and 70 %.

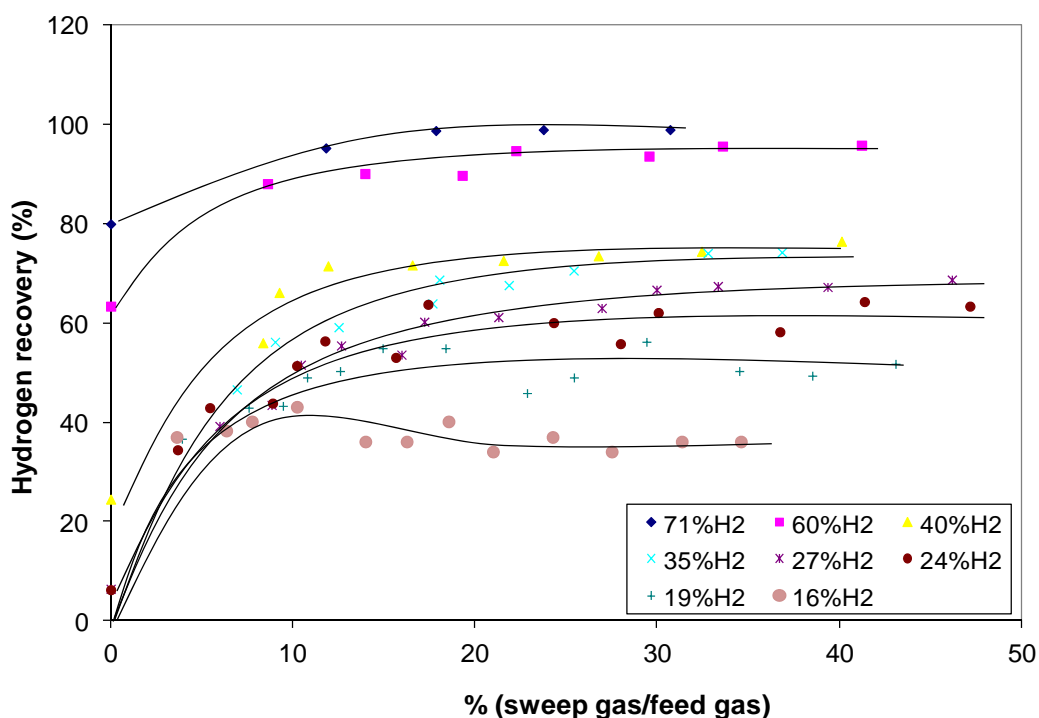


Figure 6.11. Hydrogen recovery of M7 (membrane area of 53.7 cm<sup>2</sup>) in the membrane module with 0.54 NL/min of H<sub>2</sub> diluted with Ar to obtain different feed gas compositions and using different sweep gas flows at 2.0 bar pressure difference across the membrane and 773 K.

The negative effect of not using sweep gas on the hydrogen recovery was more noticeable in this case. The hydrogen partial pressure in the feed side of the membrane was lower and therefore also the hydrogen pressure difference across the membrane, which is the driving force for hydrogen permeation. However, the maximum hydrogen recovery was achieved again when using a sweep gas flow of around 15-20 % of the flow fed into the MM.

Regardless the composition of the flow fed into the MM, that could vary in time in a real processes due to catalyst deactivation or feed composition fluctuations, the optimal sweep gas flow can be determined just measuring the flow fed into the membrane module and using a sweep gas flow of around a 20 % of this value.

### 6.3 Membrane performance under complex mixtures

Hydrogen recovery from a gas mixture is not only affected by hydrogen dilution and hydrogen partial pressure difference across the membrane, as studied before, but also by the mixture components. When producing hydrogen from methane, as in this work, hydrogen is always mixed at least with N<sub>2</sub>, CO, CO<sub>2</sub>, H<sub>2</sub>O and CH<sub>4</sub> provided that sulphur compounds accompanying the natural gas have been removed before. The CO is known to have an important inhibition effect on membrane performance [4-7]. About water vapour influence, contradictory information is reported in the literature. It was considered negligible for a PdAg membrane by Nguyen et al. [8], whereas a reduction of around 70 % was observed by Gielens et al. [9] for Pd and PdAg membranes. Regarding CO<sub>2</sub>, CH<sub>4</sub> and argon they do not affect the membrane so strongly [10, 11]. CO has been found to cause more inhibition than the same concentration of CO<sub>2</sub> [12]. In the present work the CO percentage was around four times that of CO<sub>2</sub>, so the study was focused on the CO effect on the prepared PdCu membranes performance, supposing a negligible effect of CO<sub>2</sub>.

In this section the results of the tests where hydrogen was produced via CPO and wet-CPO processes in the R1 catalytic reactor and separated in counter-current mode in the MM are presented. In the hydrogen production via wet-CPO process different water/methane ratios were tested to analyse the effect of water addition on membrane performance. The catalytic reactor R1 was operated at 1073 K and 600 h<sup>-1</sup> of WHSV.

The membrane module operated at 773 K, the feed pressure of the system was 3.5 bar(g), the sweep side was at atmospheric pressure, and the used sweep gas flow was 20 % of the flow produced in R1 and fed into the MM. The conversion plotted in the following figures refers to the conversion in the catalytic reactor R1. The membranes seemed to have no influence on the conversion. The calculated global conversion and R1 conversion differed by less than 2 percentage points, which could be due to the experimental error rather than to the catalytic activity of the PdCu layer. The hydrogen yield is also calculated for the catalytic reactor, R1. The effect of the gas mixture components and the water content on the membrane performance was analysed with three membranes: M6, M7 and M8.

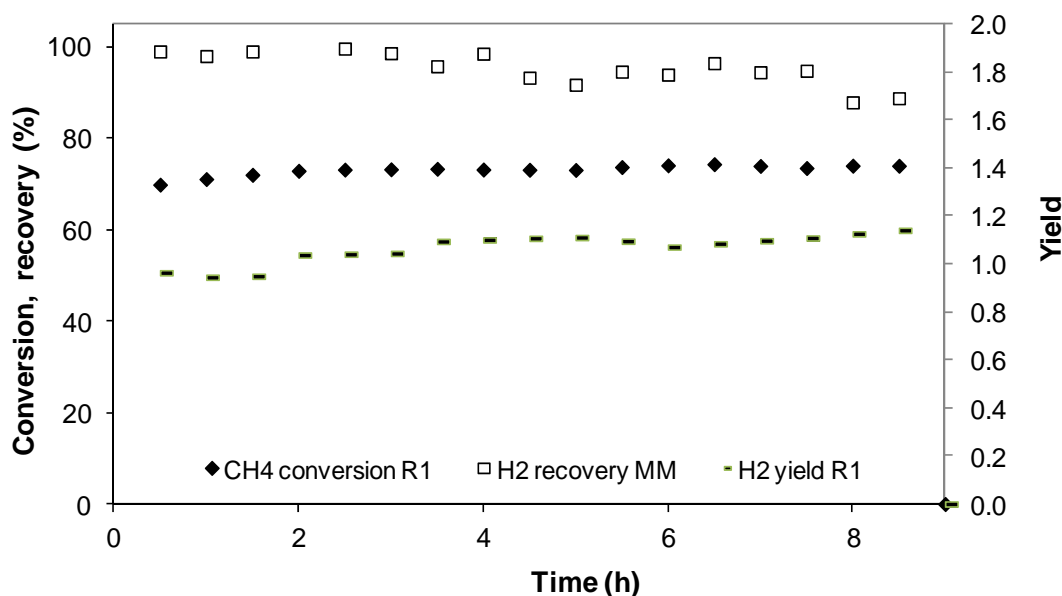


Figure 6.12. Hydrogen production via CPO in R1 at 1073 K with 0.35 g of catalyst and  $600 \text{ h}^{-1}$  of WHSV and purification in MM with M7(membrane area  $53.7 \text{ cm}^2$ ) at 773 K with a 20 % of sweep gas and 3.5 bar of pressure difference.

With the M7 membrane hydrogen was purified from a complex mixture produced in R1 via CPO. Figure 6.12 shows the methane conversion measured in R1 and the hydrogen recovery recorded in the membrane module throughout the operation time. The catalyst activity was stable during the test. As CPO conversion is negatively affected by a pressure increase, the conversion shown in Figure 6.12 was lower than the one obtained in Chapter 4 at the same temperature and space velocity but at atmospheric pressure. The measured conversion was around 70-75 % and the hydrogen yield was around 1.1.

The average H<sub>2</sub> and CO percentages in the mixture were 27.5 % and 14.0 % respectively. The hydrogen recovery decreased along time on stream towards 85 %. Mixture components fed into the membrane module seemed to have a slightly negative influence on the membrane performance, but the test was not long enough to obtain final conclusions.

With the M6 membrane longer mixture tests were carried out. The mixture fed to the MM was produced in R1 via methane CPO and wet-CPO alternating over time. The operating conditions and the average mixture composition produced in R1 in each time segment are summarized in Table 6.5. The catalyst activity and membrane hydrogen recovery results are depicted in Figure 6.13. Between the different testing days the membrane was kept in inert atmosphere at 673 K, identified in the figure with thicker lines. In the figure, the positive effect of sweep gas addition in the first hours can be observed, when CPO was performed without sweep gas, segment A, and then with sweep gas, segment B. Methane conversion and hydrogen production in the R1 reactor were reasonably stable, 85-90 % and 0.5-0.6 NL/min, respectively. The highest hydrogen yield in R1 was obtained at the highest S/C ratio due to higher H<sub>2</sub>/CH<sub>4</sub> ratio in the reforming process, operating conditions F. When changing the reaction conditions in the R1 the composition of the mixture produced in R1 and fed to the membrane module changed.

Table 6.5. The employed process operating conditions and mixtures dry composition in the complex mixtures tested with M6.

	A	B	C	D	E	F
Process	CPO		Wet-CPO			
S/C			0.02	0.11	0.50	0.90
Sweep gas	No	550 NmL/min				
T reactor (K)	1073					
T membrane (K)	673					
CO (mol%)	18.0	17.8	18.1	17.5	14.8	
H <sub>2</sub> (mol%)	20.4	19.4	19.7	21.6	22.6	
CH <sub>4</sub> (mol%)	4.4	4.6	4.6	4.4	2.9	
CO <sub>2</sub> (mol%)	2.4	2.7	2.7	4.7	7.0	
O <sub>2</sub> (mol%)	nd	nd	nd	nd	nd	
Feed flow to MM (NL/min)	2.4	2.5	2.4	2.5	2.6	

nd: not detected

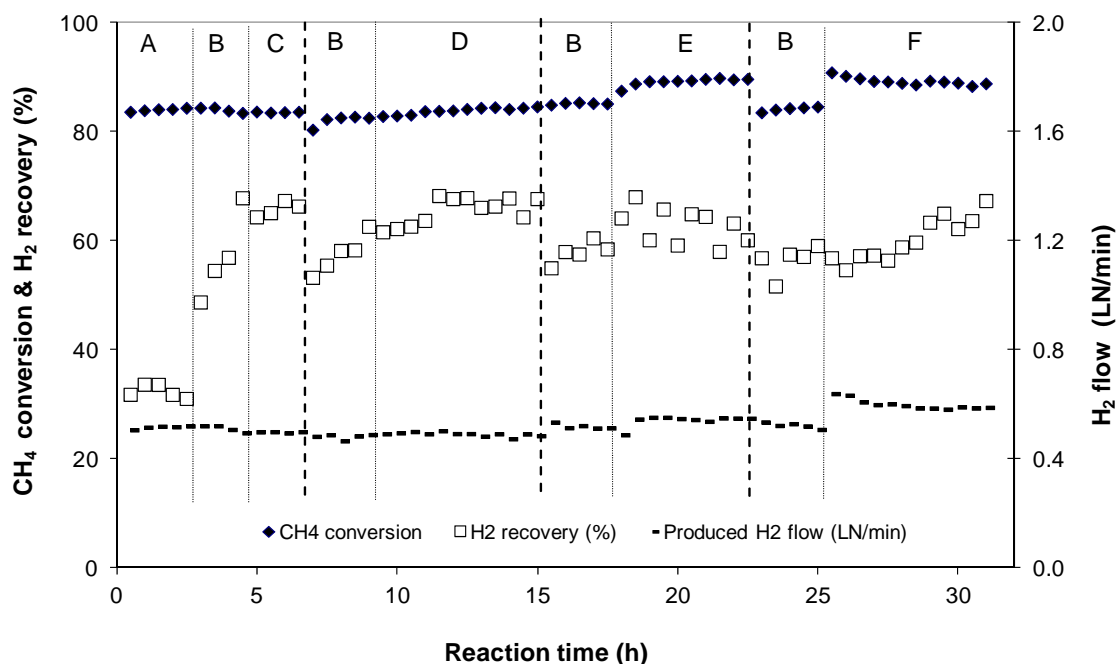


Figure 6.13. Performance of the CPO-membrane system. R1 at 1073 K with 0.35 g of catalyst and 600 h<sup>-1</sup> of WHSV, membrane module with M6 (membrane area of 58.9 cm<sup>2</sup>) at 673 K with a 20 % of sweep gas, feed pressure=3.5 bar(g) and sweep gas at atmospheric pressure.

The variation in the mixture composition fed to the membrane module had no significant negative effect on membrane performance, as the hydrogen recovery was around 60 % during all the testing time at 673 K. Two of the compounds may have an impact on membrane performance: carbon monoxide and water. Carbon monoxide is known to have a major inhibiting effect. When operating under B conditions, CPO without water, hydrogen recovery seemed to be lower than under wet-CPO conditions (C, D, E or F segments). The lowest carbon monoxide concentration, 14 %, was produced under F conditions with the highest S/C ratio. The good performance of the system under F conditions compared to the others, taking into account the decreasing CO percentage, showed that the positive effect of water probably overrules the expected negative effect of carbon monoxide on the membrane performance. Between 60 and 70 % of the hydrogen produced in the first reactor was recovered by the membrane, regardless of operating conditions and mixture compositions.

The hydrogen recovery of the M6 membrane in a H<sub>2</sub>:N<sub>2</sub> mixture, with 25 % hydrogen and 550 mL/min of sweep gas flow, was around 80 %. Therefore, hydrogen recovery

decreased to 60-70 % due to operation under complex mixture conditions, so there was a reduction by 10 to 20 percentage points. Similar data have been obtained in the literature. A reduction of 20 percentage points of hydrogen recovery is reported by Li et al. [12] when operating a Pd membrane in a simulated WGS mixture at 673 K. It has been observed that membrane permeance can decrease when operating with carbon monoxide due to coke formation at low water/carbon monoxide ratios, as used in this work [13, 14]. Cheng et al. [15] observed a rapid decrease in hydrogen recovery after 12 h operation of a Pd membrane installed in a methane CPO reactor, due to coke formation from carbon monoxide at 773 K. Whereas in other works when operating in a simulated gas mixture with water/carbon monoxide ratios 3 and 19, carbon monoxide had no significantly negative effect at 573 K, permeance decreased by 8 % and remained constant during further operation [16]. High temperature, 673 K, and water addition seemed to be the reasons for not observing coke in the tests with M6.

Complex mixture tests were also performed with the M8 membrane. Catalyst activity and hydrogen recovery results are shown in Figure 6.14. Table 6.6 summarizes the average compound percentages obtained in the different hydrogen producing processes performed in the R1. As it can be observed in the table, the hydrogen percentage in the mixture increased when adding water, due to additional reforming reactions. As a consequence of the process modification adding water, the selectivity of the catalytic process in R1 varied, decreasing the percentage of CO in the outflow mixture.

Table 6.6. Average percentages of the outflow of the catalytic reactor and fed to the membrane module at different operating conditions.

S/C	CPO	Wet-CPO				
		0.5	1.0	1.5	2.0	2.5
CO (mol%)	15.5	13.6	11.9	10.8	8.9	8.3
H <sub>2</sub> (mol%)	27.4	27.5	28.1	31.2	34.1	32.0
CH <sub>4</sub> (mol%)	5.3	4.4	3.1	1.3	2.8	2.0
CO <sub>2</sub> (mol%)	1.6	2.8	3.6	4.2	6.0	5.8
O <sub>2</sub> (mol%)	nd	nd	nd	nd	nd	nd

nd: not detected

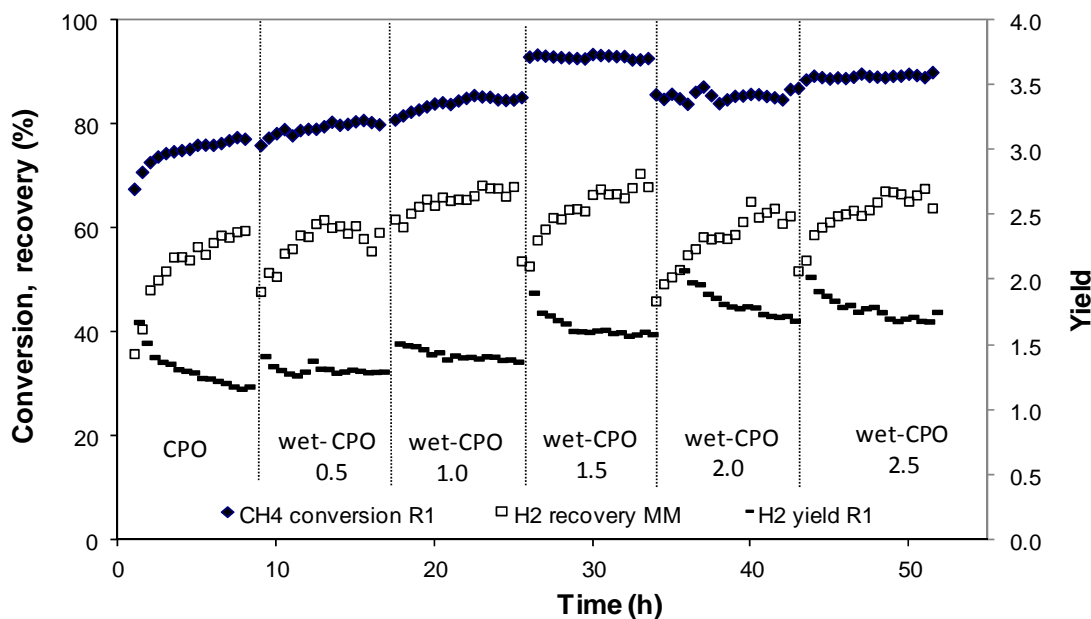


Figure 6.14. Hydrogen production in the catalytic reactor R1 at 1073 K with 0.35 g of catalyst and  $600 \text{ h}^{-1}$  of WHSV and purification with M8 (membrane area of  $33.0 \text{ cm}^2$ ) at 773 K in the MM with a 20 % of sweep gas at 3.5 bar of pressure difference.

The obtained conversion in CPO was lower than the one obtained in Chapter 4 in the PP, which can be due to the negative thermodynamic effect of increasing pressure. On the other hand, the higher pressure seemed to benefit the wet-CPO process. At the same temperature with the same amount of methane moles, a higher pressure in the reactor implies higher concentration of reactants that favours the kinetics. As the conversion is far from the equilibrium conversion (around 95 % shown in Figure 4.5) the process is limited by the kinetics with some influence of the internal diffusion. When pressure is increased to 3.5 bar(g), the concentration increase improves the reaction rate and offsets the slightly negative thermodynamic effect of increasing operating pressure. At each operating conditions conversion tended to increase, whereas hydrogen yield decreased, indicating that the hydrogen selectivity had declined.

The process in the MM required quite a long time to stabilize. Each condition was tested during one working day. The membrane module was kept at 773 K during night, but under inert atmosphere. At the beginning of the process the membrane permeability increased and by the end of the day it started to stabilize, which could be due to a reactivation in presence of hydrogen during the test. Once it was near to the steady state,

hydrogen recovery was around 60, 60, 67, 67, 63 and 67 %, respectively, at each operating condition. Water addition increased the hydrogen production, increasing the hydrogen mole fraction in the feed to the membrane, which can explain the slightly increasing tendency of the hydrogen recovery in the MM. The CO percentage did not seem to damage the membrane, and neither the rest of the gases such as steam, CO<sub>2</sub> or CH<sub>4</sub>. The obtained hydrogen recovery was around 60-67 %, regardless the operating conditions and the mixture composition during more than 50 hours. As observed before in the similar test performed with the M6 membrane, the positive effect of water could have overruled the expected negative effect of carbon monoxide

As a conclusion from the hydrogen purification tests carried out in the membrane pilot plant with complex mixtures, it can be said that between the 60 and 70 % of the hydrogen produced in R1 was purified in the membrane module, regardless the used operating conditions and mixture composition. This value is close to the 70 % obtained in a membrane reactor with methane reforming by Basile et al. [17]. As adsorption on the membrane surface decreases at high temperatures, 773 K could have been a high enough temperature to avoid inhibitive adsorption to occur. The combination of CO concentration decrease and water concentration increase seemed to have a positive effect on hydrogen recovery, together with the fact that at higher S/C ratio the hydrogen percentage in the mixture was higher.

#### 6.4 Membrane lifetime during pure H<sub>2</sub> and complex mixture tests

In this section an overview of the lifetime of the three tested membranes (M6, M7 and M8) with H<sub>2</sub> or complex mixtures is given. All the permeance measurements shown in the figures of this section were carried out with pure hydrogen or pure nitrogen at a feed pressure of 2 bar(g), with atmospheric pressure in the permeate side and at temperatures of 673 or 773 K. In the upper side of the figures the prevalent operating conditions during each period are shown. In order to check the membrane performance pure nitrogen or pure hydrogen permeation measurements were performed during their time on stream. Segments where “inert” appears mean that the membrane was kept under Ar or N<sub>2</sub> atmosphere. “Air” description means that the membrane module was taken out from the system and, therefore, exposed to atmospheric air. During the time where



“mixture” appears, hydrogen purification from complex mixture tests were performed and during nights membranes were kept under inert gas at elevated temperature.

Figure 6.15 summarizes the main tests performed with the M6 membrane and the hydrogen and nitrogen flows measured through the membrane during its lifetime in pure H<sub>2</sub> or N<sub>2</sub>. The selectivity of the membrane varied throughout its lifetime from 1500 to 250 at 773 K, but in all cases the nitrogen flow through the membrane was low compared to the hydrogen flow. The difference between hydrogen flow at 100 h and 650 h is because of the temperature increase from 673 to 773 K. The hydrogen permeance through the membrane, measured in pure hydrogen, decreased over time from around  $1.3 \cdot 10^{-3}$  to  $4.5 \cdot 10^{-4}$  mol/sm<sup>2</sup>Pa<sup>0.5</sup> at 673 K, measured at 75 h and 2700 h, respectively. From 900 h to 1800 h and from 3300 h on, the membrane was kept in air at 298 K.

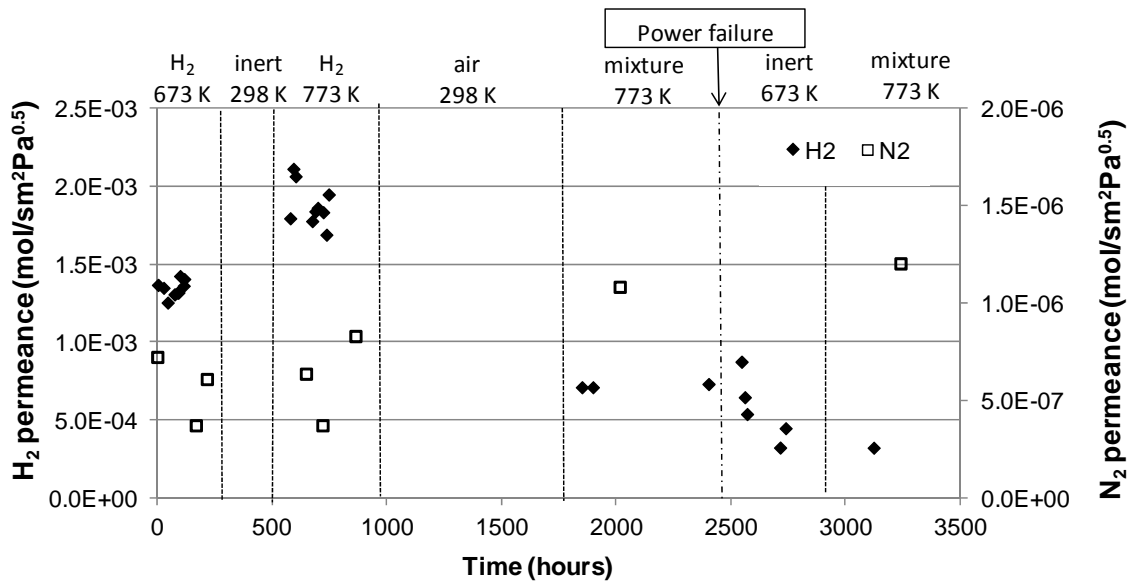


Figure 6.15. Pure hydrogen and nitrogen permeance throughout the M6 lifetime (feed pressure=2 bar(g) and sweep gas at atmospheric pressure).

The first hydrogen permeance shown in the “mixture 773 K” segment, after 1850 h, is from the day before the mixture tests were started. The lower hydrogen permeance at 1850 h might be due to the storage in air. Earlier tests showed that it takes at least 150 hours in hydrogen atmosphere to achieve a stable hydrogen flow through the membrane after its storage in air. During the period when the membrane was operated under complex mixtures, the hydrogen permeance was stable at around  $7.2 \cdot 10^{-4}$  mol/sm<sup>2</sup>Pa<sup>0.5</sup>.

At around 2450 h, there was a power failure in the system, and the membrane cooled without control from 773 K to room temperature in H<sub>2</sub> containing atmosphere. Up to this moment, the permeance had been slowly increasing during the mixture tests, from  $7.1 \cdot 10^{-4}$  to  $7.3 \cdot 10^{-4}$  mol/sm<sup>2</sup>Pa<sup>0.5</sup>. However, after the power failure the hydrogen permeance decreased to values of around  $3.2 \cdot 10^{-4}$  mol/sm<sup>2</sup>Pa<sup>0.5</sup>. At 3200 h, the membrane was cooled to 298 K in inert gas at 1 K/min. It was re-heated to 673 K at 3600 h to continue the tests, but it was not selective any more, 1.2 NL/min of nitrogen passed through the membrane with a pressure difference of 2 bar. The membrane was removed from the module, and it was observed that the metal layer of the membrane had peeled off, as Figure 6.16 shows.



Figure 6.16. M6 membrane peeling off detected at 3600 h.

The analysis of the hydrogen and nitrogen flow values throughout the entire lifetime of the M6 membrane leads to several conclusions. The nitrogen flow did not increase significantly during the lifetime of the membrane, so this flow can be most probably due to a leak in the ceramic-metal sealing or to membrane defects that remained unchanged. However, the hydrogen flow decreased during its lifetime. When calculating membrane permselectivity from the data given in Figure 6.15, a variation from 1500 to 250 was observed. This selectivity decrease was not due to pore formation in the metallic layer but to a decrease in hydrogen diffusion through the membrane. Therefore, it can be concluded that membrane deterioration was not caused by open pore formation but by a change in the metal structure that entailed a worsening of its hydrogen bulk diffusion capacity, which can be caused by aging or slow poisoning of the membrane.

The power failure occurred in the system at 2424 h and the subsequently uncontrolled cooling in hydrogen atmosphere had a negative effect on the hydrogen flow through the membrane. Figure 5.13 and Figure 5.14 showed that controlled cooling in hydrogen

atmosphere did not affect the membrane permeance. Thermal cycling of the hydrogenated metallic layer has been observed in the literature to produce membrane failure, characterized by crack formation and metal film peeling [18], like observed with the M6 membrane. In the case of the M6 membrane, controlled cooling or heating did not seem to compromise membrane performance, whereas the same thermal cycle without controlling the rate had an irreversibly negative effect. Nonetheless, further investigation by longer thermal cycling tests should be conducted to determine if uncontrolled cooling in hydrogen is the reason for membrane failure.

The detached M6 membrane metal layer was analysed using XRD and SEM techniques. The outer surface of the metal layer had deep grain boundaries, see Figure 6.17, not observed before (in Chapter 5). The oxygen observed on the membrane surface of the membranes alloyed in the third batch, Figure 5.16 and Table 5.11, could have had a negative influence causing a morphological change in the metallic layer. Grain boundaries and rough areas are weak places where leakage and finally detachment of the membrane film can occur. As concluded from the M6 lifetime figure with hydrogen and nitrogen flows, open pores were not created in the metal layer, as the N<sub>2</sub> flow did not increase.

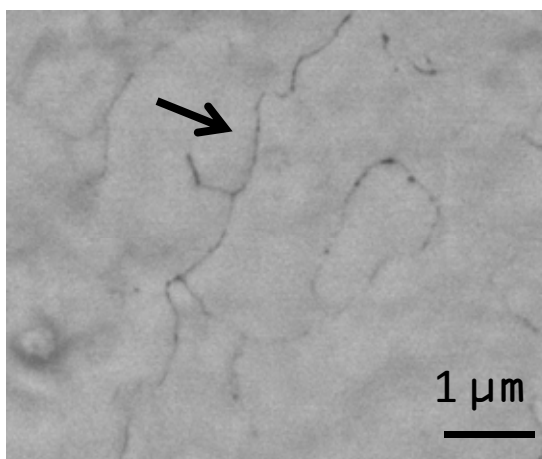


Figure 6.17. SEM image of the detached M6 metal layer, x18000 magnification.

The metal foil that peeled off had many ceramic particles on the support side, indicating numerous stresses at the interface. This pattern occurs normally after cooling in a hydrogen-filled membrane system, which was the case with the M6 membrane when the power failure occurred during operation. Deep grain boundaries, but no open pores,

were most probably created due to stress (thermal or chemical) until the metal foil peeled off and the membrane failed completely.

The composition of the metal layer was analysed with SEM-EDX to check whether coke formation had occurred when working under mixture, which could lead to metallic phase deactivation [19]. Only Pd (89.6 wt%) and Cu were observed in the metal layer surface. The stable permeance observed in Figure 6.13 corroborates that the metallic layer was not deactivated during operation in complex mixtures due to carbon deposition.

The peeled off M6 membrane was analysed with XRD in order to have deeper knowledge of the metal layer. Figure 6.18 shows the diffractogram of M6 membrane sample, in dark line. As a reference, the diffractogram of a membrane prepared and alloyed in the same way as M6 is given in red. The metal layer has fcc structure as expected from the composition and explained in the previous chapter. In the diffractogram of the reference sample there are some peaks that do not appear in the M6 diffractogram at 35, 38, 43, 58 and 67 angles that correspond to the  $\text{Al}_2\text{O}_3$  from the support. In the M6 diffractogram, peaks associated to a crystalline structure between pure Pd and PdCu are observed, suggesting the PdCu solid solution formation. This means that the copper atoms are placed in the Pd net, displacing slightly the peaks to higher angles. In the literature it has also been observed that before alloying separate Pd and Cu maximums appear in the diffractogram [20-22]. Whereas, after the alloying all the characteristic peaks of Pd were in the same position for both Pd and PdCu [23, 24]. This shows the formation of PdCu interstitial alloys, which occurs when the atoms of one component are smaller than the other and the smallest atoms fit into the spaces between the largest atoms [25].

Hydrogen and nitrogen flows across the M7 membrane measured with 2 bar of pressure difference throughout its lifetime can be observed in Figure 6.19. The main events that occurred during M7 lifetime have been summarized in Table 6.7. The pure hydrogen flow between 0 and 240 h was measured at 663 K and all the rest at 773 K. As it can be observed in the table, there were some problems in the system at 750, 1130 and 1415 h. In the first one, system failure, the membrane cooled at 1 K/min but in hydrogen atmosphere. In the two power failures the membrane cooled with no temperature control

but in inert atmosphere. In the one at day 1130 it cooled to 298 K and in the last one, day 1415, to 693 K.

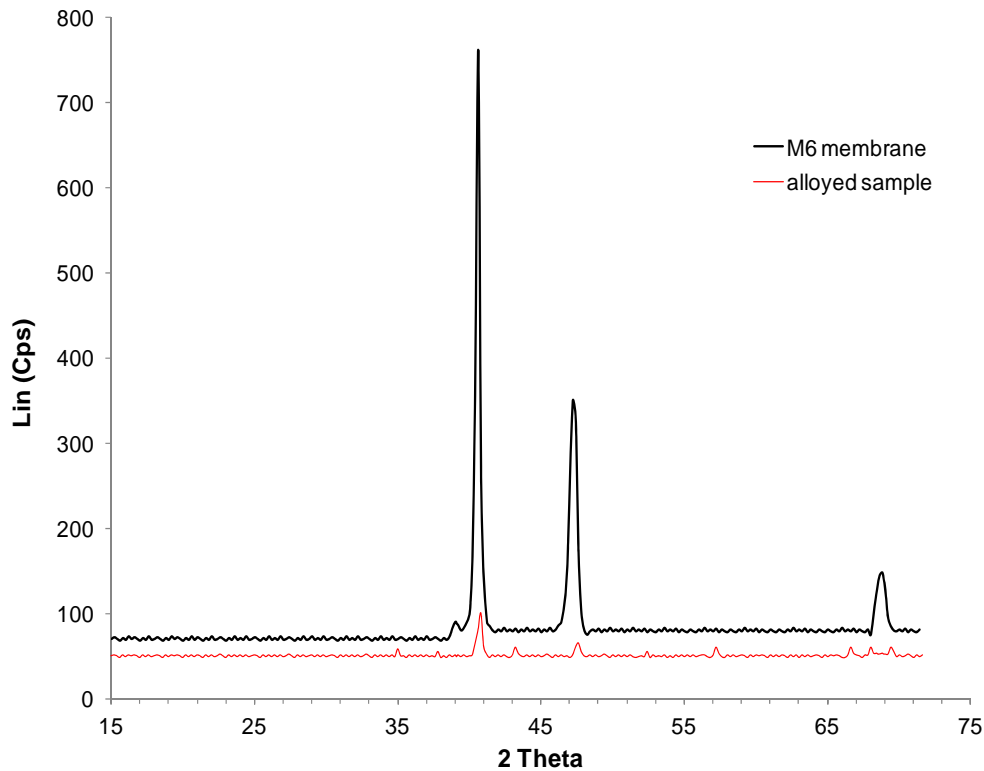


Figure 6.18. XRD diffractogram of the used M6 membrane.

Table 6.7. Lifetime summary of the M7 membrane.

Time (h)	
0 – 240	Hydrogen permeance measurements with thermal cycle at 673 K, Figure 5.12
241-410	Hydrogen permeance measurements with thermal cycle at 773 K, Figure 5.13
600-745	Hydrogen recovery Vs sweep gas flow tests at 773 K, Figure 6.10
750	System failure. Controlled cooling to 298 K
792-1050	Hydrogen recovery Vs sweep gas flow tests at 773 K, Figure 6.11
1130	Power failure. Uncontrolled cooling to 298 K
1415	Power failure. Uncontrolled cooling to 693 K

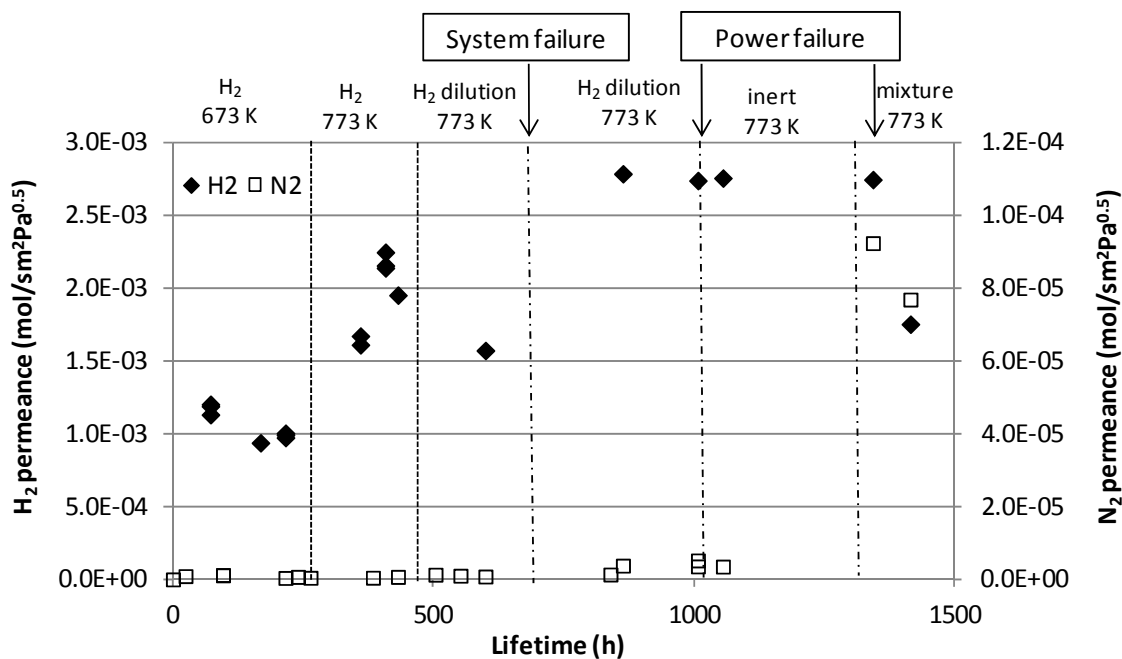


Figure 6.19. Pure hydrogen and nitrogen permeance throughout M7 membrane lifetime measured with 2 bar of pressure difference.

The consequence of the system and power failures can be observed in the measured hydrogen and nitrogen flows. After the system failure, at 750 h, the hydrogen permeance increased substantially and there was a small increase in the nitrogen permeance. After the first power failure with uncontrolled cooling, at 1130 h, the nitrogen permeance increased drastically, indicating the formation of open pores in the metal layer and implying the end of the membrane operating lifetime. The second power failure had a different effect on the membrane as nitrogen permeance remained constant and hydrogen permeance halved. This indicates that this last power failure affected the hydrogen diffusion process and not the metallic layer morphology. At around 1440 h, the membrane was found to be not selective any more, most of the flow that entered the MM was detected in the permeate side.

Figure 6.20 shows a picture of the broken M7 membrane when it was taken out of the membrane module, with a thermal stress characteristic breakage. The membrane surface morphology was analysed with SEM images in the close cap area, where metal detachment was observed, and in the open cap area as shown in Figure 6.21. Comparing these images with the ones obtained with membranes after alloying, Table 5.10, a much rougher area is observed. Uncontrolled cooling together with the possible negative

effect of oxygen during alloying on the metal morphology could have enhanced defect formation along the grain boundaries of the membrane [26]. All this could have been the reasons for the membrane failure.



Figure 6.20. Picture of the detached metal layer in the close cap area of the used M7 membrane.

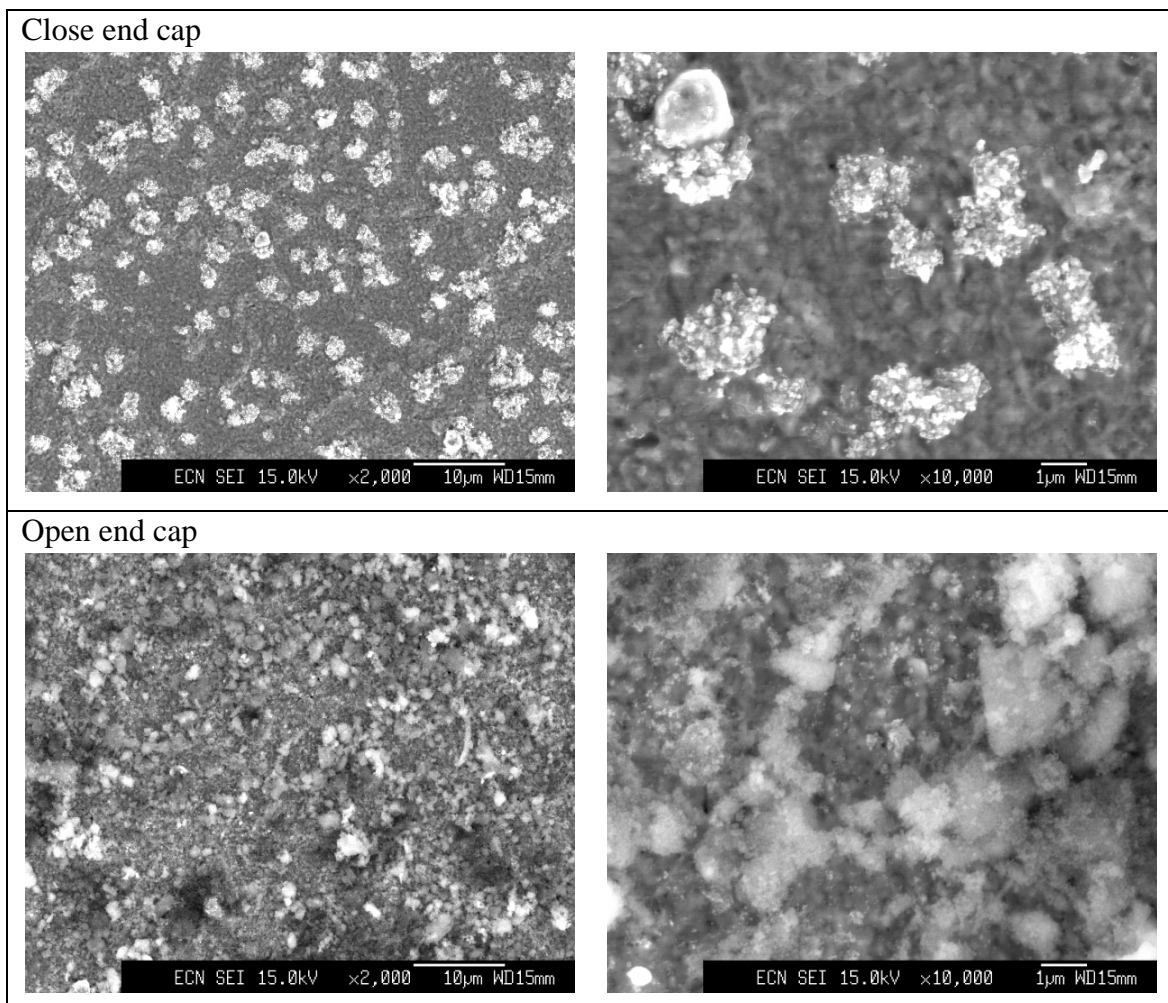


Figure 6.21. SEM images of both end caps of the M7 membrane at x2.000 and x10.000 enlargements.

Comparing the peeling off occurred in the M6 and in the M7 membranes there were some differences. In the M6 membrane it seemed that there was a unique point from which the metal layer broke. As explained in the M6 lifetime summary, no open pores occurred and the metal layer was most probably peeled off due to stress. On the other hand, during the M7 membrane lifetime pore formation was observed as the nitrogen flow increased. When looking at the broken M7 membrane it was observed that there were many places where the metal layer had been peeled off. This might indicate that the surface had become rougher, enhancing open pores formation that continue opening until the metal layer peeled off from the ceramic support. The difference in thickness can be the reason for pore formation in M7 (0.7  $\mu\text{m}$ ) and not in M6 (1.7  $\mu\text{m}$ ).

The hydrogen and nitrogen flows measured along the lifetime of the M8 membrane with  $\text{H}_2:\text{N}_2$  and complex mixture tests are shown in Figure 6.22. The main tests performed during this period are summarized in Table 6.8. During the first 210 h hydrogen and nitrogen flows were measured at 663 K and the rest of the time the membrane operated at 773 K. Throughout the M8 membrane lifetime there were no power failures, although variations in the membrane performance were observed. After the hydrogen permeance test in pure hydrogen at 773 K at time 430 h, shown in Figure 5.11, the membrane was kept in inert gas for more than 10 days, but the hydrogen permeance decreased and the leak flow increased during this time. In the period where the membrane was tested purifying the hydrogen from the mixture produced in the catalytic reactor, the hydrogen flow and leaks were quite stable. As it was concluded from hydrogen recovery test in the complex gas mixtures performed with the M8 membrane, Figure 6.14, the mixture components did not have a severe influence on the membrane performance. The M8 membrane was then tested with  $\text{H}_2\text{S}$  addition. These results and its complete lifetime are presented in the following sections.



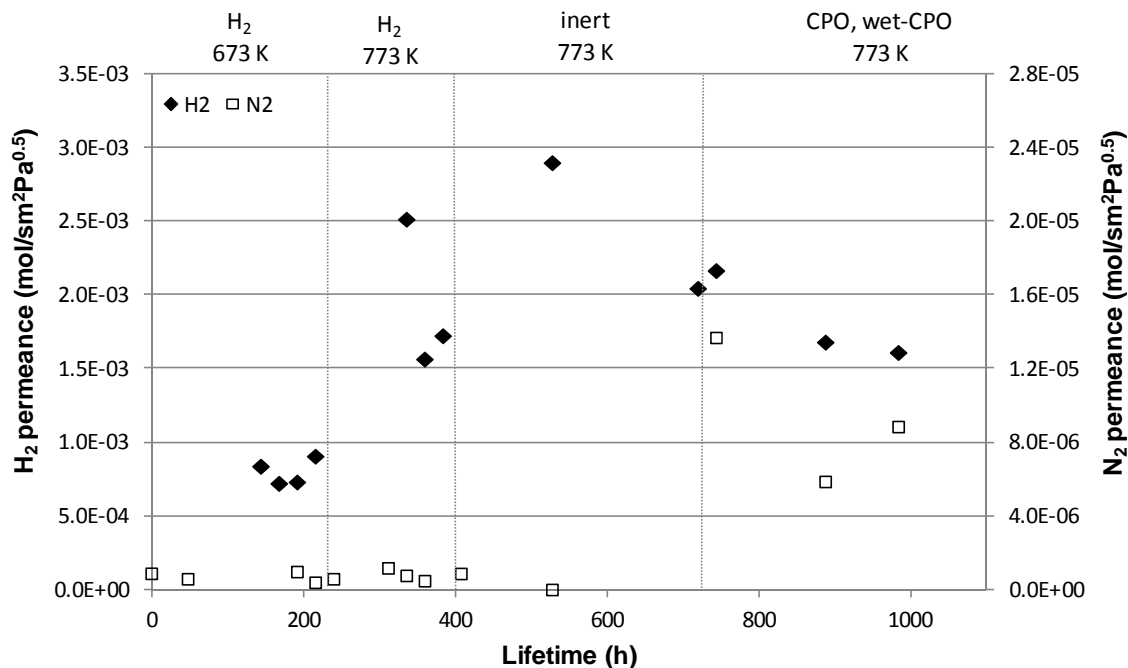


Figure 6.22. Pure hydrogen and nitrogen permeance throughout M8 membrane lifetime (feed pressure=2 bar(g) and sweep at atmospheric pressure).

Table 6.8. Lifetime summary of the M8 membrane.

Time (h)	
0 – 210	Hydrogen permeance measurements with thermal cycle at 673 K, Figure 5.12
310-400	Hydrogen permeance measurements with thermal cycle at 773 K, Figure 5.13
430-745	In inert atmosphere at 773 K
770-1030	Hydrogen production plus purification tests at 773 K, Figure 6.13

After analysing the effect that the performed tests had on the three membranes it can be concluded that uncontrolled cooling has a strong effect on membrane lifetime. After one and two power failures the M6 and M7 membranes, respectively, broke. Different effects of the stress suffered by the metallic layer due to the uncontrolled cooling were observed in the measured nitrogen and hydrogen flows. The M7 membrane started to fail with the formation of open structures in the metallic layer, increasing notably the membrane leakage. In addition a hydrogen flow decrease was observed, indicating that the hydrogen diffusion through the metallic layer had been affected (M6 and M7). Thermal stresses produce structure modification that could involve cone structure formation, enhanced by the oxygen detected during alloying, with higher surface and higher permeance. But further stress produced open pores and nitrogen flow increase

(M6). In the M7 membrane, the thermal stress produced structural changes that reduced the hydrogen diffusion through the membrane and finally, produced metal layer detachment. The metal layer detachment of the two membranes was different. In the one where conically shaped structures seemed to explain its performance, M7 membrane, detachment started in more than one site of the membrane. Whereas in the M6, where this effect was not observed, there was just one point where the detachment started.

Regarding the PdCu metal alloy, it was corroborated by XRD that membrane M6 had a fcc structure, and it was observed that the PdCu alloy was formed by a Pd crystalline net where the Cu atoms were located.

## 6.5 Membrane performance with H<sub>2</sub>S addition

In the previous sections the optimum operating parameters and the effect that cooling and complex mixtures have on the membrane performance have been analysed. Two of the membranes tested with complex mixtures (M6 and M7) failed as explained before, most probably due to thermal stresses. The third membrane, M8, was tested with H<sub>2</sub>S addition, as usually together with the methane some ppm of sulphur compounds are part of the natural gas. In this section the H<sub>2</sub>S addition effect, up to 100 ppmv, on the performance of membrane M8 is explained.

### 6.5.1 H<sub>2</sub>S and H<sub>2</sub> mixture (I)

In order to study the effect of H<sub>2</sub>S impurities on membrane performance, the hydrogen permeance was sequentially measured in H<sub>2</sub>+H<sub>2</sub>S atmospheres with H<sub>2</sub>S concentrations of 100 and 40 ppmv and in pure hydrogen at 773 K. With these cycles it was possible to analyse if the permeance was recovered when taking out the H<sub>2</sub>S from the system.

In the tests performed with H<sub>2</sub>:H<sub>2</sub>S mixtures the final area of the membrane was exposed to higher H<sub>2</sub>S concentration than the initial area, as a part of the H<sub>2</sub> diffused through the membrane. The maximum H<sub>2</sub>S concentration in the membrane module can be calculated from the H<sub>2</sub>S flow fed to the module and the measured total retentate flow. In order to obtain the desired H<sub>2</sub>S concentration and operate at 2 bar of pressure difference, the amount of H<sub>2</sub>S:H<sub>2</sub> from the standard bottle varied from one test to

another. This influenced the total amount of H<sub>2</sub>S gas fed to the module and therefore, the maximum H<sub>2</sub>S concentration achieved in the module.

Figure 6.23 shows the permeance inhibition caused by the addition of the sulphur compound to the stream. The membrane permeance decreased by approximately 80 %, but it was not a permanent poisoning, as it was recovered under H<sub>2</sub> atmosphere at 773 K. The permeance inhibition observed due to the presence of H<sub>2</sub>S was nearly identical with 40 ppmv and 100 ppmv H<sub>2</sub>S in H<sub>2</sub>:H<sub>2</sub>S mixtures. The measured hydrogen flow through the membrane with 40 ppmv of H<sub>2</sub>S was slightly higher than with 100 ppmv, 25 % of the value in pure hydrogen, and the permeance increased slowly with time. When taking out the H<sub>2</sub>S from the system the permeance recovered up to the level measured before the H<sub>2</sub>S addition. The membrane selectivity changed throughout the test. Nitrogen flow across the membrane varied from around 10 NmL/min in the first measurement to 60 NmL/min after the test with 100 ppmv of H<sub>2</sub>S. The test with 40 ppmv of H<sub>2</sub>S did not further increase the nitrogen flow across the membrane. During the test where the fed H<sub>2</sub>S concentration was 100 ppmv, the maximum H<sub>2</sub>S concentration in the module was 140 ppmv, and during the time with 40 ppmv it was also 140 ppmv.

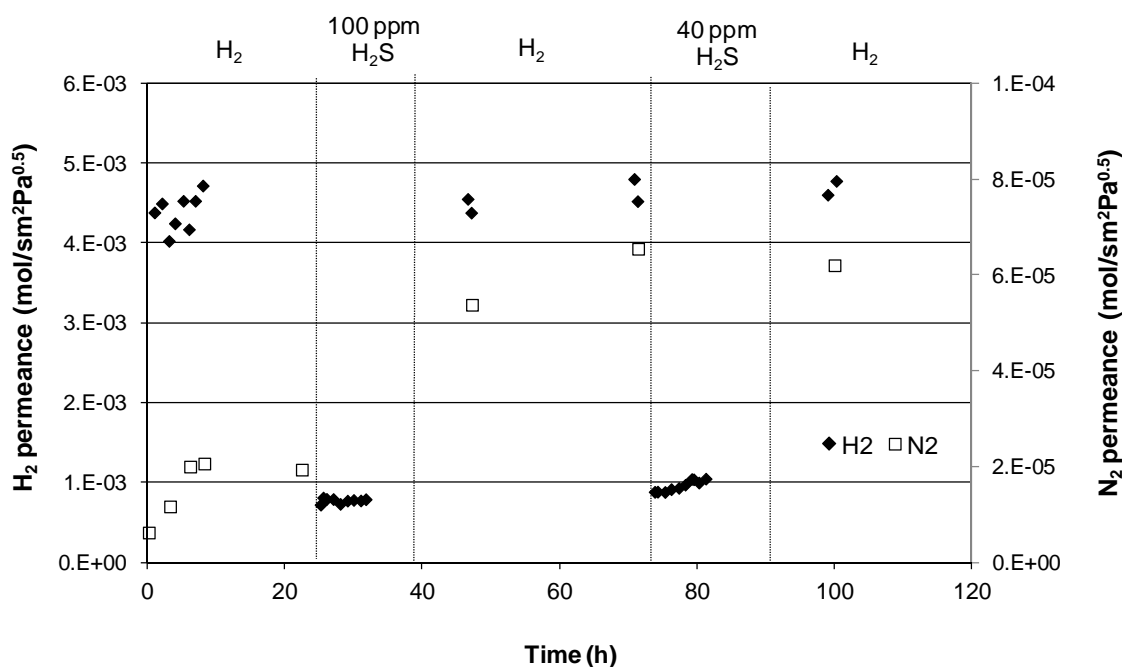


Figure 6.23. Hydrogen and nitrogen permeance through the M8 membrane in 100 and 40 ppmv H<sub>2</sub>S/H<sub>2</sub> mixtures and in pure H<sub>2</sub> at 773 K (feed pressure=2 bar(g) and sweep at atmospheric pressure).

The decrease of the hydrogen permeance could be attributed to H<sub>2</sub>S adsorption on the metallic surface. It seems that only reversible site blocking, with no irreversible bulk sulphidation, occurred under the testing conditions, as the permeance was recovered when removing H<sub>2</sub>S. The H<sub>2</sub>S/H<sub>2</sub> ratio fed to the MM in the test was lower than the threshold ratio required to form thermodynamically stable sulphides (molar ratio H<sub>2</sub>S/H<sub>2</sub>=0.0011) [27]. The high temperature employed in the test, 773 K, could have enhanced reversible sulphur adsorption [28].

The metallic PdCu surface was damaged by the H<sub>2</sub>S as nitrogen flow increased during the test. Coulter et al. [29] observed a slight decrease in the selectivity with a 33.2 μm PdAu membrane operating at 673 K in a mixture with 20 ppmv of H<sub>2</sub>S (50 % H<sub>2</sub>, 1 % CO, 30 % CO<sub>2</sub>, 19 % H<sub>2</sub>O). They observed a slight decrease of selectivity over time, and after 90 h it rapidly decreased, which was explained with pore formation.

Sulphur atoms could have attacked weak areas, possibly grain boundaries, creating open pores. The quick negative effect on selectivity of H<sub>2</sub>S could have been accelerated by the fact that the metallic layer was very thin (0.9 μm) as compared to the previously explained 33.2 μm PdAu membrane from Coulter et al. [29]. But sulphur-adsorbing sites are almost saturated at 40 ppmv, as the hydrogen permeance was almost the same with 40 and with 100 ppmv. The permselectivity of the membrane when this first analysis with H<sub>2</sub>S addition was finished was low, 70.

### 6.5.2 CPO process with H<sub>2</sub>S addition

H<sub>2</sub>S addition effect on membrane permeability was also analysed when operating under complex hydrogen containing mixtures produced in R1. Hydrogen production via CPO was performed in R1 with 0.35 g of 40Ni/MgO catalyst at 600 h<sup>-1</sup> and 1073 K. The membrane module operated at 773 K with the M8 membrane at a pressure difference of 3.5 bar and with a sweep gas flow of 0.7 LN/min (23 % of the outflow from the catalytic reactor). The sweep side pressure was atmospheric, and the hydrogen recovery was calculated based on the permeate mole fraction and flow rate.

The results are given in Figure 6.24. During the first hours the process operated without sulphur. After 3.5 h, 32 ppmv of H<sub>2</sub>S were added to the system and the conditions were

maintained constant during six hours. The catalyst activity in R1 seemed to be not affected by H<sub>2</sub>S addition at this concentration and during the testing time, as CH<sub>4</sub> conversion and H<sub>2</sub> yield were stable. This was a good result as Ni-based catalysts are usually deactivated in the presence of sulphur compounds [30]. The complex mixture produced in R1 and fed to the MM contained an average of 12.4 % CO, 1.3 % CO<sub>2</sub>, 21.2 % H<sub>2</sub>, 4.4 % CH<sub>4</sub> and 59.1 % Ar. Taking into account the fed H<sub>2</sub>S flow and the retentate outflow, the maximum H<sub>2</sub>S concentration achieved in the module was 42 ppmv. In this test the maximum concentration was similar to the fed one as it was diluted with gases that did not diffuse through the metal layer.

When H<sub>2</sub>S was added to the system, hydrogen recovery in the membrane dropped drastically from 80 % (without H<sub>2</sub>S) to 40 % (with 32 ppmv of H<sub>2</sub>S) and then it slightly increased in time to 50 %. This hydrogen recovery was lower than the one observed in complex mixtures without H<sub>2</sub>S addition, 60-65 %. On the other hand, in the H<sub>2</sub>:H<sub>2</sub>S mixture test with 40 ppmv of H<sub>2</sub>S the hydrogen flow across the membrane decreased by 75 %, much more than the 30 % observed in the mixture+H<sub>2</sub>S test comparing the permeability without and with H<sub>2</sub>S. Membrane deactivation was not more pronounced due to the simultaneous presence of complex mixture and H<sub>2</sub>S in the stream.

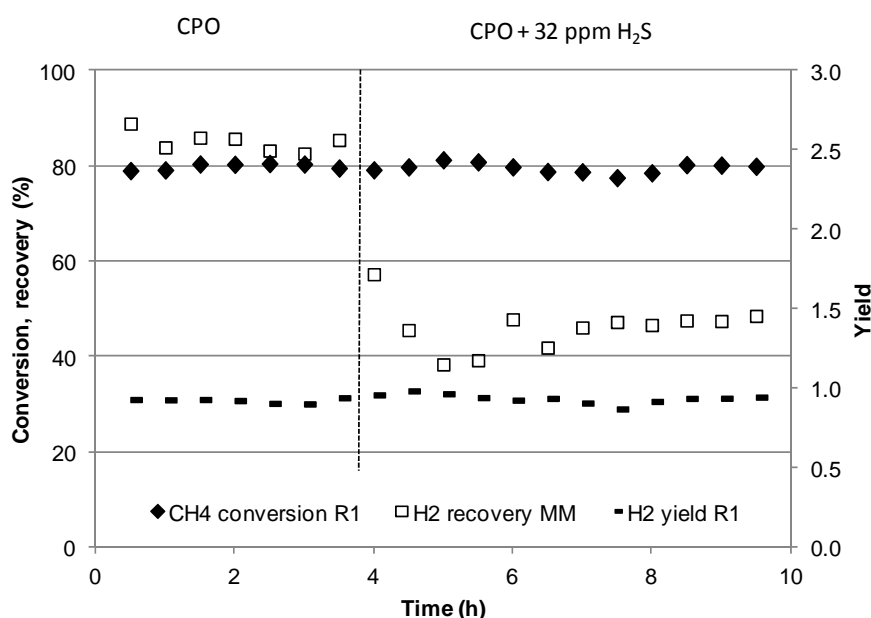


Figure 6.24. H<sub>2</sub>S addition effect on hydrogen production in R1 via CPO with 40Ni/MgO at 600 h<sup>-1</sup> (1073 K) and purification in MM with M8 (773 K) at 3.5 bar of pressure difference.

When this mixture+H<sub>2</sub>S test was finished, the nitrogen flow through the membrane at 2 bar pressure difference was measured and it was 200 NmL/min. Before this test the recorded leakage was around 60 NmL/min. The leakage increase meant that open structures continued to be forming in the metallic layer. Most probably sulphur atoms continued attacking the grain or pores boundaries forming more or bigger pores.

### 6.5.3 Permeance recovery test (I)

After the tests performed with H<sub>2</sub>+H<sub>2</sub>S and complex mixtures with H<sub>2</sub>S, the membrane leakage was very high. In order to try to decrease it, the membrane was maintained in H<sub>2</sub> atmosphere for some days. Firstly, the membrane was kept at 773 K and then, the temperature was raised as listed in Figure 6.25. In case there was some adsorbed sulphur on the membrane, desorption was expected at higher temperatures resulting in a permeance increase, since the dissociative adsorption of H<sub>2</sub>S on metals is exothermic. Different effects of the thermal treatment can be observed in this figure. As it was expected from the previous tests with H<sub>2</sub>S+H<sub>2</sub> mixture, H<sub>2</sub>S did not seem to be adsorbed on the metallic surface, as instead of increasing, the hydrogen permeance decreased.

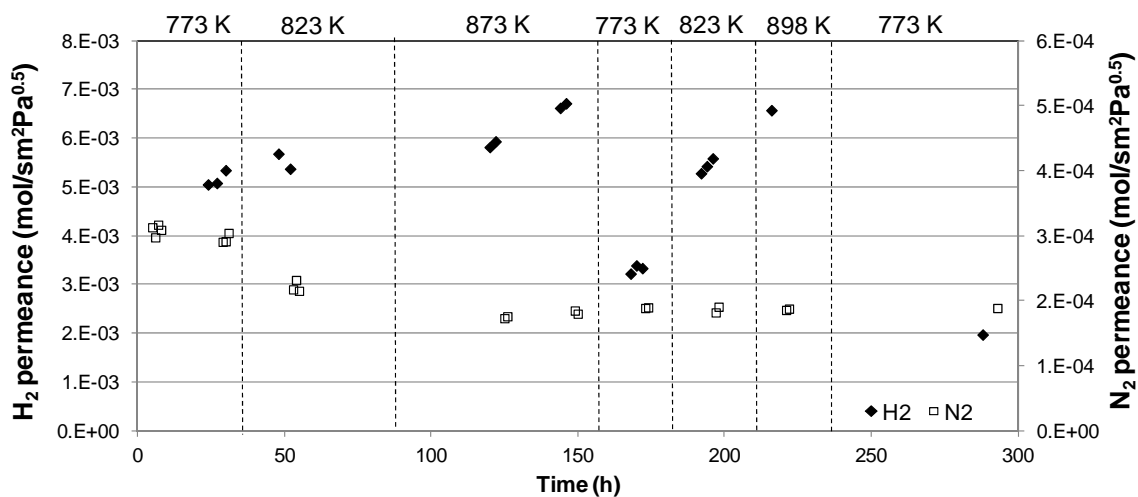


Figure 6.25. First thermal cycle in hydrogen atmosphere attempt with M8 for hydrogen permeability and leakage recovery (feed pressure=2 bar(g) and sweep at atmospheric pressure).

Concerning the nitrogen flow, depending on the size of the created pores nitrogen flow could be Knudsen or viscous flow. When increasing temperature both flows will

decrease, which was observed till 150 h. But the nitrogen flow remained the same level despite further temperature changes, signalling that the structure of the membrane had changed leading to severe reduction of the hydrogen flow. The nitrogen flow through the membrane decreased from 340 to around 200 NmL/min after the thermal cycle.

The employed temperatures seemed to be too high for the membrane. The hydrogen flow through membranes usually increases with temperature. But when checking the hydrogen flow measured at the same temperature and different times a drop is observed. At 773 K it was  $5 \cdot 10^{-3} \text{ mol/m}^2\text{sPa}^{0.5}$  after 27 h and  $2 \cdot 10^{-3} \text{ mol/m}^2\text{sPa}^{0.5}$  after 288 h. This suggests that the membrane structure was seriously damaged. Pores could have been closed due to metal diffusion at the employed high temperatures, which lead to leakage decrease. As the copper melting point is lower than that of Pd, a Cu segregation could have happened closing some pores but passivating a fraction of the membrane surface. At the end of the test, after 290 h, the membrane selectivity was too low, 10. Even then, more sulphur tests were performed with the membrane to further analyse H<sub>2</sub>S effects on the membrane surface.

#### 6.5.4 H<sub>2</sub>S and H<sub>2</sub> mixture (II)

Even though, as explained before, the selectivity of the M8 membrane was too low, some extra sulphur tests were carried out. First of all the H<sub>2</sub> + H<sub>2</sub>S mixture test was performed again. Hydrogen fluxes through the M8 membrane were measured when adding 100 and 60 ppmv of H<sub>2</sub>S alternated with permeance measurements in pure H<sub>2</sub> to establish a baseline.

Hydrogen permeance through the membrane in pure hydrogen atmosphere before performing the current test was  $2 \cdot 10^{-3} \text{ mol/m}^2\text{sPa}^{0.5}$ . Figure 6.26 shows the effect of adding 100 and 60 ppmv of H<sub>2</sub>S in a H<sub>2</sub>:H<sub>2</sub>S mixture. The obtained results were similar to the ones obtained before with 100 and 40 ppmv of H<sub>2</sub>S, Figure 6.23. In this second H<sub>2</sub>:H<sub>2</sub>S test, the hydrogen flow across the membrane also decreased significantly in presence of H<sub>2</sub>S, by 50 %. Comparing these results to those obtained in the 100 and 40 ppmv test, one observes that even if the membrane had been damaged during the thermal treatment, the measured hydrogen permeance was almost the same when H<sub>2</sub>S addition was performed, around  $9.6 \cdot 10^{-3} \text{ mol/m}^2\text{sPa}^{0.5}$ . The membrane permeability was

higher before the first H<sub>2</sub>:H<sub>2</sub>S test than before the second one, so the measured  $9.6 \cdot 10^{-3}$  mol/m<sup>2</sup>·sPa<sup>0.5</sup> represent a reduction by 80 % in the first test and by 50 % in the second one. It seems that hydrogen diffusion through the metal was affected in the same way even if the membrane quality was different, most probably due to a similar surface blocking by sulphur atoms.

The maximum H<sub>2</sub>S concentrations achieved in the membrane when feeding 100 and 60 ppmv of H<sub>2</sub>S were 910 and 160 ppmv, respectively. The high 910 ppmv H<sub>2</sub>S maximum concentration was due to a low flow of H<sub>2</sub>S fed to the module that entailed low total flow in the module and low retentate hydrogen flow.

In this test the hydrogen permeability was also restored to original values after being in pure H<sub>2</sub> at 773 K, so sulphur adsorption was reversible. The selectivity was not affected by the H<sub>2</sub>S, the leak did not increase during the test, even if a fraction of the membrane could have been exposed to H<sub>2</sub>S concentrations as high as 910 ppmv. The nitrogen flow was stable throughout the test, which can imply that H<sub>2</sub>S did not further damage the membrane surface.

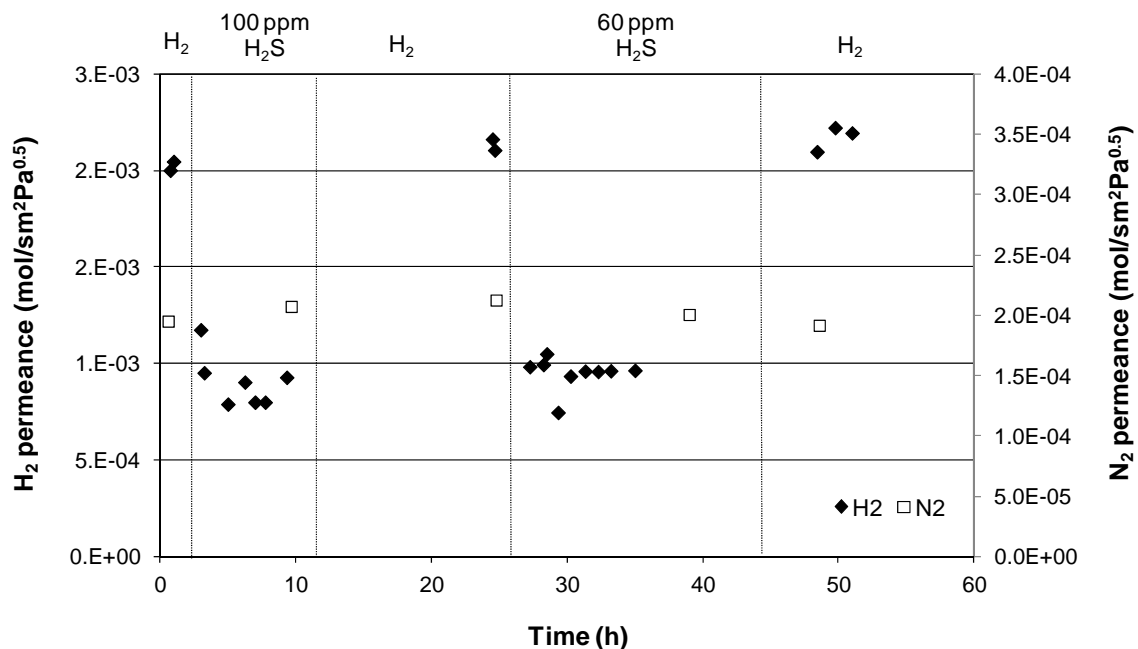


Figure 6.26. Hydrogen and nitrogen flow through the M8 membrane in 100 and 60 ppmv H<sub>2</sub>S/H<sub>2</sub> mixtures and in pure H<sub>2</sub> at 773 K (feed pressure=2 bar(g) and sweep at atmospheric pressure).



### 6.5.5 Wet-CPO process with H<sub>2</sub>S addition

The last test performed with H<sub>2</sub>S addition was hydrogen production by wet-CPO and purification with the addition of some H<sub>2</sub>S. In this test wet-CPO was performed in R1 with 0.35 g of 40Ni/MgO catalyst at 600 h<sup>-1</sup> and 1073 K. The membrane module operated at 773 K with the M8 membrane at a pressure difference of 3.5 bar and with a sweep gas flow of 0.7 LN/min (20 % of the outflow from the catalytic reactor). The sweep side pressure was atmospheric, and the hydrogen recovery was calculated based on the permeate mole fraction and flow rate. From previous results it was concluded that the addition of water improved the hydrogen production when operating with this conditions in the MP. But in this case H<sub>2</sub>S was also added and by mixing water and H<sub>2</sub>S a very corrosive medium for the system and the membrane was created. In order to minimize the corrosion, a low S/C ratio, equal to 0.5, was employed in the hydrogen production by the wet-CPO process.

During the first hours the process operated without H<sub>2</sub>S, see Figure 6.27. During the time without sulphur it can be observed that the hydrogen recovery increased from 60 to 80 %. This result is in accordance with the positive effect of water addition on the membrane performance observed already in the previous chapter. After 4 hours 33 ppmv of H<sub>2</sub>S were added to the system and these conditions were maintained during 5.5 hours. The catalyst activity in R1 was not strongly affected by H<sub>2</sub>S addition as CH<sub>4</sub> conversion and H<sub>2</sub> yield were quite stable, although a slow activity decrease was observed. When H<sub>2</sub>S was added to the system the hydrogen recovery in the MM dropped drastically from 80 % (without H<sub>2</sub>S) to 36 % and then, it slightly increased in time up to around 45 %. In this test the maximum H<sub>2</sub>S concentration achieved in the membrane module was 52 ppmv. Results are again very similar to the ones obtained in sections 6.5.1 (H<sub>2</sub>+H<sub>2</sub>S first test) and 6.5.2 (CPO+H<sub>2</sub>S test). The hydrogen recovery decreased by ca. 50 % when operating with H<sub>2</sub>S addition, similar to the situation observed with 40 and 100 ppmv of H<sub>2</sub>S before.

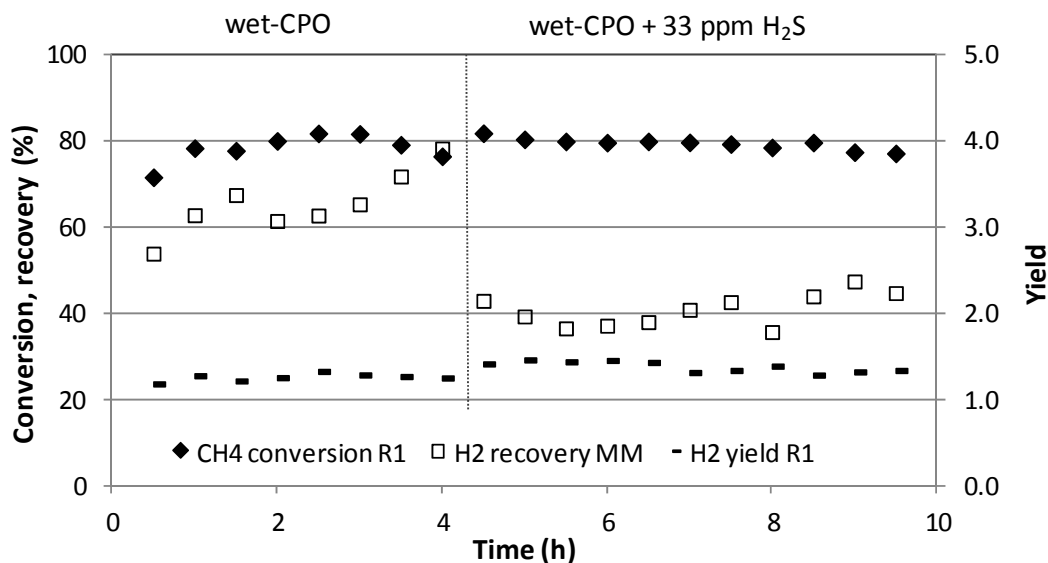


Figure 6.27. H<sub>2</sub>S addition effect on hydrogen production in R1 via wet-CPO with 40Ni/MgO at 600 h<sup>-1</sup> and 1073 K, and on purification in MM with M8 at 773 K and with 3.5 bar of pressure difference.

After performing the wet-CPO+H<sub>2</sub>S test, the nitrogen flow through the membrane was measured with 2 bar pressure difference and it had significantly increased from 200 to 500 NmL/min. Operating under wet-CPO mixture with H<sub>2</sub>S addition was more aggressive to the metallic membrane, probably creating more open pores or cracks in the thin metal layer that could explain the leak increase.

### 6.5.6 Permeance recovery test (II)

A long recovery test in hydrogen atmosphere was performed after the H<sub>2</sub>S addition in the wet-CPO hydrogen production process. By this moment the membrane was seriously damaged, but the aim of the current test was to analyse if permeance or leakage improvements could be achieved with thermal cycling. As depicted in Figure 6.28, the membrane was maintained in hydrogen atmosphere during almost 15 days. The temperature was varied and pure hydrogen and pure nitrogen flows through the membrane were measured at 773, 823 and 873 K. The high temperatures were kept for short time, as it had been observed before that they strongly damage the membrane. During the test no hydrogen permeability improvement was observed. The leakage decreased slightly when increasing the temperature to 873 K and it was then remained at

the same level despite further temperature change. Probably, some open pores were closed due to the high temperatures, but during the last days at 773 K a leakage increase was again observed. The hydrogen diffusion through the membrane measured at 773 K remained the same after 1880 h and 2000 h.

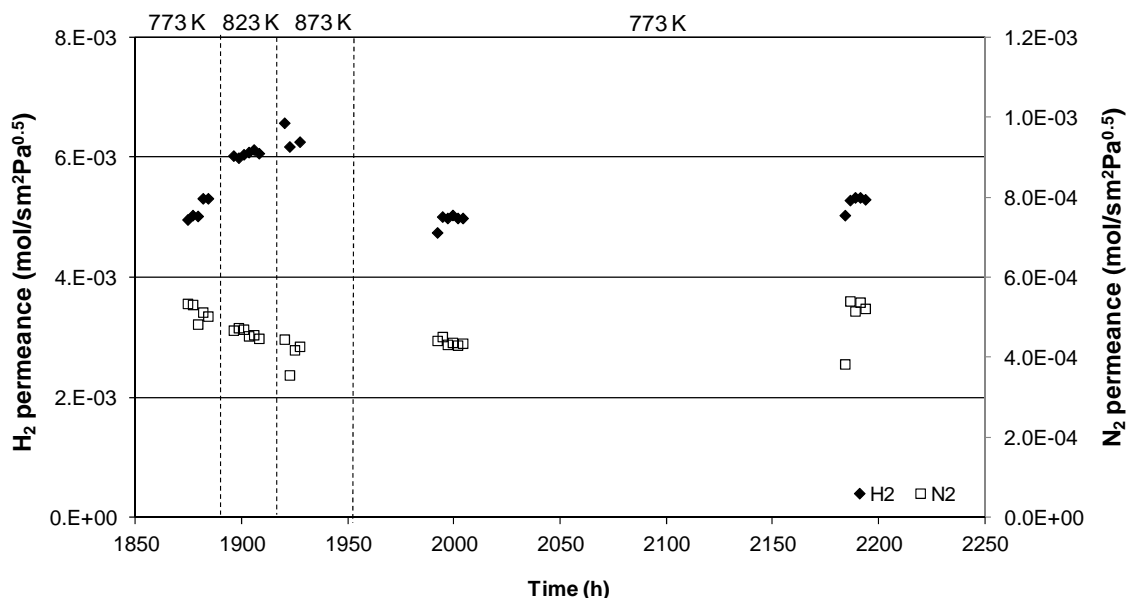


Figure 6.28. Second thermal cycle in hydrogen atmosphere attempt with M8 for hydrogen permeability and leakage recovery (feed pressure=2 bar(g) and sweep at atmospheric pressure).

### 6.5.7 Complete lifetime of the M8 membrane

In this section an overview of the M8 membrane complete lifetime is presented. Pure hydrogen and pure nitrogen flows across the membrane measured at 2 bar pressure difference are given. Results are shown in Figure 6.29. In the “recovery try” segments just the hydrogen flow measurements (see Figure 6.25 and Figure 6.28) made at 773 K are illustrated. This membrane was firstly characterized with pure hydrogen permeation tests involving thermal cycles in inert and hydrogen atmosphere at 673 and 773 K (0 to 500 h). It was then tested at 773 K in hydrogen purification from complex mixtures produced from CPO and wet-CPO in the R1 (770 to 1150 h). Finally, tests with H<sub>2</sub>S addition were performed: H<sub>2</sub>+H<sub>2</sub>S mixture (1200 to 1320 h), CPO process in R1 and purification in MM with H<sub>2</sub>S addition (1345 h), first thermal test (1390 to 1660 h),

H<sub>2</sub>+H<sub>2</sub>S mixture test (1680 to 1780 h), wet-CPO process in R1 and purification in MM with H<sub>2</sub>S addition (1900 h) and second thermal test (1920 to 2190 h).

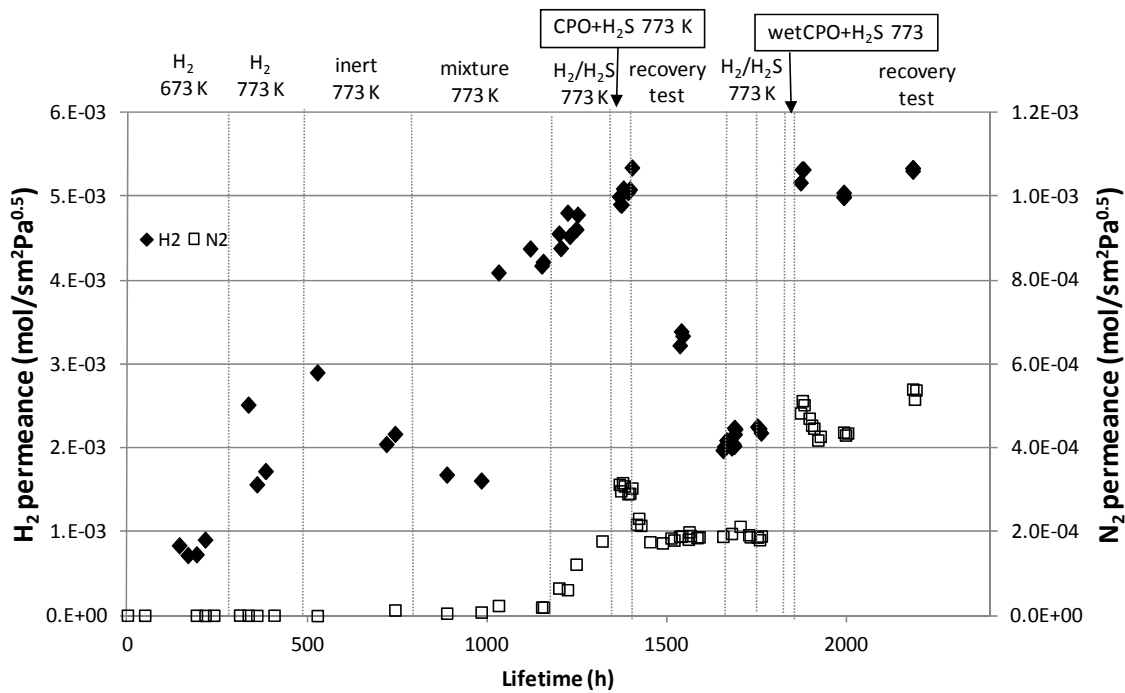


Figure 6.29. Complete lifetime summary of the M8 membrane. Pure hydrogen and nitrogen flows were measured at 2 bar(g) of feed pressure and atmospheric in the sweep.

After 1030 h the hydrogen permeance increased significantly from  $1.6 \cdot 10^{-3} \text{ mol/m}^2\text{sPa}^{0.5}$  to  $4.1 \cdot 10^{-3} \text{ mol/m}^2\text{sPa}^{0.5}$ . Water addition during operation with wet-CPO could have enhanced this variation. The nitrogen flow did not increase, so the metal layer was not damaged. The first test performed with 100 and 40 ppmv H<sub>2</sub>S did not irreversibly deactivate the membrane, but its structure was damaged as the nitrogen flow did increase. The reversible sulphur adsorption is in accordance with results from the literature. In the results from Kim et al. [31] no irreversibly sulphide formation was observed in a fcc Pd<sub>80</sub>Cu<sub>20</sub> membrane. Most probably weak areas, such as grain boundaries, were attacked by the sulphur producing open pores or regions. During the time in H<sub>2</sub>S atmosphere the hydrogen flow decreased, as hydrogen diffusion through metal sulphides is orders of magnitude slower than in pure metals. After the CPO test with H<sub>2</sub>S addition (1410 h), the nitrogen and hydrogen flow increased. In the first thermal recovery test the membrane was kept in hydrogen, but too high temperatures

were applied damaging the membrane and strongly decreasing the hydrogen flow to around  $2.1 \cdot 10^{-3} \text{ mol/m}^2\text{sPa}^{0.5}$ .

After the first permeability recovery test, a second test with 100 and 60 ppmv H<sub>2</sub>S in H<sub>2</sub>:H<sub>2</sub>S mixture was carried out. Similarly, it was observed that the metallic layer was not irreversibly deactivated, but the membrane structure was further damaged and the leaks increased. During wet-CPO with H<sub>2</sub>S addition, the hydrogen recovery increased, most probably due to the positive effect of water addition, and the nitrogen flow was stabilized. In the last recovery period the hydrogen flow was quite stable and the leakage had a slowly increasing tendency, so the membrane performance did not improve.

#### 6.5.8 M8 membrane characterization

After performing the previously explained tests with the M8 membrane, it was taken out from the MM. Visually some remarkable areas were observed on the membrane surface, illustrated in Figure 6.30. There was a split part, leakage, which started 10 mm from the close end cap. The surrounding area of several centimetres was rough. A lot of stresses must have been present to result in those small folds and roughness. During the operation, this close end cap site of the membrane was the final part of the membrane, so most of the hydrogen had diffused to the permeate side before arriving there. Therefore, H<sub>2</sub>S concentration during the performed tests in this area was much higher than the ppm added to the system and could have been as high as 910 ppmv in the test shown in Figure 6.26. This could also be corroborated by the fact that on the other side of the membrane, near the open end cap shown in Figure 6.31, the drying fold of the ceramics can be observed. This can be a suspected weak area of the membrane, but no problems were observed in this area. This area was located at the beginning of the membrane, where the H<sub>2</sub>S concentration was the lowest.

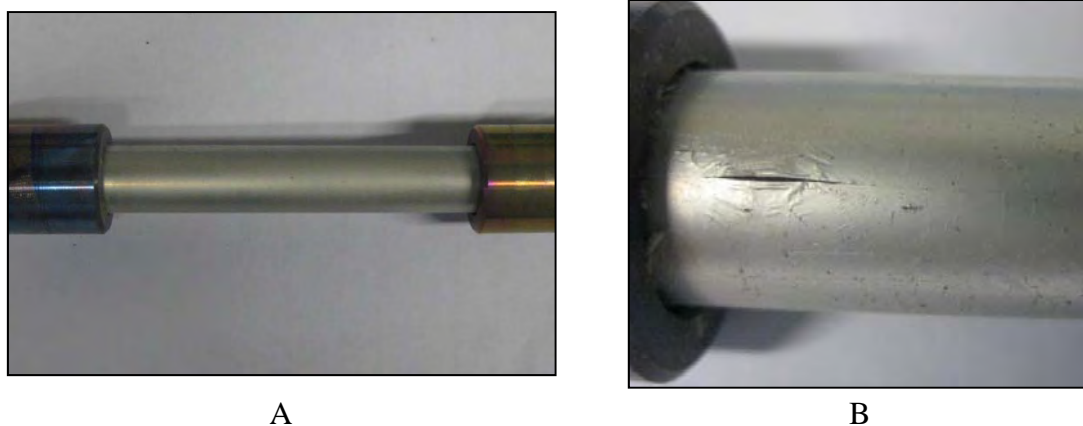


Figure 6.30. M8 membrane general image at the end of its lifetime (A) and in the area exposed to the highest  $\text{H}_2\text{S}$  concentrations (B).

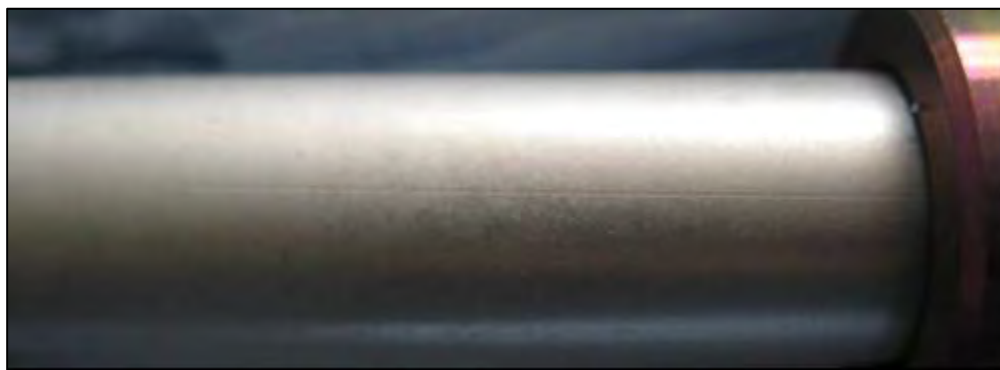


Figure 6.31. M8 membrane image at the end of its lifetime near the area exposed to the lowest  $\text{H}_2\text{S}$  concentrations.

In SEM images structural differences between the membrane areas exposed to high and to low  $\text{H}_2\text{S}$  concentrations were observed, see Figure 6.32. The area exposed to high concentrations, where the split was located, was rougher than the area exposed to lower  $\text{H}_2\text{S}$ . Some open areas, where the metal layer was thinner, could be observed in the  $\times 10,000$  enlargement image of the area exposed to high concentrations. These open pores explain the experimentally observed leakage increase after the  $\text{H}_2\text{S}$  tests. The surface was rougher than before the permeability tests, which was also observed in the literature after  $\text{H}_2\text{S}$  tests with PdCu membranes [32].

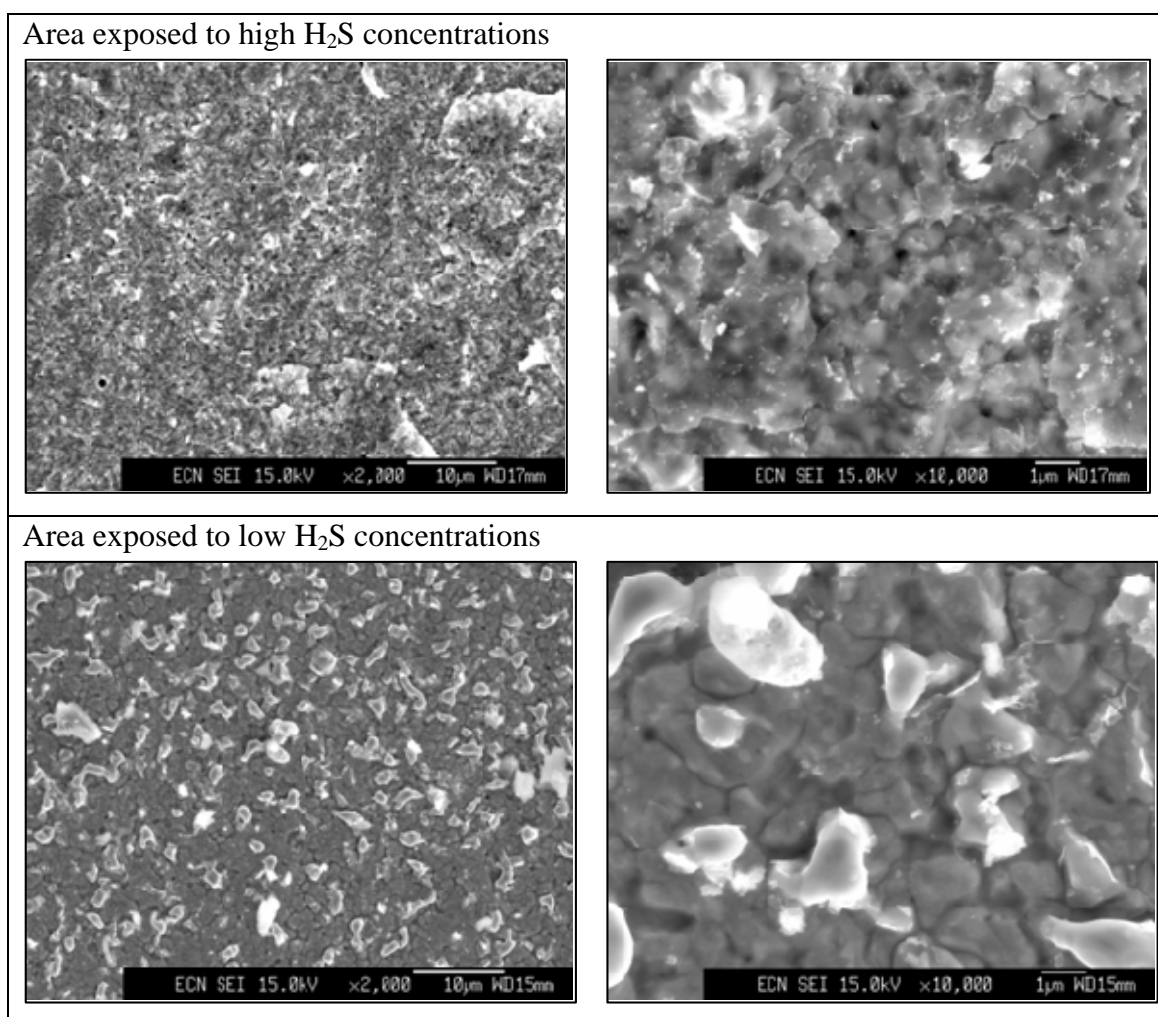


Figure 6.32. SEM images of both endings of the used M8 membrane at x2.000 and x10.000 enlargements.

In Pd foils, pinholes and crack formation have been found in the literature to be caused by the stress generated due to the difference in the lattice constant between Pd and bulk  $Pd_4S$  after  $H_2S$  exposure [33]. In the current work with PdCu membranes no sulphur compounds were found on the surface after the tests. This result is in accordance with others from the literature, where no sulphur was observed in a bcc PdCu membrane at 623 K by SEM and XRD [34] and neither in fcc PdCu phase until 700-1000 ppmv of  $H_2S$  [35]. From atomistic modelling it has been demonstrated that irreversible adsorption of S monolayers on most PdCu alloys is not favoured [36]. Even if no irreversibly adsorbed sulphur compounds were found in the M8 membrane, during operation some Pd could have reversibly formed  $Pd_4S$  and generated the stress that caused the observed splits.

Using EDX technique, the elemental composition was measured at three different positions of the surface areas exposed to low and high H<sub>2</sub>S concentrations. The average composition of the membrane was quite heterogeneous, as shown in Table 6.9. But it seemed that the Pd percentage in the area exposed to high concentrations was higher than in the low concentration area. This could be due to the metallic deposition method employed for membrane preparation. The membranes were located vertically to perform the electroless plating and probably the amount of Cu deposited at the bottom and at the top was not exactly the same. The second explanation to this compositional difference can be metal diffusion during the tests performed with M8 membrane. Metal diffusion can specially be affected by components other than H<sub>2</sub> (i.e. H<sub>2</sub>S). In the M8 membrane a higher Cu concentration was detected in the area that operated with higher H<sub>2</sub>S concentration. Adsorbed sulphur was not detected with the SEM-EDX composition analysis, which supported the conclusion obtained from the experimental tests that the sulphur adsorption on the membrane surface seemed to be reversible.

Table 6.9. Elemental composition measurements performed at three different positions of the M8 samples with SEM-EDX.

High H <sub>2</sub> S concentration area	At.% Pd	At.% Cu
	78.96	19.81
	73.28	23.64
Low H <sub>2</sub> S concentration area	76.07	18.27
	At.% Pd	At.% Cu
	82.09	10.77
	80.83	15.68
	81.52	12.33

The phase structure of the used M8 membrane was studied by XRD. Diffraction measurements were performed in the areas exposed to high and low H<sub>2</sub>S concentrations and both in the external and internal (the support side) surface. Results are depicted in Figure 6.33. Due to the fact that the PdCu layer of the M8 membrane was very thin, 0.87 μm, and the penetration depth of XRD is a few microns, the XRD results in both internal and external surfaces (A and B) were the same. The crystalline structure of the samples was fcc, as expected from the membrane composition. When comparing the diffraction peaks of the M8 sample with that of pure Pd, Figure 6.34, it is observed that



they were very similar. This result was also detected for the M6 membrane, Figure 6.18. Cu atoms are located inside the Pd crystalline net when alloyed and they modify the Pd net parameters only slightly. This effect is well observed at high angles. The peak splitting occurs at the highest angles because of modifications in the surroundings of the Pd coordination net due to the presence of Cu. This means that the Cu modified the structure and this distortion generated the formation of two signals at  $2\theta$  values of 68, 83 and 88.

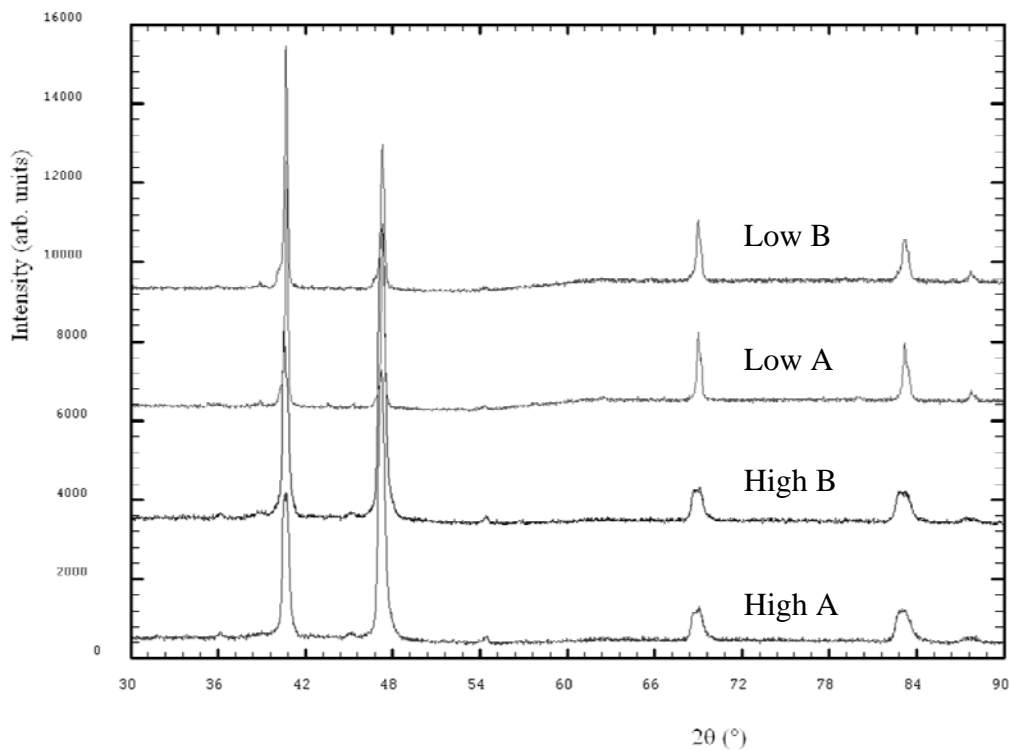


Figure 6.33. XRD diffractogram of the M8 membrane at the end of its lifetime in the area exposed to the high  $H_2S$  concentrations (High) and the low concentrations (Low) in both internal (A) and external (B) surface of the metal layer.

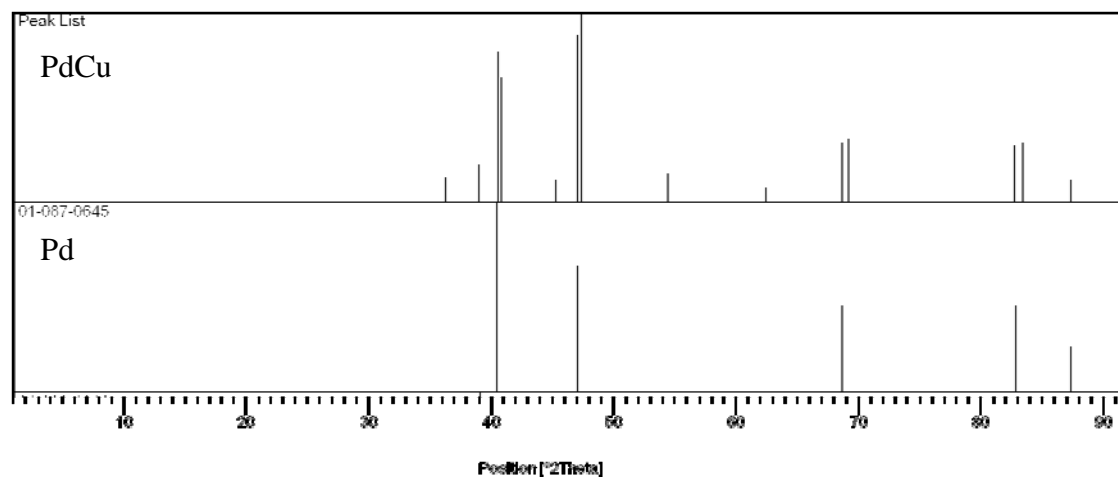


Figure 6.34. Position of the most intense diffractogram peaks observed in the M8 membrane and the characteristic maximums of pure Pd.

In the two X-ray diffraction measurements performed in the area exposed to the highest  $\text{H}_2\text{S}$  concentration (A and B), the splitting of the peaks is more pronounced than in the open cap side. This would involve that the metal alloy of the close cap area had more Cu atoms into the Pd net than in the open cap area. No adsorbed sulphur in the metal foil was detected by XRD, also found in the literature with a  $\text{Pd}_{47}\text{Cu}_{53}$  foil [37].

The used PdCu M8 membrane metal alloy surface was also analysed by XPS. The peaks for  $\text{Cu}^{2+}$  2p<sub>3/2</sub>,  $\text{Cu}^0$  2p<sub>3/2</sub> and  $\text{Pd}^0$  5/2 were measured at binding energies of 932, 952 and 335 eV, respectively [38-40]. The calculated Pd/Cu ratio was higher in the area exposed to high  $\text{H}_2\text{S}$  concentrations than in the one exposed to lower concentrations. Therefore, according to this technique, there was more Cu in the area that operated under low  $\text{H}_2\text{S}$  concentration than in the area operated under high concentration. This result is opposite to the one obtained by EDX and XRD. In work reported by Miller et al. [41] it was observed that S interactions with  $\text{Pd}_{70}\text{Cu}_{30}$  membranes enhanced the Pd surface concentration. The explanation of the differences found between the characterization methods employed can be that due to the small thickness of the PdCu metal foil, XRD and EDX were measuring bulk concentrations, whereas XPS was measuring just the outer surface. Therefore, Pd surface diffusion when operating in high  $\text{H}_2\text{S}$  concentration is in accordance with results found in the literature. And the copper concentration differences between areas exposed to low and high concentrations measured by EDX and XRD are most probably due to the employed plating method.

## 6.6 Discussion

During the first tests of process integration with hydrogen production in R1 and hydrogen purification in MM, coke formation was observed. This problem was solved by changing the MM tube and using a stainless steel tube with the inside wall covered by hard chrome plating. With this covering the contact between the gas mixture and the stainless steel was limited and coke was not generated any more. The hard chrome plated tube was operated for more than 3 years without coke formation.

After solving the coke formation problem, process parameters were optimized to improve hydrogen production and recovery, such as feed pressure and sweep gas flow. The aim of both of them was to increase the hydrogen partial pressure difference across the membrane to enhance the hydrogen recovery. The hydrogen production step was unfavoured by high pressure, and the use of sweep gas is expensive, so they needed to be optimized. The highest hydrogen recovery in the MM was obtained with 3.5 bar(g) feed pressure and atmospheric pressure in the permeate side using a sweep gas flow equal to around 20 % of the flow produced in R1 and fed to the MM.

The membrane performance under complex mixtures was analysed carrying out both CPO and wet-CPO processes in the R1 at a space velocity of  $600 \text{ h}^{-1}$  ( $\text{g}_{\text{gas}} \cdot \text{h}^{-1} \cdot \text{g}_{\text{cat}}^{-1}$ ) with 0.35 g of catalyst. The obtained hydrogen recovery in the MM was around 60-65 % regardless the composition of the mixture, which depended on the hydrogen production process carried out in the catalytic reactor R1. This hydrogen recovery was around 10-20 percentage points lower than obtained with the same hydrogen percentage in a  $\text{H}_2:\text{N}_2$  mixture. Mixture components like CO,  $\text{CO}_2$  and  $\text{CH}_4$  seemed to have no dramatically negative effect on the hydrogen permeance at the tested concentrations, whereas water addition seemed to have a positive effect on it. No coke formation was observed on the membranes, which could have caused a hydrogen permeance decrease. The operating temperature of the membrane was quite high, 773 K, which could have also minimized the adsorption of inhibitors on the metallic surface.

From  $\text{H}_2\text{S}$  addition tests performed with 40, 60 and 100 ppmv of  $\text{H}_2\text{S}$  in  $\text{H}_2:\text{H}_2\text{S}$  mixtures, it was concluded that sulphur was not irreversibly adsorbed on the metallic surface, but it affected the metallic structure. The hydrogen permeance was recovered

when taking out the sulphur compound from the system, but the nitrogen flow through the membrane increased. Open pores were detected by SEM images in the membrane area where the  $\text{H}_2\text{S}$  concentration was higher than the feed ppm. This indicated that sulphur atoms mainly attacked weak areas producing open structures. Afterwards nitrogen flow did not further increase, but the hydrogen permeance decreased.

Two different mechanisms may be responsible for the inhibition of hydrogen transport through the membranes with  $\text{H}_2\text{S}$ : poisoning of the catalytic dissociation of  $\text{H}_2$  at the surface, which was directly observed when  $\text{H}_2\text{S}$  was added to the system; and reduced permeability of hydrogen through the bulk of the membrane, which was observed in the lifetime summary. The temperature employed in the tests, 773 K, and the fact that the membrane was fcc, being more resistant than the bcc phase to sulphur, could have been the reasons for the reversibility of sulphur adsorption.  $\text{H}_2\text{S}$  addition increased the nitrogen flow through the membrane, which was facilitated by the thin metal layer of the membrane (0.866  $\mu\text{m}$ ). This flow could be reduced keeping the membrane under hydrogen atmosphere at high temperature, but temperatures around 873 K damaged the metal structure and reduced the hydrogen permeability.

When operating in complex mixtures with  $\text{H}_2\text{S}$  addition, the hydrogen recovery by the membrane decreased but to a lesser extent than when  $\text{H}_2:\text{H}_2\text{S}$  mixtures were used. In complex mixtures, gases other than hydrogen do not permeate through the membrane, implying that the  $\text{H}_2\text{S}$  concentration was lower throughout the membrane than in  $\text{H}_2:\text{H}_2\text{S}$  tests. Nevertheless, the membrane performance was strongly affected also when  $\text{H}_2\text{S}$  was added to a water containing feed.

In none of the three characterization techniques employed with the used M8 membrane adsorbed sulphur was observed, which was also expected from the hydrogen permeability tests carried out with  $\text{H}_2\text{S}$  addition. This observation is in accordance with the experimental post mortem SEM-EDX results. The prepared PdCu membranes seemed to be able to operate with temporary addition of 100 ppmv  $\text{H}_2\text{S}$ , or lower, without irreversibly decreasing the hydrogen permeability, but affecting their selectivity.

Two of the membranes were strongly affected by uncontrolled cooling that occurred due to power failures in the system. Controlled cooling and heating, even in hydrogen, did not seem to affect their properties, but after the uncontrolled cooling leakage appeared and the metal layer was peeled off. In the membrane tested with H<sub>2</sub>S addition, no power failures occurred and its lifetime was longer. In this membrane, the cause for its continuous decrease of selectivity was the sulphur attack to grain or pore boundaries. When the third membrane was taken out from the module a split was observed in the area where the H<sub>2</sub>S concentration was the highest.

## Reference list

- [1] C. M. Chun, S. Desai, T. A. Ramanarayanan, *ECS Trans.* **2012**, *41*, 61.
- [2] C. Chen, C. Zhou, G. Hu, N. Lei, *Nanjing Gongye Daxue Xuebao, Ziran Kexueban* **2008**, *30*, 25, 37.
- [3] D. Mendes, V. Chibante, J. M. Zheng, S. Tosti, F. Borgognoni, A. Mendes, L. M. Madeira, *Int. J. Hydrogen Energy* **2010**, *35*, 12596.
- [4] T. B. Flanagan, D. Wang, K. Shanahan, *Sep. Purif. Technol.* **2011**, *79*, 385.
- [5] D. Wang, T. B. Flanagan, K. L. Shanahan, *J. Membr. Sci.* **2005**, *253*, 165.
- [6] T. B. Flanagan, S. Luo, J. D. Clewley, *J. Alloys Compd.* **2003**, *356-357*, 13.
- [7] H. Amandusson, L.-G. Ekedahl, H. Dannetun, *Appl. Surf. Sci.* **2000**, *153*, 259.
- [8] T. H. Nguyen, S. Mori, M. Suzuki, *Chem. Eng. J.* **2009**, *155*, 55.
- [9] F. C. Gielens, R. J. J. Knibbeler, P. F. J. Duysinx, H. D. Tong, M. A. G. Vorstman, J. T. F. Keurentjes, *J. Membr. Sci.* **2006**, *279*, 176.
- [10] J. Hulme, M. Komaki, C. Nishimura, J. Gwak, *Curr. Appl. Phys.* **2011**, *11*, 972.
- [11] X. Zhang, G. Xiong, W. Yang, *Stud. Surf. Sci. Cat.* **2007**, *167*, 219.
- [12] H. Li, J. W. Dijkstra, J. A. Z. Pieterse, J. Boon, R. W. van den Brink, D. Jansen, *J. Membr. Sci.* **2010**, *363*, 204.
- [13] A. S. Augustine, Y. H. Ma, N. K. Kazantzis, *Int. J. Hydrogen Energy* **2011**, *36*, 5350.
- [14] H. Li, A. Goldbach, W. Li, H. Xu, *J. Membr. Sci.* **2008**, *324*, 95.
- [15] Y. S. Cheng, M. A. Peña, K. L. Yeung, *J. Taiwan Inst. Chem. Eng.* **2009**, *40*, 281.
- [16] M. Abdollahi, J. Yu, P. K. T. Liu, R. Ciora, M. Sahimi, T. T. Tsotsis, *J. Membr. Sci.* **2012**, *390-391*, 32.
- [17] A. Basile, S. Campanari, G. Manzolini, A. Iulianelli, T. Longo, S. Liguori, M. De Falco, V. Piemonte, *Int. J. Hydrogen Energy* **2011**, *36*, 1531.
- [18] S. Tosti, L. Bettinali, S. Castelli, F. Sarto, S. Scaglione, V. Violante, *J. Membr. Sci.* **2002**, *196*, 241.
- [19] A. Kulprathipanja, G. O. Alptekin, J. L. Falconer, J. D. Way, *Ind. Eng. Chem. Res.* **2004**, *43*, 4188.
- [20] S. K. Ryi, J. S. Park, S. H. Kim, S. H. Cho, D. W. Kim, K. Y. Um, *Sep. Purif. Technol.* **2006**, *50*, 82.
- [21] H. Gao, S. Lin, Y. Li, B. Zhang, *J. Membr. Sci.* **2005**, *265*, 142.
- [22] S. E. Nam, K. H. Lee, *J. Membr. Sci.* **2001**, *192*, 177.
- [23] N. Pomerantz, Y. H. Ma, *J. Membr. Sci.* **2011**, *370*, 97.
- [24] J. Y. Yang, M. Komaki, C. Nishimura, *Int. J. Hydrogen Energy* **2007**, *32*, 1820.
- [25] M. S. Islam, M. M. Rahman, S. Ilias, *Int. J. Hydrogen Energy* **2012**, *37*, 3477.
- [26] A. Goldbach, L. Yuan, H. Xu, *Sep. Purif. Technol.* **2010**, *73*, 65.
- [27] O. Iyoha, R. Enick, R. Killmeyer, B. Howard, M. Ciocco, B. Morreale, *J. Membr. Sci.* **2007**, *306*, 103.
- [28] J. Y. Yang, C. Nishimura, M. Komaki, *J. Membr. Sci.* **2008**, *309*, 246.
- [29] K. E. Coulter, J. D. Way, S. K. Gade, S. Chaudhari, G. O. Alptekin, S. J. de Voss, S. N. Paglieri, B. Pledger, *J. Membr. Sci.* **2012**, *405-406*, 11.
- [30] A. Shamsi, *Catal. Today* **2009**, *139*, 268.

- [31] Ki Chul Kim, Sung Gu Kang, David S. Sholl, *Ind. Eng. Chem. Res.* **2012**, *51*, 301.
- [32] T. A. Peters, T. Kaleta, M. Stange, R. Bredeesen, *Catal. Today* **2012**, *193*, 8.
- [33] Chao-Huang Chen, Yi Hua Ma, *J. Membr. Sci.* **2010**, *362*, 535.
- [34] C. P. O'Brien, B. H. Howard, J. B. Miller, B. D. Morreale, A. J. Gellman, *J. Membr. Sci.* **2010**, *349*, 380.
- [35] P. R. Subramanian, D. E. Laughlin, *J. Phase Equilib.* **1991**, *12*, 231.
- [36] S. M. Opalka, O. M. Løvvik, S. C. Emerson, Y. She, T. H. Vanderspurt, *J. Membr. Sci.*, **2011**, *375*, 96.
- [37] C. P. O'Brien, B. H. Howard, J. B. Miller, B. D. Morreale, A. J. Gellman, *J. Membr. Sci.* **2010**, *349*, 380.
- [38] H. Gao, S. Lin, Y. Li, B. Zhang, *J. Membr. Sci.* **2005**, *265*, 142.
- [39] E. B. Fox, S. Velu, M. H. Engelhard, Y. H. Chin, J. T. Miller, J. Kropf, C. Song, *J. Catal.* **2008**, *260*, 358.
- [40] M. Khanuja, B. R. Mehta, S. M. Shivaprasad, *Thin Solid Films* **2008**, *516*, 5435.
- [41] J. B. Miller, B. D. Morreale, A. J. Gellman, *Surf. Sci.* **2008**, *602*, 1819.





# **7. CONCLUSIONS AND FUTURE RESEARCH**

This chapter reviews the achievements fulfilled after the research carried out, shows how the work presented in this thesis meets the planned objectives and makes some suggestions for future work.



## Evaluation of the results

The aim of the work presented in this thesis was three-fold: i) to prepare Ni-based catalysts for hydrogen production from methane, ii) to prepare PdCu hydrogen selective membranes for hydrogen purification and iii) to integrate both processes in a hydrogen production and purification system. Each main objective was divided into different sub-topics as depicted in Figure 7.1. The catalysts for hydrogen production from methane were prepared by wet-impregnation over basic and acid supports, their activity was analysed in CPO, wet-CPO and SR processes at different operating conditions and they were characterized using composition, structural and morphological techniques (Chapter 4). PdCu membranes for hydrogen purification were prepared by electroless plating and characterized with permeability tests in pure hydrogen and with morphologic techniques (Chapter 5). When integrating both processes several operating parameters had to be optimized and then, hydrogen recovery tests from complex mixtures were carried out analysing the effect hydrogen dilution and compounds other than hydrogen had on the membrane performance (Chapter 6). Finally, a sulphur compound was added to the mixture fed to the integrated system and it allowed studying its effect on catalyst activity, membrane performance and hydrogen recovery (Chapter 6).

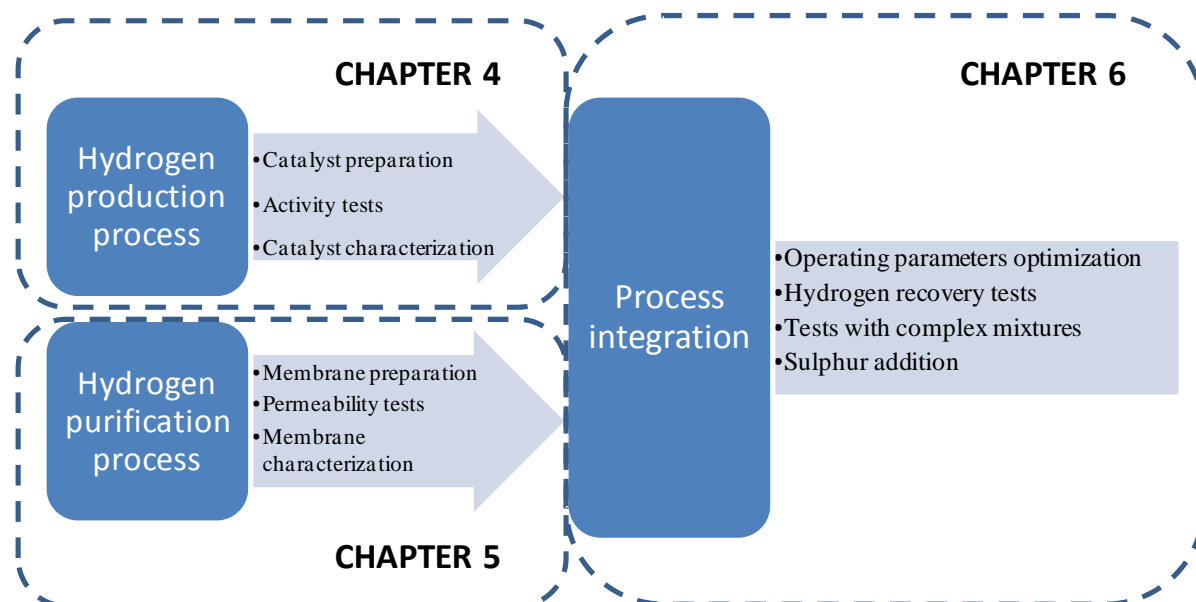


Figure 7.1. Structure and approach of the research presented in this thesis.

Activity, performance and characterization results analysis and discussion allowed obtaining the conclusions that are enumerated below.

#### Testing facility development

1. A versatile bench-scale pilot plant was designed, built and operated, in order to test various process configurations.
2. Coke formation problems located in stainless steel areas in contact with CO containing gases took place after high residence times and could be prevented with hard chromium plating. This treatment kept its properties for at least three years under operation.

#### Hydrogen catalytic production from methane

3. The prepared Ni-based catalysts over MgO and Al<sub>2</sub>O<sub>3</sub> supports presented conversion values close to the equilibrium ones at 1073 K and 1200 h<sup>-1</sup> in CPO process. No remarkable differences were observed when increasing the Ni content from 30 to 40 wt% or between both supports. Both catalysts showed low BET surface area.
4. External and internal diffusion limitations were predicted for CPO, where internal limitations appeared to be more pronounced, implying that the use of supports with higher porosity particle size would be beneficial.
5. Methane reforming processes presented low conversion with the prepared catalysts, especially in SR. With low amounts of water in wet-CPO, S/C=0.5, conversion was around 85 % with an increase in the produced hydrogen yield.
6. At the operating conditions applied, a better performance of the MgO-based catalysts than the Al<sub>2</sub>O<sub>3</sub>-based one was observed taking into account both conversion and stability.
7. The Ni/MgO catalysts showed high metal dispersion as observed by SEM and TEM images and solid solution formation was detected using XRD. This

implied that nickel reduction was more difficult as observed in TPR, XPS and activity tests at 898 K. The nickel reduction when supported on MgO was difficult but the conversion results showed that there was enough reduced Ni as to reach conversions close to the equilibrium in CPO.

8. The 40Ni/MgO catalyst was not deactivated when operating with 33 ppmv of H<sub>2</sub>S during 6 hours in CPO or wet-CPO with S/C=0.5.
9. The Ni/Al<sub>2</sub>O<sub>3</sub> catalyst also presented good metal dispersion in SEM and TEM images and some sintering of crystallites was observed by XRD. This could be the main reason for deactivation after wet-CPO and SR process. In the TPR analysis the catalyst showed a main peak of NiO, and XPS data showed that a fraction of this NiO was strongly interacting with the support as aluminates.

#### Hydrogen purification process with PdCu membranes

10. Thin, dense and highly hydrogen permeable and selective PdCu membranes were prepared by plating Cu over Pd membranes using the quick and easy electroless plating method. The main difficulty was to determine the composition of the prepared membranes. Around 20 hours of alloying were enough to obtain membranes with high and stable permeance, even if incomplete alloying was observed in SEM images.
11. Membranes in the range of 44-82 wt% Pd were prepared with thicknesses between 0.9-1.7 μm. They presented good thermal stability with controlled cooling, even under hydrogen atmosphere. Both surface and bulk diffusion processes were responsible for hydrogen flux resistance through the membranes due to their low thickness.
12. The highest permeance was observed with the 60 wt% Pd membrane,  $4.4 \cdot 10^{-3}$  mol/(sm<sup>2</sup>Pa<sup>0.5</sup>), and it increased with temperature from 673 to 773 K. Temperatures higher than 873 K irreversibly deteriorated the membranes.

13. Once the membranes were activated, to take them out from the system and keep them in air at room temperature seemed to affect their hydrogen diffusion capacity.
14. Uncontrolled cooling induced structural changes that led to pore formation, and therefore the hydrogen selectivity decreased. In all the cases the stress ended in metal layer detachment.
15. H<sub>2</sub>S was not irreversibly adsorbed on the PdCu membranes, but it attacked grain boundaries decreasing the membrane selectivity. The prepared membranes could operate with complex mixtures containing less than 100 ppmv of H<sub>2</sub>S. The hydrogen permeability was recovered when the sulphur compound was eliminated from the feed.
16. The membrane crystalline structure observed by XRD was a Pd net with copper atoms in it. This solid solution was formed during the alloying and was not affected by complex mixtures or H<sub>2</sub>S addition.
17. The Pd superficial diffusion of Pd from regions with higher H<sub>2</sub>S content to regions with lower content seems to occur based on XPS observations.

#### Process integration

18. The optimum operating conditions achieved after process integration in the designed bench-scale pilot plant were 3.5 bar(g) feed pressure, atmospheric pressure in the sweep side, R1 at 1073 K, 773 K in the membrane module and a sweep gas flow equal to 20 % of the flow fed to the membrane module.
19. When purifying hydrogen from complex mixtures, the PdCu membranes presented a stable hydrogen recovery, around 60-65 %, regardless of the complex mixture composition.
20. Water presence in the integrated process seemed to have a positive effect on the hydrogen recovery through the membranes, overlaying the negative effect of the CO.

21. Membrane deactivation due to coke formation was not observed during the tests carried out, most probably due to water presence and high temperature that prevented coke precursor adsorption on the surface.

### **Future work**

This Ph.D thesis opens future possible research lines. Some of them are presented below.

- Further development of Ni-based catalysts improving their properties for CPO, wet-CPO and SR processes; for example with the incorporation of promoters or testing other preparation methods to increase the active species dispersion.
- Catalysts activity tests and process integration studies using natural gas from the distribution mains.
- Longer activity tests with the most promising catalysts to check their stability, including experiments with H<sub>2</sub>S in the feeds.
- Incorporation of a selective oxygen membrane in the catalytic reactor that would allow to decrease hot spot formation in catalyst beds and to decrease hydrogen dilution by N<sub>2</sub> in the mixture fed to the membrane module.
- Longer thermal cycling tests with the membranes to get deeper information about the effect of uncontrolled and controlled cooling on their performance.
- Analysis of the membrane behaviour when purifying hydrogen from complex mixtures with H<sub>2</sub>S addition with longer tests.
- Comparison of PdCu membrane behaviour purifying hydrogen from complex mixtures and with H<sub>2</sub>S addition with other Pd or Pd-alloy membranes such as PdAg or PdAu.





# **APPENDIX**

**Publications related to the present Doctoral Thesis**



In the present Appendix the articles related to the present doctoral thesis are listed, as well as the contributions to different conferences.

### **Publications**

E. Acha, J. Requies, V.L. Barrio, J.F. Cambra, M.B. Güemez, P.L. Arias, *Water effect in hydrogen production from methane*, International Journal of Hydrogen Energy, 35, 2010, 11525-32.

E. Acha, Y.C. van Delft, J. Overbeek, P.L. Arias, J.F. Cambra, *Copper deposition on Pd membranes by electroless plating*, International Journal of Hydrogen Energy, 36, 2011, 13114-21.

E. Acha, J. Requies, V.L. Barrio, J.F. Cambra, M.B. Güemez, P.L. Arias, Y.C. van Delft, *PdCu membrane applied for hydrogen production from methane*. Journal of Membrane Science, 415-416, 2012, 66-74.

E. Acha, J. Requies, V.L. Barrio, J.F. Cambra, M.B. Güemez, P.L. Arias, Y.C. van Delft, *PdCu membrane integration and lifetime in the production of hydrogen from methane*. International Journal of Hydrogen Energy, preparing the proof for being published.

Note: Section 6.5. of this thesis will be submitted for publication.

### **Presentations at conferences**

*Producción de gas de síntesis a partir de gas natural mediante catalizadores de Ni-álumina en una planta piloto provista con un reactor de membrana selectiva*, GEO2, Bilbao, Spain, 2008. POSTER

*Water effect in hydrogen production from methane*. Hyceltec 2011, Vila Real, Portugal, 2009. ORAL

*Comparison of CPO, wet-CPO and SR of methane on Nickel catalysts*, EuropaCat IX, Salamanca, Spain, 2009. POSTER

*PdCu membrane integration in a hydrogen production process from methane*, Hypothesis IX, San José, Costa Rica, 2011. ORAL

*PdCu membranes by electroless plating for hydrogen purification*, ICOM, Amsterdam, The Netherlands, 2011. ORAL

*PdCu membrane integration in hydrogen production from natural gas process*, Hyceltec 2011, Zaragoza, Spain, 2011. ORAL

*Hydrogen purification with hydrogen selective ceramic membranes*, GERG-AGATEC2011, Copenhagen, Denmark, 2011. POSTER

*PdCu membranes for hydrogen purification in a CPO produced mixture*, LCES-2011, Dalian, China, 2011. Invited oral

*H<sub>2</sub>S addition effect on hydrogen production from methane*, GERG-AGATEC2012, Brussels, Belgium, 2012. ORAL

*H<sub>2</sub>S effect on PdCu membrane*, 12<sup>th</sup> ICIM, Enschede, The Netherlands, 2012. ORAL

*H<sub>2</sub>S effect on hydrogen production and purification process*, CHISA 2012, Prague, Czech Republic, 2012. ORAL



